Alma Mater Studiorum – Università di Bologna

DOTTORATO DI RICERCA IN

Scienze Chimiche

Ciclo XXII

Settori scientifici-disciplinari di afferenza: CHIM/02, CHIM/03

Electrode Materials for Ionic Liquid Based-Supercapacitors

Presentata da: **Mariachiara Lazzari**

Coordinatore Dottorato
Prof. Giuliano Longoni

Relatore
Prof. Marina Mastragostino

Correlatore
Dr. Francesca Soavi

Esame finale anno 2010

Abstract

The development of safe, high energy and power electrochemical energy-conversion systems can be a response to the worldwide demand for a clean and low-fuel-consuming transport. This thesis work, starting from a basic studies on the ionic liquid (IL) electrolytes and carbon electrodes and concluding with tests on large-size IL-based supercapacitor prototypes demonstrated that the IL-based asymmetric configuration (AEDLCs) is a powerful strategy to develop safe, high-energy supercapacitors that might compete with lithium-ion batteries in power assist-hybrid electric vehicles (HEVs). The increase of specific energy in EDLCs was achieved following three routes: i) the use of hydrophobic ionic liquids (ILs) as electrolytes; ii) the design and preparation of carbon electrode materials of tailored morphology and surface chemistry to feature high capacitance response in IL and iii) the asymmetric double-layer carbon supercapacitor configuration (AEDLC) which consists of assembling the supercapacitor with different carbon loadings at the two electrodes in order to exploit the wide electrochemical stability window (ESW) of IL and to reach high maximum cell voltage (V_{max}).

Among the various ILs investigated the N-methoxyethyl-N-methylpyrrolidinium bis(trifluoromethanesulfonyl)imide ($PYR_{1(2O1)}TFSI$) was selected because of its hydrophobicity and high thermal stability up to 350 °C together with good conductivity and wide ESW, exploitable in a wide temperature range, below 0°C. For such exceptional properties $PYR_{1(2O1)}TFSI$ was used for the whole study to develop large size IL-based carbon supercapacitor prototype.

This work also highlights that the use of ILs determines different chemical-physical properties at the interface electrode/electrolyte with respect to that formed by conventional electrolytes. Indeed, the absence of solvent in ILs makes the properties of the interface not mediated by the solvent and, thus, the dielectric constant and double-layer thickness strictly depend on the chemistry of the IL ions.

The study of carbon electrode materials evidences several factors that have to be taken into account for designing performing carbon electrodes in IL. The heat-treatment in inert atmosphere of the activated carbon AC which gave ACT carbon featuring ca. 100 $F g^{-1}$ in IL demonstrated the importance of surface chemistry in the capacitive response of the carbons in hydrophobic ILs. The tailored mesoporosity of the xerogel carbons is a key

parameter to achieve high capacitance response. The CO_2-treated xerogel carbon X3a featured a high specific capacitance of 120 F/g in $PYR_{14}TFSI$, however, exhibiting high pore volume, an excess of IL is required to fill the pores with respect to that necessary for the charge-discharge process. Further advances were achieved with electrodes based on the disordered template carbon DTC7 with pore size distribution centred at 2.7 nm which featured a notably high specific capacitance of 140 F g^{-1} in $PYR_{14}TFSI$ and a moderate pore volume, $V_{>1.5\ nm}$ of 0.70 cm^3 g^{-1}.

This thesis work demonstrated that by means of the asymmetric configuration (AEDLC) it was possible to reach high cell voltage up to 3.9 V. Indeed, IL-based AEDLCs with the X3a or ACT carbon electrodes exhibited specific energy and power of ca. 30 Wh kg^{-1} and 10 kW kg^{-1}, respectively. The DTC7 carbon electrodes, featuring a capacitance response higher of 20%-40% than those of X3a and ACT, respectively, enabled the development of a $PYR_{14}TFSI$-based AEDLC with specific energy and power of 47 Wh kg^{-1} and 13 kW kg^{-1} at 60°C with V_{max} of 3.9 V.

Given the availability of the ACT carbon (obtained from a commercial material), the $PYR_{1(2O1)}TFSI$-based AEDLCs assembled with ACT carbon electrodes were selected within the EU ILHYPOS project for the development of large-size prototypes. This study demonstrated that $PYR_{1(2O1)}TFSI$-based AEDLC can operate between -30°C and +60°C and its cycling stability was proved at 60°C up to 27,000 cycles with high V_{max} up to 3.8 V. Such AEDLC was further investigated following USABC and DOE FreedomCAR reference protocols for HEV to evaluate its dynamic pulse-power and energy features. It was demonstrated that with V_{max} of 3.7 V at $T \geq 30$ °C the challenging energy and power targets stated by DOE for power-assist HEVs, and at $T \geq 0$ °C the standards for the 12V-TSS and 42V-FSS and TPA 2s-pulse applications are satisfied, if the ratio $w_{module}/w_{SC} = 2$ is accomplished, which, however, is a very demanding condition.

Finally, suggestions for further advances in IL-based AEDLC performance were found. Particularly, given that the main contribution to the ESR is the electrode charging resistance, which in turn is affected by the ionic resistance in the pores that is also modulated by pore length, the pore geometry is a key parameter in carbon design not only because it defines the carbon surface but also because it can differentially “amplify” the effect of IL conductivity on the electrode charging-discharging process and, thus, supercapacitor time constant.

Table of Contents

Chapter 1
Introduction

1.1. Supercapacitors as electrochemical energy storage/conversion systems

Supercapacitors are electrochemical energy storage/conversion systems of high specific power, able to be charged and discharged in a short time (in the order of seconds). Supercapacitors are composed of two electrodes immersed in an electrolyte, with an ion permeable separator located between the electrodes [1.1].

The electrodes for supercapacitors can be divided into two main classes: the carbonaceous electrodes in which the main charge/discharge process is electrostatic and the pseudocapacitive electrodes in which the charge/discharge process is faradic and fast reversible redox reactions occur. Figure 1.1 reports a series of carbon based- and pseudocapacitive based-electrodes with the corresponding capacitance response.

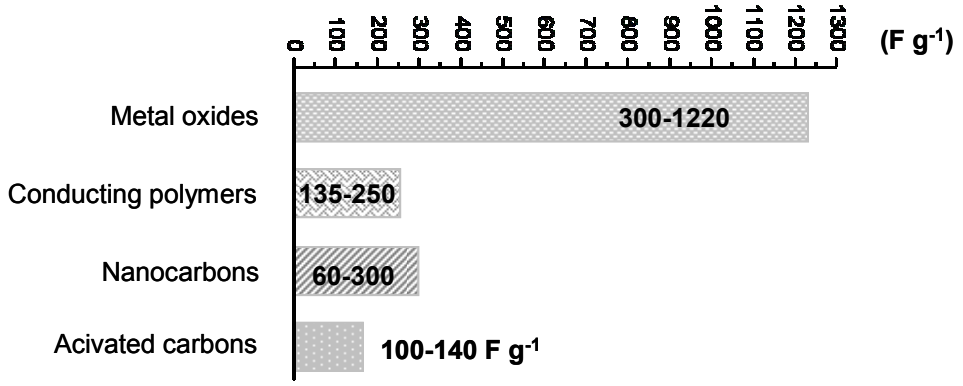

Figure 1.1. Various electrode materials for supercapacitors with indication of their specific capacitance [1.6].

Pseudocapacitive materials have the great advantage to achieve higher values of specific capacitance than those of double-layer carbon electrodes. Indeed, while in the latter the charge process involves only the electrode surface, in the former the charge is stored in the bulk electrode material. The main pseudocapacitive materials are based on electronically conducting polymers, mainly thiophene-based polymers [1.2], and transition metal oxides such as RuO_2, which can reach capacitance values up to more than 600 F g^{-1} at the expenses of high cost [1.3]. Recently, several studies have been devoted to MnO_2 as a low-

cost alternative to RuO_2, which delivers capacitances even higher than 400 F g^{-1} when it is deposited as thin film [1.4]. However, both these oxides operate in aqueous electrolyte, which constrains the operative cell voltage below 1.5 V [1.5].

The supercapacitors can be assembled with several configurations such as electrochemical double layer supercapacitor (EDLC) where the two electrodes are composed of carbon, the hybrid supercapacitor where one electrode is made of carbon and the other is composed of pseudocapacitive material and the pseudocapacitive supercapacitor where both the electrodes consist of pseudocapacitive materials. The electrochemical double layer supercapacitors (EDLCs) store charge in the double-layer without chemical reactions and physical changes in the electrode materials and, hence, the charge/discharge processes are highly reversible and fast. This implies the advantage to achieve long cycle-life (at least 500,000 cycles) and high power.

The maximum energy (E_{max}) and power (P_{max}) of supercapacitors are calculated according to eq. 1.1 and 1.2, respectively.

$$E_{max} = 3/8\ C_{SC} V_{max}^2 \qquad \text{(eq. 1.1)}$$

$$P_{max} = V_{max}^2 / 4\ ESR \qquad \text{(eq. 1.2)}$$

where C_{SC} is expressed in Farads, V_{max} is the maximum cell voltage in Volts and ESR is the equivalent series resistance in ohms. The eq. 1.1 is referred to the maximum energy delivered between V_{max} and $V_{max}/2$.

The value of V_{max} is mainly limited by the electrolyte stability; as reported in Table 1.1 the aqueous electrolytes (acids or alkalis) allow V_{max} of just 1.0-1.5 V while organic electrolytes (propylene carbonate or acetonitrile containing dissolved quaternary alkylammonium salts) make possible V_{max} of 3 V at maximum. In the last decade a new kind of electrolytes based on ionic liquids (ILs) is having much attention since they make feasible to largely overcome V_{max} reached by conventional electrolytes with a consequence of a significantly increase of the supercapacitor specific energy. This is possible because the electrochemical stability windows (ESWs) of ILs is largely higher than that of conventional organic electrolytes [1.1, 1.3, 1.5, 1.7].

Figure 1.2 reports the so called 'Ragone plot' of typical energy storage and conversion systems in terms of their specific energy and power. Supercapacitors are able to store an amount of energy markedly higher than that of electrolytic capacitors and lower than that of batteries and fill the gap of several orders of magnitude in energy and power

between such electrochemical devices. In the supercapacitors group, EDLCs are those featuring the highest power and pseudocapacitors are those featuring the highest energy, however the latter may suffer for long cycle-life due to reversibility of redox processes.

Table 1.1. Properties of various electrolytes [1.5].

Electrolyte	**Density** $g\ cm^{-3}$	**Resistivity** $\Omega\ cm$	V_{max} **V**
KOH	1.29	1.9	1.0
Sulfuric acid	1.2	1.35	1.0
Propylene carbonate	1.2	52	2.5-3.0
Acetonitrile	0.78	18	2.5-3.0
ILs	1.3-1.5	125 (25°C) 28 (100°C)	4.0 3.25

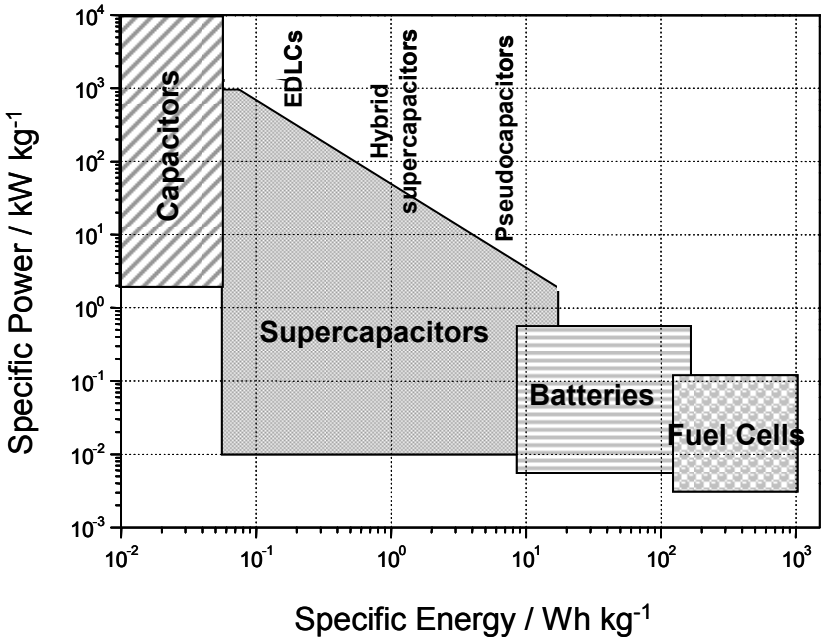

Figure 1.2. Ragone plot for various energy storage and conversion devices.

First patents on supercapacitors based on high surface area carbon electrodes date back to 1957. They have been largely used in consumer electronic products where they mainly serve as backup sources for memories, microcomputers, system boards and clocks [1.3]. Over the last years many applications have emerged in the frame of electric energy

production and sustainable transportation. In particular, supercapacitors are called upon for those functions that do not require high charge storage capacity, but for which high recharge rate and long cycle life of the storage system are crucial. Supercapacitors can be used to enhance electric grid reliability and regulation by buffering the small and rapid ($\leq$ minute) fluctuations in electric power and they can provide short-time uninterruptible power in UPS (uninterruptible power supply) systems of commercial and public buildings. They are also increasingly exploited in hybrid diesel-electric seaport cranes being used to load and unload container ships and where they capture energy otherwise wasted as heat in the repetitious up and down movement of heavy shipping containers.

In transportation, supercapacitors can store energy from regenerative braking in hybrid electric vehicles (HEVs) and they are already being introduced for such purpose in light rail systems. They can also provide and/or assist power train in heavy electric vehicles (EVs) and HEVs of limited driving range with frequent stop-and-go, such as in demonstrative electric buses operating in Moscow or in the hybrid city transit service in southern California [1.8-1.9]. Currently great efforts are devoted to the development of electrochemical energy storage devices for power assist-HEVs. Such application involves that the internal combustion engine operates in synergic combination with the electrochemical system in a way that the engine is maintained at constant regime so as to work at the maximum efficiency with the consequences of fuel economy and pollution emission reduction. The requirements for power assist-HEV application are a discharge pulse power of at least 625 W kg^{-1} for 10 s with a total available energy of 7.5 Wh kg^{-1}, energy efficiency >90% with temperature operating range -30/52°C and it is of primary importance safety [1.10].

Figure 1.3 shows the energy and power performance evaluated by protocols tailored for automotive applications and, differently from the traditional Ragone plot reported in Figure 1.2, the Figure 1.3 reports the energy available within different states of charge where given 10s-pulse discharge power applies; such plot better captures the complexity of HEV operation. In the plot it is also reported the straight line that corresponds to the energy-to-power ratio (E/P) of 43.2 s which is necessary for an energy-storage system in power-assist HEV. Figure 1.3 compares the simulated performance of electrochemical energy storage systems such as lithium-ion batteries of different chemistry and EDLCs and shows that lithium-ion batteries already satisfy the energy requisite, but still safety

concerns limit their use in transportation. The EDLCs available today on the market (which can operate with V_{max} of 2.7 V) meet the power requisite but do not satisfy the energy requisite [1.11]. The simulation evidences that only by 3 fold increase of capacitance or by increase of V_{max} up to 3.7 V it is possible to achieve with EDLCs the requisite for power-assist HEV.

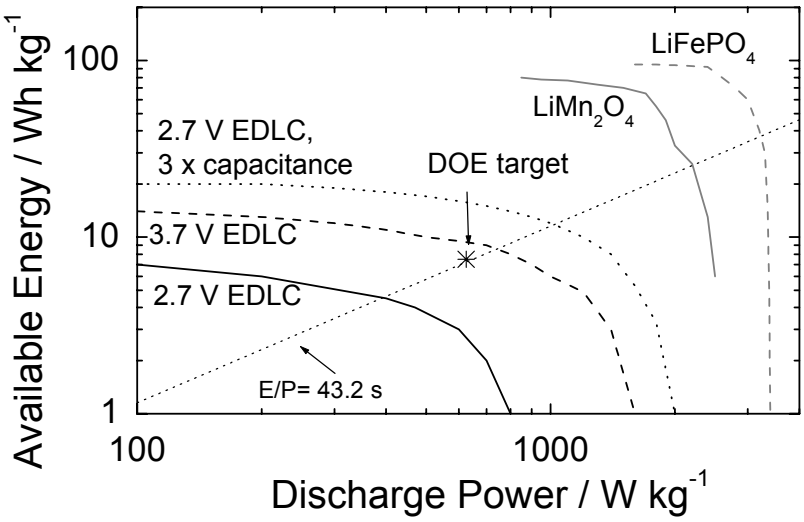

Figure 1.3. Simulations of available energy vs. 10s pulse-discharge power of lithium-ion batteries with different cathodic materials, commercial EDLC (2.7 V) and EDLCs of increased V_{max} of 3.7 V and of 3 fold increased capacitance, it is also reported the DOE target for power-assist HEV. The results plotted include the weight of current collectors but do not account for packaging weight [1.11].

On the other hand, EDLCs have the advantages to feature high energy efficiency, higher than 90%, and as a consequence they release small amount of heat, upon cycling, which is easily dissipated particularly when compared to power lithium-ion batteries. Furthermore, EDLCs featuring equal the positive and the negative electrode materials, are intrinsically safer than the batteries, in which unpredictable internal short circuits may trigger dangerous, thermal runaway reactions.

EDLCs are usable in a wide temperature range; particularly at low temperature, they substantially outperform conventional batteries [1.1, 1.3, 1.8]. However the operating temperature is strongly related to the nature of the electrolyte, therefore aqueous or acetonitrile based-electrolytes limit the operation temperature under 100°C and propylene carbonate based-electrolytes allow a bit higher temperature while a marked higher limit is given by the use of ionic liquids as electrolytes that feature negligible vapour pressure, decomposition temperature even over 400°C and nonflammability characteristic [1.12].

Thus, research in EDLCs is mainly devoted to increase their specific energy by enhancing the supercapacitor capacitance (C_{SC}) and the maximum cell voltage (V_{max}) by the development of novel carbon electrode and electrolyte materials.

1.2. Electrochemical double-layer supercapacitor

As shown in Figure 1.4 EDLC consists of two electrodes composed of high surface area carbon, which is characterized by a high polarizability and electrical conductivity. In EDLC each electrode/electrolyte interface represents a capacitor so that the complete cell can be roughly considered as two capacitors and a resistance connected in series. Thus, the supercapacitor capacitance (C_{SC}) depends on the capacitances of the two electrodes (C_1 and C_2) as in eq. 1.3

$$1/C_{SC} = 1/C_1 + 1/C_2 \qquad \text{(eq. 1.3)}$$

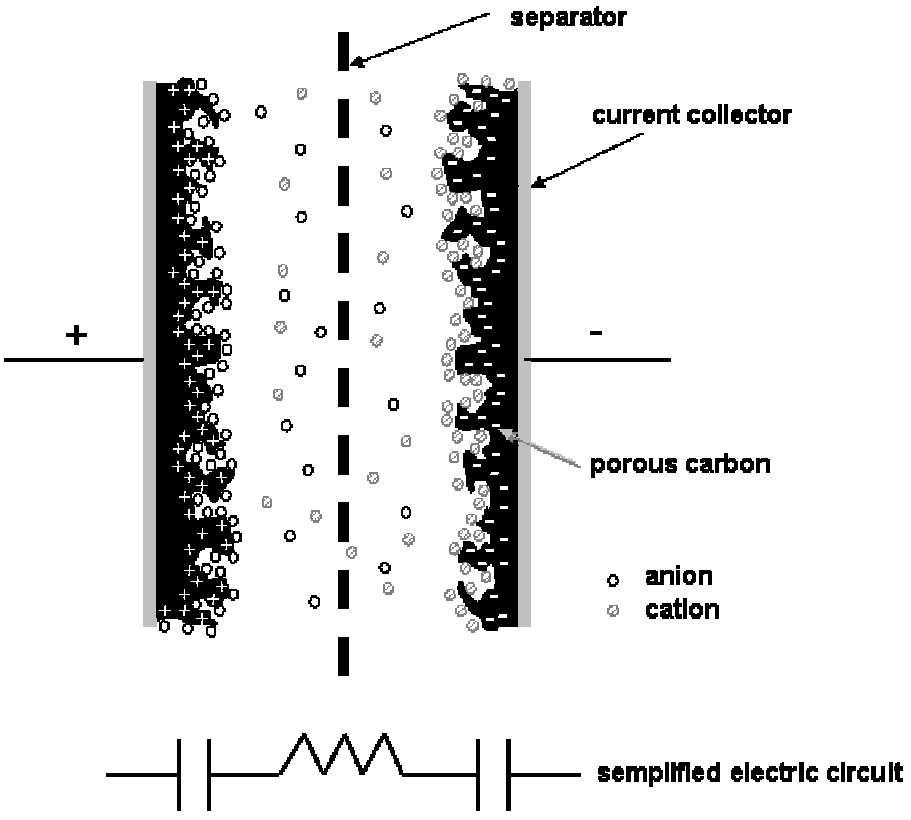

Figure 1.4. Schematic illustration of electrochemical double-layer supercapacitor (EDLC) upon charge [13].

Upon the charge process the carbon electrode surface is electrostatically charged, the electrolyte at the boundary of the electrode is reorganized to counterbalance the charge on

the electrode surface and charge separation with the formation of double-layer occurs in the order of 10^{-8} s at the electrode/electrolyte interface [1.8].

Carbons, being semiconductors, do not feature high density of charge carriers (hole or electrons). The distribution of the charge carriers extends into the bulk of the semiconductor over a relatively large distance (screening length) that is inversely related to the charge-carrier density; such region is called space-charge region and it is shown in Figure 1.5. When an electric field is applied, in the space-charge region a potential gradient takes place with the formation of a double-layer in the solid side and space-charge capacitance (C_c) develops. On the electrolyte side the formation of a compact layer of ions of the same charge, Helmholtz layer, at the closest distance from the electrode and of a diffuse layer occur in order to balance the electrode charge. Therefore, the capacitance at each electrode C_{dl} is given in eq. 1.4

$$1/C_{dl} = 1/C_c + 1/C_H + 1/C_{diff} \qquad \text{(eq. 1.4)}$$

where C_{dl} and C_c have been already defined and C_H and C_{diff} are the capacitances which arise from the compact Helmholtz layer (at the interfase electrode/first layer of ions) and of the diffuse layer (ions concentration gradient), respectively. Hence, C_{dl} will be determined by the smaller of the capacitance components [1.1, 1.13-1.15].

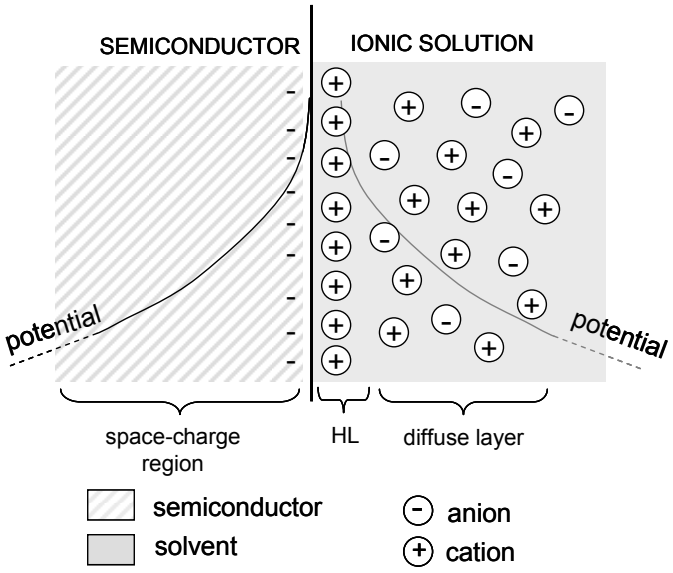

Figure 1.5. Scheme of double-layer at the interfase semiconductor/electrolyte with formation of the space-charge region in the solid side, Helmotz layer and diffuse layer in the electrolyte side.

According to Helmholtz model for concentrated solutions the capacitance C_H at each electrode interface is displayed by the following equation

$$C_H = k_0 \varepsilon A / \delta_{dl} \qquad \text{(eq. 1.5)}$$

where k_0 is the vacuum permittivity (8.85 10^{-12} F m^{-1}), ε is the dielectric constant of the electrical double-layer region, *A* the surface-area of the electrode and δ_{dl} is the thickness of the double-layer. Given that the electrode capacitance depends on the reciprocal of the double-layer thickness which is in the order of 10^{-10} m, and it is directly related to the carbon surface area, typically of several hundreds m^2 g^{-1} of carbon, the capacitance of EDLCs is significantly higher than that of the dielectric and electrolytic ones. The specific capacitance expressed per unit of surface area is typically about 25 μF cm^{-2}, hence, with large accessible surface area carbon electrodes, high double layer capacitances on the order of 100-150 F g^{-1} can be achieved [1.1].

Table 1.2 reports the best performing commercially available EDLCs which operate in organic electrolytes and feature specific energy ≤ 8 Wh kg^{-1} and V_{max} ≤ 3.3 V. Improvement in specific energy of EDLCs is achievable by increasing C_{SC} and $V_{max,}$ which are dependant on the carbon morphology and electrolyte electrochemical stability window (ESW), respectively. The use of electrolyte with wide ESW is a promising strategy to develop high energy supercapacitor. However, the electrolyte resistance (resistivity) increases coming from aqueous to organic electrolytes and ionic liquids at least an order of magnitude (see Table 1.1), hence moving to organic electrolytes and ionic liquids is not as much as convenient in terms of time constant (τ), which is the time required to discharge the supercapacitor of 67% with respect to its capacity. Indeed, the conductivity of the electrolyte affects the value of ESR and τ, which, however, are also influenced by the electronic resistance of the electrode material, the interfacial resistance between the electrode and the current-collector and the ionic resistance of ions moving in small pores [1.13].

Table 1.2. Performances of commercial EDLCs. The reported values are referred to RT and the specific energy is normalized to the device weight including the packaging weight [1.5].

EDLC	Cell Voltage V	Capacitance F	ESR mΩ	Energy Wh/kg
Maxwell	2.7	2800	0.48	4.45
Maxwell	2.7	650	0.8	2.5
Maxwell	2.7	350	3.2	4.4
Ness	2.7	1800	0.55	3.6
Ness	2.7	3640	0.30	4.2
Ness	2.7	5085	0.24	4.3
Asahi Glass (PC)	2.7	1375	2.5	4.9
Panasonic (PC)	2.5	1200	1.0	2.3
Panasonic	2.5	1791	0.30	3.44
Panasonic	2.5	2500	0.43	3.70
EPCOS	2.7	3400	0.45	4.3
LS Cable	2.8	3200	0.25	3.7
Power Sys. (activated carbon, PC)	2.7	1350	1.5	4.9
Power Sys. (advanced carbon, PC)	3.3	1800	3.0	8.0

1.3. Ionic liquids as electrolytes

Ionic liquids (ILs) give a chance to develop safe, “green”, high voltage EDLCs free of toxic and/or flammable organic solvents and able to operate even in high temperature regimes that are not feasible for state of art of commercial supercapacitors. Indeed, ILs are molten salts at room temperature and entirely composed of cations and anions, the nature of which determines the chemical/electrochemical and physical properties of ILs. These molten salts, featuring low vapor pressures, are characterized by high boiling/decomposition points even higher than 400°C and, thus, are considered green

solvents. Given their low melting points they have a large liquidus range [1.12, 1.16]; they are also nonflammable, thermally and electrochemically stable and with good conductivity above RT.

The conductivity is influenced by the chemistry of the IL ions and by their interactions, indeed, if sufficiently long-lived ion pairs are formed, they appear neutral in the electric field and thus cannot contribute to the conductivity [1.17]. At room temperature (RT) ILs feature conductivities (0.1-14 mS cm^{-1}) markedly lower (even two order of magnitude) than those of aqueous electrolytes (400-700 mS cm^{-1}), while the conductivity difference with organic electrolytes is less evident (tetralkylammonium salts in acetonitrile, 60 mS cm^{-1}, and propylene carbonate, 11 mS cm^{-1}). However at 60-80°C ILs conductivities reach the values of 20-30 mS cm^{-1}. Such increase is related to the temperature dependence of the viscosity and the ionic diffusion coefficient which affect the conductivity following an Arrhenius type exponential trend. Since in ILs the ions are not separated by solvent molecule, it is difficult to define the number of charge carriers, so the "free space model" seems to be the most efficient way of describing the mechanism of ionic conductivity. Such model suggests that the conduction occurs by a redistribution of the ions through the free volumes between them, constantly fluctuating in size, due to thermal motions, which increase with temperature [1.16].

ILs are resistant for electrochemical reduction and oxidation, they have wide electrochemical stability window (ESW) even higher than 5 V evaluated on glassy carbon or Pt smooth electrodes. For their wide ESW and their high thermal stability they are safe electrolytes particularly interesting for electrochemical devices and to develop high energy electrochemical supercapacitors. The ESW limits are roughly determined by the ions composing the IL, indeed while the cation influences the negative potential limit, the anion affects the positive potential limit of the ESW.

In order to guarantee high cycle life of supercapacitors based on ILs it is of primary importance the idrophobicity of such salts which depends on the properties of the ions composing the IL. The idrophobicity is determined by substituents of the cations and decreases for the anions in the order $CF_3CO_2^-$, $CH_3CO_2^-$ (idrophilic) > $CF_3SO_3^-$, BF_4^- > PF_6^-, $(CF_3SO_2)_2N^-$ (idrophobic) [1.16].

The ILs mainly studied for supercapacitors application are imidazolium, pyrrolidinium, and asymmetric, aliphatic quaternary ammonium salts of anions like

tetrafluoroborate (BF_4^-), trifluoromethanesulfonate (Tf^-), bis(trifluoromethanesulfonyl)imide ($TFSI^-$), bis(fluorosulfonyl)imide (FSI^-) and hexafluorophosphate (PF_6^-), and all feature an ESW wider than that of the conventional organic electrolytes at RT [1.8]. In this PhD research work the 1-ethyl-3-methylimidazolium bis(trifluoromethanesulfonyl)imide (EMITFSI), N-butyl-N-methyl-pyrrolidinium bis(trifluoromethanesulfonyl)imide ($PYR_{14}TFSI$) and N-methoxyethyl-N methylpyrrolidinium bis(trifluoromethanesulfonyl)imide ($PYR_{1(2O1)}TFSI$) ILs were investigated as electrolytes for high voltage superacapacitors and their structures are shown in Figure 1.6.

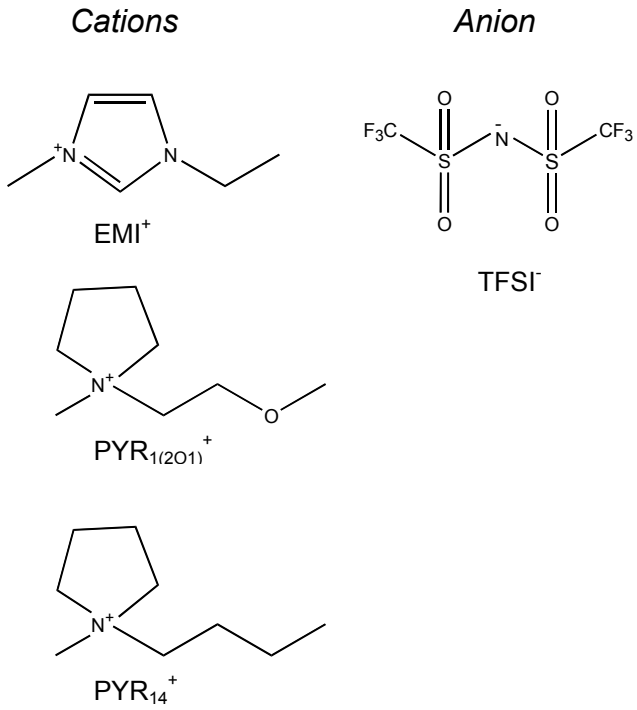

Figure 1.6. Structures of cations and anion of the selected ILs.

Table 1.3 reports melting temperature, ESW evaluated on glassy carbon or Pt smooth electrodes, conductivity and formula weight of the EMITFSI, $PYR_{1(2O1)}TFSI$ and $PYR_{14}TFSI$ ILs. The melting temperature reflects on IL conductivity performance and marks the temperature limit for its application in EDLCs [1.8]. While EMITFSI remains liquid down to low temperatures (-50°C) and displays the highest conductivities, reaching ca. 10^{-2} S cm^{-1} at RT, the acidic proton of the imidazolium ring limits the cathodic stability potential. Thus, the imidazolium-based ILs feature ESWs narrower than those of the

pyrrolidinium-based ILs and this is the main obstacle in the practical use of the hydrophobic EMITFSI in high voltage supercapacitors. Although pyrrolidinium salts display the widest ESW, even exceeding 5V, their conductivity is lower than that of EMITFSI.

Table 1.3. Melting temperature, ESW, conductivity and formula weight of the ILs EMITFSI, $PYR_{1(2O1)}TFSI$ and $PYR_{14}TFSI$.

	EMITFSI [1.16]	$PYR_{1(2O1)}TFSI$ [1.18]	$PYR_{14}TFSI$ [1.18]
Melting temperature	-50°C	<-90°C	-3°C
ESW at RT	4.1 V	5.0 V	5.5 V
Conductivity at 60°C	25 mS cm^{-1}	8.4 mS cm^{-1}	6.0 mS cm^{-1}
at RT	9.2 mS cm^{-1}	3.8 mS cm^{-1}	2.6 mS cm^{-1}
formula weight	391 g mol^{-1}	424 g mol^{-1}	422 g mol^{-1}

1.4. Carbon electrodes for EDLCs

The choice of carbon as supercapacitor electrode material comes from its chemical and physical properties. Indeed carbon features good corrosion resistance, high temperature stability, good conductivity, high surface area range (~1 to 2000 m^2 g^{-1}) with controlled pore structure, processability and compatibility in composite materials and relatively low cost. In the optimization of the carbonaceous electrode material, high specific capacitance and low electronic resistance, that is reflected in the ESR value, are required in order to achieve high specific energy and power according to eq. 1.1 and 1.2 [1.13].

Synthetic carbons features a large variety of nanotextures with microcrystalline domains that lead to several degrees of order (graphitization). They exhibit semiconducting properties and their resistivity depends on their chemical and structural properties (graphitic domains), which derive by the precursors and the preparation conditions, such as temperature and time of pyrolysis and activation processes. High temperature treatments in the absence of oxygen can undergo local graphitization in synthetic carbons. The degree of order (the extension of graphitic domains), porosity and surface chemistry influence the intrinsic resistivity of carbons [1.19].

Carbon electrodes are usually prepared by a blend of carbon and binder defined as composite material. The binders generally used are polytetrafluoroethylene (pTFE), poly(vinylidene fluoride) (pVdF) and carboxymethylcellulose (CMC). The resistance of

the electrode arises from intrinsic resistivity of the carbon and from additional contributions of interparticle contact resistance and composite material/current collector contact resistance. To reduce the electrode resistance, conductive additives can be added to the blend which are typically carbon blacks and acetylene blacks. They are produced by the partial combustion or thermal decomposition of hydrocarbons in the gas phase and their conductivity is typically in the range 10^{-1} to 10^{2} S cm^{-1} [1.13].

The carbons investigated as active material for supercapacitor electrodes are activated carbons, aero/cryo/xerogel carbons, template carbons, carbon fibers and carbon nanotubes. However, carbon fibers and carbon nanotubes typically feature low specific surface area which gives rise to low capacitive response, thus, in this thesis work only activated carbons, aero/cryo/xerogel carbons and template carbons were investigated for IL based-supercapacitors.

1.4.1. Activated carbons

Activated carbons, largely utilized in commercial EDLCs for their low cost, are typically produced by carbonization of materials like nutshells, peat, wood, lignite and coal and by successive activation processes [1.19]. Figure 1.7 shows a schematic representation of the structure of activated carbons, which gives an idea of how a disorder array of graphene layers, also folded, can be arranged. They feature high specific surface area (>1500 m^2 g^{-1}) and are usually rich in surface functional groups.

Figure 1.7. Schematic representation of the microstructure of activated carbons [1.20].

The activation processes are physical or chemical [1.20]. The physical activation consists of a high temperature treatment, generally between 800°C and 1100°C, in the presence of

suitable oxidizing gases such as steam, CO_2, air or any mixture of these gases. The active oxygen in the activating process burns away the more reactive portions of the carbon skeleton as CO and CO_2 and the extent of burn-off depends on the nature of the gas employed and the activation temperature and time. The activation reaction occurs in two steps. In the first step the disorganized carbon is burned out and the blocked pores are opened. In the second stage the carbon of the aromatic ring system starts burning, producing active sites and wider pores. The choice of the parameters of the activation process such as temperature, time, type of activating agent allows a control of the microporosity and mesoporosity to some extent [1.21].

The chemical activation involves the treatment of the starting material with concentrated solution of activating agent. The most widely used activating agents are H_3PO_4, $ZnCl_2$ and H_2SO_4 and their common feature is that they are dehydrating agents. Chemical activation is usually carried out at temperature between 400°C and 800 °C. The pyrolized product is cooled and washed to remove the activating agent. The pore size distribution in the final carbon product is determined largely by the degree of impregnation and the pore size increase by raising the degree of impregnation [1.22].

The activation processes modify the carbon porosity increasing the specific surface area, even by a significant contribution in microporosity (micropore size < 2 nm), and also produce/increase functional groups on carbon surface. [1.19, 1.23].

1.4.2. Mesoporous aero/cryo/xerogel carbons

Meoporous aero/cryo/xerogel carbons (mesopore size is between 2 nm and 50 nm) are usually synthesized by the poly-condensation of resorcinol and formaldehyde, via sol-gel process. Organic aerogels were prepared firstly by Pekala in 1989 [1.24]. An aqueous solution of resorcinol, formaldehyde and a basic or acid catalyst in a closed container is heated at a certain temperature for a period of time to form a stable crosslinked gel. The major reactions between resorcinol and formaldehyde are reported in Figure 1.8 and include an addition reaction in which the basic catalyst favors the reaction and a condensation reaction. Once the gel is formed, it is washed, in order to exchange the pore water with an organic solvent appropriate for the subsequent drying step. Next, the wet gel is dried. The resulting carbon porosity is controlled by the synthesis conditions such as

dilution and ratio of the precursors, gelation temperature and time and pH of the initial solution [1.25-1.26].

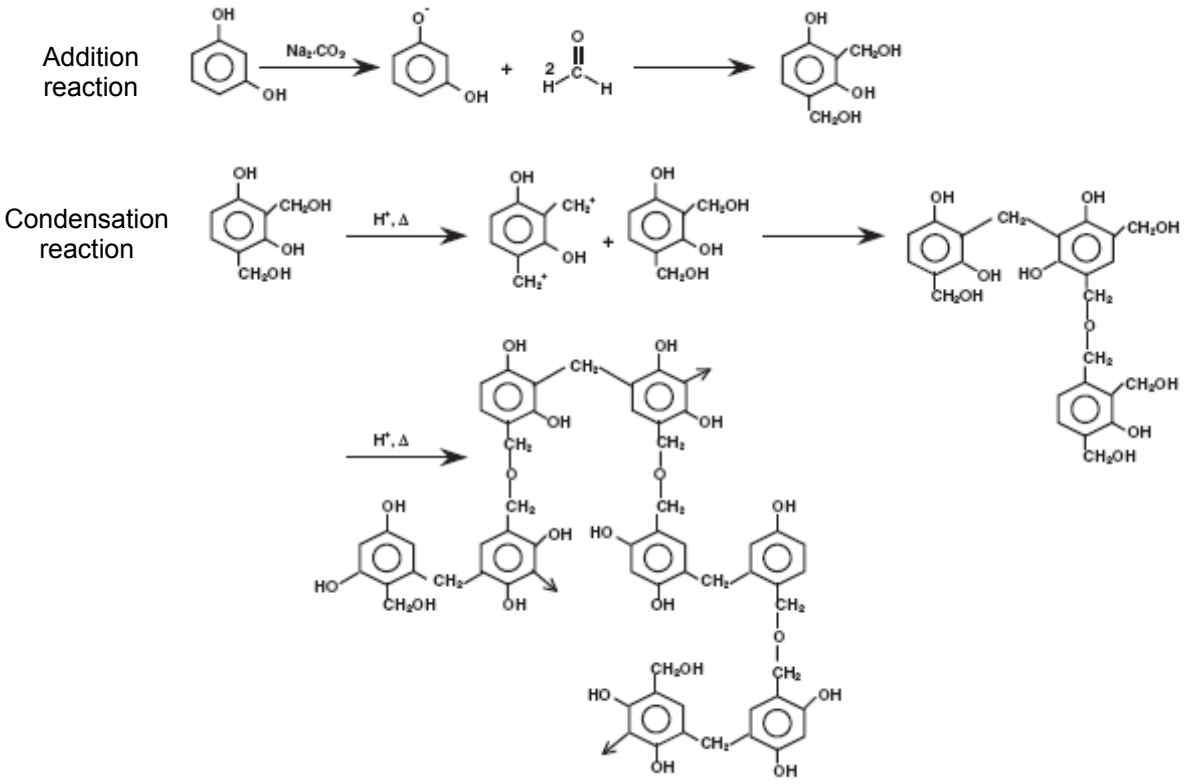

Figure 1.8. Polymerization mechanism of resorcinol and formaldehyde. S.A. Al-Muhtaseb, J.A. Ritter: Preparation and Properties of Resorcinol-Formaldehyde Organic and Carbon Gels. *Adv. Mater.* (2003) 15, *101*. Copyright Wiley-VCH Verlag GmbH & Co. KGaA. Reproduced with permission.

The evaporative drying is reputed texture-destructive, therefore organic gels are usually dried by supercritical drying with CO_2 to eliminate surface tensions and avoid shrinkage in the dried material which, in this case, is called aerogel. Note that the supercritical drying, involving high pressure, is expensive, dangerous and difficult to mass production, therefore the development and the optimization of the subcritical drying was necessary and it was important the selection of suitable solvents to minimize collapse of the wet gel structure during drying. A way to avoid shrinkage is to use freeze-drying treatment. After freezing the solvent is removed by sublimation under low pressure and the resulting material is designated as cryogel. It has been also demonstrated that by using exchange solvents (acetone or cyclohexane) featuring a surface tension lower than that of

water, the evaporative drying at ambient conditions does not destroy the pore structure of the gel and, in this case, the dried gel was named xerogel [1.25, 1.27-1.29].

The dried gel is carbonized in inert atmosphere to produce the carbon. The aero/cryo/xerogel solid matrix is composed of interconnected polymeric chains so as after pyrolysis, the resulting carbons are more electrically conductive than most activated carbons [1.13, 1.30]. However, as shown in Figure 1.9, the aero/cryo/xerogel carbons are disordered with respect to the ordered templated carbons which are described in the next Section.

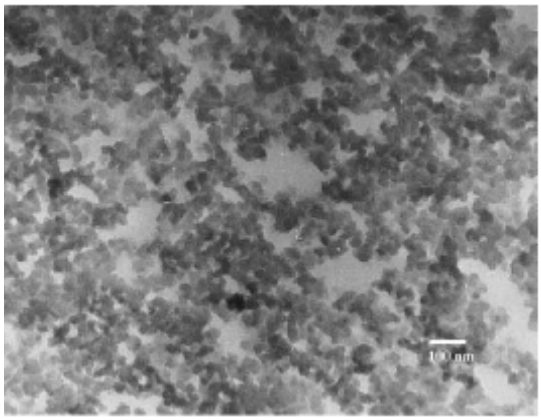

Figure 1.9. TEM image of xerogel carbon obtained by polycondensation of resorcinol and formaldehyde. Reprinted from Carbon, 42, N. Job, R. Pirard, J. Marien, J.-P. Pirard, "Porous carbon xerogels with texture tailored by pH control during sol–gel process", 619-628, Copyright (2004), with permission from Elsevier.

1.4.3. Mesoporous template carbons

Template carbons are prepared by carbonization of carbon precursors in precence of a templating materials which, once dissolved, produce the porosity into the carbons. Template carbons can be divided into ordered template carbons (OTC) and disordered template carbons (DTC).

The preparation of OTCs is schematically reported in Figure 1.10 and consists in the preparation of the inorganic template, formation of the composite by infiltration of carbon precursor into the inorganic template, carbonization and removal of the inorganic template usually by HF or NaOH solutions. In order to prepare ordered mesoporous carbons the best candidates of inorganic templates are ordered mesoporous silica materials. As an example, Figure 1.11 reports the TEM image and the corresponding Fourier diffractogram of a nano-pipe-type mesoporous carbon, designated as CMK-5, synthesized from the partial wetting

of poly(furfuryl alcohol) onto the SBA-15 mesoporous silica channels and subsequent carbonization and removal of the silica template. The CMK-5 carbon is rigidly interconnected into a highly ordered hexagonal array by carbon spacers, which are formed between adjacent cylinders [1.31-1.33].

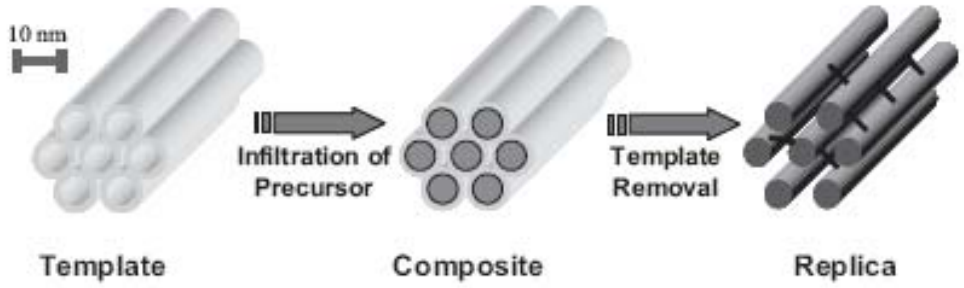

Figure 1.10. Schematic illustration of the nanocasting pathway. A.-H. Lu, F. Schüth: Nanocasting: A Versatile Strategy for Creating Nanostructured Porous Materials. *Adv. Mater.* (2006) 18, *1793*. Copyright Wiley-VCH Verlag GmbH & Co. KGaA. Reproduced with permission.

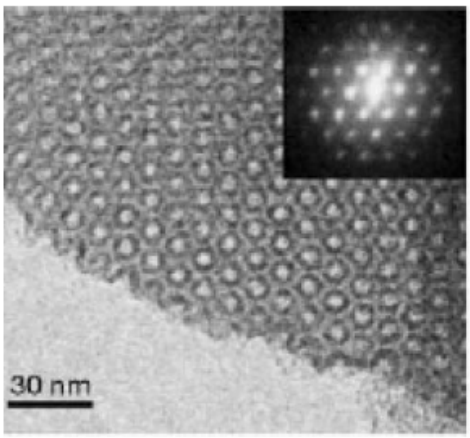

Figure 1.11. TEM image viewed along the direction of the ordered nanopipe-type carbon and corresponding Fourier diffractogram. Reprinted by permission from Macmillan Publishers Ltd: S. H. Joo, S. J. Choi, I. Oh, J. Kwak, Z. Liu, O. Terasaki and R. Ryoo, Nature (2001) 412, *169*, copyright 2001.

The DTCs are prepared using disorder inorganic template such as SiO_2 and MgO nanoparticles [1.32, 1.34] and generally the synthesis consists of mixing carbon precursor with template nanoparticles, which, after pyrolysis, are chemically removed. The synthesis by MgO developed by M. Inagaki involve also a variation, which consists in the mixing of carbon precursor and MgO precursor with the formation of MgO template in situ during carbonization, then the MgO template is removed by sulfuric acid solution. Figure 1.12

shows TEM and FE-SEM images of a carbon obtained from powder mixture of MgO with poly(vinyl alcohol) and it is representative of the disorder of such carbons [1.35-1.36]. The template syntheses of mesoporous carbons allow a good control of the porosity of carbons because the amount of template is accurately set with respect to that of the carbon precursors, so that, after pyrolysis and template removal, it is possible to obtain certain pore volume/carbon ratios while keeping the same pore size distribution, which in turn depends only on template size. The geometry of the templating agent is replicated in the pores and affects the specific surface of the carbon. The synthesis of DTCs based on MgO is particular appealing because it has the advantage of the pore size control typical of the template synthesis and it is faster and cheaper with respect to ordered template and aero/cryo/xerogel methods.

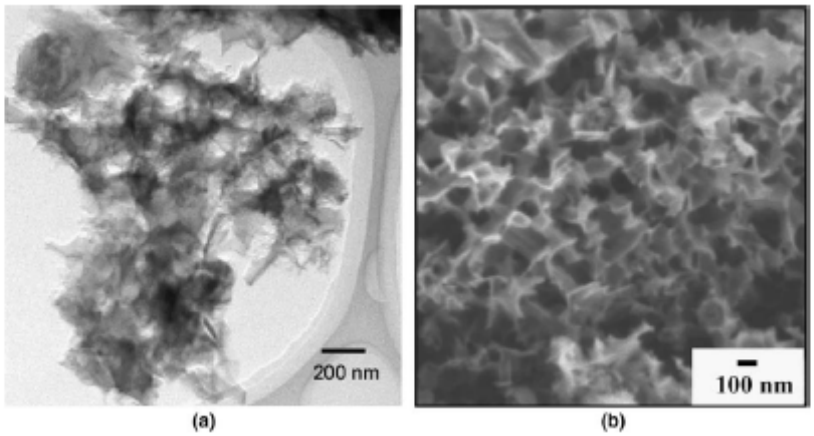

Figure 1.12. TEM and FE-SEM images of carbons obtained from powder mixture of MgO with poly(vinyl alcohol). Reprinted from Carbon, 44, T. Morishita, Y. Soneda, T. Tsumura, M. Inagaki "Preparation of porous carbons from thermoplastic precursors and their performance for electric double layer capacitors", 2360-2367, Copyright (2006), with permission from Elsevier.

1.5. Carbon porosity and surface chemistry

High double layer capacitance is achievable by tailoring the morphology of the carbon in terms of porosity and surface chemistry. IUPAC classifies the pores on the base of size as follows: i) pores with size higher than 50 nm are defined as macropores; ii) pores with size between 2 nm and 50 nm are defined as mesopores; iii) pores with size lower than 2 nm are defined as micropores. The pores are also defined on the basis of their shapes that can be of cylindrical or slit-shaped geometry. Figure 1.13 reports, as example, the TEM image of an activated carbon where it is evident a cylindrical mesopore of 15-20 nm in diameter and a slit-shaped micropore in zone M of 0.5 nm in size.

Upon charge, the double-layer formation implies that the counterions of the electrolyte go into the carbon pores to balance the charge at the carbon surface. Thus, the specific surface area effectively "active" in the double layer formation is generated by pores accessible to the electrolyte ions. Generally, the capacitive response in aqueous electrolytes is higher than that in organic ones. Beside the different dielectric constants of water and organic solvents, this is also because the lower size limit of pores, under which the electrolyte can not access the pores, depends on the electrolyte used, i.e. on the dimensions of the ions, which increase from the aqueous electrolytes, where the counterions are small and provided by KOH for alkali electrolytes and H_2SO_4 for acidic ones, to the organic ones that are based on tetralkylammonium salts in acetonitrile or propylene carbonate or ionic liquids consisting of large cations and anions.

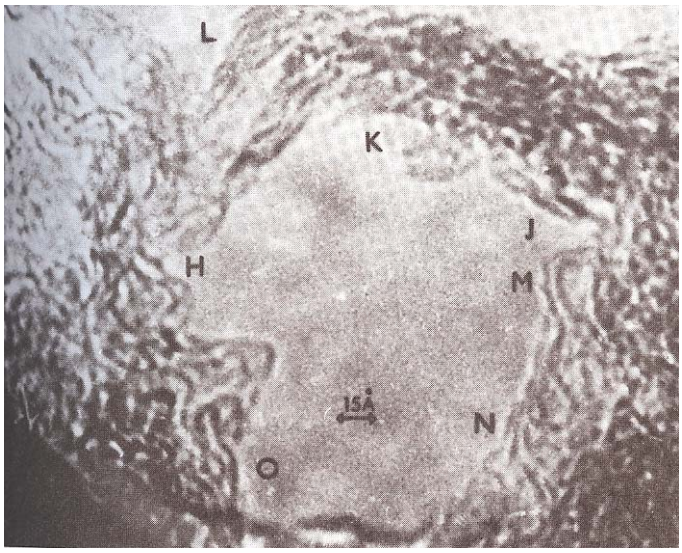

Figure 1.13. TEM micrograph of activate carbon U-02 with a slit-shaped micropore of 0.5 nm in size (M), at the edge of a cylindrical mesopore [1.20].

There is a considerable debate in order to define the lower size of accessible pores, indeed, while studies reported that in aqueous electrolytes micropores >0.5 nm are accessible to simple hydrated ions and in organic electrolytes such pore size limit should involve larger micropores [1.37-1.38], other studies reported that also in organic electrolytes small micropores are accessible (~ 0.7 nm) because the electric field imposed by the polarization of the electrode induces desolvation and distorsion of ions [1.39-1.41]. On the other hand a suitable porosity consists of regularly interconnected mesopores. Small micropores, even in the case they are accessible, should lead to high τ with consequent loss of high rate

capability because the ionic motion in such small pores is slow and difficult [1.13, 1.23, 1.33].

Several studies showed a trend of the specific capacitance increase with the specific surface area according to eq. 1.5. Nevertheless, in certain case such trend goes to a plateau, which occurs mainly for very high specific surface area carbons (>1000 m^2 g^{-1}) and this has been explained in different ways [1.15]. Such deviation can be due to a degree of inaccessibility of the specific surface area (sieving effect) [1.38] or to an overestimation of such surface area calculated by the BET equation [1.42]. Some studies indicated that the microporous specific capacitance is lower than the mesoporous one [1.42]. Therefore, carbons of high specific surface area may feature lower capacitance response than expected because of their high microporosity contributions to the specific surface area. Kotz and coworkers demonstrated that in the case of high surface area carbon, when the wall thickness becomes as small as the screening length of the electrified field in the electrode (~ 1 nm), the adjacent space charge regions inside the solid begin to overlap, giving charge storage limitation at the carbon side [1.14-1.15]. On the basis of eq. 1.4, when the capacitance of the solid side, C_c, is small, it will lead to a C_{dl} lower than expected [1.13-1.15].

Functional groups on carbon surface have an important role in the capacitive response of the carbon, indeed, they influence point of zero charge, electronic properties, polarizability, wettability and can be responsible for pseudocapacitive phenomena [1.13]. Functional groups are mainly located in the edge sites of the graphene planes where the reactivity of the carbon atoms with unsaturated valences is greater than that in the basal sites as shown in Figure 1.14. Therefore the chemical properties of carbons vary with the relative fraction of edge sites and basal plane sites; with the ratio of edge to basal sites generally increasing with the degree of disorder.

The most common functional groups are those with heteroatoms as oxygen, nitrogen, sulfur, hydrogen; they are derived from the carbon precursors as a result of incomplete carbonization and can also be incorporated during activation processes pursued to increase surface area. Activation processes carried out in oxidizing atmosphere can be used to increase the concentration of surface oxygen groups, such as carboxyl, carbonyl, phenol, quinone and lactone groups, while heating under inert atmosphere may be used to selectively remove some of these functionalities [1.43-1.44].

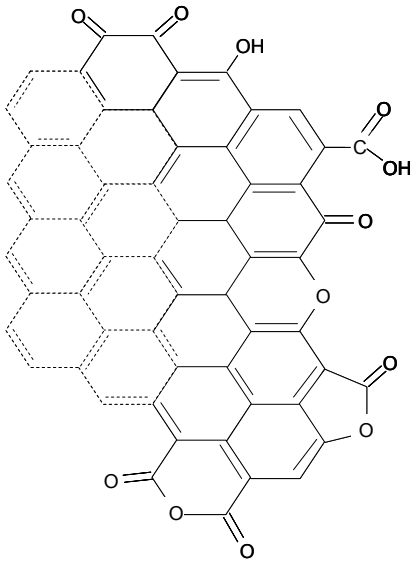

Figure 1.14. Example of functional groups located in the edge sites of the graphene layer of a high surface area carbon.

Surface functionality on the carbon surface can give reversible redox-processes which enhance carbon capacitive response but are not as stable as the electrostatic process and thus, are detrimental for the long cycle-life (> 10^5 cycles) required by EDLCs.

1.6. Design of carbon electrodes for EDLCs based on idrophobic ILs

The carbon/electrolyte interface in IL is not mediated by any solvent, thus the carbon porosity and surface chemistry features have to be designed in view of the used IL.

Given that in IL the double-layer is different respect to those in conventional electrolytes since the solvent is absent, the double-layer can not be described by the Helmholtz model developed for conventional concentrated electrolyte solutions, as pictured in Figure 1.15a. In such solutions the solvent molecules in the inner Helmholtz plane (IHP) separate electrode surface charges and electrolyte counterions located in the outer Helmholtz plane (OHP) by a distance, δ_{dl}, so that solvent molecular size, rather than ion size, and solvent dielectric constant (ε) significantly affect the double-layer capacitance of the Helmholtz compact layer (C_H), which is given by eq. 1.5, and therefore the double layer capacitance C_{dl} (see eq. 1.4). In the case of solvent-free ILs the electrified electrode surface is set up against the IL counterions located in the inner Helmholtz plane (IHP) as shown in Figure 1.15b. Thus, the relation between C_{dl} and A depends on IL ion chemistry and structure of the electrode/IL interface. Size, orientation under electric field and polarizability of IL ions

directly affect thickness, the dielectric constant of the double-layer and the capacitive response of the electrodes [1.8].

Furthermore, when idrophobic ILs are used as electrolytes the hydrophilic surface groups, such as oxygen groups, has to be avoided in order to have good wettability of carbon surface from the IL and guarantee long cycle life [1.8, 1.23].

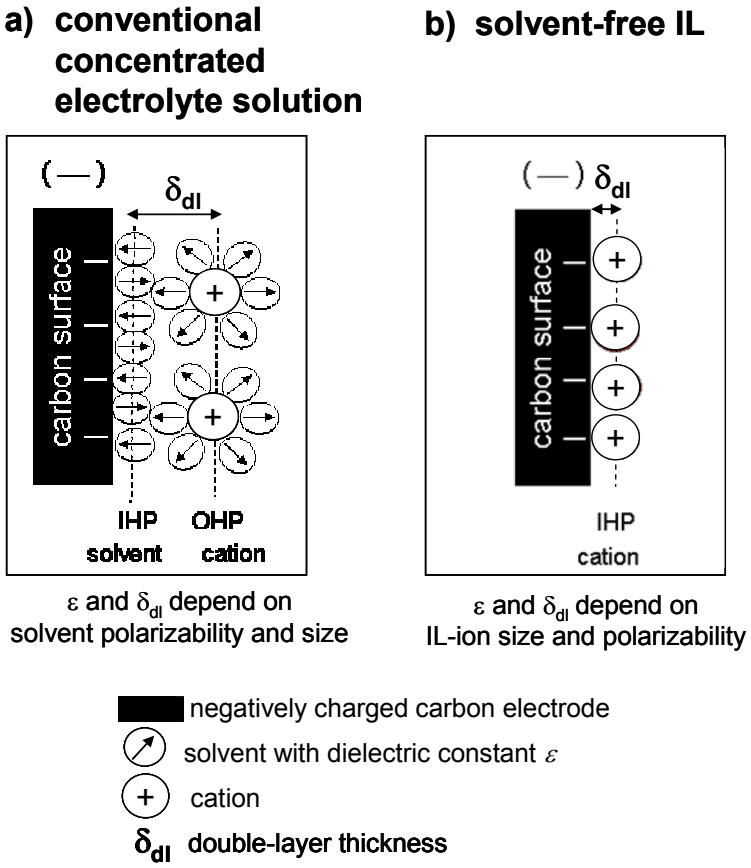

Figura 1.15. Scheme of double layer formation at the interface of carbon/conventional electrolyte (a) and carbon/IL (b).

If a typical capacitance value of 20 μF cm^{-2} for carbon in IL is assumed, a specific surface area of at least 500 m^2 g^{-1} has to be reached in order to achieve high specific capacitance ≥ 100 F g^{-1}. On the basis of geometric considerations, in the case of cylindrical shaped-pores, such area should arise from small mesopores narrower than 8 nm. The pore walls have to be coated at least by an IL monolayer in order to take advantage of all the accessible carbon surface and to avoid charge limitation on the electrolyte side and this results in constraints in the design of the void volumes in the carbons. Indeed, surface area

from pores narrower than 2-3 nm, even if they are accessible to the IL ions, would not be fully exploited for the double-layer capacitance because the corresponding pore volume would be lower than that required to cover the whole cylinder surface by an IL monolayer. Mesopores wider than 10 nm not only are less effective for surface area but provide high pore volume > 1 cm^3 g^{-1} and carbon electrodes of low density, which is detrimental to capacitance density (F cm^{-3}), carbon electronic conductivity, contact resistances and module-specific capacitance. Since ILs fill the carbon pores, high pore volume leads to a significantly higher content of electrolyte than the amount required for charge/discharge and, hence, to a non-optimized distribution of the component weights in the modules, particularly when high density and formula weight ILs are used [1.8].

1.7. Objective of the thesis

This thesis work is focused on the development of safe, double layer carbon supercapacitors of high energy able to operate in a wide range of temperature for application in sustainable transportation. One strategy was to increase V_{max} above 3 V by the use of ILs as electrolytes that feature a wide ESW. Another strategy was to prepare mesoporous carbons suitable to operate in ILs with high capacitance response (>100 F g^{-1}) combined with a useful and proper porous volume (within 1 cm^3 g^{-1}). Finally, a novel carbon double-layer configuration with different loadings of carbon at the two electrodes (AEDLC) was developed in order to exploit the whole ESW of the electrolyte upon charge/discharge processes. Several AEDLCs were also assembled and investigated and this study contributed to the development of pre-series IL-based AEDLCs within the EU project ILHYPOS.

1.8. European Union Project ILHYPOS

The European Union (EU) Project ILHYPOS (**I**onic **L**iquid-based **Hy**brid **Po**wer **S**upercapacitors, Contract No. TST4-CT-2005-518307) involved three university groups (University of Bologna, University Paul Sabatier, and CNAM), four industrial partners (Evonik-Degussa, Leclanché Lithium, Arcotronics Technologies and Micro-vett) and the governmental energy agency ENEA, which coordinated the Project. The Project focused on "green" materials and technologies to minimize environmental impacts of supercapacitors in construction, use and disposal. Thus, the ionic liquid-based

supercapacitors were investigated and developed with the aim of increasing supercapacitor energy without sacrificing power, safety and long cycle life.

The challenging target of the Project was the development of supercapacitor prototypes which outperform the electrochemical double-layer capacitors (EDLCs) on the market by featuring maximum cell voltage (V_{max}) higher than 3.5 V, maximum specific energy higher than 32 Wh/kg of total electrode material, and 15 Wh/kg of packaged device, operating at up to 60°C.

The university groups were charged with the basic studies for electrode and electrolyte materials development and selection, cell design, and working condition specifications; Evonik-Degussa and Leclanché Lithium with large scale electrolyte production and electrode lamination, respectively; ENEA with the development and optimization of ionic liquids (ILs) with electrochemical stability window (ESW) $\geq$ 5 V and good ionic conductivity in a temperature range from -20 °C up to 60 °C, and, together with Micro-vett, with the definition of testing procedures for specific applications in automotive and with the tests of pre-series cells, stacks and modules; and Arcotronics Technologies with the cell and module design, based on spiral wound technology, and development of pilot machinery for cell assembly.

1.9. References

1.1) B.E. Conway, *Electrochemical Supercapacitors*, Kluwer Academic/Plenum, New York (1999).

1.2) K. Naoi, M. Morita *Interface* 17 (2008) *44*.

1.3) R. Kotz, M. Carlen, *Electrochim. Acta* 45 (2000) *2483*.

1.4) D. Bélanger, T. Brousse, J. W. Long *Interface* 17 (2008) *49*.

1.5) A. Burke, *Electrochim. Acta* 53 (2007) *1083*.

1.6) K. Naoi, P. Simon, *Interface* 17 (2008) *34*.

1.7) A. Balducci, R. Dugas, P.L. Taberna, P. Simon, D. Plée, M. Mastragostino, S. Passerini, *J. Power Sources* 165 (2007) *922*.

1.8) M. Mastragostino, F. Soavi, *Electrochemical Capacitors: Ionic Liquid Electrolytes*. In: J. Garche, C. Dyer, P. Moseley, Z. Ogumi, D. Rand, B. Scrosati, editors. *Encyclopedia of Electrochemical Power Sources*, Vol 1. Amsterdam: Elsevier (2009) *649*.

1.9) J. Miller, A. F. Burke, *Interface* 17 (2008) *53*.

1.10) E. Karden, S. Ploumen, B. Fricke, T. Miller, K. Snyder, *J. Power Sources* 168 (2007) *2*.

1.11) S.G. Stewart, V. Srinivasan, J. Newman, *J. Electrochem. Soc.* 155 (2008) *A664*.

1.12) S. Zhang, N. Sun, X. He, X. Lu, X. Zhang, *J. Phys. Chem. Ref. Data* 35 (2006) *1475*.

1.13) A.G. Pandolfo, A.F. Hollenkamp, *J. Power Sources* 157 (2006) *11*.

1.14) M. Hahn, M. Baertschi, O. Barbieri, J.-C. Sauter, R. Kötz, R. Gallay, *Electrochem. Solid-State Lett.* 7 (2004) *A33*.

1.15) O. Barbieri, M. Hahn, A. Herzog, R. Kötz, *Carbon* 43 (2005) *1303*.

1.16) M. Galiński, A. Lewandowski, I. Stępniak, *Electrochim. Acta* 51 (2006) *5567*.

1.17) D.R. MacFarlane, M. Forsyth, E.I. Izgorodina, A.P. Abbott, G. Annat, K. Fraser, *Phys. Chem. Chem. Phys.* 11 (2009) *4962*.

1.18) C. Arbizzani, M. Biso, D. Cericola, M. Lazzari, F. Soavi, M. Mastragostino, *J. Power Sources* 185 (2008) *1575*.

1.19) L.R. Radovic, *Chemistry and Physics of Carbon*, Marcel Dekker, Inc., New York and Basel (2001).

1.20) R.C. Bansal, J.-B. Donnet, F. Stoeckli, *Active Carbon*, Marcel Dekker, Inc., New York and Basel (1988).

1.21) F. Rodríguez-Reinoso, M. Molina-Sabio, M. T. González, *Carbon* 33 (1995) *15*.

1.22) M. Molina-Sabio, F. Rodríguez-Reinoso, *Colloids and Surfaces A: Physicochem. Eng. Aspects* 241 (2004) *15*.

1.23) E. Frackowiak, *Phys. Chem. Chem. Phys.* 9 (2007) *1774*.

1.24) R.W. Pekala, *Low Density, Resorcinol-Formaldehyde Aerogels*, United States Patent N° 4,873,218, (1989).

1.25) N. Job, A. Théry, R. Pirard, J. Marien, L. Kocon, J.-N. Rouzaud, F. Béguin, J.-P. Pirard *Carbon* 43 (2005) *2481*.

1.26) N. Job, R. Pirard, J. Marien, J.-P. Pirard *Carbon* 42 (2004) *619*.

1.27) O. Czakkel, K. Marthi, E. Geissler, K. László, *Micropor. Mesopor. Mater.* 86 (2005) *124*.

1.28) H. Tamon, H. Ishizaka, T. Yamamoto, T. Suzuki, *Carbon* 37 (1999) *2049*.

1.29) J. Li, X. Wang, Q. Huanga, S. Gamboa, P.J. Sebastian, *J. Power Sources* 158 (2006) *784*.

1.30) S.A. Al-Muhtaseb, J.A. Ritter, *Adv. Mater.*, 15 (2003) *101*.

1.31) A.-H. Lu, F. Schüth, *Adv. Mater.* 18 (2006) *1793*.

1.32) J. Lee, S. Han, T. Hyeon, *J. Mater. Chem.* 14 (2004) *478*.

1.33) A.B. Fuertes, G. Lota, T.A. Centeno, E. Frackowiak, *Electrochim. Acta* 50 (2005) *2799.*

1.34) T. Morishita, Y. Soneda, T. Tsumura, M. Inagaki, *Carbon* 44 (2006) *2360*.

1.35) M. Inagaki, M. Kato, T. Morishita, Kazuhiro Morita, K. Mizuuchi, *Carbon* 45 (2007) *1121*.

1.36) T. Morishita, K. Ishihara, M. Kato, M. Inagaki, *Carbon* 45 (2007) *209*.

1.37) J. Koresh, A. Soffer, *J. Electrochem. Soc.* 124, (1977) *1379*.

1.38) G. Salitra, A. Soffer, L. Eliad, Y. Cohen, D. Aurbach, *J. Electrochem. Soc.* 147 (2000) *2486*.

1.39) J. Chmiola, G. Yushin, Y. Gogotsi, C. Portet, P. Simon, P.L. Taberna, *Science* 313 (2006) *1760*.

1.40) P. Simon, Y. Gogotsi, *Nature Mater.* 7 (2008) *845*.

1.41) C.O. Ania, J. Pernak, F. Stefaniak, E. Raymundo-Piñero, F. Béguin, *Carbon* 47 (2009) *3158*.

1.42) H. Shi, *Electrochim. Acta* 41 (1996) *1633*.

1.43) J.L. Figueiredo, M.F.R. Pereira, M.M.A. Freitas, J.J.M. Órfão, *Carbon* 37 (1999) *1379*.

1.44) G. de la Puente, J.J. Pis, J.A. Menéndez, P. Grange, *J. Anal. Appl. Pyrolysis* 43 (1997) *125*.

Chapter 2
Techniques and Analysis

2.1. Materials

The pristine activated carbon (AC) Picactif BP10 from Pica was treated at 1050°C in Ar (200 cm^3 min^{-1}) for 2h with a heating rate of 10°C min^{-1} in a furnace (ZE Muffle Furnace) in order to remove surface moieties and the treated carbon is named ACT (see Section 4.1.1).

The cryogel and xerogel carbons were prepared by polycondensation of resorcinol (Riedel de Haen, 99.0–100.5%) and formaldehyde (37% aqueous solution, Aldrich) in MilliQ ultrapure water (Milli-Q simplicity system, Millipore Co.) with Na_2CO_3 (Riedel de Haen, >99.8%) as gelation catalyst, followed by water/*t*-butanol (Fluka, >99.7%) or water/acetone solvent exchange, freeze or RT drying, respectively, and pyrolysis. The pyrolysis step was carried out at 800-1050°C with heating rate 10°C min^{-1} under moderate flux of Argon (200 cm^3 min^{-1}); the preparation details are reported in Sections 4.1.2. The aerogel carbon CA1 was purchased from Marketech.

The DTCX carbons were prepared from magnesium salts auch as Mg D-gluconate hydrate (≥98%, Sigma), Mg acetate tetrahydrate (puriss. p.a., ACS reagent, ≥99.0%, Riedel-de Haën), Mg citrate tribasic nonahydrate (Ultra; ≥98%, Fluka) and Mg bis(monoperossiphtalate) (tech., 80% Aldrich) and from thermoplastic polymers such as poly(ethylene terephthalate) (pellets, Aldrich, 29.9% ash) and polystyrene (pellets, Aldrich M_w= 192000). The poly(ethylene terephthalate) and polystyrene were grounded by universal mill M20 (IKA) and then mixed to the magnesium salts using planetary mill (Pulverisette) in agate jar. The mixture was pyrolysed at 900°C for 1 h with heating rate of 5°C min^{-1} in Ar (200 cm^3 min^{-1}) in the above mentioned furnace. The resulting powder was milled at 400 rpm and for 1h with the planetary mill and then washed with H_2SO_4 2 M to dissolve MgO template, which was formed upon pyrolysis. Preparation details are reported in Section 4.1.3.

The ILs, EMITFSI (Solvent Innovation 99%) and $PYR_{14}TFSI$ (Solvent Innovation 98%) were dried in Büchi Glass Oven B-580 over night at 80°C under dynamic vacuum before use and displayed water content ≤ 30 ppm checked by Karl Fisher titration (684 KF

Coulometer Metrohm); the $PYR_{1(2O1)}$ TFSI, which featured water content < 20 ppm, was provided by Evonik-Degussa in the frame of EU Project ILHYPOS and was used as received.

2.2. Chemical-physical characterizations

The carbon powders were characterized by TGA and FTIR-ATR to investigate their surface chemistry. Porosity analysis of carbons were carried out by nitrogen adsoption at 77 K and XRD and Raman spectroscopy were carried out to investigate the degree of crystallinity of carbons.

The thermogravimetric analysis (TGA) were carried out with a Mettler Toledo TGA/SDTA A851 System in N_2 or O_2 flow at a scanning rate of 20°C min^{-1} in the temperature range between 25°C and 600-1050°C. The differential analysis were calculated to evidence the temperature of the main decomposition processes which occur.

Fourier transform infrared-attenuated total reflectance (FTIR-ATR) spectroscopy was carried out by a Perkin Elmer Spectrometer Spectrum ONE (FTIR-ATR) with 40 scans and 4 cm^{-1} resolution.

The porosity of carbons were evaluated by nitrogen adsorption at 77 K with an ASAP 2020 system (Micromeritics); the carbon powders were dried for at least 2h at 120 °C before testing. The total pore volume (V_{tot}) was evaluated by the quantity of N_2 adsorbed at $p/p° = 0.995$; the specific pore volume ($V_{>1.5\ nm}$) and surface area ($S_{>1.5\ nm}$) related to pores of size between 1.5 nm and 200 nm and the pore size distribution (PSD) were evaluated by the density functional theory (DFT) and assuming a cylinder pore geometry [2.1].

X-ray diffraction measurements (XRD) were performed with a Philips X'Pert diffractometer, a Cu Kα (λ = 1.5406 Å) radiation source and Ni filter by step-scanning mode (0.05° 2θ step; 0.05° 2θ s^{-1} scan rate). Figure 2.1 reports the main parameters of an ideal crystal of graphite. The inter-layer distance d_{002} of the prepared carbons was evaluated by the Bragg's law $d_{002} = n\lambda/2sen\theta_{002}$, where n is the diffraction order, λ=1.54 nm and θ_{002} is the diffraction angle which is of 26.5 °2θ for graphite (ID N. 23-0064) and is related to the (002) family of lattice planes. The size of the graphene crystals along the c-axis (L_c, normal to the graphene plane) and the a-axis (L_a, along the graphene plane) was evaluated from the half height width β of the reflexes (002) and (100) (the latter found at

44.6 °2θ in graphite) by the equation L = kλ/βcosθ, where λ is the wavelength of the incident radiation (1.54 nm) and k = 0.94 for Lc and 1.84 for La, respectively [2.2].

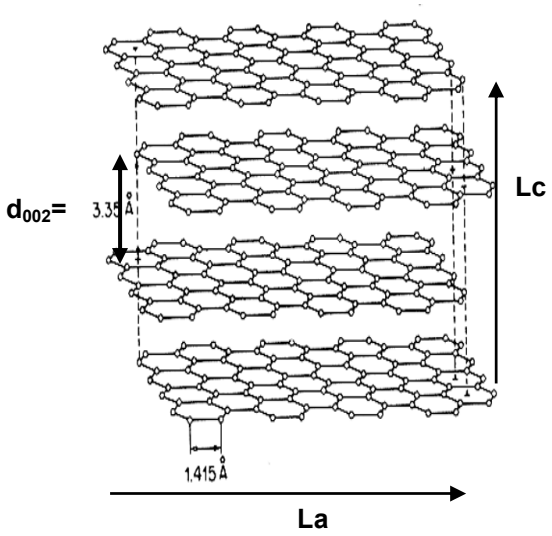

Figure 2.1. Crystal structure of graphite.

The Raman spectra of carbonaceous materials give information of the carbon microstructure and its level of graphitization. Indeed the carbon spectra show a G band at around 1580 cm^{-1} which is related to the symmetric vibrational mode (E2g) of the ideal graphitic lattice and a D1 band at around 1350 cm^{-1} which corresponds to the symmetric vibrational mode (A1g) of the disordered graphitic lattice. Indications of the level of graphitization are given by the $w_{G,}$ which is the width of the G band, and the I_{D1}/I_G, which is the ratio between the heights of the D1 and G bands and if such parameters are high with respect to graphite, the carbon is disordered [2.3-2.4].

The Raman spectra were recorded by a Raman Microscope RENISHAW Mod. INVIA, with Argon ion laser (λ = 514 nm, 5% of 300 mW full power, 4 scans, 10s per scan, 2 cm^{-1} resolution, magnification 50). The spectra were collected at low power (1%=3 mW and 5%=15 mW) and with a limited number of scans because the carbon may over heat. The intensity ratios I_{D1}/I_G were averaged over the data obtained with different spectra collected on different parts of each sample.

2.3. Preparation of electrodes and cell configuration

The carbon electrodes (0.6-0.7 cm^2 geometric area, 8–15 mg cm^2 carbon loading) were prepared by mixing 95% w/w carbon and 5% w/w polytetrafluoroethylene binder

(Du-Pont) to yield a paste which was then laminated on carbon coated aluminum grids (Lamart Corp.).

Three-electrode Swagelok-type cells were used for single-electrode and supercapacitor tests. For single-electrode studies, double-layer carbon counter-electrodes with charge storage capability significantly higher than that of the working electrode were used so as not to limit the capacitance response of the latter. Silver disk was used as quasi-reference electrode for cyclic voltammetry (CV), electrochemical impedence spectroscopy (EIS) and to check electrode potentials during supercapacitor galvanostatic cycling. The potential of silver disk, which was measured in conventional cells prior to electrochemical tests by adding the highly reversible redox couple ferrocene/ferrocinium (Fc/Fc^+) to the medium, was $E_{Ag} = E_{Fc/Fc+}$ - (0.200 ± 0.010) V. The cells were assembled in dry box (MBraun Labmaster 130, H_2O and O_2 < 1 ppm) by sandwiching two carbon composite electrodes either side of a fiberglass separator (Durieux, 200 μm thick when pressed).

2.4. Electrochemical analysis of carbon electrodes

The electrochemical characterization of carbon electrodes were performed by cyclic voltammetry (CV) to evaluate the capacitive response of the carbonaceous materials, the electrochemical tests of double-layer carbon supercapacitors were performed by galvanostatic charge-discharge cycles to evaluate the performance of the system such as C_{SC}, E_{max}, P_{max}, ESR and cycle-life. Also impedence spectroscopy was carried out both on the single-electrodes and supercapacitors to investigate the electrode charge resistance.

During the electrochemical tests the cells were kept at controlled temperatures by a Thermoblock (FALC) or a cryostat HAAKE K40).

Cyclic voltammetry (CV) and galvanostatic charge-discharge cycles were performed with a Perkin–Elmer VMP multichannel potentiostat/galvanostat. The specific capacitances of the carbon electrodes were evaluated by CV at 20 mV s^{-1}, otherwise indicated, from the slope of the integral over time of the discharge voltammetric current vs. electrode potential plot.

The long cycle-life tests were performed by galvanostatic charge-discharge cycles at 10-20 mA cm^{-2} and the conventional Ragone plots and those for HEV applications were performed in the current density range of 0.5-40 mA cm^{-2}.

The impedance spectroscopy measurements were performed by a Solartron SI 1255 frequency-response analyzer coupled to a 273A PAR potentiostat/galvanostat. Impedance spectra were recorded with 5 mV AC perturbation in the 100 kHz to 10 mHz frequency range at DC -1.2 V vs. Fc/Fc^{+} for the single-electrode tests (three electrodes test) and at 0 OCV for the supercapacitor test (two electrodes test).

2.5. References

2.1) P.A. Webb, C. Orr, *Analytical Methods in Fine Particle Technology*, Micromeritics Instrument Corp., Norcross (1997).

2.2) B.E. Warren, *Phys. Rev.* 59 (1941) *693*.

2.3) A. Sadezky, H. Muckenhuber, H. Grothe, R. Niessner, U. Pöschl, *Carbon* 43 (2005) *1731*.

2.4) T. Gruber, T. W. Zerda, M. Gerspacher*, Carbon* 32 (1994) *1377*.

Chapter 3
Ionic liquids used as electrolytes

3.1 Chemical-physical properties of the investigated ionic liquids: EMITFSI, $PYR_{14}TFSI$ and $PYR_{1(2O1)}TFSI$

Ionic liquids (ILs) are room-temperature molten salts which are promising electrolytes for developing safe, high energy carbon double-layer supercapacitors and in this PhD research work the 1-ethyl-3-methylimidazolium bis(trifluoromethanesulfonyl)imide (EMITFSI), N-butyl-N-methyl-pyrrolidinium bis(trifluoromethanesulfonyl)imide ($PYR_{14}TFSI$) and N-methoxyethyl-N-methylpyrrolidinium bis(trifluoromethanesulfonyl)imide ($PYR_{1(2O1)}TFSI$) salts were selected and investigated as electrolytes. EMITFSI and $PYR_{14}TFSI$ were commercial products (Solvionic and Solvent Innovation) which were available with a good level of purity (≥ 98%) and were dried before use. $PYR_{1(2O1)}TFSI$ was provided at higher purity level by Evonik-Degussa in the frame of the ILHYPOS EU project and was used as received. Figure 3.1 shows the conductivity vs. temperature plots of the investigated ILs in the temperature range 20°C/80°C (Figure 3.1a) and -40°C/80°C (Figure 3.1b). Figure 3.1a reports also the conductivity vs. temperature plot of tetraetylammonium tetrafluoroborate in propylencarbonate (PC-Et_4NBF_4), which is a conventional organic electrolyte used in commercial EDLCs.

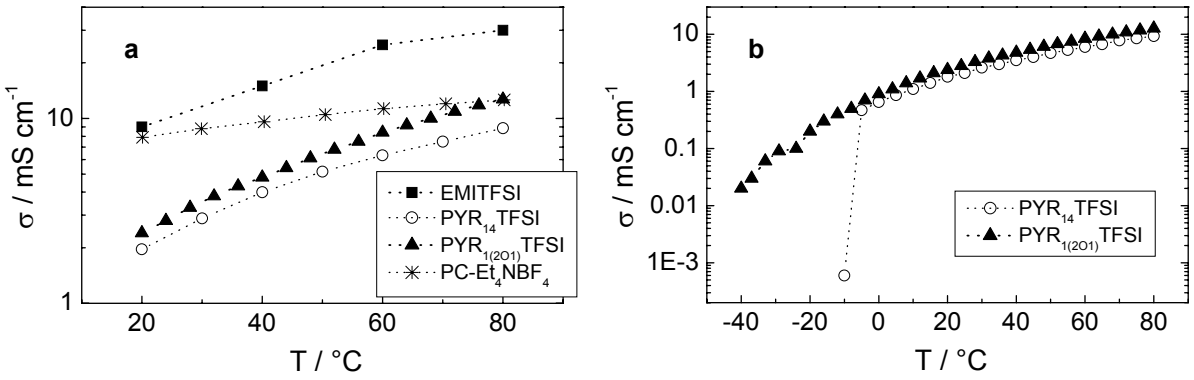

Figure 3.1. Conductivity vs. temperature plots f the ionic liquids investigated in the temperature range 20°C/80°C (a) and -40°C/80°C (b) [3.1-3.3].

EMITFSI was chosen for its good conductivity, while the pyrrolidinum based-ILs were investigated for their wide electrochemical stability window (ESW). EMITFSI conductivity is of the same order than that of the PC-Et_4NBF_4. $PYR_{1(2O1)}TFSI$ conductivity is higher than $PYR_{14}TFSI$'s and, given that it freezes below -90°C, it features appreciable ion conductivity down to -40°C, while $PYR_{14}TFSI$ features a sharp drop of the conductivity just above 0°C where such IL freezes.

Figure 3.2a displays the ESWs evaluated by linear sweep voltammetry (LSV) at 60°C on glassy carbon of the EMITFSI and $PYR_{14}TFSI$ ILs and shows that the cathodic stability of $PYR_{14}TFSI$ is almost 1 V wider than that of EMITFSI. Figure 3.2b shows the comparison of the electrochemical stability evaluated by voltammetry at 20 mV s^{-1} and 60°C of $PYR_{14}TFSI$ using a flat glassy carbon electrode or a porous high surface area carbon electrode. While the porous carbon electrode features notable capacitive voltammetric current because of its high surface area, the glassy carbon electrode features a negligible capacitive current given that its surface area is comparable to its geometric area (ca. 5 order of magnitude lower than that of high surface area porous carbons).

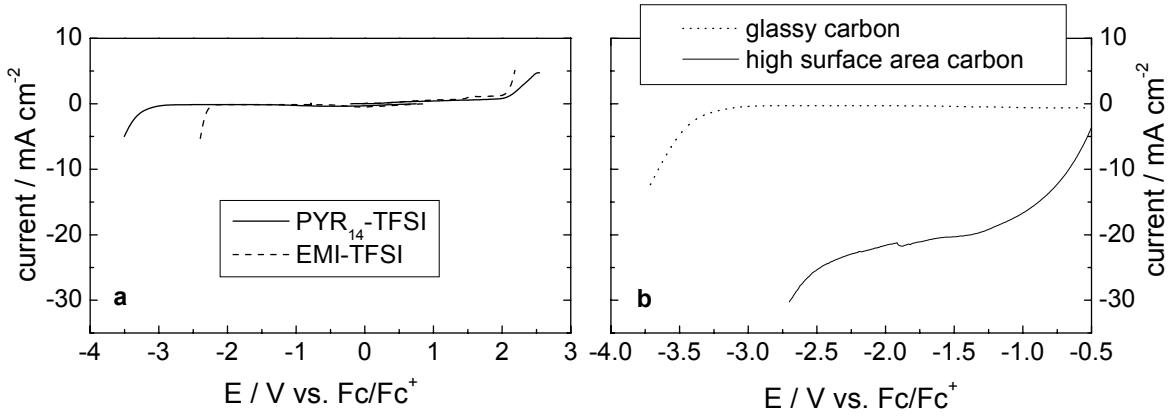

Figure 3.2. ESWs of EMITFSI and $PYR_{14}TFSI$ on glassy carbon evaluated by linear sweep voltammetry at 5 mV s^{-1} and 60°C (a); comparison of the ESWs in the negative potential domain on the glassy carbon and high surface area carbon (X3a, see Chapter 4 and 5) evaluated by voltammetric measurements in $PYR_{14}TFSI$ at 20 mV s^{-1} and 60°C (b) [3.1].

The high surface area of the porous carbon also results in faradic currents which are higher than those recorded by glassy carbon electrode and are magnified in the former because of the high surface area and the presence of surface functional groups that could catalyze redox processes in the IL. This implies that, as shown in Figure 3.2b, the cathodic stability

limit of the IL is ca. 1 V narrower when evaluated by the porous carbon electrode. This explains why the ESWs of the ILs investigated using porous high surface area carbon electrodes and reported in Table 3.1, are narrower than those obtained on flat electrodes reported in Table 1.3 in Chapter 1.

Table 3.1. ESWs evaluated by cyclic voltammetry at 60°C and 20 mV s^{-1} on high surface area carbon with coulombic efficiency of at least 95%.

Ionic liquids		
EMITFSI	**$PYR_{1(2O1)}TFSI$**	**$PYR_{14}TFSI$**
3.7 V	4.0 V	4.2 V

The thermal stability of the ionic liquids selected in this work was investigated by TGA in O_2 and N_2. Figure 3.3a shows the thermal stability under N_2 atmosphere, while the Figure 3.3b shows the thermal stability in presence of O_2.

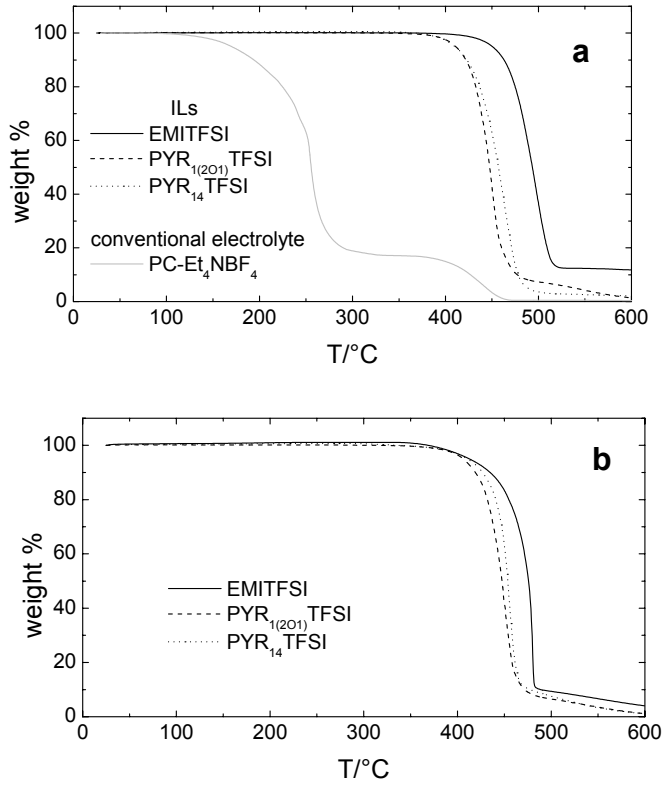

Figure 3.3. TGA of the ILs EMITFSI, $PYR_{1(2O1)}TFSI$ and $PYR_{14}TFSI$ in nitrogen [3.1] (a) and oxygen (b) atmosphere, it is also shown the TGA in nitrogen of a conventional organic electrolyte tetraetylammonium tetrafluoroborate in propylencarbonate ($PC\text{-}Et_4NBF_4$) [3.4].

The results indicate that all the ILs are thermally stable up to more than 350°C both in nitrogen and oxygen atmosphere and that they are much more stable than conventional

organic electrolytes as PC-Et_4NBF_4, whose TGA is also reported in Figure 3.3a for a comparison. The result obtained in presence of oxygen is particularly important because it evidences the nonflammability of these ILs, which can be used in safe electrochemical devices.

3.2. Conclusions

On the basis of the above reported results, the most promising IL for the development of EDLCs based on solvent-free electrolytes is $PYR_{1(2O1)}$TFSI that was also selected within the EU ILHYPOS project because of its hydrophobicity exhibited together with good conductivity and wide ESW, exploitable in a wide temperature range, below 0°C. For such exceptional properties $PYR_{1(2O1)}$TFSI was used for the whole study to develop large size IL-based carbon supercapacitor prototypes [3.4] as illustrated in Chapter 6.

3.3. References

[3.1] D. Cericola, *Materiali carboniosi e liquidi ionici per supercapacitori a doppio strato.* Graduate Thesis, SMETEC Department, University of Bologna, Italy, October 2007.

[3.2] G. B. Appetecchi, M. Montanino, D. Zane, M. Carewska, F. Alessandrinia, S. Passerini, *Electrochim. Acta* 54 (2009) *1325*.

[3.3] M. Conte, *23rd International Electric Vehicle Symposium* (EVS23), Anaheim, CA, December 2–5 (2007).

[3.4] C. Arbizzani, M. Lazzari, F. Soavi, M. Mastragostino, M. Conte, *ECS Trans.* (2010) in press.

Chapter 4
Carbons as electrode materials

4.1. Preparation of carbon materials

In this PhD research work much effort was focused on the development of carbonaceous materials as electrodes for IL-based supercapacitors. The strategies adopted were primarily devoted to enhance the carbon capacitive response in ILs. Thus, mesoporous carbons of high specific surface area that can be easily accessed by the IL electrolyte, were synthesized with attention to porosity and surface chemistry in order to avoid charge limitation from the liquid and solid part of the electrode/electrolyte interphase [4.1]. Indeed, the carbons should display a pore volume high enough to prevent electrolyte starving and pore walls thicker than the screening length of the electric field (see Chapter 1) [4.1-4.3]. Moreover the carbons should feature a pore size wider than the IL counterions which, as reported in Section 1.6, on the basis of geometric considerations should be of 2-3 nm [4.1]. Carbons should also have a tailored surface chemistry which in turn affects carbon wettability by IL ions, the electronic properties of the carbon itself and its surface polarizability. Several synthetic routes were pursued: i) surface modification of commercial activated carbon (AC) [4.4, 4.5]; ii) synthesis of mesoporous aero/cryo/xerogel carbons (ACX) which feature high and tunable mesoporosity that can be controlled by chemical synthesis conditions, narrow pore-size-distribution, high electrical conductivity and hydrophobic surface [4.4-4.7]; and iii) synthesis of disordered template mesoporous carbons (DTCX) where the choice of the template and the mass ratio between carbon precursor and template allows to control the porosity of the resulting material [4.8-4.11].

4.1.1. Surface modification of commercial activated carbon

The activated carbon (AC, Picactif BP10) was provided by Pica and was treated at 1050 °C in Ar atmosphere (200 cc/min) for 2 h in order to remove surface functionalities which are typically present in such carbons after chemical activation processes. The surface cleaning was demonstrated by TGA and FTIR analyses. The TGA plot of AC carbon reported in Figure 4.1 demonstrates the presence of functional groups which starts to decompose at ca.

300°C and with the main fraction removed at 500°C; over 800°C a further decomposition occurs [4.12]. Figure 4.2 shows the FTIR-ATR spectra of the pristine carbon (AC) and the heat treated carbon (ACT) and shows that the bands of C=O at 1760 cm^{-1} and 1570 cm^{-1} and of CO_2 (chemisorbed on the surface) at 2340 cm^{-1} decrease after heat treatment [4.5]. Note that such moieties are indicative of hydrophilic character of the carbon surface.

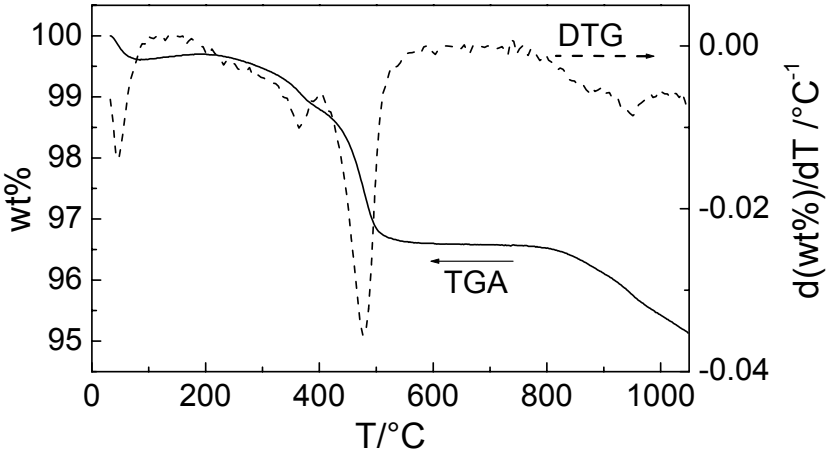

Figure 4.1. TGA plot (solid line) and its differential (DTG, dashed line) of the pristine activated carbon AC [4.12, 4.13].

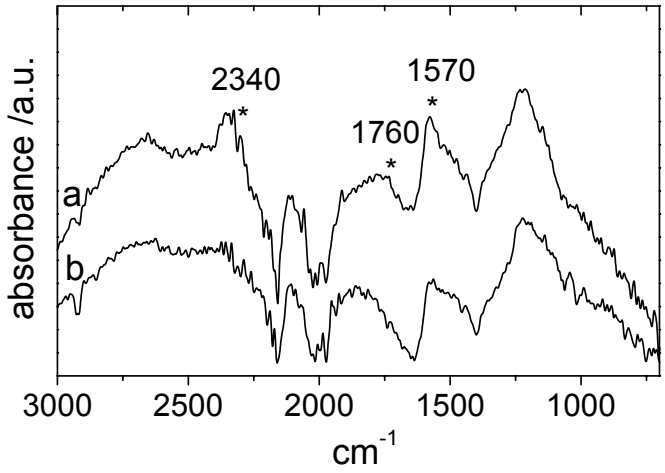

Figure 4.2. FTIR-ATR spectra of pristine activated carbon AC (a) and heat treated activated carbon ACT (b) [4.12, 4.13].

Figure 4.3a shows the N_2 adsorption-desorption isotherms of AC and ACT carbons which are of type IV [4.14] suggesting the mesoporous nature of the carbons. Figure 4.3b reports the trend of the differential specific pore volume (dV/d*w*) *vs.* pore width (*w*) calculated by the DFT theory, and shows that the pore-size distribution (PSD) is centered at 2.7 nm and

the porosity is mainly distributed at pore size > 1.5 nm, wide enough to be filled with the IL ions.

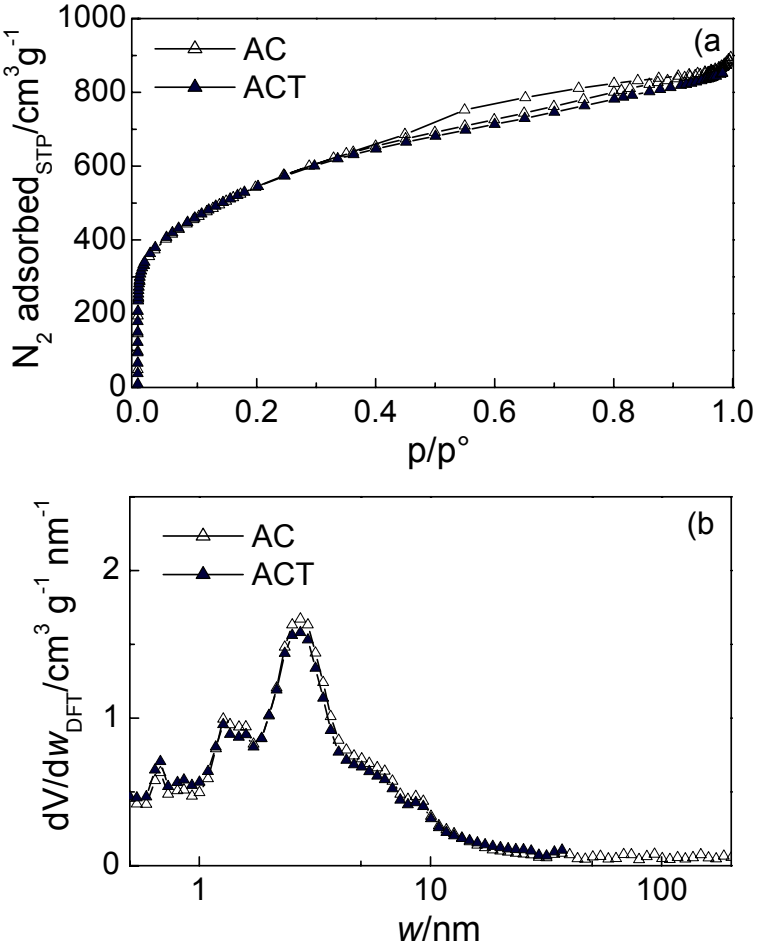

Figure 4.3. N_2 adsorption-desorption isotherms (a) and DFT specific differential pore volume vs. pore size (b) of the AC and ACT carbons.

Table 4.1 reports the total pore volume (V_{tot}), the specific pore volume ($V_{>1.5\ nm}$) and specific surface area ($S_{>1.5\ nm}$) from pores with size in the 1.5 nm – 200 nm range, and main pore size (<*w*>) of the AC and ACT carbons. The porosity analysis shows that the heat treatment does not modify the porosity of the AC carbon. Such carbons, AC and ACT, were electrochemically tested and the results are reported in Section 4.2. Figure 4.4 reports the XRD spectra of the pristine AC and treated ACT carbon powders and evidences that the high temperature treatment in Ar does not modify the crystalline properties of the carbon.

Table 4.1. Total pore volume (V_{tot}), DFT specific pore volume ($V_{>1.5\ nm}$) and specific surface area ($S_{>1.5\ nm}$) from pores with size in the 1.5 nm – 200 nm range, and main pore size (<*w*>) of the AC and ACT carbons.

Code	V_{tot} $cm^3\ g^{-1}$	$V_{>1.5\ nm}$ $cm^3\ g^{-1}$	$S_{>1.5\ nm}$ $m^2\ g^{-1}$	<*w*> nm
AC	1.38	0.84	1020	2.7
ACT	1.34	0.84	972	2.7

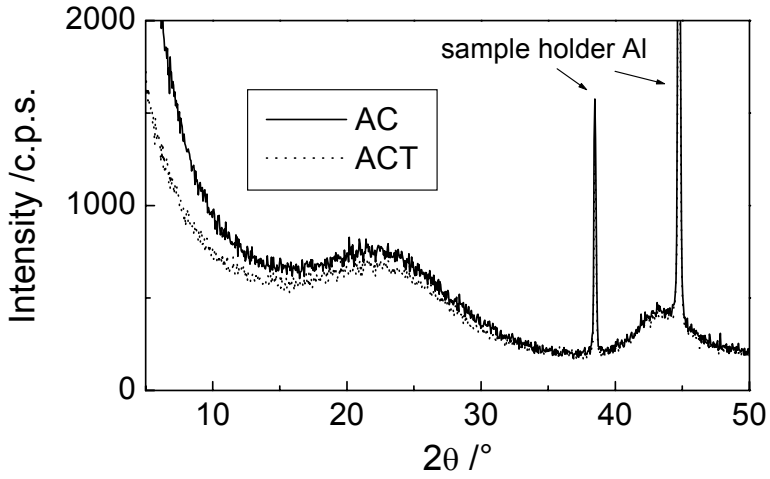

Figure 4.4. XRD spectra of the pristine AC and the treated ACT carbon powders.

Table 4.2 reports the distance between the graphene layers (d_{002}), the size of the graphene crystals along the c-axis (L_c, normal to the graphene plane) and the a-axis (L_a, along the graphene plane) of the pristine AC and treated ACT carbons evaluated as discussed in Chapter 2 [4.15]. The data in Table 4.2 evidence that the AC and ACT are amorphous carbons composed of small graphene crystallites which are constituted by few (2-3) graphene layers spaced by a 3.8 Å distance higher than that of ideal graphite crystals (3.4 Å), and 37 Å wide (note that a graphene ring is ca 2.8 Å wide).

Table 4.2. Distance between the graphene layers (d_{002}), size of the graphene crystals along the c-axis (L_c) and the a-axis (L_a) of the pristine AC and treated ACT carbons.

Carbone	d_{002} Å	L_c Å	L_a Å
AC	3.8	8.7	37.4
ACT	3.9	8.6	36.4

The AC and ACT carbons were analyzed by Raman spectroscopy and Table 4.3 reports the main features of the collected spectra, i.e. the mean values (calculated over different

spectra for each sample) of the position (λ_G) and width (w_G) of the G band and of the ratio of the heights of the D1 and G bands (I_{D1}/I_G). [4.15, 4.16].

The data in Table 4.3 show that both the carbons exhibit an amorphous character in agreement with the XRD analyses and are very similar in the microcrystalline structure. The I_{D1}/I_G ratio of ACT carbon is slightly higher then that of AC and this is due to the increase of not functionalized graphene edges. Such results suggest that upon thermal treatment in Ar loss of functional groups which typically anchor on the graphene edges occurs.

Table 4.3. Mean values of the position (λ_G) and width (w_G) of the G band and of the ratio of the heights of the D1 and G bands (I_{D1}/I_G) of the pristine AC and treated ACT carbons.

Carbon	λ_G	w_G	I_{D1}/I_G
AC	1597 ± 4	61 ± 4	0.97 ± 0.05
ACT	1592 ± 3	69 ± 2	1.09 ± 0.04

4.1.2. Synthesis of mesoporous aero/cryo/xerogel carbons

The cryogel and xerogel carbons were prepared as in Chapter 2 by polycondensation of resorcinol (R) and formaldehyde (F) in water (W) with Na_2CO_3 (C) as gelation catalyst. The Table 4.4 summarizes the synthesis conditions of the cryo/xerogel carbons that were prepared with a molar ratio between resorcinol and formaldehyde of 0.5 and different values of the dilution factor D (= $mol_W/(mol_R+mol_F+mol_C)$), the ratio between resorcinol and catalyst R/C, and the initial pH of the gelation solution which was adjusted adding HNO_3 or NH_4OH concentrated solutions. The gelation was carried out in the temperature range between RT and 85°C over several days (3-11 days) and, in some cases, the gel was put in a stirred aqueous solution of 5% w/w acetic acid at 45°C for few days to promote the crosslinking of the polymer [4.17, 4.18]. Then the next step consisted in water/*t*-butanol (Fluka, >99.7%) or water/acetone solvent exchange and freeze or RT drying, to yield organic cryogel and xerogel, respectively. The pyrolyses of the organic gels were carried out at 800-1050°C for 2 hours under Ar flow (200 cc min^{-1}) both upon heating and cooling.

Note that also a commercial aerogel carbon purchased from Marketech (CA1) was investigated for comparison to the synthesized cryo/xerogel carbons and the name ACX here is used to indicate the whole group of aero/cryo/xerogel carbons.

Table 4.4. Synthesis conditions (D= dilution factor, R/C= resorcinol to catalyst ratio, pH of sol, time and temperature (T) of gelation and temperature (T) of pyrolysis of cryogel (indicated as cryo or C as initial name letter) and xerogel (indicated as xero or X as initial name letter) carbons.

Sample name	D	R/C	pH	Gelation time and T	Pyrolysis T
X19100	1.9	100	7.1	3 days at 80°C	1050°C
X19200	1.9	200	-	4 days at 80°C	1050°C
X25100	2.5	100	7.3	3 days at 80°C	1050°C
CRFB1/xero	2.5	200	6.4	11 days at 80°C	850°C
X1	2.5	200	-	4 days at 80°C	1050°C
X2.5200C	2.5	200	6.4	11 days at 80°C	1050°C
CRFB4/cryo	2.5	800	6.4	7 days at 85°C	1050°C
X4400A	4	400	6.4	40h at RT, 6 days at 80°C	900°C
X4400B	4	400	5.8	40h at RT, 6 days at 80°C	900°C
X3	4	400	6.5	7 days at 80°C	850°C
X5.750A	5.7	50	6.3	5 days at 80°C	900°C
X5.750C	5.7	50	6.8	7 days at 80°C	850°C
X5.7100A	5.7	100	6.3	5 days at 80°C	900°C
X5.7100C	5.7	100	6.7	7 days at 80°C	850°C
X2	5.7	300	6.5	1 day RT, 4 days at 80°C, 7 days in 5% acetic acid washing	900°C
X5.7300B	5.7	300	6.7	7 days at 80°C	850°C
CRFB5/cryo	5.7	500	6.6	4 days at 85°C	1050°C
CRFC5/xero	5.7	500	6.6	4 days at 85°C	1050°C
X6.5500BA	6.5	500	6.0	5 days at 80°C	900°C
X7.5100	7.5	100	6.3	5 days at 80°C	850°C
X7.5100B	7.5	100	7.1	1 day RT, 2 days 80°C, 5 days in 5% acetic acid washing	900°C
X7.5200	7.5	200	6.3	4 days at 80°C	1050°C
C7.5200	7.5	200	6.4	6 days at 80°C	900°C
X15.81500	15.8	1500	6.7	1 day RT, 6h 50°C, 2.5 days at 85°C, 5 days in 5% acetyic acid washing	900°C
X165B	16	5	6.4	5 days at 80°C	900°C
X1625a	16	25	7.7	5 days at 80°C	1050°C
C1625b	16	25	7.7	5 days at 80°C	900°C
X1625d	16	25	6.2	5 days at 80°C	1050°C
C1625e	16	25	6.3	6 days at 80°C	900°C
X1625H	16	25	6.2	7 days at 80°C	1050°C
C16200	16	200	6.3	6 days at 80°C	900°C
X16800	16	800	6.3	6 days at 80°C	1050°C
X6050A	60	50	5.5	7 days at 85°C	800°C
X6050B	60	50	6.3	7 days at 85°C	800°C

Several cryo/xerogel carbons were prepared, as shown in Table 4.4, with the aim to reach $S_{>1.5\ nm}$ (specific surface area arisen from pores wider than 1.5 nm) ≥ 500 $m^2\ g^{-1}$ that should guarantee high capacitance response in ILs. Therefore synthesis parameters were changed such as the dilution factor D, which was modified from 1.9 for the most concentrated gelation solution that yielded compact and, in some cases, poorly porous carbon materials, to D of 16 and 60 for the most diluted ones that yielded brittle porous carbons with broad pore-size-distribution (PSD). The catalyst amount (defined by R/C ratio) and the pH of the gelation solution were also modified and carbons with higher degree of porosity where obtained with pH between 6.3 and 6.6 while pH down to 5.8 or up to 7.2 yielded poorly porous carbons.

The carbons synthesized with D<16 and the CA1 carbon were available as hard pieces, thus, was necessary to get carbon powder by milling in order to prepare electrodes. The milling was carried out by planetary mill, which in some cases significantly modified the morphology of the ACX carbons. Indeed, the data in Table 4.5, which reports the gelation bath composition and some porosity features ($V_{>1.5\ nm}$ and $S_{>1.5\ nm}$) for the carbons not milled, hand grounded (soft milling) and milled in WC jar at 250 rpm for 20 minutes (hard milling), show that hard milling reduced significantly the mesopore volume and surface for ACX carbons and this is particular evident for the X6050B and X165B, which are those obtained with the highest dilution factors.

Table 4.5. Carbon type (aerogel, cryogel, xerogel carbons), gelation bath composition (D, R/C, pH), $V_{>1.5\ nm}$ and $S_{>1.5\ nm}$ for the carbon not milled, hand grounded (soft milling) and milled in WC jar 250 rpm 20 minutes (hard milling).

SAMPLE	**type/D_R/C_pH**	**$V_{>1.5\ nm}$ (cm^3/g)**			**$S_{>1.5\ nm}$ (m^2/g)**		
		No milled	*Soft milling*	*Hard milling*	*No milled*	*Soft milling*	*Hard milling*
CA1	aero/Marketech	0.19	-	0.15	180	-	130
X6050B	xero/60_50_6.34	-	0.54[a]	0.17	-	224[a]	76
C1625e	cryo/16_25_6.35	3.00	2.93	-	372	360	-
X165B	xero/16_5_6.36	0.47	0.29	0.08	144	56	32
CRFB5	cryo/5.7_500_6.6	1.41	-	1.12	260	-	242
CRFC5	xero/5.7_500_6.6	1.04	-	0.69	307	-	215
X2	xero/5.7_300_6.5	-	0.91	0.78[b]	-	357	308[b]
X2.5200CA	xero/2.5_200_6.4	-	0.24	0.13	-	196	89
CRFB4	cryo/2.5_800_ 6.4	-	0.29	0.23	-	176	133

[a]milled 5 minutes at 250 rpm in WC jar.
[b]milled 2 minutes at 150 rpm and 2 minutes at 250 rpm in agate jar.

Indeed, to high D correspond less bulky organic gels that brings about brittle carbons. Therefore, planetary mill was used with agate jar at 250 rpm for 4 minutes in order to get a fine carbon powder and to avoid significant decrease of the carbon porosity.

Table 4.6 summarizes the synthesis conditions and the porosity data evaluated from the N_2 adsorption isotherms of the xerogel carbons which featured the highest $S_{>1.5\ nm}$, among those prepared and of the CA1. Despite the high pore volume of ca. 1.0 $cm^3\ g^{-1}$ (mainly from mesopores) the X2 and X3 carbons displayed $S_{>1.5\ nm}$ of ca. 310 $m^2\ g^{-1}$. It was found that though the pore volume increased with D, it also widened the pore size, so that it was not very effective in the increase of $S_{>1.5\ nm}$. Thus, in order to reach high specific capacitance response (≥ 100 F g^{-1}), the prepared xerogel carbons were activated in CO_2 flow - followed by thermal treatment in inert atmosphere. The treatment was carried out with CO_2 flow of 200 cc/min at 850°C over different time intervals (t_{CO_2}), then the sample was kept 1h in Ar (200 cc/min) at the same temperature, heating (10°C/min) and cooling were carried out in Ar. The activation step was followed by thermal treatment in Argon atmosphere so as to eliminate eventual hydrophilic surface moieties that may arise from the burn-off in CO_2 and which are detrimental for the hydrophobic IL permeation into the carbon. The CO_2/Ar treated carbons are labelled with "a" at the end of the original name. The CO_2/Ar treatments significantly increased total pore volume (micropores included) of the carbons without modifying their mesopore size distribution and with the X2a and X3a carbons $S_{>1.5\ nm}$ values of 412 and 564 $m^2\ g^{-1}$, respectively, were achieved. As an example, Figure 4.5 shows the DFT incremental pore volume vs. pore size of the pristine X3 and treated X3a xerogel carbons to evidence that the pore size distribution is not altered by the activation step. On the basis of these results also the commercial aerogel carbon CA1 was activated by CO_2 following the same procedure used for the xerogel carbons and the porosity of the treated carbons (CA1a) is reported in Table 4.6. The CA1 pristine carbon featured a narrow pore size distribution centred at 6 nm and displayed a low mesoporous surface which increased up to more than 600 m^2/g after activation.

Figure 4.6 reports the XRD spectra of the pristine CA1, CRFB4 and CRFB5 carbons and Table 4.7 reports the distance between the graphene layers (d_{002}) and the size of the graphene crystals L_c and L_a, which were evaluated as reported in Chapter 2 [4.15]. The data in Table 4.7 evidence that also in the case of the cryo/xero/aerogel carbons (ACX) the

level of graphitization is low, and it seems even lower than that of the AC and ACT carbons.

Table 4.6. Synthesis conditions (R/C, D, pH and CO_2 activation time, t_{CO2}), total pore volume at p/p°= 0.995 (V_{tot}), pore volume ($V_{>1.5\ nm}$) and specific surface area ($S_{>1.5\ nm}$) related to pores of size between 1.5 nm and 200 nm, main mesopore size (<*w*>) of the pristine and CO_2/Ar treated (X1a, X2a, X3a, CA1a) ACX carbon powders from the DFT analysis of the corresponding N_2 adsorption isotherms at 77 K.

Code	Synthesis conditions				Porosity			
	R/C	D	pH	t_{CO_2} h	V_{tot} cm^3g^{-1}	$V_{>1.5\ nm}$ cm^3g^{-1}	$S_{>1.5\ nm}$ m^2g^{-1}	<*w*> nm
X1	200	2.5	6.4	-	0.36	0.17	152	5
X2	300	5.7	6.5	-	1.02	0.80	307	14
X3	400	4	6.5	-	1.08	0.87	312	15
X1a	200	2.5	6.4	2.5	1.08	0.51	372	6
X2a	300	5.7	6.5	4.0	1.39	0.99	412	14
X3a	400	4	6.5	5.5	1.91	1.33	564	15
CA1	aerogel carbon Marketech			-	0.35	0.15	130	6
CA1a	activated CA1			9.5	1.17	0.62	610	6
CRFB4	800	2.5	6.4	-	0.47	0.23	134	9
CRFB5	500	5.7	6.6	-	1.49	1.12	242	20
CRFC5	500	5.7	6.6	-	0.99	0.66	216	15
C1625e	25	16	6.3	-	3.63	2.93	360	10-100

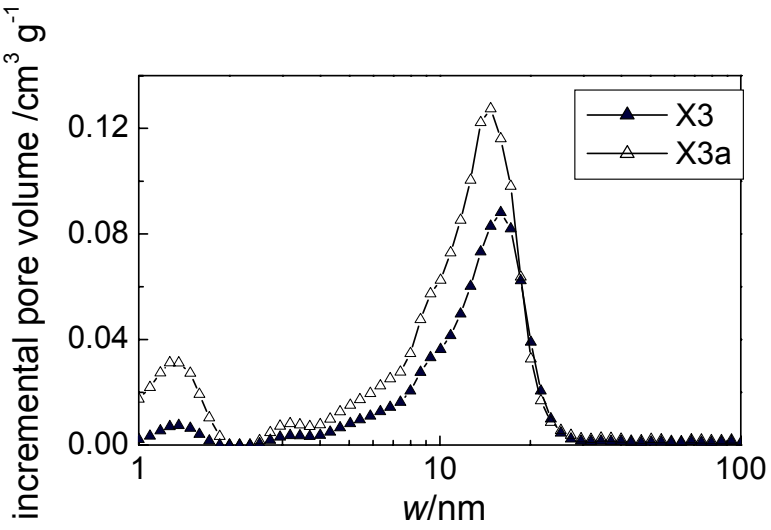

Figure 4.5. DFT incremental pore volume vs. pore size of the pristine X3 and treated X3a xerogel carbons.

Indeed, the CA1, CRFB4 and CRFB5 carbons display L_c values lower than those of the AC and ACT carbons and indicates that graphene crystallites are constituted by 1-2 graphene layers 3.8 Å distant from each other (note that d-spacing for ideal graphite is 3.4 Å) and 32 Å wide (10% smaller than those of the AC and ACT carbons).

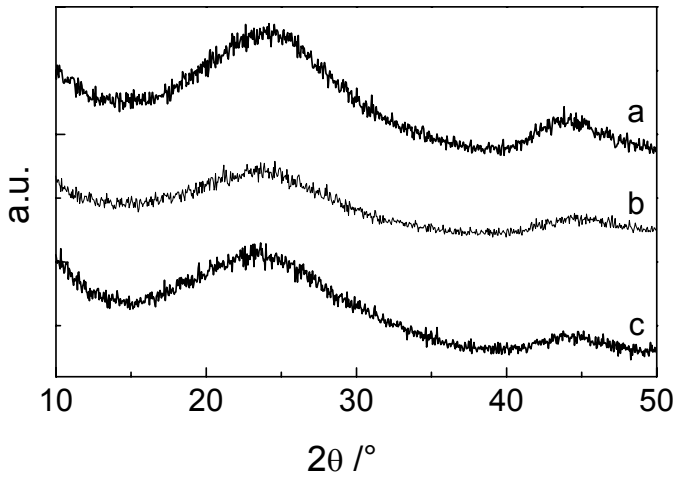

Figure 4.6. XRD spectra of a) CA1, b) CRFB4 and c) CRFB5 carbons.

Table 4.7. Distance between the graphene layers (d_{002}), size of the graphene crystals along the c-axis (L_c) and the a-axis (L_a) of the CA1, CRFB4, CRFB5 carbons.

Carbon	**d_{002} Å**	**L_c Å**	**L_a Å**
CA1 Marketech	3.7	6.2	32.0
CRFB4	3.8	5.4	30.8
CRFB5	3.8	5.3	32.6

Some of the ACX carbons were characterized by Raman spectroscopy and Table 4.8 reports the main features of the spectra [4.15, 4.16] and show that all the carbons exhibit an amorphous character in agreement with the XRD analyses and are very similar in their microcrystalline structure.

Table 4.8. Mean values of the position (λ_G) and width (w_G) of the G band and of the ratio of the heights of the D1 and G bands (I_{D1}/I_G) of CRFB5, CRFB4 and X1a carbons.

CARBON	**λ_G**	**w_G**	**I_{D1}/I_G**
CRFB5	1589 $\pm$ 2	82 $\pm$ 1	0.90 $\pm$ 0.05
CRFB4	1590 $\pm$ 2	66 $\pm$ 2	0.96 $\pm$ 0.03
X1a	1590 $\pm$ 5	77 $\pm$ 3	0.94 $\pm$ 0.01

The absence of carboxyl groups on the carbon surface is demonstrated by TGA where the functional groups of the X3a starts to decompose over 500°C as shown in Figure 4.7 and by the FTIR-ATR spectrum reported in Figure 4.8 where the band at ca. 1700 cm^{-1} characteristic of the carboxyl groups is absent and the bands at 3150 cm^{-1}, 2160 cm^{-1}, 2040 cm^{-1}, 1970 cm^{-1}, 1540 cm^{-1} and 1100 cm^{-1} are related to the O-H, C-O, C≡C, C=O, C=C and C-O stretchings, respectively [4.19, 4.20].

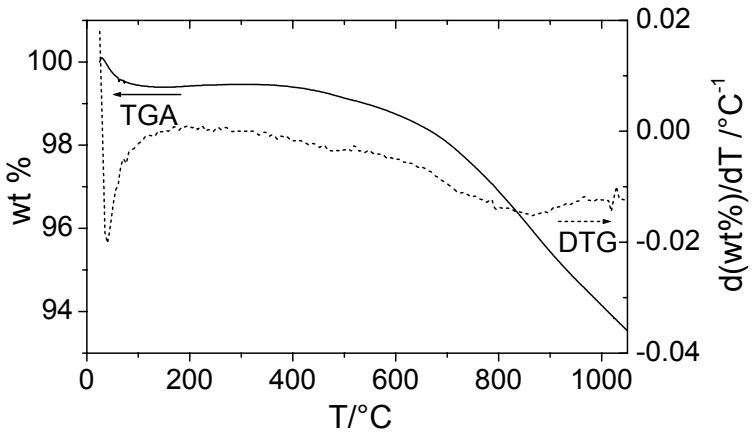

Figure 4.7. TGA plot (solid line) and its differential (DTG, dashed line) of the xerogel carbon X3a.

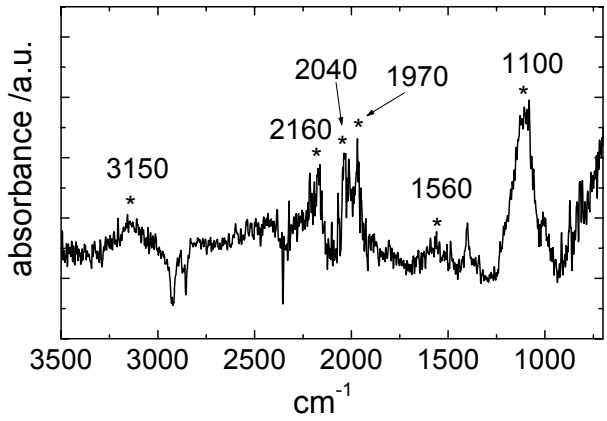

Figure 4.8. FTIR-ATR spectra of the xerogel carbon X3a.

Figure 4.9 shows the pore-size-distribution in terms of incremental pore volume from DFT analyses of the ACX carbons selected for electrochemical investigation. The highest values of $S_{>1.5\ nm}$ is obtained with the CO_2/thermal treatment aero/xerogel carbons CA1a, X1a, X2a and X3a.

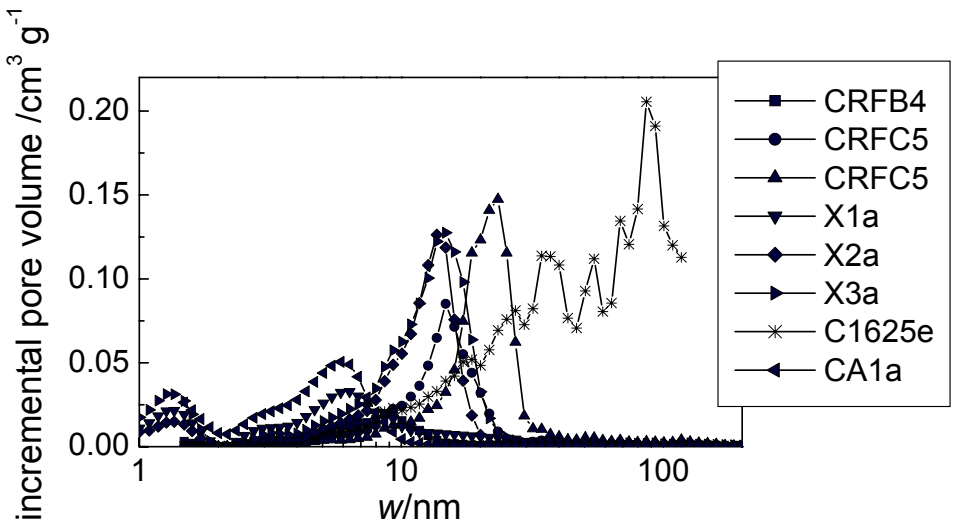

Figure 4.9. DFT incremental pore volume vs. pore size of the ACX carbons selected for electrochemical investigation.

4.1.3. Synthesis of disordered MgO template mesoporous carbons

The disordered MgO template mesoporous carbons (DTCX) were prepared by mixing organic salts of Mg, which is the precursor of both templating agent MgO and carbon, with thermoplastic polymer, which avoids MgO agglomeration upon pyprolysis and may contribute to carbon yield, using planetary mill in agate jar at 250 rpm for 5 minutes. The mixture was pyrolysed at 900°C for 1h with heating rate of 5°C min^{-1} in Ar (200 cc min^{-1}). The resulting powder was milled at 400 rpm for 1h and then washed with H_2SO_4 2 M at RT to dissolve MgO template, which was formed upon pyrolysis [4.8-4.10].

The MgO template precursors used were Mg D-gluconate hydrate, Mg acetate tetrahydrate, Mg citrate tribasic nonahydrate and Mg bis(monoperossiphtalate) and their structures are shown in Figure 4.10. The use of the first three precursors was already reported in literature [4.8-4.10], while Mg bis(monoperossiphtalate) was selected for the possibility to improve the electronic properties of the resulting carbon because of the presence of the aromatic ring in its structure.

The thermoplastic polymers (TPs) were poly(ethylene terephthalate) (PET) and polystyrene (PS), which have the aromatic ring in their monomeric units, as shown in Figure 4.11.

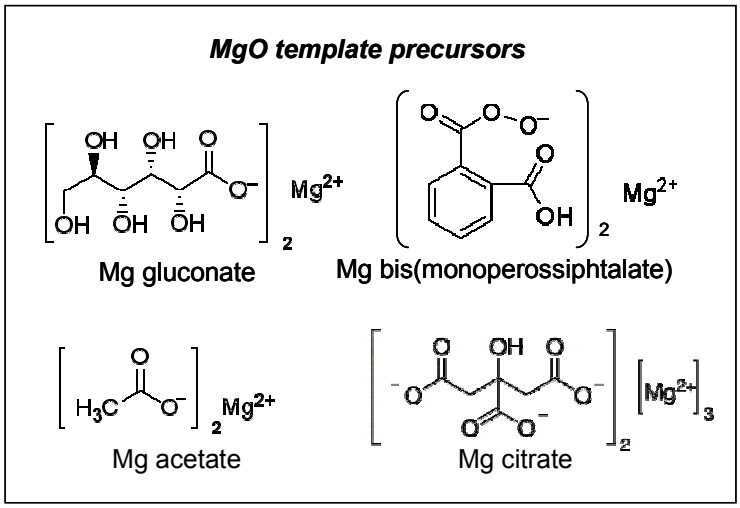

Figure 4.10. Structures of DTCXs precursors used.

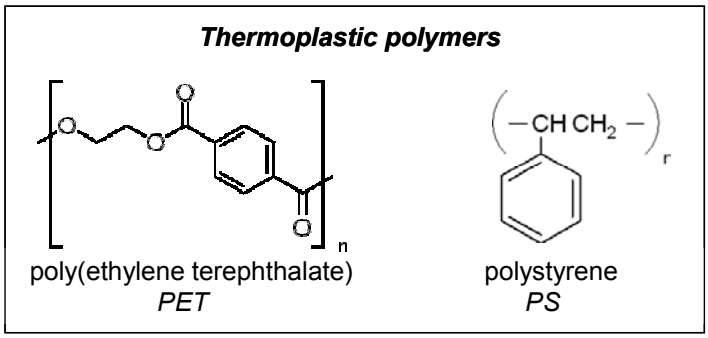

Figure 4.11. Structures of thermoplastic polymers used.

The most interesting DTCX carbons were obtained using Mg citrate salt, as shown by the data in Table 4.9 that reports the thermoplastic polymer (TP), the MgO precursor and the weight ratio TP/MgO used, where the MgO weight was determined on the basis of the mass of MgO that was expected to be formed from the magnesium salt upon pyrolisis. The Table reports also the porous properties of the DTCX carbons. The Mg citrate-based carbons, i.e. the carbons from DTC3 to DTC8, are the most porous ones. In these materials the acid treatment of such carbons, carried out at RT in order to remove MgO template, was effective as shown in Figure 4.12a which reports, as an example, the XRD spectra of the DTC7 carbon before and after the acid treatment. The XRD spectrum before the acid treatment displays all the reflexes of MgO (related to (111), (200), (220), (311) and (222) family of lattice planes) observable in the 2θ range investigated, which disappear in the XRD spectrum of the carbon after acid washing. The spectrum of the resulting carbon

displays the reflex (100) of graphite at ca. 43.7° 2θ which is quite broad suggesting the amorphous character of such carbon. In the case of the synthesis based on Mg gluconate and Mg bis(monoperossiphtalate), the acid treatment, even carried out at reflux, did not remove the MgO template as shown by XRD spectra of the DTC9 carbon reported, as example, in Figure 4.12b, while the synthesis based on Mg acetate was not further investigated because the resulting carbon was poorly porous, as shown by the data reported in Table 4.9.

Table 4.9. Thermoplastic polymer (TP), weight ratio between thermoplastic polymer and expected MgO, total pore volume at p/p°= 0.995 (V_{tot}), $V_{>1.5\ nm}$, $S_{>1.5\ nm}$, <*w*> and percentage of inorganic material of the DTCX carbon series.

Code	TP	MgO precursor	ratio TP/MgO	porosity				inorganic material w/w %
				V_{tot} cm^3g^{-1}	$V_{>1,5nm}$ cm^3g^{-1}	$S_{>1,5nm}$ m^2g^{-1}	<*w*> nm	
DTC1	PET	Mg gluconate	1/9	-	-	-	-	-
DTC2		Mg acetate	2.5/7.5	0.11	0.05	43	-	-
DTC3		Mg citrate	5/5	0.80	0.32	355	3.5	36
DTC4			2.5/7.5	1.17	0.54	575	4.5	21
DTC5			1.5/8.5	1.18	0.52	685	3.0	12
DTC6	PS	Mg citrate	2.5/7.5	1.46	0.73	950	3.0	2.5
DTC7			5/5	0.95	0.70	1018	2.7	4.9
DTC8	-	Mg citrate	-	1.45	0.91	1180	3.3	6
DTC9	-	Mg bis(monoperossiphtalate)	-	-	-	-	-	-

It was reported that Mg citrate gives nano-sized particles of MgO through pyrolysis at a temperature below 200 °C [4.8] and PET and PS feature decomposition process at 450°C and 420°C, respectively, evaluated by TGA in nitrogen. Therefore, such thermoplastic polymers play a role during the formation of MgO particles by avoiding their agglomeration. Table 4.9 reports, in the last column, the weight percentage of residual inorganic material in the carbon which was evaluated by TGA in O_2 and, given that the PET contributes to the carbon yield and its composition involves 30% of ash, the carbons prepared with PET (DTC3, DTC4 and DTC5) feature a significant amount of inorganic material, which is dead weight detrimental for the carbon specific performances. PS is a pure polymer, however, decomposes in volatile compounds [4.21] upon pyrolisis, thus, it has only the role to avoid agglomeration of the MgO template particles. The carbons

prepared with both Mg citrate and PS (DTC6 and DTC7) and with Mg citrate without PS (DTC8) are the most promising carbons because feature the highest degree of porosity and the lowest inorganic impurity content.

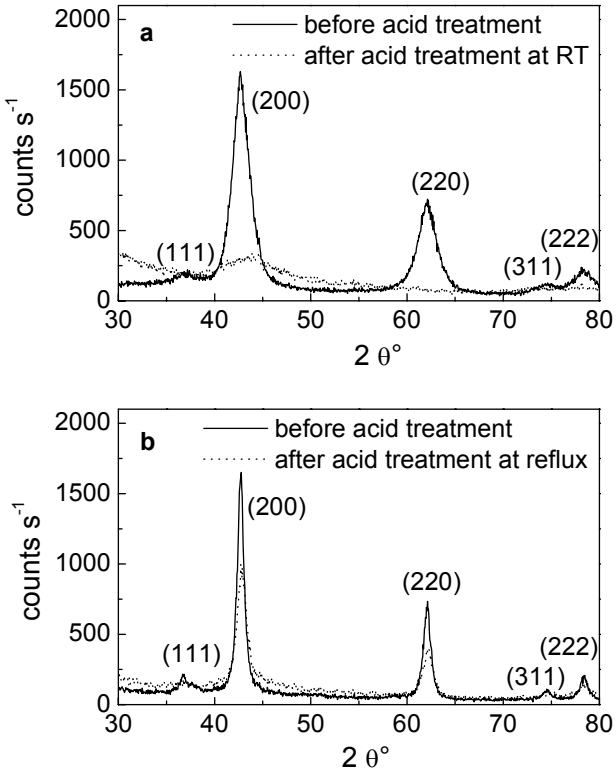

Figure 4.12. XRD spectra before and after acid treatment of the carbons DTC7 (a) and DTC9 (b).

The FTIR analysis demonstrated that DTCX carbons have surface chemistry free from carboxyl-acid groups as Figure 4.13 shows for carbons DTC3 and DTC8 as an example. Indeed both of these spectra do not display the band related to carboxyl groups (ca. 1700 cm^{-1}), while display the bands at 1580 cm^{-1} and 1950-2040 cm^{-1} which correspond to the C=C of the aromatic ring and the C=O (probably from CO_2 physisorbed). They show also bands at 2160 cm^{-1}, 2300 cm^{-1} corresponding to O-H and at 2390-2640 cm^{-1} related to C-H stretching. The broad band at 840-1260 cm^{-1} is related to C-O stretching and is present only in the spectrum of DTC3 carbon, the main part of such ether groups probably derived from PET, which is rich of oxygen.

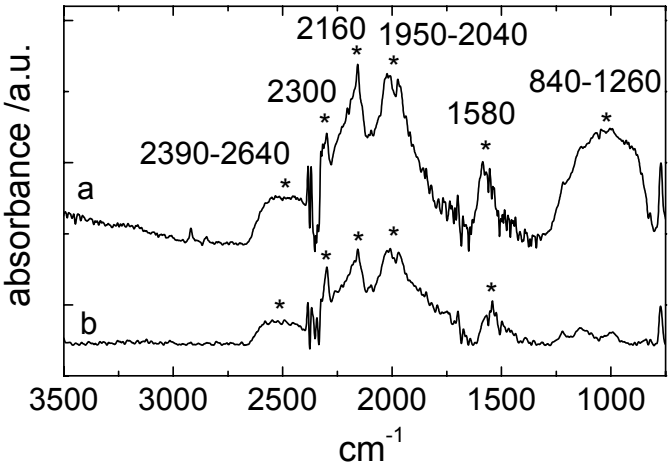

Figure 4.13. FTIR-ATR spectra of the carbons DTC3 (a) and DTC8 (b).

Figure 4.14 shows the pore size distribution (PSD) of carbons from DTC4 to DTC8 and evidences how these distributions are narrower with respect to AC/ACT carbons and ACX carbon series (see Figure 4.3 and 4.9). Such carbons appeared as the most promising for EDLC application for the high value of $S_{>1.5nm}$ (> 500 m^2 g^{-1}) and were further investigated by electrochemical test.

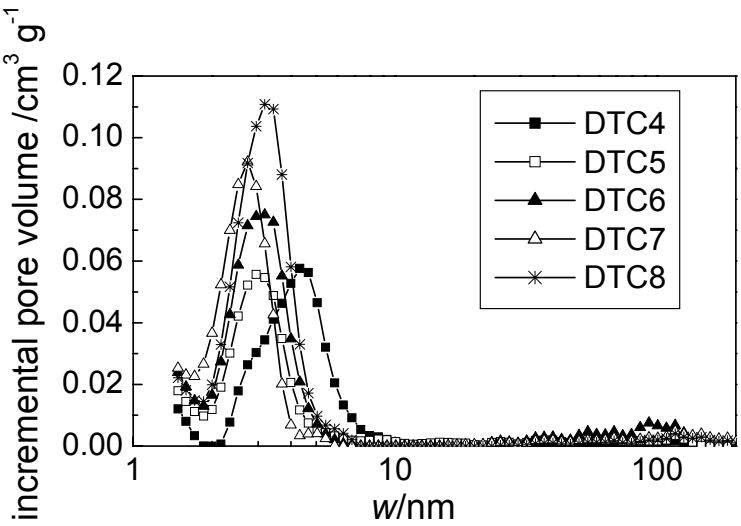

Figure 4.14. DFT incremental pore volume vs. pore size (*w*) of the DTCX carbons selected for electrochemical investigation.

4.2. Electrochemical characterization of carbon electrodes

The mesoporous carbons which exhibited porosity and surface chemistry of interest for EDLC applications were characterized by cyclic voltammetry (CV) at 20 mV s^{-1} and 60°C in two different ILs, EMITFSI and $PYR_{14}TFSI$, which have different ion conductivities, to evince the role played by the chemistry and structure of the IL ions in the electric double-layer [4.5]. Then, the effect of IL nature and carbon porosity on capacitive response and charge-discharge rate was investigated in $PYR_{14}TFSI$ by CV and impedence spectroscopy. Given that $PYR_{14}TFSI$ is a commercial product quite similar to $PYR_{1(2O1)}TFSI$, which is the one that much satisfies the requisite for HEV application, the former was used for a screening of the carbonaceous materials in order to identify the most promising carbon (Sections 4.2.1 and 4.2.2) and $PYR_{1(2O1)}TFSI$ was used only to test selected carbonaceous electrodes. In the Sections 4.2.3 and 4.2.4 the capacitance response in the selected ionic liquid $PYR_{1(2O1)}TFSI$, of the ACT carbon, chosen for its availability on the market and its good porosity and surface chemistry features after the heat treatment, and of DTC7 carbon is reported.

4.2.1. Comparison of capacitance response of mesoporous carbons in different ILs, EMITFSI and $PYR_{14}TFSI$

The mesoporous carbons featuring the highest $S_{>1.5\ nm}$ were characterized by CV at 20 mV s^{-1} and 60°C in EMITFSI and $PYR_{14}TFSI$ in the same negative potential domain -2.1 V/-0.2 V vs. Fc/Fc^+. Table 4.10 reports the porosity and double-layer capacitance responses of composite electrodes in the ILs as evaluated by the slope of the integral over time of the discharge voltammetric current vs. electrode potential plot. The main result in Table 4.10 is that at 60°C each carbon displays specific capacitance 20%-50% higher in EMITFSI than in $PYR_{14}TFSI$. This can not be explained by a different accessible surface area of the carbons for the double-layer formation in the two ILs. Indeed, the maximum size of the EMI^+ and PYR_{14}^+ counterions involved in the double-layer is not very different: they are less than 1 nm wide [4.22, 4.23] and all the examined carbons display pore-size distributions centered at values wider than 2 nm. The cause of the different capacitance in the two ILs is thus to be found in the different dielectric constant and thickness of the double-layer, which are related to the different properties of EMITFSI and $PYR_{14}TFSI$ at the interface [4.5].

Table 4.10. DFT specific pore volume ($V_{>1.5\ nm}$) and specific surface area ($S_{>1.5\ nm}$) from pores with size in the 1.5 nm – 200 nm range, main pore size (<*w*>) and specific capacitance in the same negative potential domain between -2.1/-0.2 vs. Fc/Fc^+ of the carbons investigated for IL based-supercapaciotors.

Carbon		**Porosity**			**C_{dl} in ILs of negatively charged carbons**	
		$V_{>1.5\ nm}$ cm^3g^{-1}	**$S_{>1.5\ nm}$ m^2g^{-1}**	**<*w*> nm**	**F g^{-1}**	
					EMITFSI	**$PYR_{14}TFSI$**
Aero/cryo/xerogel (ACX)	CA1	0.15	130	6	52	23
	CRFB4	0.23	134	9	52	23
	CRFB5	1.12	242	20	61	36
	CRFC5	0.66	216	15	56	33
	X1a	0.51	372	6	90	75
	X2a	0.99	412	14	106	82
	X3a	1.33	564	15	125	100
	C1625e	2.93	360	10-100	109	57
Activated carbons	AC	0.84	1020	2.7	85	50
	ACT	0.84	972	2.7	107	87
Disordered template (DTCX)	DTC8	0.91	1180	3.3	127	82

Given that the ILs feature the same anion and different cations, the different capacitance responses are arguably related to the different polarizability and structure of the EMI^+ and PYR_{14}^+ counterions, thus suggesting that in the double-layer of negatively charged carbons the IL cations occupy the IHP. While unambiguous values of dielectric constant at the interface of the two cations are not available [4.24-4.28], EMI^+ can be termed a *soft* cation with the positive electric charge delocalized in the imidazolium ring and a dipole moment presumably higher than that of the PYR_{14}^+, which features the electric charge in the sp^3 nitrogen atom and can thus be considered as a relatively *hard* cation. Consequently, the former should provide higher dielectric constant in the double-layer than the latter with a positive effect on the electrode capacitance. These considerations are well supported by the different bulk properties of EMITFSI and $PYR_{14}TFSI$ like viscosity, conductivity and normalized solvent polarity as well as by molecular dynamics studies [4.29, 4.30]. Indeed, the viscosity and ionic resistivity at 25°C of $PYR_{14}TFSI$, i.e. 85 mPa s and $5 \cdot 10^2$ Ω cm [4.29], are higher than EMITFSI's, i.e. 34 mPa s and $1 \cdot 10^2$ Ω cm [4.29], because of the higher cation–anion interactions in the former than in the latter, which in turn depend on

the different polarizability of the cations and affect the different polarizability of the bulk IL.

In effect, the normalized solvent polarity E^N_T (defined on the basis of the 2,6-diphenyl-4-(2,4,6-triphenylpyridinium-1-yl)phenolate betaine solvatochromism in different solvents, with E^N_T = 0 for TMS and 1 for water) of $PYR_{14}TFSI$ (0.544) is lower than EMITFSI's (0.676) [4.31]. According to the E^N_T data, $PYR_{14}TFSI$ displays a lower affinity than EMITFSI towards the betaine dye, which is a large polarizable aromatic π electron system with a weak electron pair acceptor (the positively charged nitrogen atom) and a strong electron pair donor (the negatively charged oxygen ion) and, hence, well mimics the negatively charged carbon. This means that IL polarizability may also affect the double-layer thickness at the carbonaceous electrode.

The orientation of the IL cation under the applied electric field and its stereochemistry are also important for double-layer thickness. Conformational studies by spectroscopy proved that in imidazolium-based ILs the plane of the imidazolium ring is normal to the surface [4.32, 4.33] and twists towards it when this latter becomes even more negatively polarized [4.34]. By contrast, it can be expected that the reorientation of the PYR_{14}^+ under the electric field is hindered both because of the strong interaction of the cation with the $TFSI^-$ anion and the steric hindrance of its alkyl groups [4.35]. Thus, the double-layer thickness δ_{dl} is wider in $PYR_{14}TFSI$ than in EMITFSI, and the electrode specific capacitance is lower in the former than in the latter.

The data in Table 4.10 show that the various $S_{>1.5\ nm}$ bring about different capacitive responses (C_{dl}) in both the ILs. The highest C_{dl} were achieved through different preparation methods with the xerogel X3a, the ACT and the DTC8 carbons which feature 125 F g^{-1}, 107 F g^{-1} and 127 F g^{-1} in EMITFSI, respectively, and 100 F g^{-1}, 87 F g^{-1}, 82 F g^{-1} in $PYR_{14}TFSI$, respectively. Figure 4.15 reports the CVs of such carbons (coulombic efficiency >99%) in terms of specific current and differential capacitance, the latter obtained by dividing the specific current by the scan rate.

Figure 4.16 reports the C_{dl} values at 60°C in EMITFSI and $PYR_{14}TFSI$ vs. $S_{>1.5\ nm}$ of all the mesoporous carbons investigated in the two ILs. The figure shows that the specific capacitance C_{dl} of the aero/cryo/xerogel carbons (ACX) increases with the $S_{>1.5\ nm}$, fairly linearly in both of the ILs giving a value of 20-30 μF cm^{-2}, thus, high capacitance values ≥100 F g^{-1} in ILs could be achieved by using carbon featuring at least 500 m^2 g^{-1} of surface

area $S_{>1.5\ nm}$ [4.1, 4.4]. The ACX carbon series were prepared by the same precursors with similar treatments (pyrolysis in inert atmosphere at high temperature) and therefore should exhibit the same surface chemistry.

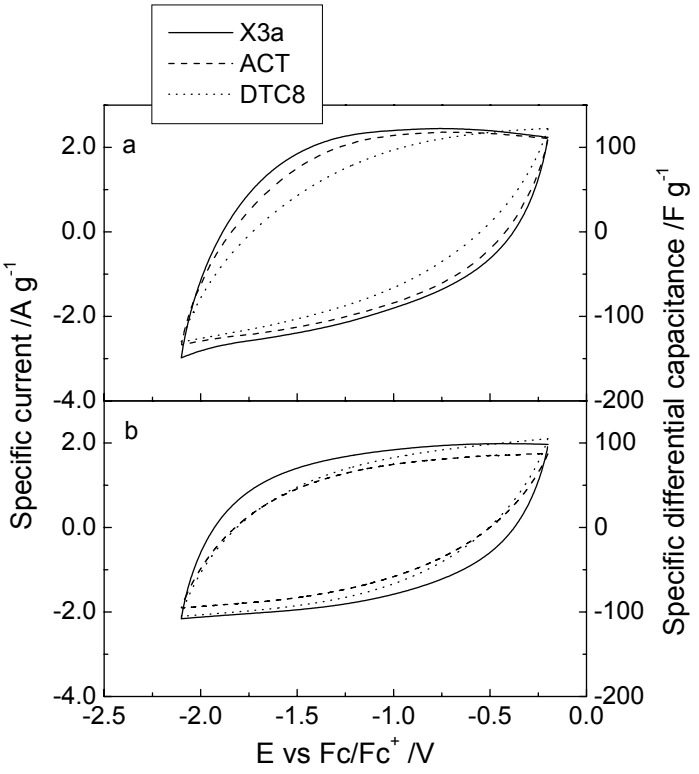

Figure 4.15. Cyclic voltammetries of the X3a, ACT, DTC8 carbon electrodes at 20 mV s^{-1} and 60°C in EMITFSI (a) and $PYR_{14}TFSI$ (b).

The capacitance values achieved with AC, ACT and DTC8 carbons are not so high when compared to their $S_{>1.5\ nm}$, which is 40-50% higher than X3a's. Given their high values of $S_{>1.5\ nm}$ and $V_{>1.5\ nm}$ this behaviour may be explained by C_{dl} capacitance limitation at the electrode/IL interface due to a low C_c space-charge capacitance in the carbon, because of the thin thickness of pore walls (see eq. 1.4) [4.3, 4.11, 4.36].

As it concerns AC and ACT, also the nature and surface chemistry of the carbon plays a crucial role in its capacitive response, as evinced by the fact that in both ILs the specific capacitance of the heat-treated ACT carbon is significantly higher than that of the pristine AC, which exhibits almost the same $S_{>1.5\ nm}$ as the former. This difference can be explained by the fact that the heat treatment partially removes hydrophilic moieties from

the AC carbon, thus providing a better carbon permeation with the hydrophobic IL and, consequently, a higher accessible surface area for the double-layer charging process.

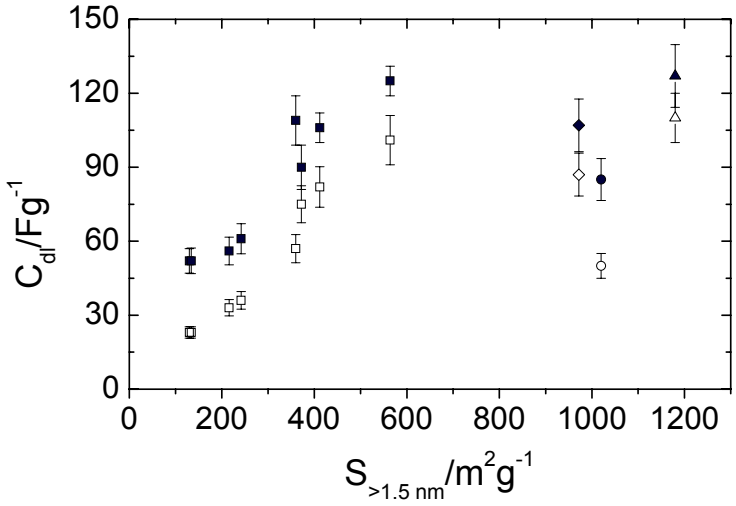

Figure 4.16. Specific capacitance (C_{dl}) from CVs at 20 mV s^{-1} and 60°C in EMITFSI (solid symbols) and $PYR_{14}TFSI$ (open symbols) in the potential range -2.1/-0.2 V vs. Fc/Fc^+ of ACX (square), AC (circle), ACT (diamond), DTC8 (triangle) carbons vs. $S_{>1.5\ nm}$.

4.2.2. Capacitance response of mesoporous carbons negatively and positively charged in $PYR_{14}TFSI$

Mesoporous carbons were investigated in $PYR_{14}TFSI$ by CV at 20 mV s^{-1} and 60°C in the negative and positive potential domains extending the potential excursion up to the potential limits which guarantee coulombic efficiency > 95%. Thus, in such conditions the negative potential limit is -2.6 V vs. Fc/Fc^+ (i.e. more negative than that of EMITFSI investigated in Section 4.2.1) and the positive potential limit is +1.6 V vs. Fc/Fc^+. Table 4.11 reports the porosity in terms $V_{>1.5nm}$, $S_{>1.5nm}$ and $<w>$ and the double-layer capacitance responses C_{dl} obtained by CV in the positive and negative potential domains, -2.6 V/-0.2 V and -0.2 V/+1.6 V vs. Fc/Fc^+, respectively.

The DTC7 specific capacitance of 140 F g^{-1} in the negative potential domain and 158 F g^{-1} in the positive potential domain is the highest value obtained up to now in $PYR_{14}TFSI$. Moreover this DTC7 carbon is obtained by a synthesis procedure which is cheaper and faster than the aero/xero/cryogel method and leads to moderate mesopore volume which should limit IL excess in the electrode.

Table 4.11. DFT specific pore volume ($V_{>1.5\ nm}$) and specific surface area ($S_{>1.5\ nm}$) from pores with size in the 1.5 nm – 200 nm range, main pore size (<*w*>) and specific capacitance in the negative potential domain between -2.6 V/-0.2 V vs. Fc/Fc^+ of the carbons investigated in $PYR_{14}TFSI$.

Carbon		**Porosity**			**C_{dl} in $PYR_{14}TFSI$**	
		$V_{>1.5nm}$ cm^3g^{-1}	**$S_{>1.5nm}$ m^2g^{-1}**	**<*w*> nm**	**F g^{-1}**	
					-2.6/-0.2 V vs. Fc/Fc^+	**-0.2/+1.6 V vs. Fc/Fc^+**
Aero/cryo/xerogel (ACX)	CRFB5	1.12	242	20	36[b]	60[a]
	X2a	0.99	412	14	87	112[a]
	X3a	1.33	564	15	108	120[c]
	C1625e	2.93	360	10-100	65	-
	CA1a	0.62	610	6	100	114
Activated carbons	ACT	0.84	972	2.7	95	97
Disordered template (DTCX)	DTC5	0.52	685	3.0	70	71
	DTC4	0.54	575	4.5	74	77
	DTC6	0.73	950	3.0	114	105
	DTC7	0.70	1018	2.7	140	158
	DTC8	0.91	1180	3.3	110	120

[a] -0.2/+1.3 V vs. Fc/Fc^+
[b] -2.1/-0.2 V vs. Fc/Fc^+
[c] -0.2/+1.4 V vs. Fc/Fc^+

However, all the DTCX carbons, as well as ACT, feature capacitance responses normalized to $S_{>1.5\ nm}$ lower than the values displayed by the ACX series (ca. 20 μF cm^{-2}) in the same $PYR_{14}TFSI$ IL. This could be explained by a non-optimized ionic connection between the disordered pores of the DTCX carbons and by not sufficient cleaning of the ACT carbon. Furthermore, given that both ACT and DTCX carbons feature high $V_{>1.5nm}$, their C_{dl} values may be limited by a low C_c (see eq. 1.4) [4.3, 4.36], as reported in the previous Section. Indeed, on the basis of geometric considerations, the DTC carbon pore walls have an average thickness in the order of few graphene layers that is close to the screening length of the electric field in the carbon. Thinner walls can be estimated for the ACT carbon, which exhibit significantly lower C_{dl} than DTC's at the same <*w*> value but higher pore volume and larger PSD as shown in Figure 4.17.

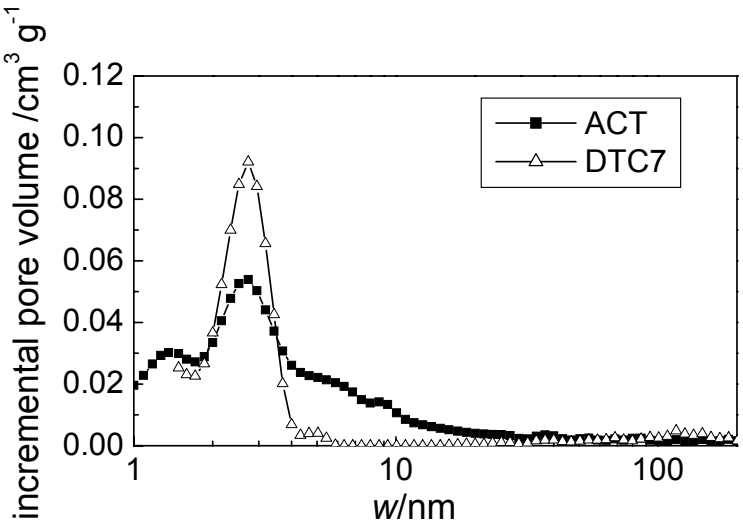

Figure 4.17. DFT incremental pore volume vs. pore size (*w*) of ACT and DTC7.

4.2.3. Capacitance response of modified activated carbon (ACT) in $PYR_{1(2O1)}TFSI$

The heat treated PICA carbon, ACT, given the commercial availability of the pristine carbon (AC) and the high values of specific capacitance already demonstrated in $PYR_{14}TFSI$, was characterized both in the negative and positive potential domains by CV at 20 mV s^{-1} and 60°C in $PYR_{1(2O1)}TFSI$ which is the most promising IL for supercapacitor application in HEV. Table 4.12 reports the specific capacitances of ACT-based electrodes and the coulombic efficiency (η%) evaluated in the positive and negative potential domains reported in the Table by the CVs that are shown in Figure 4.18 [4.12]. In Table 4.12 the electrochemical performance of thick (15.3 mg cm^{-2}) and thin electrodes (8.5 mg cm^{-2}) are reported to underline how the thickness of the electrode can affect its capacitive response.

Table 4.12. Carbon loading (w_c), specific capacitance of ACT carbon based composite electrodes (95% carbon, 5% pTFE) with the corresponding coulombic efficiency (η%) of the charge/discharge processes, as evaluated by CV at 20 mV s^{-1} and 60°C in $PYR_{1(2O1)}TFSI$ in the positive and negative potential domains (ΔV).

w_c mg cm^{-2}	Negative domain			Positive domain		
	ΔV V vs. Fc/Fc^+	F g^{-1}	η%	ΔV V vs. Fc/Fc^+	F g^{-1}	η%
15.3	-2.4/-0.2	86	98.9	-0.2/1.6	89	96.6
8.5	-2.4/-0.2	100	97.0	-0.2/1.6	111	96.3

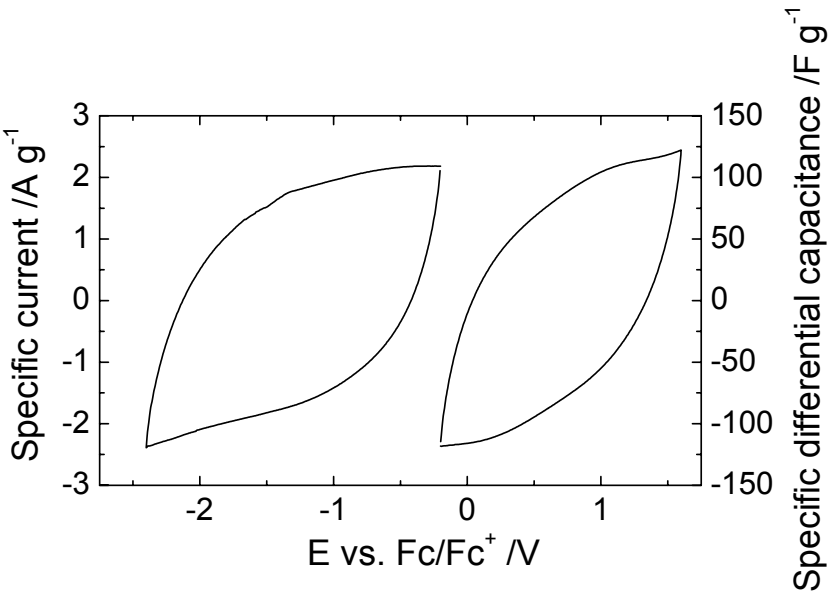

Figure 4.18. CVs at 20 mV s^{-1} and 60°C in $PYR_{1(2O1)}TFSI$ in the positive and negative potential domains of the ACT carbon based electrode (w_c= 8.5 mg cm^{-2}).

At 60°C the ACT carbon can be cycled at high coulombic efficiency (≥ 96%) in $PYR_{1(2O1)}TFSI$ in the range -2.4/1.6 V vs. Fc/Fc^+ and such potential limits were taken as electrode cut-off voltages upon $PYR_{1(2O1)}TFSI$ based- supercapacitors galvanostatic cycling (see Chapter 6).

4.2.4. Investigation of double-layer charge/discharge rate of mesoporous carbon electrodes in ILs

The DTC7 template carbon, given its high capacitive performances, is of interest for developing high energy supercapacitor and, hence, it was further investigated in order to evaluate its charge-discharge rate capability in different ILs. This study was performed by voltammetric and impedence studies at various temperatures.

The voltammetric study of the DTC7 carbon electrodes was performed at 30°C and 60°C in $PYR_{14}TFSI$ and $PYR_{1(2O1)}TFSI$ in the negative potential domain at different scan rates. Table 4.13 reports the results and shows the normalized capacitance ($\%C_{dl}/C_{dl,max}$), i.e. the electrode double-layer capacitance (C_{dl}) divided by the maximum value exhibited at the lowest scan rate ($C_{dl,max}$), at different voltammetric scan rates and the data for electrodes featuring 5% of carbon conducting additive (SuperP).

Table 4.13. Normalized capacitance at different voltammetric scan rates and temperatures of the DTC7 electrodes (with and without SuperP conducting additive) in $PYR_{14}TFSI$ and $PYR_{1(2O1)}TFSI$ in the electrode potential ranges -2.2/-0.2 V and -2.1/-0.2 V vs. Fc/Fc^+, respectively.

T/°C	scan rate / mV s^{-1}	$\%C_{dl}/C_{dl,max}$		
		$PYR_{14}TFSI$		$PYR_{1(2O1)}TFSI$
		0% Super P	5% SuperP	0% Super P
60	5	100	100	100
	10	90	90	90
	20	75	85	75
	30	65	75	70
	40	55	70	65
	50	50	60	50
30	5	100	100	100
	10	90	95	90
	20	80	80	75
	30	60	70	70
	40	50	60	65
	50	45	55	50

The $\%C_{dl}/C_{dl,max}$ vs. scan rate trend is representative of the rate capability of the electrode, i.e. of the time constant of the charge-discharge process, and it should be affected by electrolyte and electrode resistances. In both the ILs and at each temperature, the $\%C_{dl}/C_{dl,max}$ values reported in Table 4.13 decrease as the scan rate increases, i.e. with the voltammetric charge-discharge current increase. This is a typical response of porous carbon electrodes that has already been observed with conventional organic electrolytes and explained by ionic diffusion limitation upon the double-layer charge-discharge of the electrodes' smallest pores [4.37]. However, what we can see in Table 4.13 is that the $\%C_{dl}/C_{dl,max}$ vs. scan rate trend is not much different in the case of the test carried out in $PYR_{14}TFSI$ and $PYR_{1(2O1)}TFSI$, at the different temperatures and with or without electronically conducting additive in the carbon electrode. This suggests that the time constant for the double-layer charging process (τ) is not much affected by the bulk ionic conductivity of the electrolytes, of 6.0 and 8.4 mS cm^{-1} at 60°C and 2.6 and 3.8 mS cm^{-1} at 30°C for $PYR_{14}TFSI$ and $PYR_{1(2O1)}TFSI$, respectively, and by the electronic conductivity of the electrodes. Indeed, τ is proportional to electrode charging resistance (R) and to C_{dl} and while the R decreases with the increasing temperature, i.e. with the IL conductivity, the C_{dl} increases, thus, the variation of τ is not significant. The capacitive response, as underlined previously, is affected by IL ion association and polarizability [4.36, 4.38, 4.39] and, as an example, the specific capacitance of DTC7 in $PYR_{14}TFSI$ at 20 mV s^{-1} and 60°C is 10% higher than at 30°C.

To investigate the rate capability of the DTC7 carbon, the impedence spectra of this carbon were carried out and compared with those of ACT and C1625e carbons. The Nyquist plots of negatively charged carbon electrodes in various ILs at different temperatures are reported in Figures 4.19, 4.20 and 4.22 and exhibit common features. The uncompensed resistance (R_u, impedance at 100 kHz), which is directly related to IL ionic conductivity, is less than 30% of total electrode impedance at 10 mHz. The high frequency semicircle is due to contact resistances and is affected by the quality of cell assembly. The mid-frequency electrode impedance is described by a 45° transmission line ($Z_{45°}$) that reflects the porous nature of the electrode. This $Z_{45°}$ term is related to pore capacitance and charging resistance, the latter depending on carbon electronic resistance and IL ionic conductivity in the pores. At the lowest frequencies the Nyquist plots deviate from the straight line expected for ideal capacitors both because of the porous nature of the electrode and the slow adsorption or rearrangement of IL ions at the electrode surface [4.38].

Figure 4.19 shows the impedance plots of DTC7 electrodes with and without conducting additive in the same $PYR_{14}TFSI$ IL at 60°C and without additive in $PYR_{1(2O1)}TFSI$ at 60°C and 30°C and confirm the findings obtained by the voltammetric study. Indeed, the τ values, which can be roughly estimated by the frequency at which the fitting lines of $Z_{45°}$ and of the limit capacitance (line almost parallel to $-Z_i$ axis) cross, are very similar in all the plots.

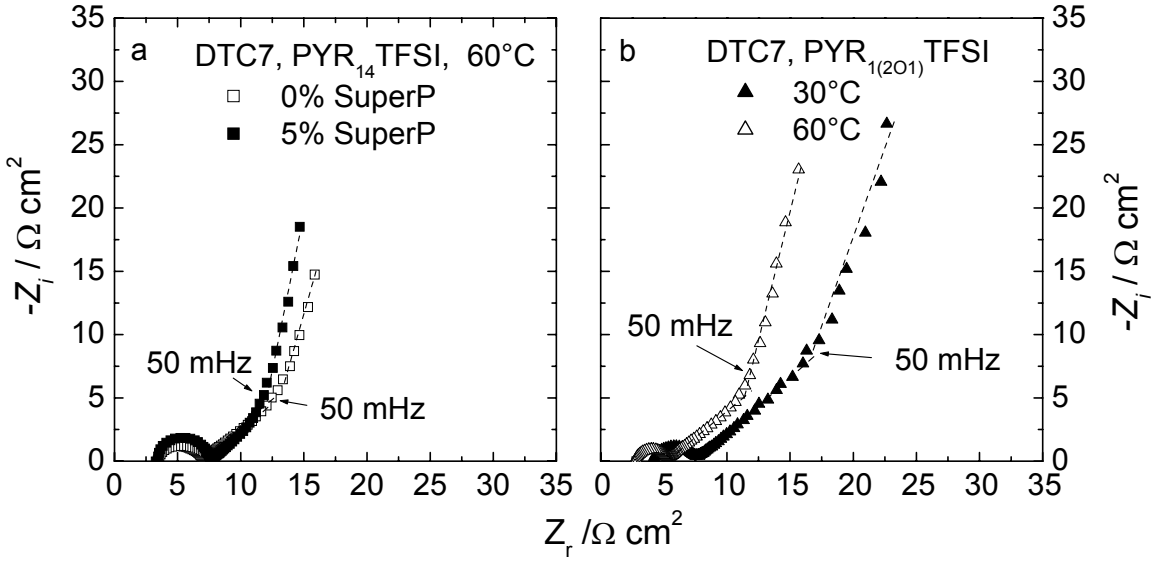

Figure 4.19. Nyquist plots of DTC7 electrodes with almost the same carbon content with and without carbon conducting additive at 60°C (a); without carbon conducting additive in $PYR_{1(2O1)}TFSI$ at 30°C and 60°C (b).

Figure 4.19a indicates that the presence of conducting additive in the electrode does not modify the real part of $Z_{45°}$, thus suggesting that the transmission line impedance is mainly affected by the ionic conductivity of the IL in the pores. Indeed, as evinced by the plots in Figure 4.19b, the real part of $Z_{45°}$ decreases when the temperature rises, i.e. when ionic conductivity increases. However, if only $PYR_{1(2O1)}TFSI$ conductivity is taken into account, τ should follow the response of the real part of $Z_{45°}$, and differently, the plots in Figure 4.19b show that τ is almost the same because, as noted above, the increase of temperature in the case of ILs also raises the capacitance response so that the C_{dl} increase almost offsets the resistance drop.

The interplay of IL conductivity and carbon capacitance and their effect on τ is further highlighted by Figure 4.20, which shows the Nyquist plots of ACT carbon electrodes at 60°C in EMITFSI and $PYR_{14}TFSI$. The former IL exhibits 4-fold higher conductivity then the latter's (25 mS cm^{-1} at 60°C) and features imidazolium aromatic cations, which are much more polarizzable than the pyrrolidinium ones. Hence, while the real part of $Z_{45°}$ is significantly lower in EMITFSI (of 4 Ω cm^2) than in $PYR_{14}TFSI$ (of 7 Ω cm^2), τ is almost the same because of the concomitant gain in the capacitive response.

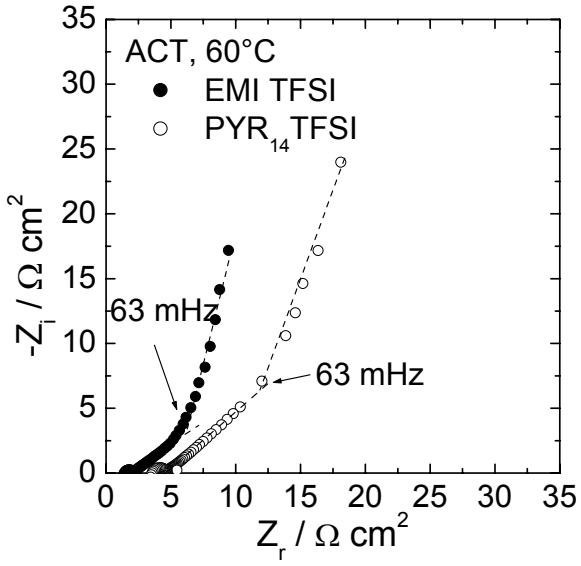

Figure 4.20. Nyquist plots of ACT carbon electrodes at 60°C in EMITFSI and $PYR_{14}TFSI$.

Figures 4.20 and 4.22 show that the electrode resistances of the DTC7 and ACT carbons are mainly determined by the real part of $Z_{45°}$, which is thus the main contributor to the

ESR for the double-layer charging process of carbonaceous electrodes in IL. The real $Z_{45°}$ impedance increases with carbon pore depth, so that it is modulated by the porous nature of the electrodes [4.40]. Hence, the electrodes based on carbons DTC7, ACT and C1625e, whose PSDs are displayed in Figure 4.21, were selected for a comparison of their impedence responses because, while DTC7 and ACT carbons displays similar porosity features with PSDs centered at 2.7 nm, the C1625e is basically a meso-macroporous carbon with pores of 10-100 nm and, on the basis of geometric considerations and of the pore volume in Table 4.11, the latter is presumably made of pores much shallower than the former. Figure 4.22 shows the Nyquist plots in $PYR_{14}TFSI$ ionic liquid at 60°C of the DTC7, ACT and C1625e carbon electrodes. The DTC7 and ACT electrodes display comparable impedance responses while the C1625e electrode exhibits the real part of $Z_{45°}$ that is half that of the DTC7 and ACT carbons. Given that the real part of $Z_{45°}$ gives the main contribution to the electrode charging resistance these measurements highlight that the carbon pore lengths are a fundamental parameter to take into account for the optimization of carbonaceous materials for high power supercapacitor.

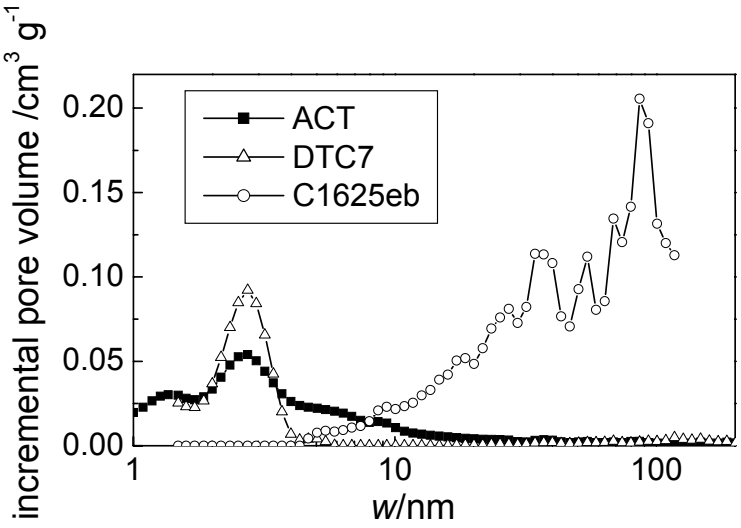

Figure 4.21. DFT incremental pore volume vs. pore size (*w*) of ACT, DTC7 and C1625e.

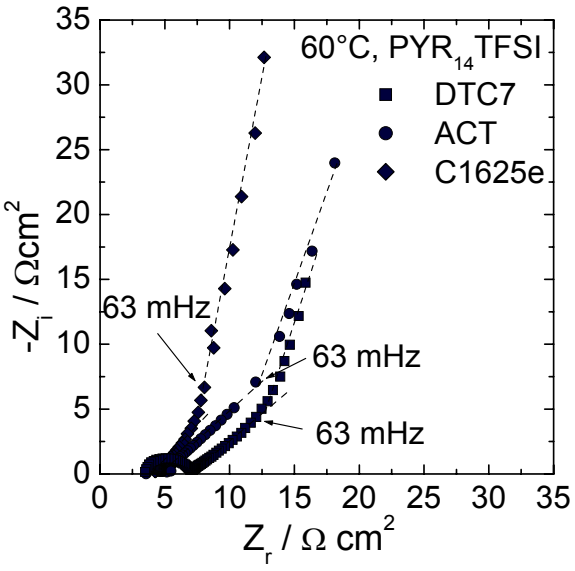

Figure 4.22. Nyquist plots of DTC7, ACT and C1625e electrodes in $PYR_{14}TFSI$ at 60°C.

4.3. Conclusions

Different synthetic routes were followed to achieve high performing carbon electrodes operating in ILs. The faster and cheaper route was the disordered template method that gave the DTC7 carbon featuring 140 F g^{-1} in $PYR_{14}TFSI$ at 60°C. From a commercially point of view the most interesting carbon developed was ACT, given that the pristine carbon AC is commercial and can be available in large quantity and upon high temperature treatment in inert atmosphere ACT features 100 F g^{-1} which is of interest for IL-based supercapacitor in HEV applications.

The comparison of capacitive responses of carbon electrodes in different ILs demonstrated the importance of ion chemistry and structure of the IL in the interface properties because of the intimate contact of the carbon surface with the electrolyte which is not mediated by the solvent. Indeed the double-layer capacitance of negatively charged carbon electrodes is strongly determined by the cation polarizability, which affects the dielectric constant in the double-layer as well as double-layer thickness, which in turn also depends on the preferred orientation of the cation under the applied electric field.

The design of mesoporous carbon electrodes for the development of IL-based EDLCs of high performance has to take into account the carbon porosity and surface chemistry.

Carbon should feature high accessible surface area to guarantee high capacitive response together with a low pore volume to limit the IL content in the final device. Moreover, the disadvantage of high pore volume matched to high surface area can give carbons with too thin pore wall thicknesses with the consequence of charge limitation from the carbon side.

An optimized carbon electrode should display short time constant for the double-layer charging-discharging process, thus, the charging resistance should keep low. Such resistance is affected by the ionic resistance in the pores and depends on IL ionic conductivity and it is also modulated by pore length. Hence, pore geometry is a key parameter in carbon design not only because it defines the carbon surface but also because it can differentially "amplify" the effect of IL conductivity on the electrode charging-discharging process.

The surface chemistry should be tailored to improve carbon wettability by ILs. Indeed, the characterization of AC and ACT carbons and the FTIR-ATR measurements of carbons demonstrated that surface moieties affect the carbon's electrochemically accessible surface area and, thus, modify the capacitive response of the carbons.

4.4. References

4.1) M. Mastragostino, F. Soavi, *Electrochemical Capacitors: Ionic Liquid Electrolytes*. In: J. Garche, C. Dyer, P. Moseley, Z. Ogumi, D. Rand, B. Scrosati, editors. *Encyclopedia of Electrochemical Power Sources*, Vol 1. Amsterdam: Elsevier (2009) *649*.

4.2) M. Hahn, M. Baertschi, O. Barbieri, J.-C. Sauter, R. Kötz, R. Gallay, *Electrochem. Solid-State Lett.* 7 (2004) *A33*.

4.3) O. Barbieri, M. Hahn, A. Herzog, R. Kötz, *Carbon* 43 (2005) *1303*.

4.4) C. Arbizzani, S. Beninati, M. Lazzari, F. Soavi, M. Mastragostino, *J. Power Sources* 174 (2007), *648*.

4.5) M. Lazzari, M. Mastragostino, F. Soavi, *Electrochem. Commun.* 9 (2007) *1567*.

4.6) S.A. Al-Muhtaseb, J.A. Ritter, *Adv. Mater.* 15 (2003) *101*.

4.7) M. Mastragostino, F. Soavi, *J. Power Sources* 174 (2007), *89*.

4.8) T. Morishita, Y. Soneda, T. Tsumura, M. Inagaki, *Carbon* 44 (2006) *2360*.

4.9) M. Inagaki, M. Kato, T. Morishita, Kazuhiro Morita, K. Mizuuchi, *Carbon* 45 (2007) *1121*.

4.10) T. Morishita, K. Ishihara, M. Kato, M. Inagaki, *Carbon* 45 (2007) *209*.

4.11) M. Lazzari, F. Soavi, M. Mastragostino, *Fuel Cells* submitted.

4.12) C. Arbizzani, M. Biso, D. Cericola, M. Lazzari, F. Soavi, M. Mastragostino, *J. Power Sources* 185 (2008) *1575*.

4.13) D. Cericola, *Materiali carboniosi e liquidi ionici per supercapacitori a doppio strato.* Graduate Thesis, SMETEC Department, University of Bologna, Italy, October 2007.

4.14) P. A. Webb, C. Orr, *Analytical Methods in Fine Particle Technology*, Micromeritics Instrument Corp., Norcross (1997).

4.15*)* T. Gruber, T. W. Zerda, M. Gerspacher*, Carbon* 32 (1994) *1377*.

4.16) A. Sadezky, H. Muckenhuber, H. Grothe, R. Niessner, U. Pöschl, *Carbon* 43 (2005) *1731*.

4.17) R.W. Pekala, *Low Density, Resorcinol-Formaldehyde Aerogels*, United States Patent N° 4,873,218, (1989).

4.18) C: Liang, G. Sha, S. Guo, *J. Non-Cryst. Solids* 271 (2000) *167*.

4.19) A. Dandekar, R. T. K. Baker, M. A. Vannice, *Carbon* 36 (1998) *1821*.

4.20) J.L. Figueiredo, M.F.R. Pereira, M.M.A. Freitas, J.J.M. Órfão, *Carbon* 37 (1999) *1379*.

4.21) Z. Ahmad, N.A. Al-Awadi, F. Al-Sagheer, *Polymer Degradation and Stability* 92 (2007) *1025*.

4.22) A.B. McEwen, H.L. Ngo, K. LeCompte, J.L. Goldman, *J. Electrochem. Soc.* 146 (1999) *1687*.

4.23) H. Shirota, A. M. Funston, J. F. Wishart, E.W. Castner Jr., *J. Chem. Phys.* 122 (2005) *184512*.

4.24) S. Baldelli, *J. Phys. Chem. B* 109 (2005) *13049*.

4.25) C. Wakai, A. Oleinikova, M. Ott, H. Weingärtner, *J. Phys. Chem. B* 109 (2005) *17028*.

4.26) F.V. Bright, G.A. Baker, *J. Phys. Chem. B* 110 (2006) *5822*.

4.27) C. Wakai, A. Oleinikova, H. Weingärtner, *J. Phys. Chem. B* 110 (2006) *5824*.

4.28) J. Wu, J.P. W. Stark, *Meas. Sci. Technol.* 17 (2006) *781*.

4.29) M. Galiński, A. Lewandowski, I. Stępniak, *Electrochim. Acta* 51 (2006) *5567*.

4.30) C. Schröder, T. Rudas, O. Steinhauser, *J. Chem. Phys.* 125 (2006) *244506*.

4.31) C. Reichardt, *Green Chem.* 7 (2005) *339*.

4.32) T. J. Gannon, G. Law, P. R. Watson, *Langmuir* 15 (1999) *8429*.

4.33) G. Law, P. R. Watson, A. J. Carmichael, K. R .Seddon, *Phys. Chem. Chem. Phys.* 3 (2001) *2879*.

4.34) N. Nanbu, Y. Sasaki, F. Kitamura, *Electrochem. Commun.* 5 (2003) *383*.

4.35) T. Fujimori, K. Fuji, R. Kanzaki, K. Chiba, H. Yamamoto, Y. Umebayashi, S. Ishiguro, *J. Mol. Liq.* 131-132 (2007) *216*.

4.36) Md. M. Islam, M. T. Alam, T. Okajima, T. Ohsaka, *J. Phys. Chem. C* 113 (2009) *3386.*

4.37) R. Kötz, M. Carlen, *Electrochim. Acta* 45 (2000) *2483*.

4.38) M. V. Fedorov, A. A. Kornyshev, *Electrochim. Acta* 53 (2008) *6835.*

4.39) V. Lockett, R. Sedev, J. Ralston, M. Horne, T. Rodopoulos, *J. Phys. Chem. C* 112 (2008) *7486*.

4.40) B.E. Conway, *Electrochemical Supercapacitors*, Kluwer Academic/Plenum, New York (1999).

Chapter 5
EDLCs with asymmetric configuration

5.1. Asymmetric configuration for IL-based EDLCs

The electrochemical stability windows (ESWs) of ILs, as well as of conventional electrolytes, evaluated by the high surface area porous carbon electrodes are narrower than those measured by flat carbon electrodes. Indeed, the high surface area of porous carbons amplifies the faradic contribution to the voltammetric currents related to IL oxidation and reduction when the potentials that mark the ESW limits are approached. Thus, the potential excursions of EMITFSI, $PYR_{14}TFSI$ and $PYR_{1(2O1)}TFSI$ exploitable for IL-based carbon supercapacitors evaluated by CV at 60°C and 20 mV s^{-1}, reported in Figure 5.1, are narrower than the ESWs collected with glassy carbon or Pt smooth electrodes reported in Table 1.3. Note that the electrochemical stability reported in Figure 5.1 is mainly a kinetic stability, not thermodynamic, thus, it is influenced by the current density involved in the voltammetry test. The anodic stability limit of all the TFSI-based ILs investigated is 1.6 V vs. Fc/Fc^+ and is mainly affected by the chemistry of the $TFSI^-$ anion.

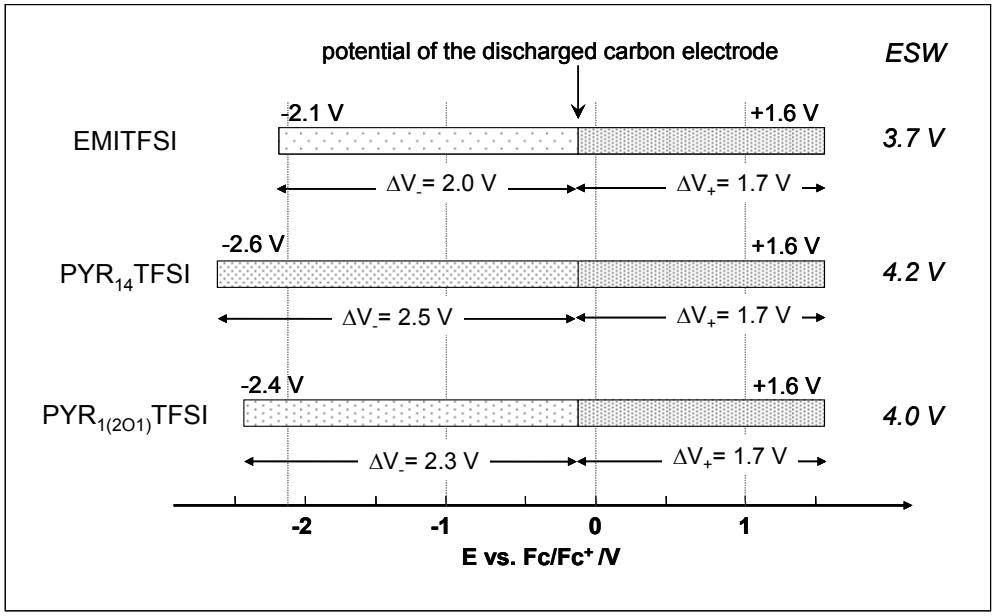

Figure 5.1. ESWs of EMITFSI, $PYR_{14}TFSI$ and $PYR_{1(2O1)}TFSI$ evaluated with high surface area mesoporous carbons at 60°C by CV at 20 mV s^{-1} with coulombic efficiency >95%.

The cathodic stability limit is affected by the nature of the IL cation and is -2.1 V vs. Fc/Fc^+ for EMITFSI, -2.6 V and -2.4 V vs. Fc/Fc^+ for $PYR_{14}TFSI$ and $PYR_{1(2O1)}TFSI$, respectively. Thus the ESWs feasible for EDLC applications are of 3.7 V, 4.2 V and 4.0 V for EMITFSI, $PYR_{14}TFSI$ and $PYR_{1(2O1)}TFSI$, respectively, as reported in Figure 5.1.
Given that the typical potential of the discharged electrodes is ca. -0.1 V vs. Fc/Fc^+, the maximum potential excursion for the positive electrode (ΔV_+) upon an EDLC charge is 1.7 V, and narrower than that feasible with the negative electrode (ΔV_-), which can be of 2.0 V in EMITFSI, 2.5 V in $PYR_{14}TFSI$ and 2.3 V in $PYR_{1(2O1)}TFSI$ [5.1, 5.2]. Thus, in a conventional symmetric configuration of EDLC, where the two electrodes have the same carbon loading and almost the same specific capacitance, the maximum potential excursion for the negative electrode would be limited by that of the positive, as shown in Figure 5.2a and evidenced by eq. 5.1

$$\Delta V_- = C_+ w_+ \Delta V_+ / (C_- w_+) \qquad \text{(eq. 5.1)}$$

where C_+, w_+ and C_-, w_- are the specific capacitance and carbon loading of the positive and negative electrode, respectively. In other words, symmetric EDLCs can safely operate below 3.4 V with all the ILs investigated and, particularly in the case of $PYR_{14}TFSI$, do not take full advantage of the electrolyte's wide ESW (which is always higher than 3.5 V, see Figure 5.1). Indeed, as reported in Figure 5.2b, since the mid-point of the ESW of the ILs is not usually found at the potentials of the discharged carbon electrodes, only by assembling asymmetric EDLC configurations (AEDLC) featuring different loadings of the same carbon at the two electrodes is it possible to charge each electrode up to the limit potential defined by IL stability and, hence, to reach maximum cell voltages significantly higher than those achievable with symmetric EDLC configurations [5.3]. Thus, by an asymmetric configuration and with $PYR_{14}TFSI$, $PYR_{1(2O1)}TFSI$ and EMITFSI V_{max} up to 4.2 V, 4.0 V and 3.7 V, could be achieved, respectively.

The following Sections report the studies performed to demonstrate the viability of the use of IL, particularly, Section 5.2 shows the performance of AEDLCs based on X3a xerogel carbon with EMITFSI and $PYR_{14}TFSI$ ILs [5.1], and Section 5.3 that of AEDLC based on DTC7 template carbon with $PYR_{14}TFSI$ [5.4].

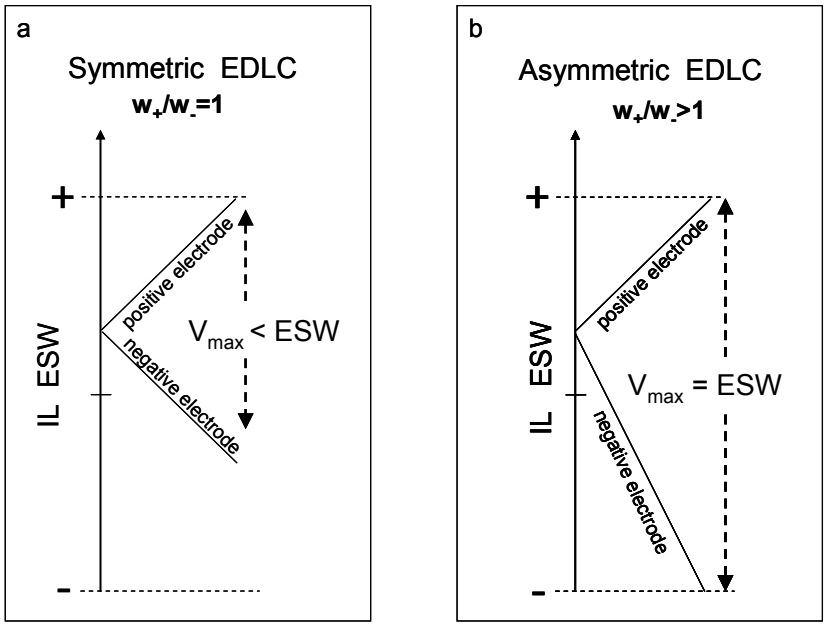

Figure 5.2. Scheme of potential excursion of symmetric configuration (a) and asymmetric configuration (b) of IL-based EDLCs with indication of ESW of the IL.

5.2. AEDLCs with mesoporous xerogel carbon in EMITFSI and $PYR_{14}TFSI$

The best performing xerogel carbon, X3a, featuring high $S_{>1.5\ nm}$ and $V_{>1.5\ nm}$ which guarantee high IL uptake, gave high electrode capacitive responses in EMITFSI and $PYR_{14}TFSI$ as shown in Table 5.1 where the C_{dl} values evaluated by CV at 20 mV s^{-1} and 60°C in the widest negative and positive potential domains allowed by the IL used are reported.

Asymmetric EDLCs (AEDLCs) with X3a xerogel carbon and both ILs, EMITFSI and $PYR_{14}TFSI$, were assembled using positive to negative mass loading ratio $R_{+/-}$ >1 as reported in Table 5.2, which also shows the total composite electrode mass loadings of the supercapacitors (w_{SC}, positive and negative electrodes together). The EMITFSI and $PYR_{14}TFSI$-based AEDLCs were tested at 60°C with $V_{max} \leq$ 3.4 V and $\leq$ 3.7 V, respectively, in order to keep the cells sufficiently far from the envisioned potential limits in view of long-term cycling tests and with operating potentials still significantly higher than those feasible with commercial supercapacitors [5.1, 5.5]. Figure 5.3 shows the galvanostatic profiles of the charge/discharge cycles at 10 mA cm^{-2} with V_{max} = 3.3 V and 3.7 V of the X3a/EMITFSI/X3a and X3a/$PYR_{14}TFSI$/X3a AEDLCs and of the corresponding electrodes collected after 5,600 and 15,300 cycles, respectively, at 20 mA cm^{-2}; the dashed lines indicate the electrode potential limits defined by the ILs.

Table 5.1. DFT specific pore volume ($V_{>1.5\ nm}$) and specific surface area ($S_{>1.5\ nm}$) from pores with size in the 1.5 nm – 200 nm range, main pore size (<*w*>), potential domain (ΔV) and double-layer capacitance (C_{dl}) of the treated xerogel carbon X3a in EMITFSI and $PYR_{14}TFSI$ at 60°C as evaluated from the voltammetric discharges at 20 mV s^{-1} by the slope of the electrode potential vs. integral over time of the current.

Carbon	porosity			EMITFSI		$PYR_{14}TFSI$	
	$V_{>1.5\ nm}$ $cm^3\ g^{-1}$	$S_{>1.5\ nm}$ $m^2\ g^{-1}$	<*w*> nm	ΔV V vs. Fc/Fc^+	C_{dl} $F\ g^{-1}$	ΔV V vs. Fc/Fc^+	C_{dl} $F\ g^{-1}$
X3a	1.33	564	15	-2.1/-0.2	125±6	-2.6/-0.2	108±15
				-0.2/1.3	128±12	-0.2/1.4	120±20

Table 5.2. $R_{+/-}$, w_{SC}, V_{max}, C_{SC} (on the basis of w_{SC}), maximum specific energy (E_{max}), ESR (by the ohmic drop after 0.1 s from the beginning of discharge) and maximum specific power (P_{max}) of the AEDLCs with EMITFSI and $PYR_{14}TFSI$ electrolytes at the 12,000th and 11,000th galvanostatic cycle, respectively, at 20 mA cm^{-2} and 60°C.

IL	$R_{+/-}$	w_{SC} $mg\ cm^{-2}$	V_{max} V	C_{SC} $F\ g^{-1}$	E_{max} $Wh\ kg^{-1}$	ESR $\Omega\ cm^2$	P_{max} $kW\ kg^{-1}$
EMITFSI	1.4	20.4	3.4	26	31	15	9.5
$PYR_{14}TFSI$	1.6	15.0	3.7	21	30	20	11.4

While in Figure 5.3a the electrode potential profiles indicate that in the X3a/EMITFSI/X3a electrode mass balance is almost optimized, the profiles in Figure 5.3b indicate that in the X3a/$PYR_{14}TFSI$/X3a the $R_{+/-}$ parameter could be increased slightly in order to attain higher V_{max} by a wider sweep of the negative electrode potential ΔV_- while keeping the same ΔV_+.

Both supercapacitors were tested over several thousand cycles at 20 mA cm^{-2} and 60°C; Table 5.2 reports V_{max}, C_{SC} and the maximum specific energy E_{max} of the supercapacitors after more than 10,000 galvanostatic cycles. At the 12,000th cycle, the X3a/EMITFSI/X3a delivers 26 F per gram of total composite electrode materials and a maximum specific energy between 3.4 V and 1.7 V of 31 Wh/kg. At the 11,000th cycle, the supercapacitor with $PYR_{14}TFSI$ delivers a slightly lower capacitance of 21 F/g (as expected on the basis of single electrode tests) and the corresponding energy delivered between 3.7 V and 1.85 V is of 30 Wh/kg, a value which can be increased if a better electrode balancing that enables to reach at least 4.0 V is used.

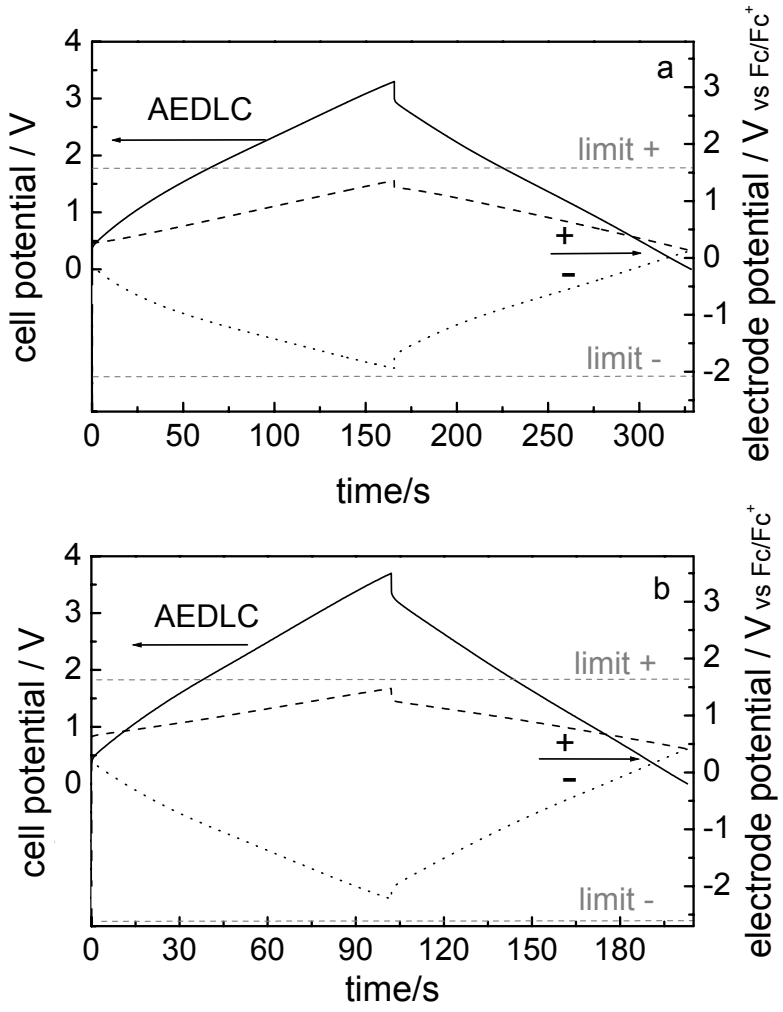

Figure 5.3. Voltage profiles at 10 mA cm^{-2} and 60°C of the (a) X3a/EMITFSI/X3a (5,600th cycle, V_{max} = 3.3 V) and (b) X3a/PYR_{14}TFSI/X3a (15,300th cycle, V_{max} = 3.7 V) AEDLCs and of their positive and negative electrodes; dashed lines indicate electrode potential limit defined by the two ILs.

These results are very interesting not only because the E_{max} exceeds by 30% that delivered by symmetric EDLC with PYR_{14}TFSI and commercial activated carbons [5.6], thus demonstrating the efficacy of the asymmetric configuration and of xerogel carbons, but mainly because they were quite stable over several thousand cycles as shown in Figure 5.4. This figure reports the trend of C_{SC} over cycling at 60 °C and 20 mA cm^{-2} for the two AEDLCs carried out with V_{max} up to 3.4 V in the case of X3a/EMITFSI/X3a and with V_{max} up to 3.7 V in the case of X3a/PYR_{14}TFSI/X3a (800 cycles were also performed with V_{max} = 3.9 V). Table 5.2 also shows the ESR by the ohmic drop after 0.1 s from the beginning of the discharge at 20 mA cm^{-2}, roughly corresponding to the value attainable at

10 Hz by impedance spectroscopy, and maximum specific power P_{max} of the two AEDLCs at 60°C.

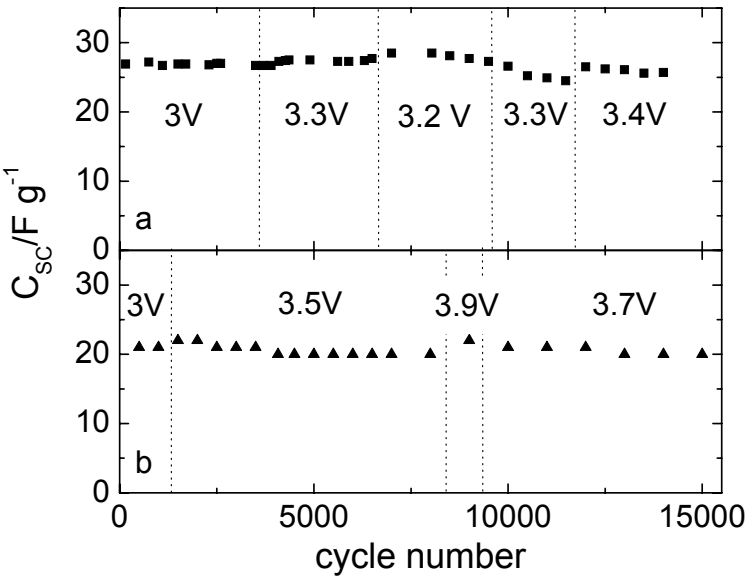

Figure 5.4. Trend of C_{SC} (based on total composite electrode materials) over cycling at 60 °C and 20 mA cm^{-2} of the X3a/EMITFSI/X3a (a) and X3a/PYR_{14}TFSI/X3a (b) AEDLCs with the indications of maximum cell voltages reached upon cycling.

The X3a/PYR_{14}TFSI/X3a AEDLC displays a higher ESR than X3a/EMITFSI/X3a, mainly because of the ion conductivity of PYR_{14}TFSI, which is 6 mS cm^{-1} at 60°C and lower than that of EMITFSI (25 mS cm^{-1} at the same temperature). However, the higher V_{max} of the former AEDLC also ensures a higher P_{max} of 11.4 kW kg^{-1}. Note that the ESR in Table 5.2 is markedly affected by cell assembly. Indeed, the AEDLCs featured a very thick, 200 μm separator, which significantly contributes to ESR. This can be seen in the Nyquist plot of the X3a/PYR_{14}TFSI/X3a AEDLC reported as an example in Figure 5.5, where the impedance value at the highest frequency arising from electronic and ionic resistances is 7 Ω cm^2. A reduction of the ionic resitsance is feasible by using a ten-fold thinner separator, which does not limit the capacitance of the carbon electrodes because the high porosity of the X3a carbon provides an IL-reservoir for double-layer formation. On the other hand, we used home-made electrodes and it is well known that automatic lamination procedures help to decrease electrode contact resistances, which contribute to the resistive component of the high-frequency semicircle in the impedance spectrum in Figure 5.5. Thus, the P_{max} values reported in Table 5.2 are to be taken as underestimated. The fast charge-discharge response of the X3a/PYR_{14}TFSI/X3a and X3a/EMITFSI/X3a AEDLCs at

60° C is clearly evinced by the trends of their capacitance vs. frequency reported in Figure 5.6; in these plots the capacitance was calculated from the imaginary component of the impedance at each frequency and normalized for the different AEDLCs to the corresponding limit capacitance at 10 mHz. Indeed, the double-layer charging process begins for both the AEDLCs at 10 Hz and the capacitance reaches the limit value at ca. 10^{-1} Hz, which means that the maximum storage/delivery capability can be reached in ca. 10 s [5.1].

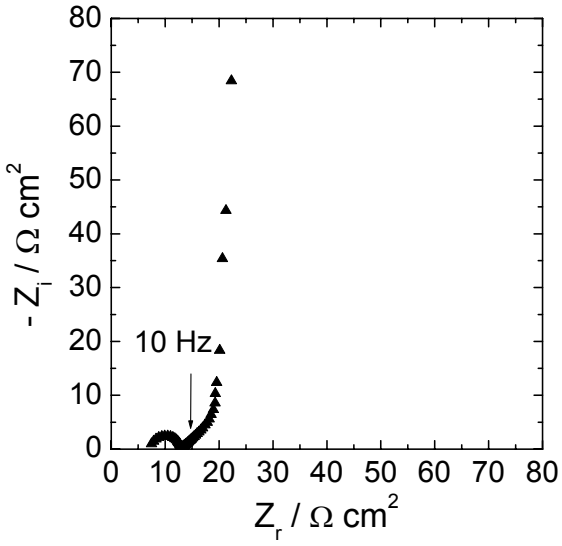

Figure 5.5. Nyquist plot of the discharged X3a/PYR_{14}TFSI/X3a AEDLC at 60°C (5 10^{4}-10^{-2} Hz frequency range).

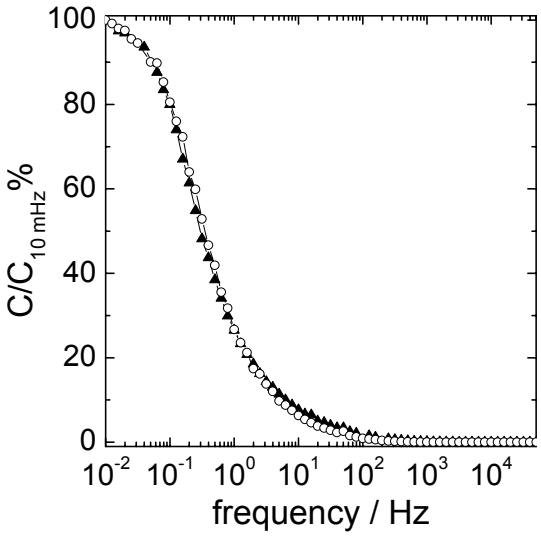

Figure 5.6. Trends of the capacitance normalized to the limit value at 10 mHz (C/C_{10mHz} %) vs. frequency of the X3a/EMITFSI/X3a and X3a/PYR_{14}TFSI/X3a AEDLCs from impedance measurements at 60°C.

5.3. AEDLC with DTC7 mesoporous template carbon and $PYR_{14}TFSI$

The disordered template carbon DTC7 displayed narrow pore size distribution (PSD) centered at 2.7 nm, value wide enough to provide IL ions with easy access to the carbon surface, moderate $V_{>1.5\ nm}$ which avoids excess of IL into the carbon pores of the electrode and high $S_{>1.5\ nm}$ value which brings about high capacitive responses (C_{dl}) in $PYR_{14}TFSI$, as reported in Table 5.3, of 140 F g^{-1} and 158 F g^{-1} in the negative and positive potential domains, respectively [5.4].

Table 5.3. DFT specific pore volume ($V_{>1.5\ nm}$) and specific surface area ($S_{>1.5\ nm}$) from pores with size in the 1.5 nm – 200 nm range, main pore size (<*w*>), potential domain (ΔV) and double-layer capacitance (C_{dl}) of the disordered template carbon DTC7 in $PYR_{14}TFSI$ at 60°C as evaluated from the voltammetric discharges at 20 mV s^{-1}.

Carbon	**porosity**			**$PYR_{14}TFSI$**	
	$V_{>1.5\ nm}$ $cm^3\ g^{-1}$	**$S_{>1.5\ nm}$ $m^2\ g^{-1}$**	**<*w*> nm**	**ΔV V vs. Fc/Fc^+**	**C_{dl} F g^{-1}**
DTC7	0.70	1018	2.7	-2.6/-0.2 -0.2/1.6	140±11 158±11

The DTC7 carbon was used to assemble an AEDLC in $PYR_{14}TFSI$ with $R_{+/-}$ of 1.3 and w_{SC} of ca. 20 mg cm^{-2} as reported in Table 5.4. Figure 5.7 shows the cell voltage profile upon the 1100th charge-discharge galvanostatic cycle of the supercapacitor at 20 mA cm^{-2} and 60°C with maximum cell voltage of 3.9V. Table 5.4 reports V_{max}, C_{SC}, E_{max}, ESR and P_{max} as evaluated by the analysis of the profile shown in Figure 5.7.

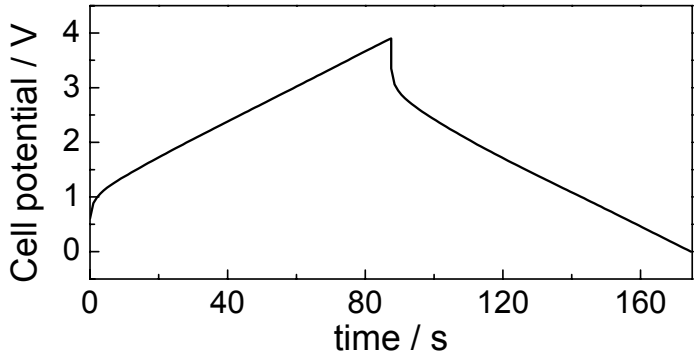

Figure 5.7. Voltage profile of the $PYR_{14}TFSI$-based AEDLC with DTC7 electrodes upon the 1100th galvanostatic charge-discharge at 20 mA cm^{-2} and 60°C.

Table 5.4. $R_{+/-}$, w_{SC}, V_{max}, C_{SC} (on the basis of w_{SC}), specific capacity (Q), coulombic efficiency (η), E_{max}, ESR and P_{max} of the DTC7/PYR_{14}TFSI/DTC7 AEDLC at the 1,100th galvanostatic cycle at 20 mA cm^{-2} and 60°C.

$R_{+/-}$	w_{SC} mg cm^{-2}	V_{max} V	C_{SC} F g^{-1}	Q mAh g^{-1}	η %	E_{max} Wh kg^{-1}	ESR Ω cm^2	P_{max} kW kg^{-1}
1.3	20.0	3.9	30	23	99.4	47	14	13

The high capacitance and cell voltage of the DTC7/PYR_{14}TFSI/DTC7 AEDLC result in an exceptionally high specific energy value, i.e. it is ca. 35% higher than that obtained with X3a carbon in IL electrolytes reported in Section 5.2 [5.1]. The ionic liquid volume required to balance the Q charge reported in Table 5.4 is ca. 0.5 cm^3 per gram of carbon and lower than the $V_{>1.5nm}$ pore volume of the DTC7 carbon (0.70 cm^3 g^{-1}). It is a volume that avoids electrolyte starving, at least in the cycling conditions adopted, and makes it possible to achieve a composite electrode-to-electrolyte loading ratio of ca. 1, so that the complete supercapacitor module might weigh 2.5 or 3 times w_{SC} depending on the contribution of current collectors, separator and case to total mass. Specific energy and power values related to complete cell weight of 16-18 Wh kg^{-1} and 4-5 kW kg^{-1} are, thus, feasible. These are very interesting results and indicate that the use of the DTC7 carbon in PYR_{14}TFSI-based AEDLC makes it possible to triple the energy of the best performing EDLCs on the market (see Table 1.2). However, the increase in power is not as marked as expected on the basis of the high operating voltage of the cell. In effect, the ESR does not seem to be competitive with that of conventional EDLC with organic electrolytes and also implies that the time constant (τ) for the charge-discharge process of the IL-based system is higher than that of the commercial ones. For example, 1.2 kF-PYR_{14}TFSI-based AEDLC with DTC7 carbon electrodes and w_{comp} of 20 mg cm^{-2} would feature an ESR of 7 mΩ and τ of *ca.* 8 s, which are 8 times higher than those of a 1.2 kF Panasonic ultracapacitor operating with propylene carbonate – tetraethyl ammonium tetrafluoroborate, although this ultracapacitor features only V_{max} of 2.5 V, E_{max} = 2.3 Wh kg^{-1} at almost the same P_{max} of 4.6 kW kg^{-1} (see Table 1.2) [5.5]. Indeed, the investigation reported in Section 4.2.4 demonstrated that the main contribution to ESR is electrode charging resistance, which in turn is affected by the ionic resistance in the pores. While the electrode charging resistance depends on IL ionic conductivity, it is also modulated by pore length. Hence, pore geometry is a key parameter in carbon design not only because it defines the carbon surface but also because it can differentially "amplify" the effect of IL conductivity on the

electrode charging-discharging process. Further improvement in the performance of $PYR_{14}TFSI$-based AEDLC could be achieved by lowering ESR by proper design of electrode porosity [5.4].

5.4. Conclusions

The development of the asymmetric configuration of EDLCs which consists of carbon loading at the positive electrode higher than that at the negative has been demonstrated to be a promising strategy to develop high specific energy IL-based double-layer supercapacitor without sacrificing power, safety and cycling stability. Indeed, while the symmetric configuration with the same carbon loading at the two electrodes allow to reach V_{max} of 3.4 V at maximum, the asymmetric one makes possible to charge each electrode up to the limit potentials defined by the ESW of each IL and thus, to overcome such V_{max}. It has been shown that the AEDLCs were stable over several thousands galvanostatic cycles at 60°C with V_{max} up to 3.9 V and delivered specific energy of ca. 30 Wh Kg^{-1} in the case of IL-AEDLCs based on the xerogel X3a and even up to 47 Wh Kg^{-1} in the case of the $PYR_{14}TFSI$-AEDLC with the template carbon DTC7, thereby in both cases outperforming commercial supercapacitors.

The moderate mesopore volume of DTC7 limits the IL amount in the electrodes and, hence, in the supercapacitor so that specific energy and power values of 16-18 Wh kg^{-1} and 4-5 kW kg^{-1} for a complete cell are feasible.

On the basis of these studies the last part of the work was devoted to the development of large size prototype and such work is described in the next Chapter.

5.5. References

5.1) M. Lazzari, F. Soavi, M. Mastragostino, *J. Power Sources* 178 (2008) *490*.

5.2) C. Arbizzani, M. Biso, D. Cericola, M. Lazzari, F. Soavi, M. Mastragostino, *J. Power Sources* 185 (2008) *1575*.

5.3) M. Mastragostino, F. Soavi, *J. Power Sources* 174 (2007) *648*.

5.4) M. Lazzari, F. Soavi, M. Mastragostino, *Fuel Cell* submitted 2009.

5.5) A. Burke, *Electrochim. Acta* 53 (2007) *1083*.

5.6) A. Balducci, R. Dugas, P.L. Taberna, P. Simon, D. Plée, M. Mastragostino and S. Passerini, *J. Power Sources* 165 (2007) *922*.

Chapter 6
Towards $PYR_{1(2O1)}TFSI$-based AEDLCs scaling up

In Chapter 5 the high cycling performance of AEDLC assembled with different ILs and carbons and operating above RT with V_{max}> 3.5 V was demonstrated.

In this chapter the study performed within the ILHYPOS Project to develop large size prototypes of IL-based AEDLCs is reported. In the project ACT carbon was selected for the electrodes because the pristine AC is commercially available and the treated ACT shows good capacitance performance. The IL was $PYR_{1(2O1)}TFSI$, provided by Evonik-Degussa, and was selected mainly for its good ESW, conductivity and wide operating temperature range.

The work included massive treatment and validation of porosity features and electrochemical performance of the ACT carbon, assembling and electrochemical tests of lab-scale cells of AEDLCs with carbon electrodes prepared at preindustrial scale and the electrochemical performance of large size prototypes.

6.1. Massive treatment of ACT carbon

In the frame of the European Union (EU) Project ILHYPOS the heat treated activated carbon ACT was selected as electrode material for automatic electrode production.

Thus, 1 kg of the activated carbon AC (BP10 from Pica) was treated under Ar flow (200 cc/min) for 4h at 1050°C with a heating rate of 10°C/min. Every day a batch of ca. 40-50 g was treated up to reach the amount needed to prepare ACT electrodes in order to assemble large size IL-based asymmetric EDLC prototypes which were the final target of the Project. Table 6.1 summarizes the yield and production time of the different ACT carbon batches prepared. A total amount of 1047.7 g was produced and sent to Leclanché Lithium for carbon electrode preparation at pre-industrial scale.

The carbon ACT from different batches was characterized by N_2 adsorption isotherm at 77K (batches from 1 to 11 called ACT_B1-11 and batches 12-23 called ACT_B12-23) and by cyclic voltammerty in order to validate the carbon features.

Table 6.1. Yield and production time of the different ACT carbon batches

batch	w before treatment	w after treatment	yield	notes		production time	total amount
1	40 g	36 g	90 %	tested as mixture	the mixture from batch 1 to 11 was tested by N_2 adsorption and cyclic voltammetry	first week	208 g
2	45 g	43 g	96 %	tested by N_2 adsorption and cyclic voltammetry			
3	38 g	36.0 g	95 %	tested as mixture			
4	48 g	45.0 g	94 %				
5	50 g	48.0 g	96 %				
6	50 g	47.5 g	95 %	tested as mixture		second week	236.4 g
7	50 g	47.0 g	94 %				
8	50 g	47.5 g	95 %				
9	50 g	47.0 g	94 %				
10	50 g	47.4 g	95 %				
11	50 g	47.5 g	95%	tested as mixture		third week	236.5 g
12	50 g	47.5 g	95%		the mixture from batch 12 to 23 was tested by N_2 adsorption and cyclic voltammetry		
13	50 g	47.0 g	94 %				
14	50 g	47.5 g	95 %				
15	50 g	47.0 g	94 %				
16	50 g	47.5 g	95 %	tested as mixture		fourth week	235.8 g
17	50 g	47.3 g	95 %				
18	50 g	47.0 g	94 %				
19	50 g	47.0 g	94 %				
20	50 g	47.0 g	94 %				
21	50 g	47.0 g	94 %	tested as mixture		fifth week	131.0 g
22	50 g	47.0 g	94 %				
23	40 g	37.0 g	93 %				
Total amount of carbon produced							1047.7 g

Table 6.2 compare the results of porosity analyses of ACT carbon batches (see Table 6.1). The carbon ACT from the batches 1-11 and 12-23 displays almost the same porosity than ACT carbon reference.

Table 6.2. Porosity features V_{tot}, $V_{>1.5\ nm}$, $S_{>1.5\ nm}$ and $\langle w \rangle$ of the ACT carbons.

Carbon	V_{tot} cm^3g^{-1}	$V_{>1.5\ nm}$ cm^3g^{-1}	$S_{>1.5\ nm}$ m^2g^{-1}	$\langle w \rangle$ nm
ACT reference	1.34	0.84	972	2.7
ACT_B1-11 (batches 1-11)	1.33	0.75	929	2.4
ACT_B12-13 (batches 12-23	1.40	0.79	981	2.4

Electrodes from batches 1-11 and 12-23 were prepared as reported in Chapter 2 with 5% of pTFE as binder and electrode area of 0.62 cm^2 and were tested by CV at 60°C and 20 $mV\,s^{-1}$ in a three electrode cell with $PYR_{1(2O1)}TFSI$ as electrolyte. The Table 6.3 reports the results

of the electrochemical tests which confirm the success of the heat treatment on the several massive batches of ACT carbon. Indeed, such carbon featured a high specific capacitance of ca. 100 F g^{-1}.

Table 6.3. Specific capacitance (C_{dl}) of heat-treated carbon ACT in the negative and positive potential domains evaluated by CV at 20 mV/s and 60°C in $PYR_{1(2O1)}TFSI$.

Carbon ACT	Composite loading mg cm^{-2}	IL	Specific capacitance at 60°C			
			negative domain		positive domain	
			ΔV V vs. Ag	F g^{-1}	ΔV V vs. Ag	F g^{-1}
batches 1-11	9.5	$PYR_{1(2O1)}TFSI$	-2.2/0.0	106	0.0/1.7	107
batches 12-23	9.3			98		99

6.2. Validation of the capacitance performance of pre-industrial electrodes with ACT carbon from massive treatment.

The 1 kg of ACT carbon provided to Leclanchè Lithium was used to produce about 30 mt belts of composite electrodes by lamination of 90% ACT - 10% Teflon® composite on carbon-coated Al grids. Figures 6.1a and b shows the Leclanché Lithium coater for electrode belts production and Figures 6.1c and d show the final belts prepared. Table 6.4 reports the capacitive response in $PYR_{1(2O1)}TFSI$ of electrodes cut from these belts and tested in lab-scale cells by CV at 20 mV s^{-1} at RT and 60°C in the negative and positive potential domains. These preindustrial electrodes provided by Leclanchè Lithium were also used to assemble lab-scale $PYR_{1(2O1)}TFSI$ AEDLCs and the results are reported in the following sections.

Table 6.4. Specific capacitance (C_{dl}) of the composite electrodes produced by the Leclanchè Lithium pilot coating line in $PYR_{1(2O1)}TFSI$ at different temperatures from CVs at 20 mV s^{-1} in the negative and positive potential domains (potentials are given vs. Fc/Fc^{+}).

T/°C	C_{dl} / F g^{-1}	
	-2.4/0.0 V	0.0/+1.6 V
RT	88 ± 2	94 ± 2
60	112 ± 10	112 ± 10

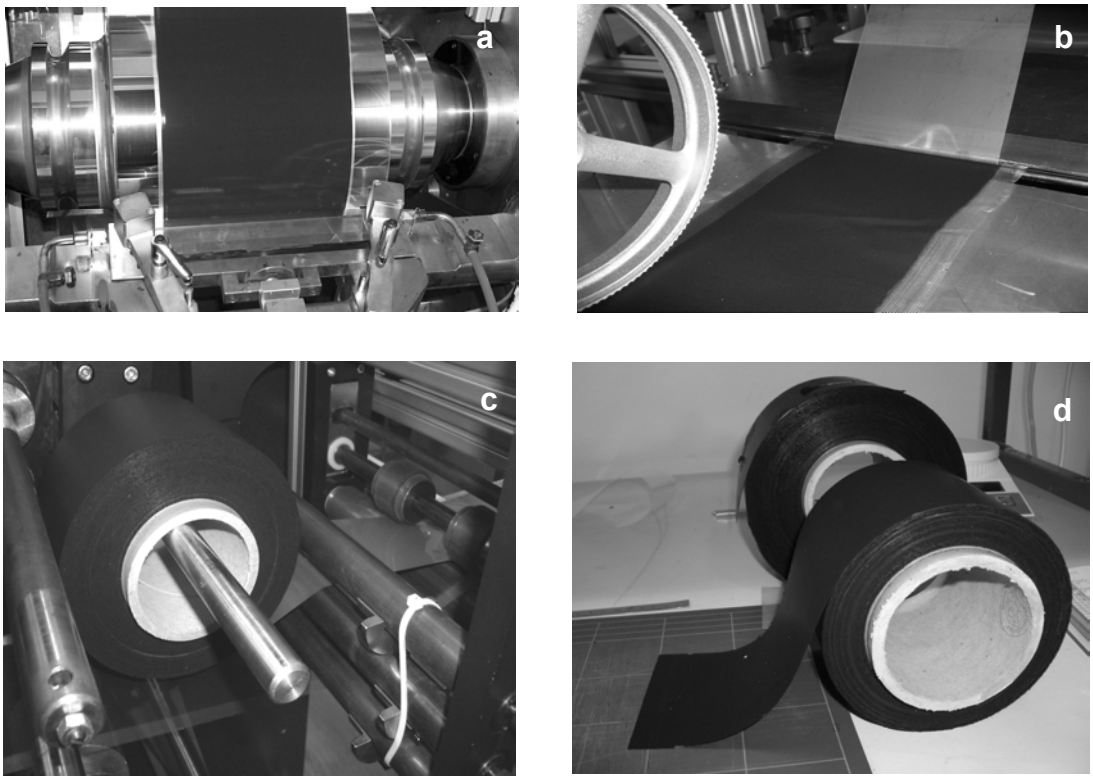

Figure 6.1. Leclanché Lithium coater for carbon electrode belts production (a and b) and belts produced (c and d) with the ACT carbon. Reproduced with permission from Leclanché Lithium.

6.3. Lab-scale AEDLCs with ACT carbon electrodes prepared at preindustrial scale and $PYR_{1(2O1)}TFSI$

In view of IL-based AEDLC scaling up, ACT/$PYR_{1(2O1)}$TFSI/ACT AEDLCs were assembled with Leclanchè Lithium pre-industrial electrodes. The ACT/$PYR_{1(2O1)}$TFSI/ACT supercapacitors were assembled using carbon electrodes with $R_{+/-}$ higher than 1, as reported in Table 6.5.

Table 6.5. $R_{+/-}$, w_{SC}, V_{max}, C_{SC}, E_{max}, ESR and P_{max} evaluated from galvanostatic discharges at 20 mA cm^{-2} and 60°C of the ACT/$PYR_{1(2O1)}$TFSI/ACT AEDLC.

$R_{+/-}$	w_{SC} mg cm^{-2}	V_{max} V	C_{SC} F g^{-1}	E_{max} Wh kg^{-1}	ESR Ω cm^2	P_{max} kW kg^{-1}
1.49	14	3.7	22	31	20	9.9

The AEDLCs were tested at 60°C over several thousand galvanostatic charge/discharge cycles (>20,000 cycles) at 10-20 mA cm^{-2}, with V_{max} > 3.5 V. Figure 6.2 shows the charge/discharge galvanostatic profiles of the ACT/$PYR_{1(2O1)}$TFSI/ACT AEDLC upon the 17,000th charge/discharge cycle at 10 mA cm^{-2} and 60°C with V_{max} = 3.8 V and of its positive and negative electrodes (right axis) which reached the end-of-charge potentials of

1.6V vs. Fc/Fc^+ and −2.2V vs. Fc/Fc^+, respectively. Table 6.5 reports the C_{SC}, E_{max}, ESR and P_{max} values evaluated from discharge cycles carried out at 20 mA cm^{-2} and 60°C with the reported V_{max} of 3.7 V. Given that it is feasible to assume that w_{SC} will be 25-33 % of the supercapacitor module weight (w_{module}), the E_{max} values in Table 6.5 become 8-10 Wh kg^{-1}, i.e. double that of the EDLCs on the market at RT [6.1]. The high-energy performance of $PYR_{1(2O1)}TFSI$-based AEDLC was exhibited without sacrificing power and cyclability, the latter being tested by deep discharge cycles from V_{max} down to 0 V at 60°C. High cycling stability was exhibited by the $PYR_{1(2O1)}TFSI$-based AEDLC, with a capacitance fade of 2% over 27,000 cycles performed with $V_{max} \leq 3.6$ V for the first 12,000 cycles and 3.7 V for the following 15,000 (3,000 cycles were also carried out with $V_{max} = 3.8$ V), as shown by the C_{SC} trend vs. cycle number in Figure 6.3 [6.2].

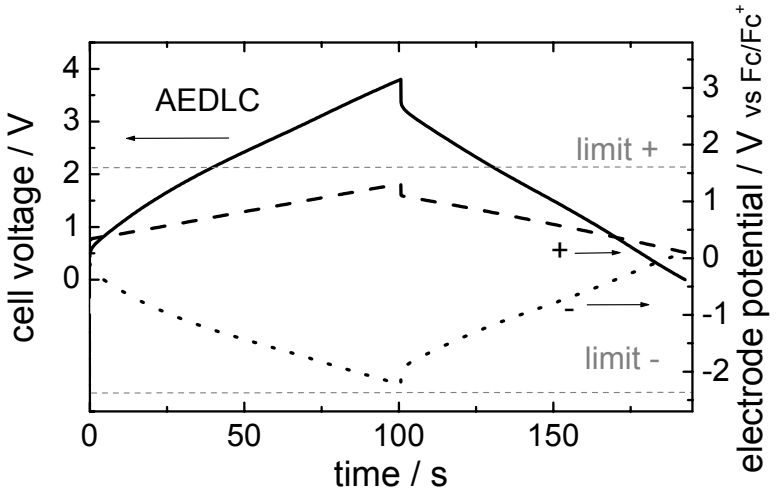

Figure 6.2. Voltage profiles of the ACT/$PYR_{1(2O1)}TFSI$/ACT AEDLC upon the 17,000th galvanostatic charge/discharge at 10 mA cm^{-2} and 60°C with $V_{max} = 3.8$ V and of its positive and negative ACT electrodes.

The power and energy performance of ACT/$PYR_{1(2O1)}TFSI$/ACT AEDLCs were tested in the -30 to 60°C temperature range for HEV application. Along with the traditional Ragone plots obtained by galvanostatic cycling at different current rates, the results of tests performed to evaluate the dynamic pulse power and energy features by the USABC and DOE FreedomCAR reference protocols are given in th next Sections.

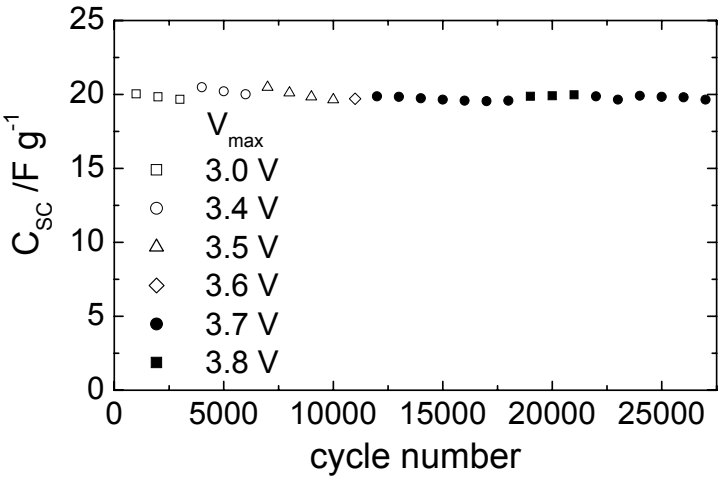

Figure 6.3. Trend of C_{SC} over cycling at 60 ◦C and 20 mA cm^{-2} at different V_{max} of the ACT/$PYR_{1(2O1)}$TFSI/ACT AEDLC.

6.3.1. Ragone plot of ACT/$PYR_{1(2O1)}$TFSI/ACT AEDLC at different temperatures

The $PYR_{1(2O1)}$TFSI-based AEDLC supercapacitors with ACT carbon electrodes were tested with V_{max} = 3.7 V, minimum cell voltage (V_{min}) equal to 55% V_{max}, as suggested by HEV applications, i.e. 2.035 V, in the temperature range -30°C/+60°C at different currents by consecutive galvanostatic charge/discharge cycles. Figure 6.4 reports the Ragone plots at different temperatures of the $PYR_{1(2O1)}$TFSI-based AEDLC with specific energy (E) and power (P) being evaluated from the galvanostatic discharges as in eq. (6.1) and (6.2), respectively:

$$E = i \int_{t_{V_{max}}}^{t_{0.55\ V_{max}}} V dt / w_{SC} \qquad \text{(eq. 6.1)}$$

$$P = E/(t_{0.55\ V_{max}} - t_{V_{max}}) \qquad \text{(eq. 6.2)}$$

where i is the current density, $t_{V_{max}}$ and $t_{0.55\ V_{max}}$ are the times at which the cells exhibit 3.7 V and 2.035 V potentials.

The data in Figure 6.4 indicate that the $PYR_{1(2O1)}$TFSI-based AEDLCs can operate in a wide temperature range. The specific energy and power lower with temperature because of the related decrease of the ionic liquid conductivity. Indeed, the latter impacts the Ohmic drop, and thus the practical cell voltage at which cell discharge begins; this is particularly evident at the highest currents.

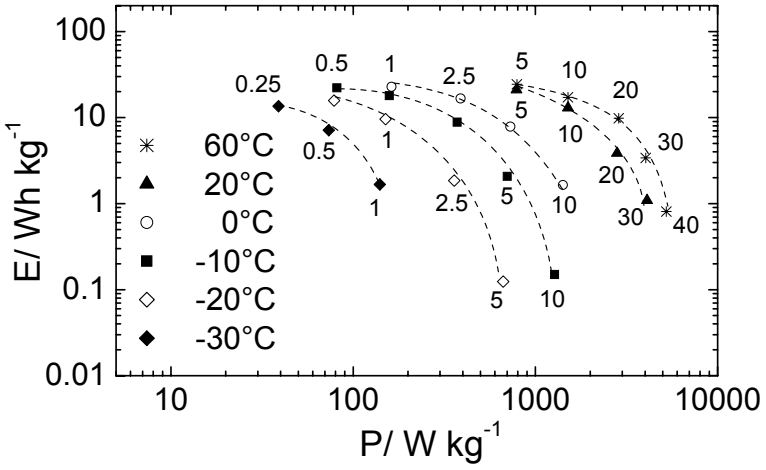

Figure 6.4. Ragone plot of the $PYR_{1(2O1)}TFSI$-based AEDLC supercapacitor at different temperatures. Specific energy (E) and power (P) values have been evaluated referring to the total composite electrode material loading as in eq. (6.1) and (6.2), respectively, from galvanostatic discharges at different currents with V_{max}= 3.7 V and V_{min}= 2.035 V; the labels indicate the current densities in mA cm^{-2}.

The equivalent series resistance (ESR) of the cell, evaluated from the Ohmic drop at the beginning of discharge, increases from 15 ± 5 ohm cm^2 at 60°C to 410 ± 130 ohm cm^2 at -30°C (at each temperature the dispersion in the ESR value is strictly related to cell assembly, which was manually performed). At the lowest currents, when the temperature changes from 60°C to -30°C, the cell specific capacitance referred only to the total composite loading (C_{SC}) varies from 26 F g^{-1} to 16 F g^{-1} (corresponding to single carbon electrode capacitance C_{dl} of ca. 100 F g^{-1} at 60°C and 60 F g^{-1} at -30°C) and a four fold increase of the current density at the two temperatures reduces the capacitance values by the 25% and 75%, respectively. At 30°C the $PYR_{1(2O1)}TFSI$-based AEDLCs capacitance well compares that of commercial EDLCs operating with conventional organic electrolytes. The capacitance decrease of the IL-based supercapacitor with temperature lowering is related to the nature of the carbon/solvent-free IL interface. Indeed, in solvent-free IL the double-layer is constituted by a monolayer of ions up against the charged carbon surface, therefore the capacitance is strictly related to IL polarizability, which affects the dielectric constant in the double-layer as the conductivity of the bulk electrolyte [6.3-6.5].

6.3.2. RCT and HPPC tests of ACT/$PYR_{1(2O1)}$TFSI/ACT AEDLC for power-assist HEV application

The characterization of the $PYR_{1(2O1)}$TFSI-based AEDLCs for HEV applications was performed following the standards stated by DOE in the "FreedomCAR Battery Test Manual For Power-Assist Hybrid Electric Vehicles" [6.6] and in the "FreedomCAR Ultracapacitor Test Manual" [6.7]. In order to evaluate if supercapacitors may replace batteries in power-assist HEVs, which need modules with a specific available energy of at least 7.5 Wh/kg for 10 s-625 W/kg pulses at 30°C, the standard tests reported in the former manual, slightly modified following the indications reported in the latter one, which takes into account the different nature of the charge/discharge processes in supercapacitors with respect to batteries, were followed.

These benchmarks include the reference capacity test (RCT), which provides the available energy of the supercapacitor at various states of charge, and the hybrid pulse-power characterization (HPPC) that gives the dynamic power and energy capabilities at different states of charge and depths of discharge (DODs) [6.6-6.8].

The RCT and HPPC tests were carried out in the -30°/60°C temperature range, including 30°C, which is the reference temperature of DOE targets. According to ref. [6.8], the specific parameters evaluated by such tests and reported in the following refer to a total module mass (w_{module}) which is twice the total composite electrode mass, i.e. $w_{module} = 2\, w_{SC}$, so as to include the other components' weights.

The RCT test is carried out to evaluate the total available energy of the supercapacitor at various states of charge and for different DODs. It was performed by a 5C galvanostatic charge up to V_{max} = 3.7 V, a potentiostatic charge at this potential for ca. 10 minutes, and a galvanostatic discharge at 5C down to V_{min} = 2.035 V. The 5C current rate, i.e. that for the supercapacitor full discharge in 1/5 hours (12 minutes), may be evaluated referring to the theoretical charge Q_t, which is given by eq. (6.3),

$$Q_t = C_{SC} (V_{max} - V_{min}) \qquad \text{(eq. 6.3)}$$

where C_{SC} is the supercapacitor capacitance. However, as reported above, the $PYR_{1(2O1)}$TFSI-based AEDLC capacitance and practical cell voltage excursion upon discharge, which is always narrower than V_{max} -V_{min}, vary with temperature. Thus, we experimentally determined the current densities for 5C discharge rates at -30°C, -20°C, 0°C, 30°C and 60°C and the values are reported in Table 6.6. The Table also shows the

experimental specific capacity ($Q_{100\%DOD}$) and specific energy ($E_{100\%DOD}$) delivered upon the 5C discharges with 100% DOD. Figure 6.5 shows the plots of the cell potential and of the specific cumulative energy removed during the discharge (E_{DOD}) vs. DOD from the RCT test at 5C and 30°C.

Table 6.6. Values at different temperatures of current density, specific capacity ($Q_{100\%DOD}$) and specific available energy ($E_{100\%DOD}$) delivered upon the RCT discharge between V_{max} = 3.7 V and V_{min} = 2.035 V (DOD = 100%) at the 5C-rate of the $PYR_{1(2O1)}TFSI$-based AEDLC. Specific values are referred to the module weight.

T °C	5C-rate mA cm^{-2}	$Q_{100\%DOD}$ mAh g^{-1}_{module}	$E_{available,\ 100\%DOD}$ Wh kg^{-1}_{module}
60	0.92	5.0	15
30	0.92	5.0	15
0	0.66	4.7	13
-20	0.55	3.5	9
-30	0.37	2.2	6

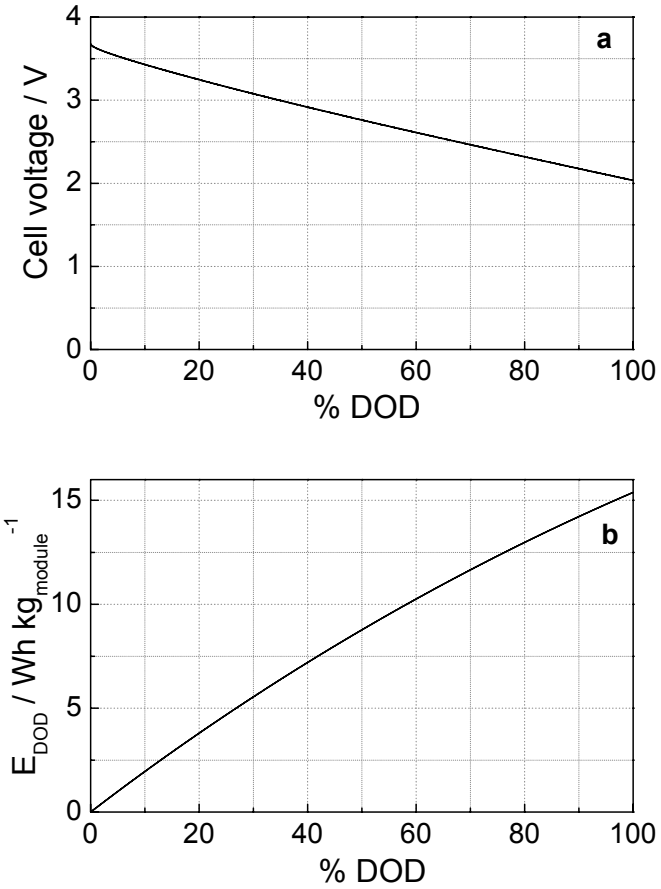

Figure 6.5. (a) Cell voltage vs. DOD and (b) specific cumulative energy (E_{DOD}, referred to module weight) vs. DOD from the RCT discharge at 5C and 30°C with V_{max} = 3.7 V and V_{min} = 2.035 V of the $PYR_{1(2O1)}TFSI$-based AEDLC supercapacitor.

E_{DOD} is evaluated from the discharge profile between V_{max}=3.7 V and the potential which marks the DOD ($V_{DOD,}$ with 2.035 V< V_{DOD} < 3.7 V), by using eq. (6.4)

$$E_{DOD} = i \int_{t_{V_{max}}}^{t_{V_{DOD}}} V \, dt / w_{module} \qquad \text{(eq. 6.4)}$$

where $t_{V_{DOD}}$ is the time at which the cell exhibits the V_{DOD} voltage.

The HPPC characterization, which provides the dynamic power and energy capabilities over the V_{max}/V_{min} voltage range by a test profile that incorporates both discharge and regenerative pulses, was performed as follows. The test begins with a 5C-galvanostatic/potentiostatic charge at a given cell potential, followed by a rest period. Then, a sequence which consists of 10 s discharge pulse at the I_{dis} current, 5 s open circuit voltage (OCV) step, 10 s regenerative pulse at the I_{reg} = 75% I_{dis} current, and a 5C galvanostatic discharge with 10% DOD is repeated until the V_{min} cut off potential is reached [6.6, 6.7]. This sequence represents an accelerated test because the suggested OCV period should be of 30 minutes-1h. The pulse currents are set in relation to the supercapacitor maximum current (I_{max}) which is a characteristic feature of the electrochemical device and that corresponds to the current required to cause an immediate (i.e., <0.1 s) 20 % voltage drop in a fully charged device [6.7]. The I_{max} of the $PYR_{1(2O1)}$TFSI-based AEDLC reported in Table 6.7 significantly lowers moving from 60°C to -30°C because the voltage drop is proportional to ESR and the latter increases when temperature decreases. The pulse sequence can be performed at two different currents: for the "low-HPPC" test the I_{dis} is 25% I_{max}, for the "high HPPC" the I_{dis} is 75% $I_{max.}$ Table 6.7 reports the I_{dis} current densities which we adopted in the HPPC tests at different temperatures. For the reference operative condition of 30°C the order of magnitude of I_{max} is 20 mA cm^{-2}, thus the low-HPPC and high-HPPC I_{dis} current densities are of ca. 5 mA cm^{-2} and 15 mA cm^{-2}, respectively. The low-HPPC sequences at -20°C and -30°C were not performed because the corresponding I_{dis} could not be considered "pulse" current being lower than the 5C-rates at the same temperatures (see Table 6.6).

Figure 6.6 reports the voltage profile of the $PYR_{1(2O1)}$TFSI-based AEDLC upon the low-HPPC test at 30°C. The specific discharge (P_{dis}) and regenerative (P_{reg}) pulse power capabilities are calculated from the HPPC sequence as in eq. (6.5-6.6):

$$P_{dis} = 2.035 \, (V_0 - 2.035)/(R_{dis} \, w_{module}) \qquad \text{(eq. 6.5)}$$

P_{reg}= 3.7 (3.7-V_2)/(R_{reg} w_{module}) (eq. 6.6)

where R_{dis} and R_{reg} are the discharge (R_{dis}) and regenerative (R_{reg}) pulse resistances, which are given by

R_{dis}= (V_1-V_0)/I_{dis} (eq. 6.7)

R_{reg}= (V_3-V_2)/I_{reg} (eq. 6.8)

Table 6.7. Maximum (I_{max}) and discharge pulse (I_{dis}) currents and DOD limits (DOD_{min}, DOD_{max}) for low-HPPC and high-HPPC tests at different temperatures with pulse time (Δt_{pulse}) of 10 s and 2 s of the $PYR_{1(2O1)}$TFSI-based AEDLC. For each temperature the C-rate is calculated referring to the corresponding experimental capacity $Q_{100\%DOD}$ reported in Table 6.6.

T **°C**	**I_{max}** **mA cm^{-2}**	**HPPC**	**I_{dis}** **mA cm^{-2}**	**C-rate**	**Δt_{pulse}** **s**	**DOD_{min} - DOD_{max}** **%**
60	20	low	5	34 C	10 2	7 – 84 2 – 92
		high	15	102 C	10 2	24 – 55 10 – 78
30	15	low	4	22 C	10 2	5 – 85 2 – 92
		high	10	61 C	10 2	18 – 63 7 - 80
0	6	low	1.5	9.5 C	10 2	1 - 85 0 - 91
		high	5	29 C	10 2	23 - 56 10 - 73
-20	2	high	1.4	12 C	10 2	10 - 65 3 - 75
-30	0.5	high	0.4	5.6 C	10 2	1 - 76 0 - 80

As marked in Figure 6.6b, V_0 and V_2 are the cell potentials at the beginning of the discharge and regenerative pulses, respectively, and V_1 and V_3 the potentials at the end of these pulses. The 10 s-pulse sequence can be used even to calculate the P_{dis}, P_{reg} , R_{dis} and R_{reg} values for a pulse time (Δt_{pulse}) of 2 s. This can be done by using in eq 6.7-6.8 the V_1 and V_3 values evaluated after 2 s from the beginning of the pulses.

R_{dis} and R_{reg} depend on the (V_1-V_0) and (V_3-V_2) values, which in turn include the ohmic drop/rise and the linear variation of the cell voltage over time, which is an intrinsic characteristic of the capacitive charge/discharge process of the supercapacitor (see Figure 6.6b). Hence, unlike batteries, supercapacitors feature R_{dis} and R_{reg} which increase with Δt_{pulse}, as shown by the pulse resistance values calculated from 10 s and 2 s low-HPPC tests at 30°C and at different DOD of the $PYR_{1(2O1)}$TFSI-based AEDLC reported in Figure 6.7.

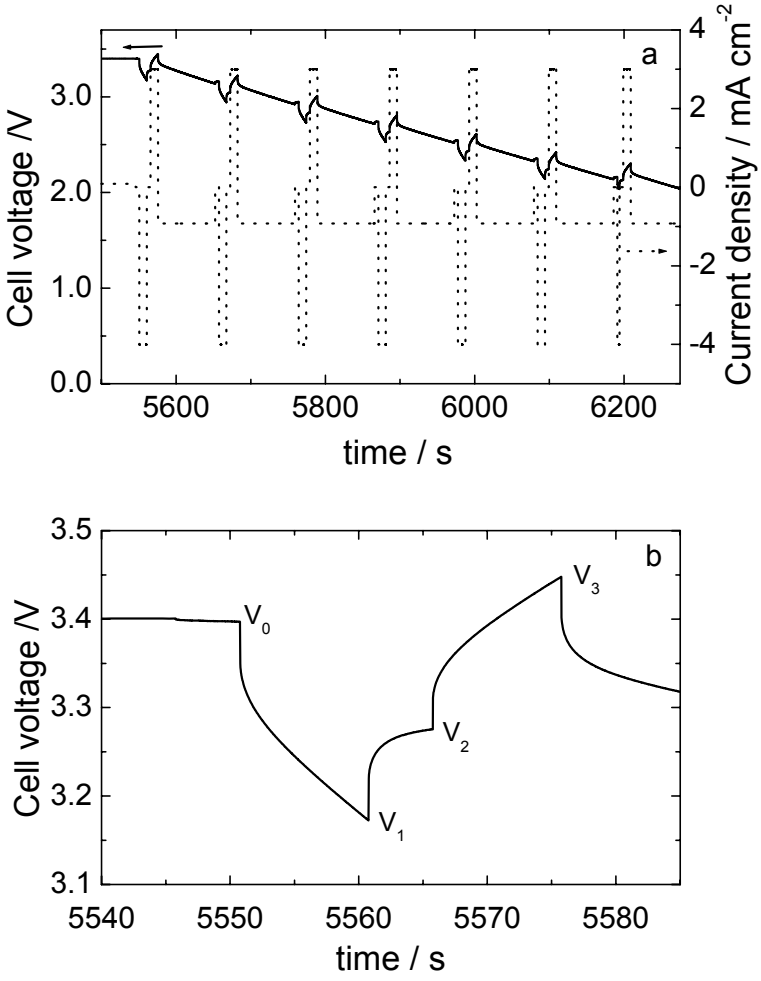

Figure 6.6. (a) Cell voltage (solid line) and current density (dotted line) vs. time upon the low-HPPC test at 30°C of the $PYR_{1(2O1)}TFSI$-based AEDLC and (b) magnification of the cell voltage profile during the first discharge/regenerative pulse.

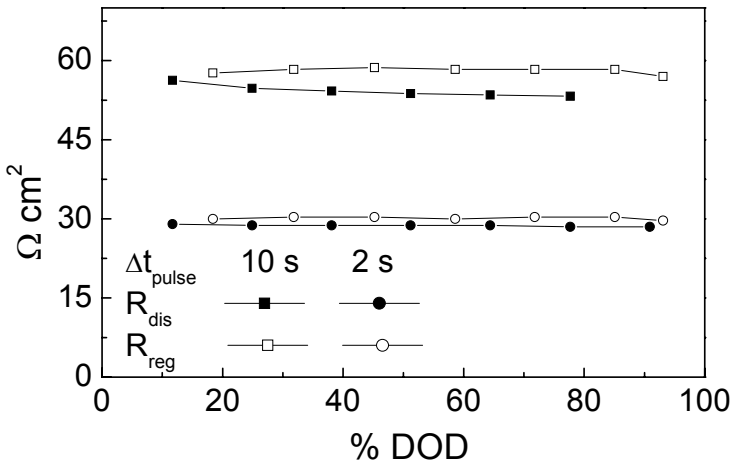

Figure 6.7. R_{dis} and R_{reg} values at different DOD of the $PYR_{1(2O1)}TFSI$-based AEDLC evaluated from low-HPPC test at 30°C with Δt_{pulse}= 10 s and 2 s.

Consequently, the P_{dis} and P_{reg} evaluated from 10 s-sequence are systematically lower than those from the 2 s pulses, as evidenced by the pulse power capability vs. DOD plots reported in Figure 6.8 which were obtained from the low-HPPC and high-HPPC tests at 30°C of the AEDLC. In Figure 6.8 the P_{reg} axis has been properly scaled as suggested in refs. [6.6, 6.7] in order to match P_{dis} with the target value of P_{reg} = 80% of P_{dis}.

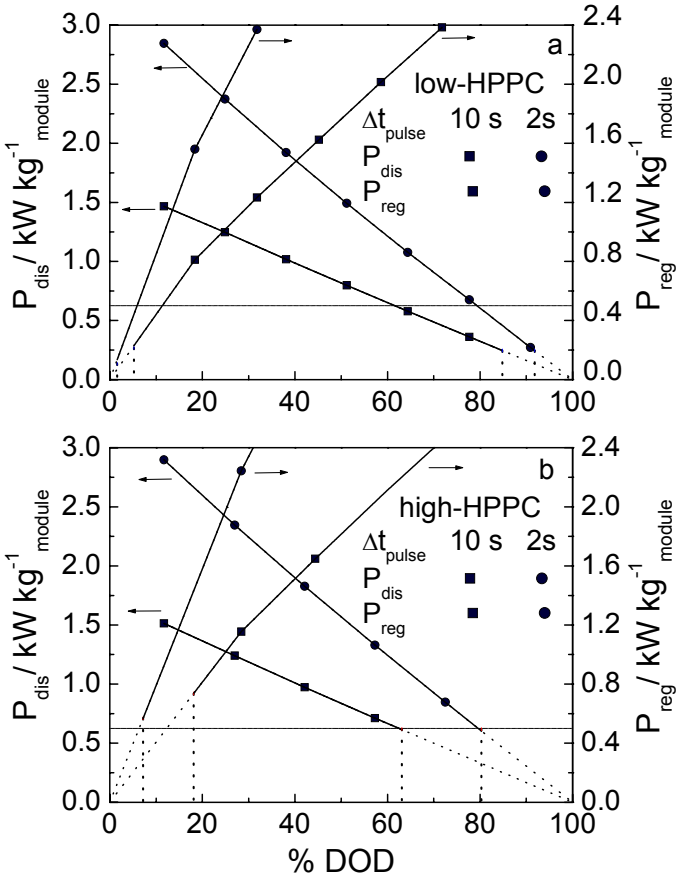

Figure 6.8. Discharge (P_{dis}) and regenerative (P_{reg}) pulse power capability referred to module weight vs. DOD of the $PYR_{1(2O1)}TFSI$-based AEDLC at 30°C from (a) low-HPPC and (b) high-HPPC tests with Δt_{pulse}= 10 s and 2 s. The horizontal dashed line indicates the DOE 10 s-P_{dis} goal.

Given that at DOD = 100% and 0% P_{dis} and P_{reg} are zero (see eq. 6.5-6.6), the interpolation of the pulse power data in Figures 6.8a and b should cross the y-axis origins. However, the HPPC sequence is cut when $V_1 \leq 2.035$ V or $V_3 \geq 3.7$ V, hence the lowest and highest values of V_0, and, consequently, the maximum (DOD_{max}) and minimum (DOD_{min}) DOD, at which complete discharge and regenerative pulses take place depend on I_{dis}, I_{reg}, R_{dis}, R_{reg} and Δt_{pulse}. For the $PYR_{1(2O1)}TFSI$-based AEDLC full duration pulses are feasible only within the DOD limits reported in Table 6.7, which, thus, cut the P_{dis} and P_{reg} vs. DOD plots. At 30°C, 10 s-pulses can be performed in the DOD ranges of 5-85 % by

low HPPC and of 18-63% by high HPPC, as marked in Figure 6.8. Within such DOD limits, the P_{dis} and P_{reg} values evaluated by the two tests at low and high currents are very similar. In both cases the discharge and regenerative curves cross at P_{dis}= 1250 W kg^{-1} and 2400 W kg^{-1} for 10 s and 2 s pulses, respectively, and at DOD of 24%. The power at this cross point, which represents the maximum value simultaneously satisfied in the discharge and the generative pulses, is significantly higher than the DOE target which is evidenced with a horizontal line in the two figures.

Starting from the cross point of the discharge and regenerative pulse-power curves, as the demand for power lowers, the usable DOD range (ΔDOD) within which the condition P_{reg} = 80% P_{dis} is satisfied, widens. Consequently, the specific available energy ($E_{available}$), which is the energy that can be removed during a 5C discharge over that ΔDOD range and that corresponds to the difference between the E_{DOD} values at the two ΔDOD limits, increases. As an example, for a 10 s-low-HPPC at 30°C, P_{dis} = 625 W kg^{-1} and P_{reg} = 500 W kg^{-1} at DOD = 61 % and 11 % (Figure 6.8a), where the E_{DOD} is 10.40 Wh kg^{-1} and 2.14 Wh kg^{-1} (Figure 6.5b), respectively. Hence, the energy available in ΔDOD = 11%-61% is 8.26 Wh kg^{-1}. For the 10 s-high-HPPC test a P_{dis} of 625 W kg^{-1} is feasible within a ΔDOD which is limited by the 18% DOD_{min} value for the regenerative pulse and 62% for the discharge pulse.

The trend of the energy available in a ΔDOD range where given discharge and regenerative pulse powers are met vs. P_{dis} is described by "HPPC-Ragone plots" like those shown in Figures 6.9-6.11. Figure 6.9a reports the HPPC- Ragone plots at 30°C of the $PYR_{1(2O1)}$TFSI-based AEDLC from the 10 s low-HPPC and high-HPPC tests of the IL-based supercapacitor and the DOE goal for 10s-pulse applications in power-assist HEV; the Figure also reports the expected performance of a commercial EDLCs operating with V_{MAX} = 2.7 [5.10]. Figure 6.9b shows the HPPC-Ragone plots at 30°C obtained from 2s low-HPPC and high-HPPC tests with the indication of the DOE goal for 2s-pulse applications in HEV such as 12 V start-stop (TSS), 42 V start-stop (FSS), and 42 V transient power assist (TPA).

The most striking result is that, as evinced in Figure 6.9a, the $PYR_{1(2O1)}$TFSI-based AEDLC meets the requirement for power-assist HEV application and because of the high V_{max} of 3.7 V it can deliver an $E_{available}$ energy sufficiently high to compete with lithium-ion batteries for 10s-625 W/kg pulses. Figure 6.9b shows that the HPPC-Ragone plots shift to

higher P_{dis} values when pulses are shortened to 2s, so that at 30°C the IL-based supercapacitor significantly overcomes the performance required for the 12V-TSS and 42V-FSS and 42V-TPA applications in HEV, which represent a quite "conventional" use of supercapacitors in transportation.

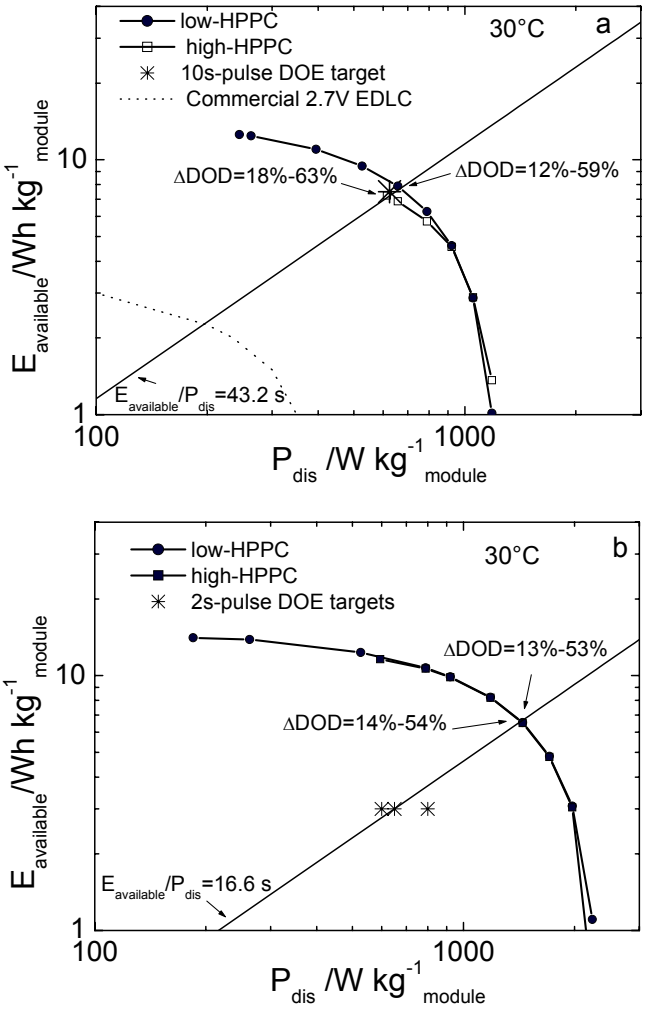

Figure 6.9. Available Energy ($E_{available}$) vs. discharge pulse power capability (P_{dis}) at 30°C of the $PYR_{1(2O1)}TFSI$-based AEDLC referred to module weight from low-HPPC and high-HPPC tests with Δt_{pulse}= 10 s (a) and 2 s (b). (∗=DOE targets; dotted line: commercial EDLCs operating with V_{max} = 2.7 from ref. [6.8]).

The HPPC-tests of the $PYR_{1(2O1)}TFSI$-based AEDLC were also run in the temperature range -30°C/+60°C and the Figures 6.10-6.11 report the corresponding HPPC-Ragone plots. At -30°C and -20°C, only the high-HPPC tests were performed because the I_{dis} current for the low-HPPC characterization is lower than that corresponding to a 5C-rate (at the same temperature). Figures 6.10-6.11 demonstrate that the $PYR_{1(2O1)}TFSI$-based

AEDLC can cycle between -30°C and +60°C, which is the envisioned temperature range for HEVs. At T≥ 30° the IL-based supercapacitor meets the power-assist HEV targets and at 0°C it features performance similar to that exhibited at 30°C by the commercial EDLC. At 0°C the $PYR_{1(2O1)}TFSI$-based AEDLC also satisfies the 2s-pulse DOE requirements [6.3].

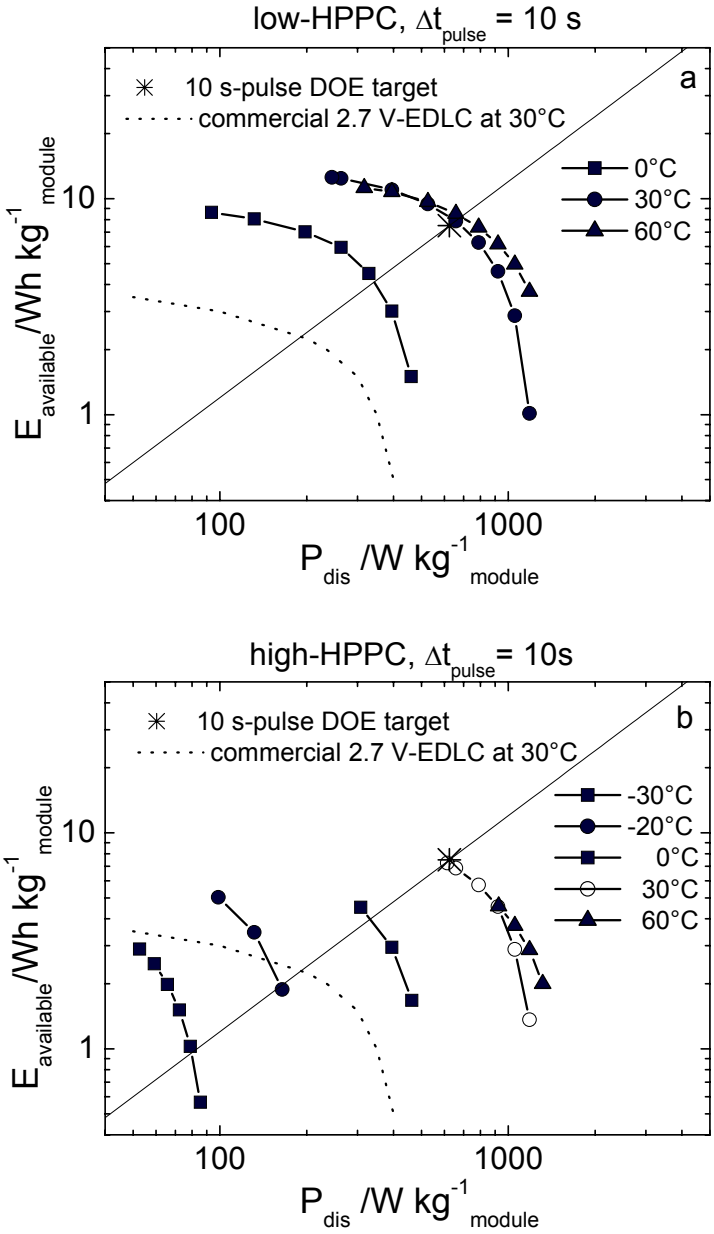

Figure 6.10. Available Energy ($E_{available}$) vs. Discharge pulse power capability (P_{dis}) with Δt_{pulse} =10s of the $PYR_{1(2O1)}TFSI$-based AEDLC referred to module weight from (a) low-HPPC and (b) high-HPPC tests at different temperatures (∗= 10s-pulse DOE target; dotted line: commercial EDLCs operating at 30°C with V_{MAX} = 2.7 from ref. [6.8]).

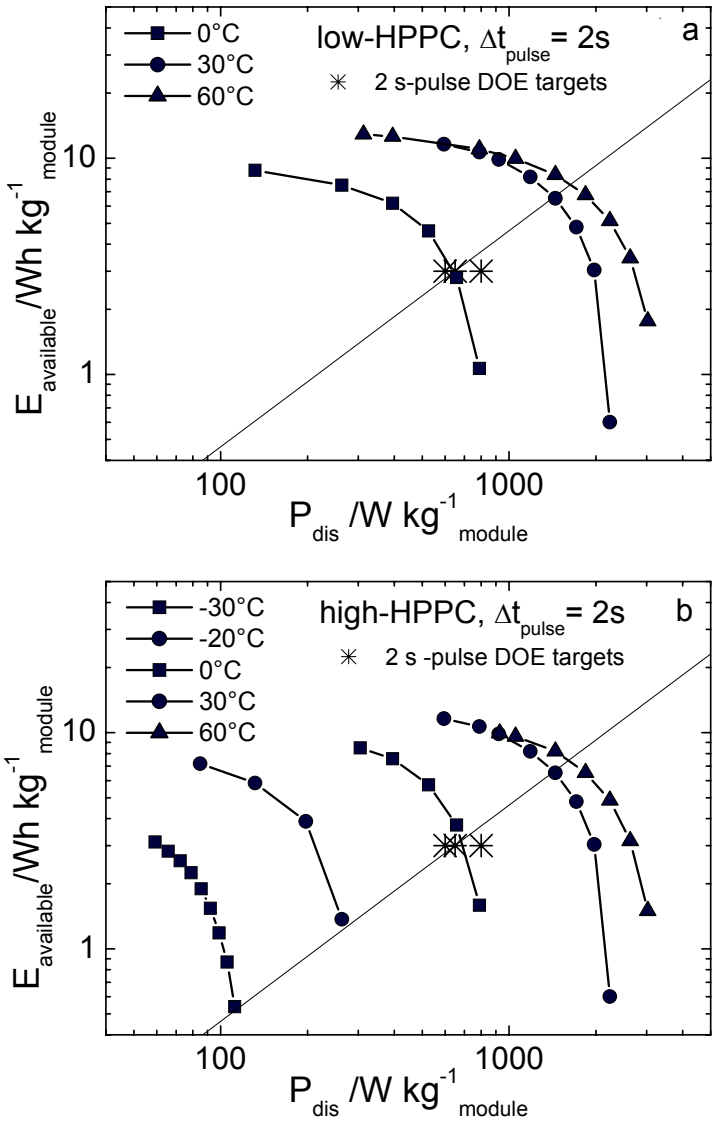

Figure 6.11. Available Energy ($E_{available}$) vs. Discharge pulse power capability (P_{dis}) with Δt_{pulse}= 2s of the $PYR_{1(2O1)}TFSI$-based AEDLC referred to module weight from (a) low-HPPC and (b) high-HPPC tests at different temperatures (∗= 2s-pulse DOE targets).

6.4. Preparation of large size prototypes and electrochemical tests

Arcotronics Technologies assembled cells of $PYR_{1(2O1)}TFSI$-based AEDLCs of size larger than that of the lab-scale tested in Section 6.3 by sandwiching different numbers of double coated positive and negative electrode couples with a ceramic Separion© separator provided by Evonik-Degussa. Table 6.8 summarizes the main features of such cells which were filled with the IL and, finally, sealed under vacuum in the Arcotronics dry-room.

The CD1 and CD6 cells were characterized by galvanostatic cycles at 30°C. The CD1 cell with only 1 electrode pair of 25 cm^2 was cycled at 0.5 A with V_{max} of 3.7 V and exhibited 18 F and an ESR of 0.5 Ω, as expected on the basis of lab-scale cells test.

Table 6.8. Pre-series IL-based AEDLC Cells

Cell Code	**CD1**	**CD6**
Number of electrode pair	1	6
Single electrode size	5 x 5 cm^2	9.3 x 9.3 cm^2
Total composite electrode loading	0.83 g	17.2 g
Double coated electrode loadings		
positive electrodes	20 mg cm^{-2}	20 mg cm^{-2}
negative electrodes	13 mg cm^{-2}	13 mg cm^{-2}
$PYR_{1(2O1)}TFSI$ Electrolyte	2.4 g (in excess)	25 g
Total cell weight (Al case in excess)	11.46 g	65.9 g

The CD6 cell with 6 electrode pairs of ca. 86 cm^2 is shown in Figure 6.12. The weight distribution of cell components in the CD1 and CD6 cells was not optimized, particularly the Al case and tabs were oversized, as evidenced by Figure 6.12. The cell CD1, also featured a large excess of IL. Indeed**,** in solvent-free ILs the carbon pores are already filled with the ions almost at the maximum concentration and the double-layer charging process should involve only a redistribution of charges within the pores. On the basis of the carbon mesopore volume of 0.84 $cm^3\ g^{-1}$ and of $PYR_{1(2O1)}TFSI$ density of 1.43 g cm^{-3}, the composite electrode/IL mass ratio can be increased up to 0.83. This was demonstrated by the performance of the CD6 cell which was assembled with a composite electrode/IL mass ratio of 0.7, an almost optimized value, and that featured 340 F upon a 1 A discharge, confirming also in this case the findings obtained with lab-scale cells.

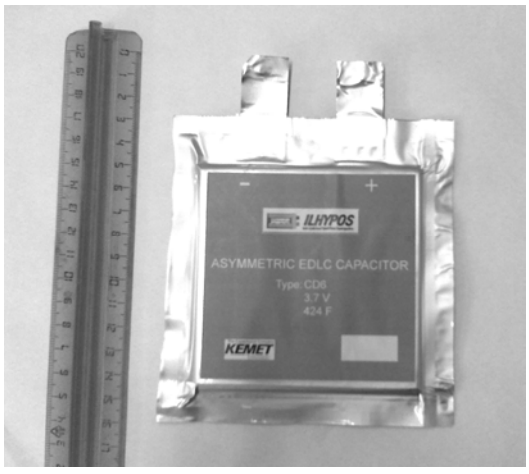

Figure 6.12. $PYR_{1(2O1)}TFSI$ based-AEDLC CD6 cell

The composite electrode/IL mass ratio of the CD6 cell affected the prototype weight which was ca. 66g (Al case excluded) so that the practical cell E_{max} was 11.5 Wh kg^{-1}. While this value approaches the ILHYPOS target of packaged device energy of 15 Wh kg^{-1}, it can be ameliorated by the use of carbon electrodes of increased specific capacitance and moderate pore volume that would prevent electrolyte excess in the electrodes and, thus, be beneficial for the weight component distribution in the modules. Indeed, an increase of 30% in specific capacitance and energy is achievable by the use of the disordered template carbon DTC7. The moderate mesoporous volume of such caron would allow to develop modules with total weight constrained within 2.5-3 time the composite electrode loadings [6.9].

6.5. References

6.1) A. Burke, *Electrochim. Acta* 53 (2007) *1083*.

6.2) C. Arbizzani, M. Biso, D. Cericola, M. Lazzari, F. Soavi, M. Mastragostino, *J. Power Sources* 185 (2008) *1575*.

6.3) M. Lazzari, F. Soavi, M. Mastragostino, *J. Electrochem. Soc.* 156 (2009) *A661*.

6.4) M. Lazzari, M. Mastragostino, F. Soavi, *Electrochem. Commun.* 9 (2007) *1567*.

6.5) S. Baldelli, *J. Phys. Chem. B* 109 (2005) *13049*.

6.6) INEEL, *"FreedomCAR Battery Test Manual For Power-Assist Hybrid Electric Vehicles"*, Prepared for the U.S. Department of Energy (2003).

6.7) INEEL, *"FreedomCAR Ultracapacitor Test Manual"*, Prepared for the U.S. Department of Energy (2004).

6.8) S. G. Stewart, V. Srinivasan, J. Newman, *J. Electrochem. Soc.* 155 (2008) *A664*.

6.9) C. Arbizzani, M. Lazzari, F. Soavi, M. Mastragostino, M. Conte, *ECS Trans.* (2010) in press.

Chapter 7
Conclusions

This thesis work, starting from a basic studies on the ionic liquid (IL) electrolytes and carbon electrodes and concluding with an applied test on large-size IL-based supercapacitor prototypes demonstrated that the IL-based asymmetric configuration (AEDLCs) is a powerful strategy to develop safe, high-energy supercapacitors that might compete with lithium-ion batteries in power assist-hybrid electric vehicles (HEVs).

Among the various ILs investigated the N-methoxyethyl-N-methylpyrrolidinium bis(trifluoromethanesulfonyl)imide ($PYR_{1(2O1)}TFSI$) was selected because of its hydrophobicity and high thermal stability up to 350 °C together with good conductivity and wide ESW, exploitable in a wide temperature range, below 0°C. For such exceptional properties $PYR_{1(2O1)}TFSI$ was used for the whole study to develop large size IL-based carbon supercapacitor prototypes which were developed within the ILHYPOS project.

This work also highlights that the use of ILs as electrolyte determines different chemical-physical properties at the interface electrode/electrolyte with respect to that formed by conventional electrolytes, which are composed of solvents and salts. Indeed, the absence of solvent in ILs makes the properties of the interface not mediated by the solvent and, thus, the dielectric constant and double-layer thickness depend on the chemistry of the IL ions, i.e. on the polarizability of these ions.

The study of carbons as electrode materials in IL-based supercapacitors covers an important part of this work and evidences several factors that have to be taken into account for designing high performing carbon electrodes in IL. The heat-treatment in inert atmosphere of the activated carbon AC which gave ACT carbon featuring ca. 100 F g^{-1} in IL demonstrated that the surface chemistry can significantly modify the capacitive response of the carbon in IL and given that hydrophobic ILs were chosen to guarantee long cycle-life, the surface chemistry of the carbon has to be free by hydrophilic functional groups, such as carboxyl acid. The tailored porosity of the carbon electrodes is a key parameter to achieve high capacitance response. The CO_2-treated xerogel carbon X3a featured a high specific capacitance of 120 F/g in $PYR_{14}TFSI$, however, exhibiting pore

size distribution centred at 15 nm and high pore volume, it was not an optimized carbonaceous material because it needs an excess amount of IL to fill the pores with respect to that required in the charge-discharge process. Further advances were achieved with electrodes based on the disordered template carbon DTC7 with pore size distribution centred at 2.7 nm which featured a notably high specific capacitance of 140 F g^{-1} in $PYR_{14}TFSI$ and a moderate pore volume, $V_{>1.5\ nm}$ of 0.70 $cm^3\ g^{-1}$.

The development of such carbons allowed to assemble high performing double-layer carbon supercapacitors. First, by the asymmetric double-layer carbon configuration (AEDLC) it was possible to exploit the whole and wide electrochemical stability windows (ESWs) of the IL electrolytes and, thus, to reach high cell voltage. Indeed, since the midpoint of the IL's ESW does not correspond to the potential of the discharge carbon electrodes it was necessary to assemble the EDLCs with different carbon loadings at the two electrodes. Several IL-based AEDLCs with high cell voltage higher than 3.5 V and up to 3.9 V were assembled. Thus, IL-based AEDLCs with the X3a or ACT carbon electrodes exhibited specific energy and power of ca. 30 Wh kg^{-1} and 10 kW kg^{-1} (only the loading of both electrodes is considered), respectively. The DTC7 carbon electrodes featuring a capacitance response higher of 20%-40% than those of X3a and ACT, respectively, enabled the development of a $PYR_{14}TFSI$-based AEDLC with specific energy and power of 47 Wh kg^{-1} and 13 kW kg^{-1} at 60°C with V_{max} of 3.9 V. The moderate mesopore volume of DTC7 limits the IL amount in the electrodes and, hence, in the supercapacitor so that specific energy and power values of 16-18 Wh kg^{-1} and 4-5 kW kg^{-1} for a complete cell are feasible. The specific energy value achieved with the DTC7-based AEDLC is 3-4 fold higher than that delivered by the best EDLCs available on the market.

Given the availability of the pristine ACT carbon (obtained from a commercial material) and the good performance of $PYR_{1(2O1)}TFSI$, $PYR_{1(2O1)}TFSI$-based AEDLCs assembled with ACT carbon electrodes were selected in order to develop large-size prototypes. At the laboratory scale the cycling stability of $PYR_{1(2O1)}TFSI$-based AEDLCs was tested at 60°C up to 27,000 cycles with high V_{max} up to 3.8 V. Such AEDLC was further investigated following USABC and DOE FreedomCAR reference protocols for HEV to evaluate its dynamic pulse-power and energy features. This study demonstrated that the $PYR_{1(2O1)}TFSI$-based AEDLC can operate between -30°C and +60°C with a high V_{max} of 3.7. The results showed that at $T \geq 30$ °C the challenging energy and power targets

stated by DOE for power-assist HEVs and at $T \geq 0$ °C the standards for the 12V-TSS and 42V-FSS and TPA 2s-pulse applications are satisfied, if the ratio $w_{module}/w_{SC} = 2$ is accomplished, which, however, is a very demanding condition.

Further improvement in the performance of IL-based AEDLCs could be achieved by lowering ESR by proper design of electrode porosity. Indeed, the main contribution to ESR is electrode charging resistance, which in turn is affected by the ionic resistance in the pores. While the electrode charging resistance depends on IL ionic conductivity, it is also modulated by pore length. Hence, pore geometry is a key parameter in carbon design not only because it defines the carbon surface but also because it can differentially "amplify" the effect of IL conductivity on the electrode charging-discharging process and, thus, supercapacitor time constant.

List of Symbols

A surface-area of the electrodeAC pristine activated carbon from Pica

AEDLC asymmetric electrochemical double layer supercapacitor

ACT heat treated activated carbon from Pica

ACX aero/cryo/xerogel carbons synthesized

C gelation catalyst

C_c space-charge capacitance

C_{diff} capacitance of the diffusion layer

C_{dl} double-layer capacitance

$C_{dl,max}$ the maximum value of double-layer capacitance exhibited at the lowest scan rate.

C_H double-layer capacitance of the Helmholtz compact layer

C_{SC} supercapacitor capacitance

CV cyclic voltammetry

d spacing between the planes in the atomic lattice

D dilution factor

DFT density functional theory

DOD depth of discharge

DOE U.S. Department of Energy

DTC, disordered templated carbon

DTCX disordered templated carbons synthesized

d_{002} interlayer distance between the graphene layers

E specific energy evaluated from the galvanostatic discharges as reported in eq. 6.1

$E_{available}$ specific available energy (energy that can be removed during a 5C discharge over a certain ΔDOD range)

EDLC electrochemical double layer supercapacitor

E_{DOD} the specific cumulative energy removed during the discharge

E_{max} maximum energy delivered between V_{max} and $V_{max}/2$

EMITFSI 1-ethyl-3-methylimidazolium bis(trifluoromethanesulfonyl)imide

ESR equivalent series resistance

ESW electrochemical stability window

EV electric vehicle

F formaldehyde

FTIR-ATR Fourier Transform Infrared – Attenuated Total Reflectance Spectroscopy

HEV hybrid electric vehicle

HPPC Hybrid Pulse Power Characterization

i current density

I_{max} supercapacitor maximum current (that corresponds to the current required to cause an immediate (i.e., <0.1 s) 20 % voltage drop in a fully charged device).

I_{dis} discharge pulse current (25% I_{max} for low-HPPC and 75% I_{max} for high-HPPC)

IHP inner Helmholtz plane

IL ionic liquid

ILHYPOS **I**onic **L**iquid-based **Hy**brid Power **S**upercapacitors (EU project Contract no. TST4-CT-2005-518307).

I_{reg} regenerative pulse current corresponding to 75% I_{dis}

IUPAC International Union of Pure and Applied Chemistry

k_0 vacuu m permittivity 8.85 10^{-12} F m^{-1}

L_a size of the graphene crystals along the a-axis along the graphene plane

L_c size of the graphene crystals along the c-axis normal to the graphene plane

OHP outer Helmholtz plane

OTC order templated carbon

P specific power evaluated from the galvanostatic discharges as reported in eq. 6.2.

P_{dis} specific discharge pulse power capability

PET poly(ethylene terephthalate)

P_{max} maximum power

P_{reg} specific regenerative pulse power capability

PS polystyrene

PSD pore-size distribution

pTFE polytetrafluoroethylene

$PYR_{1(2O1)}$TFSI N-methoxyethyl-N methylpyrrolidinium bis(trifluoromethanesulfonyl)imide

PYR_{14}TFSI N-butyl-N-methyl-pyrrolidinium bis(trifluoromethanesulfonyl)imide

Q specific capacity

R resorcinol

RCT Reference Capacity Test

R_{dis} discharge pulse resistance

R_{reg} regenerative pulse resistance

R_u uncompensed resistance

$R_{+/-}$ positive to negative mass loading ratio

RT Room Temperature

SEM scanning electron microscopy

$S_{>1.5\ nm}$ specific surface area from pores with size in the 1.5 nm – 200 nm range.

TEM transmission electron microscopy

TGA thermogravimetric analysis

TP thermoplastic polymer

$t_{V_{DOD}}$ the time at which the cell exhibits the V_{DOD} voltage

$t_{V_{max}}$ the time at which the cell exhibits V_{max} potential.

$t_{0.55\ V_{max}}$ the time at which the cell exhibits 0.55% of V_{max} potential.

USABC United States Advanced Battery Consortium

V_{DOD} the potential which marks the DOD

V_{max} maximum cell voltage

V_{min} discharge voltage limit (55% V_{max})

V_{tot} total pore volume evaluated at p/p° of 0.995

$V_{>1.5\ nm}$ specific pore volume from pores with size in the 1.5 nm – 200 nm range.

W MilliQ ultrapure water

w_c carbon loading

w_{module} supercapacitor module weight

w_{SC} total composite electrode mass loading of the asymmetric EDLC

w pore size

$\langle w \rangle$ main pore size

δ_{dl} thickness of the double layer

Δt_{pulse} pulse time

ε dielectric constant of the electrical double-layer region

η coulombic efficiency

θ angle between the incident ray and the scattering planes (XRD diffraction)

τ time constant

$Z_{45°}$ impedence region of transmission line

Acknowledgements

First of all, I wish to thank my supervisor, Prof. Marina Mastragostino for the opportunity of pursuing PhD studies and for her scientific support during this thesis project. I also wish to acknowledge Dr. Francesca Soavi for her help and encouragement, which was particularly important when good results were not easy to achieve. Thank to all my collegues of the Laboratorio di Elettrochimica dei Materiali (LEM) of the University of Bologna for their friendship.

Finally, I acknowledge the financial support provided by the European Union within EU ILHYPOS project and all the partners of the project for their collaborations. In particular, I wish to thank Dr. Karl-Heinz Pettinger for the fruitful discussions and collaboration

List of Presentation to Conferences

Supercapacitors operating with ionic liquids
M. Lazzari, F. Soavi, M. Mastragostino,
2007 International Conference on Advanced Capacitors, ICAC 2007, 28-30/05/2007 Kyoto, Japan.

Materiali elettrodici per supercapacitori ibridi operanti con liquidi ionici
M. Biso, M. Lazzari, M. Mastragostino, F. Soavi
Giornate dell'Elettrochimica Italiane – Elettrochimica per il Recupero Ambientale, GEI ERA 2007, 15-20/07/2007 Cagliari, Italia.

Carbon electrodes for supercapacitors operating with ionic liquid electrolytes
M. Lazzari, M. Mastragostino, F. Soavi
The 2nd International Conference – CESEP'07 – Carbon for Energy Storage and Environment Protection, 2-6/09/2007 Krakow, Poland.

Electrode materials for hybrid supercapacitors operating with bis(trifluoromethanesulfonyl)imide based ionic liquid electrolytes
M. Biso, M. Lazzari, F. Soavi, M. Mastragostino
The 58th Annual Meeting of the International Society of Electrochemistry– ISE 2007, 9-14/09/2007 Banff, Canada.

I supercapacitori elettrochimici per il trasporto e applicazioni stazionarie
C. Arbizzani, S. Beninati, M. Biso, L. Damen, M. Lazzari, E. Manferrari, F. Soavi, M. Mastragostino
Convegno storico-scientifico in occasione del 150° dalla nascita – Giacomo Ciamician, genio della chimica e profeta dell'energia solare, 16-18/09/2007 Bologna, Italia.

Ionic Liquids for High Energy Supercapacitors
M. Biso, D. Cericola, M. Lazzari, F. Soavi, M. Mastragostino
Advanced Energy Storage Technologies, Euro Capacitors, 7-8/11/2007 Cologne, Germany.

Supercapacitori a doppio strato a base di liquidi ionici idrofobici
M. Lazzari, F. Soavi, M. Mastragostino
VII Giornata della Chimica dell'Emilia Romagna, 18/01/2008 Modena, Italy.

Polymer and carbon materials in safe, high-energy supercapacitors operating with ionic liquids
C. Arbizzani, M. Lazzari, F. Soavi, M. Mastragostino
Europolymer conference (EUPOC 2008) Advanced Polymeric Materials for the Energy Resources Exploitation: Synthesis, Properties and Application, 1-5/06/2008 Gargnano (BS), Italy.

Ionic liquids for safe, high-energy supercapacitors for transportation
C. Arbizzani, M. Lazzari, M. Mastragostino, F. Soavi
Ionic liquid for electrochemical devices (ILED 2008), 9-11/06/2008 Rome, Italy.

Supercapacitori
Materiali e configurazioni innovative
F. Soavi, M. Lazzari, M. Mastragostino
Giornate dell'Elettrochimica Italiana Elettrochimica per il Recupero Ambientale (GEI ERA 2008), 15-20/06/2008 Genova, Italia.

Safe, high-energy supercapacitors for transportation
C. Arbizzani, M. Lazzari, M. Mastragostino, F. Soavi
The 59th Annual Meeting of the International Society of Electrochemistry– ISE 2008, 7-12/09/2008 Seville, Spain.

Material characteristics for safe, high-energy supercapacitors
C. Arbizzani, M. Lazzari, F. Soavi, M. Mastragostino
The 2nd European Chemistry Congress - ECS - Chemistry: the global science, 16-20/09/2008 Torino, Italy.
Lithium ion batteries and supercapacitors for HEV

M. Mastragostino, C. Arbizzani, S. Beninati, L. Damen, M. Lazzari, F. Soavi
International Workshp on Distributed Energy Systems: The Role of Chemical Sciences and Technologies
04/04/2009, Milan, Italy.

Dynamic Performance of $PYR_{1(2O1)}TFSI$-based Supercapacitor for HEV Application
M. Lazzari, F. Soavi, M. Mastragostino
First International Symposium on Enhanced Electrochemical Capacitors
30/06-02/07/2009, Nantes, France.

Batteries and supercapacitors for renewable energy plants and sustainable transportation
M. Mastragostino, C. Arbizzani, S. Beninati,L. Damen, M. Lazzari, F. Soavi
XXIII Congresso nazionale della Società Chimica Italiana, SCI 2009
05-10/07/2009, Sorrento, Italy.

Ionic liquid-based supercapacitor for HEV application
C. Arbizzani, M. Lazzari, F. Soavi, M. Mastragostino
216th ECS Meeting
04-09/10/2009, Vienna, Austria.

List of Publications

C. Arbizzani, S. Beninati, M. Lazzari, F. Soavi, M. Mastragostino
Electrode materials for ionic liquid-based supercapacitors
J. Power Sources 174 (2007) *648*.

M. Lazzari, M. Mastragostino, F. Soavi
Capacitance response of carbons in solvent-free ionic liquid electrolytes
*Electrochem. Commun.*9 (2007) *1567*.

M. Lazzari, , F. Soavi, M. Mastragostino
High voltage, asymmetric EDLCs based on xerogel carbon and hydrophobic ionic liquids electrolytes
J. Power Sources 178 (2008) *490*.

C. Arbizzani, M. Biso, D. Cericola, M. Lazzari, , F. Soavi, M. Mastragostino
Safe, high-energy supercapacitors based on solvent-free ionic liquid electrolytes
J. Power Sources 185 (2008) *1575*.

M. Lazzari, F. Soavi, M. Mastragostino
Dynamic Pulse Power and Energy of Ionic-Liquid-Based Supercapacitor for HEV Application
J. Electrochem. Soc. 156 (2009) *A661*.

M. Lazzari, F. Soavi, M. Mastragostino
Mesoporous Carbon Design for Ionic Liquid-based, Double-Layer Supercapacitors
Fuel Cells (*Special Issue on Supercapacitors*) submitted November 2009.

Available online at www.sciencedirect.com
ScienceDirect
Journal of Power Sources 174 (2007) 648–652
JOURNAL OF POWER SOURCES
www.elsevier.com/locate/jpowsour

Short communication

Electrode materials for ionic liquid-based supercapacitors

Catia Arbizzani, Sabina Beninati, Mariachiara Lazzari, Francesca Soavi, Marina Mastragostino *

Dipartimento di Scienza dei Metalli, Elettrochimica e Tecniche Chimiche, Via San Donato 15, 40127 Bologna, Italy

Available online 29 June 2007

Abstract

The use of ionic liquid (IL) electrolytes is a promising strategy to enhance the performance of supercapacitors above room temperature. In this paper we present the results of a study on optimization of electrode materials for IL-based supercapacitors featuring a hybrid configuration with carbon negative electrode and poly(3-methylthiophene) (pMeT) as positive operating at 60 °C with the ILs *N*-butyl-*N*-methylpyrrolidinium bis(trifluoromethanesulfonyl)imide ($PYR_{14}TFSI$) and 1-ethyl-3-methyl-imidazolium bis(trifluoromethanesulfonyl)imide (EMITFSI). As it concerns the carbon electrode two routes have been pursued: (i) surface modification of commercial activated carbon and (ii) synthesis of mesoporous cryo- and xerogel carbons. Pore size distribution and electrochemical characterization data are related and suggest that the second route should be the most promising for carbons of high specific capacitance and low time constant in IL. For the polymer electrode the nature of the galvanostatic polymerization bath plays a crucial role to provide pMeT of high specific capacitance and the best results may be obtained when pMeT is electropolymerized in the same IL used for the capacitance tests. The strategy of using the acid additive trifluoromethanesulfonimide in IL-based polymerization baths is also described in some detail. This strategy that provides pMeT featuring more than 200 $F\,g^{-1}$ in IL is a clean procedure which prevents consumption of the ionic liquid with great advantage in terms of costs.

Keywords: Hybrid supercapacitor; Ionic liquid; Activated carbon; Xerogel carbon; Cryogel carbon; Poly(3-methylthiophene)

1. Introduction

Supercapacitors for their high specific power are playing a crucial role in transportation, where they can be coupled with lithium batteries or fuel cells to provide power peaks during acceleration as well as for energy recovery during braking of electric vehicles [1–3]. For this application the typical operating temperature is higher than room temperature (RT). Thus, we pursued the strategy of using ionic liquids (ILs) for their high thermal stability, wide electrochemical stability window and good conductivity at RT as "solvent-free" electrolytes in supercapacitors for electric vehicle applications [4–8]. We already demonstrated the viability of this strategy in hybrid supercapacitors with activated carbon (AC) as the negative electrode and poly(3-methylthiophene) (pMeT) as the positive. When a high purity and hydrophobic IL such as *N*-butyl-*N*-methylpyrrolidinium bis(trifluoromethanesulfonyl)imide ($PYR_{14}TFSI$) was used, at 60 °C the AC/IL/pMeT supercapacitor provided maximum cell voltages higher than 3.4 V and specific energy and power of 18 $Wh\,kg^{-1}$ and 14 $kW\,kg^{-1}$, respectively, as well as long cycling stability over 15,000 cycles [6,8]. These results were achieved with commercial negative and positive electrode materials selected for operation in propylene carbonate (PC)-Et_4NBF_4 and that in the IL $PYR_{14}TFSI$ at 60 °C displayed ca. 50% of the specific capacitance exhibited in the conventional organic electrolyte at RT [9]. We demonstrated that improvements of the AC/IL/pMeT performance are feasible if electrodes materials are properly designed in view of their use in the IL [7,8]. Indeed, an IL-based hybrid supercapacitor with electrode materials of specific capacitance increased up to the values exhibited in PC-Et_4NBF_4 and with an IL electrolyte able to provide maximum cell voltage higher than 3.5 V should deliver specific energy higher than 30 $Wh\,kg^{-1}$ [8].

As it concerns the negative electrode, for a high specific capacitance the carbon has to display a high permeability towards the IL to provide a high surface area for the double-layer charging process and this can be obtained by optimization of carbon pore size and surface chemistry. The size of the pores at least should match that of the counterion involved in the double-

* Corresponding author. Tel.: +39 051 2099798; fax: +39 051 2099365.
E-mail address: marina.mastragostino@unibo.it (M. Mastragostino).

0378-7753/$ – see front matter © 2007 Elsevier B.V. All rights reserved.
doi:10.1016/j.jpowsour.2007.06.162

layer formation, thus it should be wider than 1 nm. Furthermore, hydrophilic moieties on the carbon surface are expected to prevent its permeation by ILs with the hydrophobic character required to provide high cycling stability. Mesoporous cryo- and xerogel carbons are particularly promising as IL-based supercapacitor electrodes for their fundamental properties, such as high and tunable mesoporosity, narrow pore-size distribution, high electrical conductivity, hydrophobic surface, which can be controlled by chemical synthesis conditions [10–13]. With respect to aerogel carbons, cryo- and xerogel carbons are more interesting for practical applications in that the supercritical drying step required for the synthesis of aerogel carbons is substituted by freeze or RT drying with great advantage in terms of cost and safety.

As it concerns the conducting polymer, we have already demonstrated that different polymerization conditions affect the pseudocapacitive behaviour of pMeT in the IL, and particularly the electropolymerization in the same IL used for the capacitance tests provides high performance pMeT electrodes [8,14].

In the present paper we report and discuss the results on the development of materials with morphologies and surface chemistry tailored for operation at 60 °C in the hydrophobic ILs $PYR_{14}TFSI$ and 1-ethyl-3-methyl-imidazolium bis (trifluoromethanesulfonyl)imide (EMITFSI). Data on thermal treated activated carbons and cryo- and xerogel carbons of different mesoporosity and on pMeT electropolymerized in ILs by a galvanostatic technique involving the additive trifluoromethanesulfonimide (HTFSI), which provides a clean electrosynthesis procedure, are reported and discussed.

2. Experimental

The cryogel and xerogel carbons were prepared by polycondensation of resorcinol (R, Riedel de Haen, 99.0–100.5%) and formaldehyde (F, 37% aqueous solution, Aldrich) in MilliQ ultrapure water (W, Milli-Q simplicity system, Millipore Co.) with Na_2CO_3 (C, Riedel de Haen, >99.8%) as gelation catalyst, followed by water/*t*-butanol (Fluka, >99.7%) or water/acetone solvent exchange, freeze or RT drying, respectively, and pyrolysis. The R/F molar ratio was 0.5 and the R/C molar ratio and dilution factor D = W/(R + F + C) were 500 and 5.7 for the CRFB5b cryogel carbon and the CRFC5 xerogel carbon and 800 and 2.5 for the CRFB4 cryogel carbon. The initial pH value was 6.4–6.6 and gelation was performed at 85 °C in sealed vessels for at least 3 days. The pyrolysis step, carried out in a furnace (ZE Muffle Furnace) at 1050 °C (2 h, heating rate 10 K min^{-1}, under moderate flux of Argon, 200 cm^3 min^{-1}), was followed by ball milling.

Nitrogen adsorption porosimetry measurements were carried out at 77 K with an ASAP 2020 system (Micromeritics); the carbon powders were dried for at least 2 h at 120 °C before testing. The total specific surface area (S_{BET}) and pore size distribution in the mesopore region of the carbon powders were evaluated from the analysis of the N_2 adsorption isotherms using the B.E.T. and B.J.H. theories.

The carbon electrodes were prepared with 95% (w/w) carbon (PICACTIF activated carbon or cryo/xerogel carbon, ca. 10–15 mg cm^{-2}) and 5% (w/w) polytetrafluoroethylene binder (Du-Pont); the current collectors were carbon coated aluminum grids (Lamart Corp.). Electrodes with pMeT electropolymerized on Pt or glassy carbon (GC) were prepared galvanostatically in a separate-compartment cell (except in the case of polymerization baths based on IL) with Pt counter electrode in ACN (distilled, Fluka)–0.5 M Et_4NBF_4 (Fluka, dried at 80 °C under dynamic vacuum over night)–0.1 M MeT (Aldrich) or in IL–0.1 M HTFSI–0.2 M MeT. Saturated calomel electrode (SCE) or Ag quasi-reference electrode was used to check the electrode potential. The pMeT electrodes with ca. 4 mg cm^{-2} of polymer were electropolymerized at RT with current density i_e = 10–11 mA cm^{-2} and were galvanostatically undoped with current density $i_u = -0.25 i_e$ in order to evaluate the electrochemical stoichiometry of the electropolymerization and, thus, the amount of pMeT polymerized. The HTFSI (Aldrich) was used as received and MeT (Aldrich) was distilled before use. The $PYR_{14}TFSI$ and EMITFSI ILs were dried over night at 100 °C under dynamic vacuum (Büchi Glass Oven B-580) and displayed ca. 30 ppm of water checked by Karl Fisher titration (684 KF Coulometer Metrohm).

Electrochemical characterization of carbon and pMeT-based electrodes was carried out in dry box (MBraun Labmaster 130, H_2O and O_2 < 1 ppm), using Ag quasi-reference electrode and double-layer carbon counter-electrodes with charge storage capability at least double that of the working electrodes; the cells were kept at the controlled temperature of 60 ± 2 °C by a Thermoblock (FALC). The electrochemical tests were performed with a Perkin-Elmer VMP multichannel potentiostat/galvanostat and a Solartron SI 1255 frequency-response analyzer coupled to a 273A PAR potentiostat/galvanostat. The specific capacitance was evaluated by cyclic voltammetry (CV) at 20 mV s^{-1} and the data were estimated from the slope of the integral over time of the discharge voltammetric current versus electrode potential plot; the maximum electrode potential sweep was −1.9/0.3 V versus Ag and 1.4/−0.5 V versus Ag for the carbon and the polymer electrode, respectively. Impedance spectra were recorded with 5 mV AC perturbation in the frequency range 10 kHz to 10 mHz taking 10 points per decade.

Scanning electron microscopy (SEM) observations were carried out with a ZEISS EVO 50 instrument.

3. Results and discussion

3.1. Carbon negative electrodes

Table 1 and Fig. 1 report some results of the porosity analysis and of the electrochemical characterization of the carbons which we investigated. Table 1 shows the specific surface area (S_{BET}) and the mean pore diameter in the mesopore region (d_{meso}), as well as the specific capacitance in the ILs $PYR_{14}TFSI$ and EMITFSI at 60 °C from CVs of the commercial activated carbon (AC), of the AC carbon treated under Ar atmosphere (200 cm^3 min^{-1}) at 1050 °C for 2 h (ACT) and of the cryo/xerogel carbons CRFB4, CRFC5 and CRFB5b. Fig. 1 shows the specific cumulative surface area in the mesopore region as evaluated from the widest to the smallest pores versus

Table 1
Specific surface area (S_{BET}), mean pore diameter in the mesopore region (d_{meso}) of the carbon powders and specific capacitance from CV at 20 mV s^{-1} in the ILs $PYR_{14}TFSI$ and EMITFSI at 60 °C of the carbon electrodes

Carbon	S_{BET} ($m^2\,g^{-1}$)	d_{meso} (nm)	Specific capacitance ($F\,g^{-1}$)	
			$PYR_{14}TFSI$	EMITFSI
AC	2480	3	50	85
ACT	1960	3	87	107
CRFB4	465	9	–	52
CRFC5	550	15	–	56
CRFB5b	610	20	–	61

pore diameter. The activated carbon AC displays a very high S_{BET} and, as evidenced in Fig. 1, a high mesopore specific surface which corresponds to ca. 45% of S_{BET} and originates from pores with mean diameter of ca. 3 nm. Despite this suitable morphology, with pores large enough to be filled with the ILs, the carbon displays a specific capacitance lower, particularly in $PYR_{14}TFSI$, than the value expected on the basis of the typical capacitance of a clean graphite surface, i.e. 20–30 μF cm^{-2}, thus suggesting that a low percentage of the AC's mesopore area is accessible by the ILs. This could be explained with the presence of surface moieties which often occur in activated carbons as oxygen functional groups (carboxyl, hydroxyl,...) and which repel the two hydrophobic ILs. It has been demonstrated that such functionalities decompose almost quantitatively at 1000 °C under inert gas [15], thus we treated the AC carbon at 1050 °C in Ar atmosphere and we obtained the ACT carbon with a slightly lower surface area and the same percentage of mesopore distribution, but a significantly higher specific capacitance than the AC carbon in both the ILs and such increase was higher in $PYR_{14}TFSI$ than in EMITFSI, as evidenced in Table 1. Thus, such treatment modifies the carbon surface chemistry and increases the compatibility of the ACT carbon with the ILs, providing up to 107 F g^{-1} in EMITFSI. The fact that the AC and ACT carbons display higher specific capacitance in EMITFSI than in $PYR_{14}TFSI$ may be related to the different chemistry of the EMI^+ and $PYR_{14}{}^+$ cations which display not only different steric hindrance but also different polarizability as suggested by the different conductivity at 60 °C of the corresponding EMITFSI and $PYR_{14}TFSI$ ILs of 25 and 6 mS cm^{-1}, respectively [6,7,16]. However, it should be mentioned that the $PYR_{14}TFSI$ features a wider electrochemical stability window than that of EMITFSI [7,17], and this could be an advantage for application in high-voltage supercapacitors.

Given that also in the ACT carbon the main part of the S_{BET} surface is not used for the double-layer charging process, we pursued the strategy of investigating the mesoporous cryo- and xerogel carbons CRFB4, CRFC5, and CRFB5b. In Table 1 their S_{BET} values range from 465 to 610 $m^2\,g^{-1}$ with the 40–50% originating from mesopores centered at 9, 15 and 20 nm and their specific capacitance at 60 °C in EMITFSI is in the range of 50–60 F g^{-1}, corresponding to 20–30 μF cm^{-2} of mesoporous surface area, thus indicating that in these carbons all the mesopore surface is used for the double-layer charging process, and that carbon surface is easily accessed by the IL.

This corresponds also to a low electrode charging resistance which is a very important feature for supercapacitor application as evidenced in Fig. 2 which shows the Nyquist plots recorded in EMITFSI at −1.0 V versus Ag for ACT and CRFB5b electrodes with almost the same amount of carbon. The high frequency

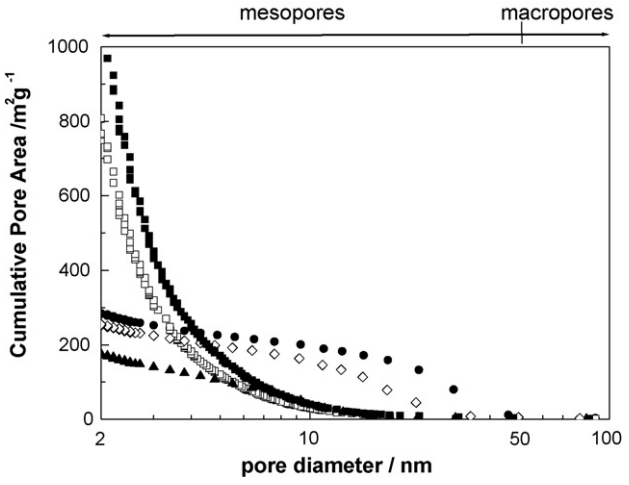

Fig. 1. Specific cumulative pore area vs. mesopore diameter of the (■) AC, (□) ACT, (▲) CRFB4, (◊) CRFC5, and (●) CRFB5b carbons.

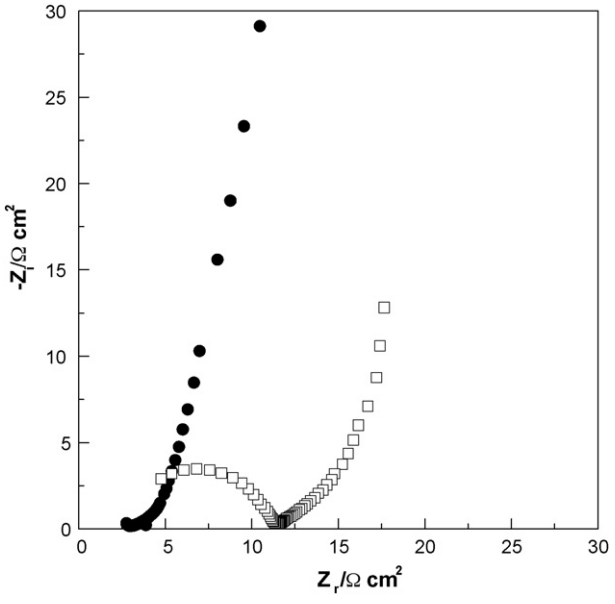

Fig. 2. Nyquist plots recorded in EMITFSI at −1.0 V vs. Ag of (□) ACT and (●) CRFB5b carbon electrodes.

Table 2
Specific capacitance from CV at 20 mV s^{-1} in the ILs $PYR_{14}TFSI$ and EMITFSI at 60 °C of pMeT galvanostatically electropolymerized at RT in different electropolymerization baths (3.3–4.5 mg cm^{-2} of pMeT)

Polymerization bath	Specific capacitance (F g^{-1})	
	$PYR_{14}TFSI$	EMITFSI
ACN-Et_4NBF_4-MeT	135	–
ACN-LiTFSI-MeT	100	135
$PYR_{14}TFSI$-HTFSI-MeT	225	–
EMITFSI-HTFSI-MeT	–	250

semicircle in the spectrum of the ACT carbon, related to electronic and ionic resistances between the smallest mesopores in parallel with the double-layer capacitance of the carbon outer surface, is absent in the CRFB5b's. Thus, work is in progress in our laboratory to synthesize by proper selection of the gelation bath composition cryo/xerogel carbons with mesoporous surface $\geq 500\,F\,g^{-1}$, which should outperform activated carbons providing $100\,F\,g^{-1}$ at a lower time constant.

3.2. Polymer positive electrodes

Table 2 reports the specific capacitance values in the two ILs at 60 °C of pMeT galvanostatically polymerized in different electropolymerization baths. Table 2 evidences that the substitution of ACN-based polymerization bath with those based on the same ILs used for the following capacitance tests provides specific capacitance values higher than $200\,F\,g^{-1}$. Particularly, the values of 225 and $250\,F\,g^{-1}$ are obtained with $PYR_{14}TFSI$ and EMITFSI electrolytes, respectively. This can be related to the different morphology exhibited by pMeT when the ACN-based bath is substituted by that with the IL, as evidenced in Fig. 3, which reports the SEM images of pMeT electropolymerized in ACN-LiTFSI and in $PYR_{14}TFSI$. Table 2 evidences that

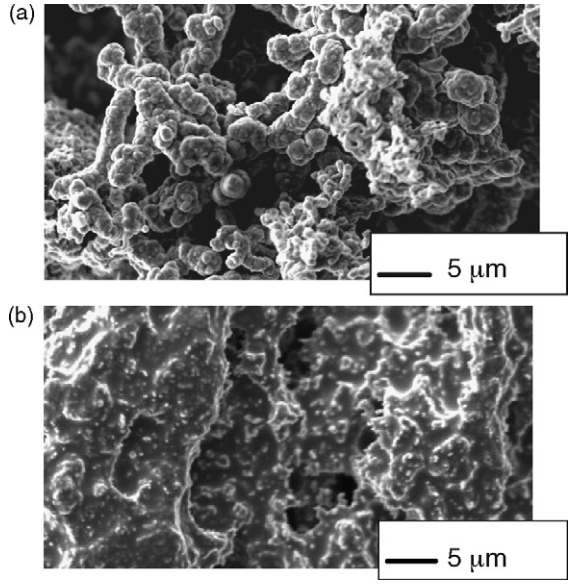

Fig. 3. SEM images of pMeT electropolymerized in (a) ACN-LiTFSI-MeT and in (b) $PYR_{14}TFSI$-HTFSI-MeT.

also in the case of the polymer electrodes the highest specific capacitance values are obtained with the EMITFSI IL.

The main drawback with galvanostatic preparation of large quantities of polymer in ILs is the formation of byproducts at the counter electrode which typically poison the polymerization bath. Thus, to control the cathodic reaction we pursued the strategy to add the acid HTFSI which dissociates to give the same anion $TFSI^-$ of the IL and the proton which in turn gives H_2 at the counter electrode while anodic polymerization takes place at the working. This clean procedure which does not modify the chemistry of the electrosynthesis solution is described by the following overall electrochemical reaction in which a stoichiometry of $2.3\,F\,mol^{-1}$ of polymerized MeT monomer unit ($CH_3C_4H_3S$) is considered:

$$0.3n\mathrm{HTFSI} + n\mathrm{CH_3C_4H_3S} \rightarrow (CH_3C_4HS^{0.3+}\mathrm{TFSI}_{0.3}{}^-)_n + 1.15n\mathrm{H_2} \quad (1)$$

From this stoichiometry 0.3 mol of HTFSI per mol of polymerized monomer unit provide that the IL is not consumed because they supply the required amount of the p-doping anion $TFSI^-$ and the protons which are reduced to H_2 along with those delivered by the polymerization reaction (2 mol of H^+ per mol of polymerized monomer unit) [14].

Fig. 4 reports the voltage profiles of the working and counter electrodes upon the galvanostatic electropolymerization of pMeT and the undoping process in $PYR_{14}TFSI$-HTFSI-MeT at RT (stirred solution) from which an electrochemical stoichiometry of $2.28\,F\,mol^{-1}$ of polymerized monomer unit has been evaluated. During polymerization the potentials of the working and counter electrode are quite stable at ca. 1.5 and −0.3 V versus Ag, respectively, which correspond to the monomer oxidation and the H^+ reduction as evidenced by Fig. 5 which displays the first linear sweep voltammetries at 20 mV s^{-1} and RT of a Pt electrode in $PYR_{14}TFSI$, $PYR_{14}TFSI$-HTFSI and $PYR_{14}TFSI$-HTFSI-MeT. Therefore, the pMeT polymerization at the working electrode is balanced by the reduction of the acid proton of HTFSI at the counter electrode. This novel galvanostatic polymerization procedure, which can be extended to prepare other polymers in ILs, does not waste the IL offering great advantage in terms of costs.

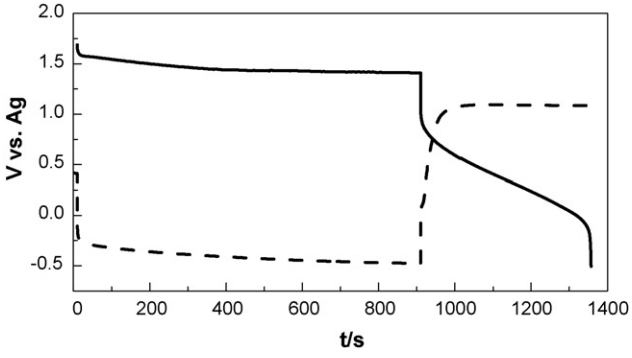

Fig. 4. Voltage profiles of the working electrode (GC, solid line) and the counter electrode (Pt, dashed line) upon the galvanostatic electropolymerization of pMeT at 11.3 mA cm^{-2} and the undoping process at −2.8 mA cm^{-2} in $PYR_{14}TFSI$-HTFSI-MeT at RT.

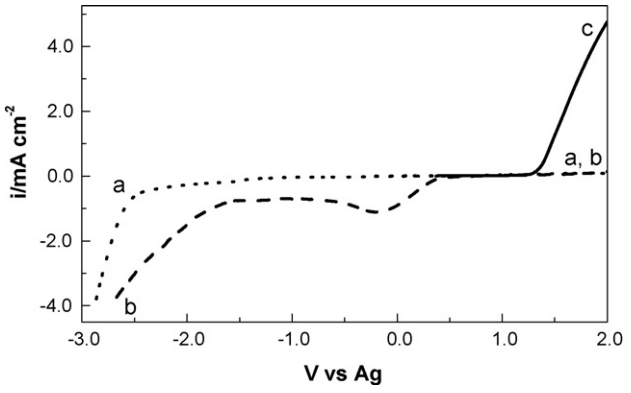

Fig. 5. Linear sweep voltammetries at 20 mV s^{-1} and RT of a Pt electrode in (a) $PYR_{14}TFSI$, in (b) $PYR_{14}TFSI$-HTFSI and (c) $PYR_{14}TFSI$-HTFSI-MeT.

4. Conclusions

With this study we have identified some routes to optimize electrode materials for hybrid supercapacitor with hydrophobic IL electrolytes and, following such routes, we have developed carbon and polymer electrode materials featuring at 60 °C up to 107 and 250 F g^{-1} in EMITFSI and 87 and 225 F g^{-1} in $PYR_{14}TFSI$, respectively. Thermal treatment at 1050 °C in Ar atmosphere of activated carbons removes/modifies the surface moieties generally present in such carbons and allows a better permeability by each IL, thus increasing the accessible surface for the double-layer charging process. A more promising strategy should be the development of cryo/xerogel carbons of mesopore specific surface area > 500 m^2 g^{-1}, which should display at least 100 F g^{-1} on the basis of the values of 20–30 μF cm^{-2} of mesoporous surface featured by the CRFB4, CRFC5, and CRFB5b carbons, with a low electrode charging resistance. As it concerns the polymer electrode, the novel galvanostatic polymerization in IL involving the acid additive HTFSI is a clean procedure which yields pMeT featuring 225 and 250 F g^{-1} in $PYR_{14}TFSI$ and EMITFSI ILs, with advantage in terms of costs because the IL is not wasted by counter electrode reaction nor consumed to balance the pMeT p-doping charge.

Acknowledgements

Research funded by ILHYPOS UE Project (TST4-CT-2005-518307, Contract Number 518307). ENEA-IDROCOMB (Casaccia, Italy) and Degussa-Creavis Technologies & Innovation (Marl, Germany) are acknowledged for providing the $PYR_{14}TFSI$ and EMITFSI ILs, respectively.

References

[1] A. Chu, P. Braatz, J. Power Sources 112 (2002) 236.
[2] P. Rodatz, G. Paganelli, A. Sciarretta, L. Guzzella, Con. Eng. Prac. 13 (2005) 41.
[3] R.J. Brodd, K.R. Bullock, R.A. Leising, R.L. Middaugh, J.R. Miller, E. Takeuchi, J. Electrochem. Soc. 151 (2004) K1.
[4] D. Adam, Nature 407 (2000) 938.
[5] A. Balducci, U. Bardi, S. Caporali, M. Mastragostino, F. Soavi, Electrochem. Commun. 6 (2004) 566.
[6] A. Balducci, W.A. Henderson, M. Mastragostino, S. Passerini, P. Simon, F. Soavi, Electrochim. Acta 50 (2005) 2233–2237.
[7] A. Balducci, F. Soavi, M. Mastragostino, Appl. Phys. A 82 (2006) 627–632.
[8] C. Arbizzani, A. Balducci, M. Mastragostino, S. Passerini, P. Simon, F. Soavi, ECS Trans. 1 (2006) 55–59.
[9] A. Laforgue, P. Simon, J.F. Fauvarque, M. Mastragostino, F. Soavi, J.F. Sarrau, P. Lailler, M. Conte, E. Rossi, S. Saguatti, J. Electrochem. Soc. 150 (2003) A645–A651.
[10] S.A. Al-Muhtaseb, J. Ritter, Adv. Mater. 15 (2003) 101–114.
[12] E. Frackowiak, F. Beguin, Carbon 39 (2001) 937–950.
[13] A.G. Pandolfo, A.F. Hollenkamp, J. Power Sources 157 (2006) 11–27.
[14] C. Arbizzani, F. Soavi, M. Mastragostino, J. Power Sources 162 (2006) 735–737.
[15] H.P. Boehm, Carbon 32 (1994) 759–769.
[16] A.B. McEwen, H.L. Ngo, K. LeCompte, J.L. Goldman, J. Electrochem. Soc. 146 (1999) 1687–1695.
[17] H. Sakaebe, H. Matsumoto, Electrochem. Commun. 5 (2003) 594–598.

Available online at www.sciencedirect.com
ScienceDirect
Electrochemistry Communications 9 (2007) 1567–1572
electrochemistry communications
www.elsevier.com/locate/elecom

Capacitance response of carbons in solvent-free ionic liquid electrolytes

Mariachiara Lazzari, Marina Mastragostino *, Francesca Soavi

Dipartimento di Scienza dei Metalli, Elettrochimica e Tecniche Chimiche, Via San Donato 15, 40127 Bologna, Italy

Received 5 February 2007; received in revised form 19 February 2007; accepted 21 February 2007
Available online 1 March 2007

Abstract

Ionic liquids (IL) are very promising "solvent-free" electrolytes for high-voltage double-layer supercapacitors (EDLCs) and to this purpose they are generally selected on the basis of their bulk properties, such as electrochemical stability and ion conductivity, without taking into account those of the electrified electrode-IL interface. This interface, which has yet to be well characterized, has features that notably affect electrode capacitance, and our paper for the first time highlights the importance of the molecular chemistry and structure of the ions for the double-layer capacitive response of carbonaceous electrodes in IL. The double-layer capacitive responses of negatively charged electrodes based on activated carbons and aero/cryo/xerogel carbons in two ILs featuring the same anion and different cations of almost the same size, i.e. the *N*-butyl-*N*-methylpyrrolidinium bis(trifluoromethanesulfonyl)imide ($PYR_{14}TFSI$) and 1-ethyl-3-methyl-imidazolium bis(trifluoromethanesulfonyl)imide (EMITFSI) are reported. The porosity, structure and surface chemistry of the carbons are compared to their capacitive response to evince the role played by these carbon properties and by the chemistry and structure of the IL ions in the electric double-layer.

Keywords: Ionic liquid; Interface; Double layer; Supercapacitor; Carbon capacitance; Ion structure

1. Introduction

Supercapacitors are becoming increasingly important as an intermittent power supply as well as for load levelling and energy storage in fields ranging from distributed energy grids to domestic and transport applications [1–3]. Double-layer supercapacitors featuring high surface-area carbon electrodes (EDLC) that are electrostatically charged by separation of charge at the electrode/electrolyte solution interface are the most advanced and are already on the market. High maximum energy $E_{max} = 1/2 C_{EDLC} V^2$ and power $P_{max} = 1/4\ V^2/R$ are reached by maximizing electrode double-layer capacitances (C_e, which are double the EDLC's capacitance C_{EDLC}) and cell voltage (V) and by minimizing the equivalent series resistance (R). This is where "solvent-free" ionic liquid electrolytes come in because they can feature the wide electrochemical stability window and high ionic conductivity that are crucial to the design of high-performance supercapacitors [4–9]. The electrified electrode-IL interface has properties that notably affect electrode capacitance but has yet to be well characterized. Indeed, IL selection for EDLC application is made solely on the basis of IL electrochemical stability and ion conductivity.

The electrode–electrolyte interface models developed for high-temperature molten salts are not completely appropriate for ILs mainly because of the weaker cation-anion interactions in ILs than in molten salts [10–13]. On the other hand, the absence of solvent in ILs precludes the use of the Helmholtz model developed for concentrated electrolyte solutions, where solvent molecules in IHP separate electrode surface charges and electrolyte counterions in OHP by a distance l and solvent molecular size, rather than ion size, and solvent dielectric constant (ε, lower than in the bulk) significantly affect electrode

* Corresponding author. Tel.: +39 051 2099798; fax: +39 051 2099365.
E-mail address: marina.mastragostino@unibo.it (M. Mastragostino).

1388-2481/$ - see front matter © 2007 Elsevier B.V. All rights reserved.
doi:10.1016/j.elecom.2007.02.021

capacitance, given that $C_e = k^0 \varepsilon A/l$, where $k^0 = 8.85 \times 10^{-12}$ F m^{-1} and A is the electrode surface area [10]. If, however, for IL we take a Helmoltz model with the counterions in the IHP, as very recently proposed by Baldelli for the Pt–IL interface on the basis of SFG spectroscopy, electrochemical impedance and CO vibrational Stark effect [14,15], the relation between C_e and A should depend, and perhaps strongly, on ion chemistry and structure at the electrode–IL interface.

For high EDLC capacitance the carbon electrodes should display a high specific surface area that can easily be accessed by the electrolyte; carbon porosity and surface chemistry are thus of primary importance. The carbons should display a high pore volume and pores at least wider than the size of the counterions, although pore walls should be thicker than the screening length of the electric field in the solid part of the double layer so as not to limit the charge accommodation on the two sides of the carbon walls [7,16,17]. Thus, mesoporous aero/cryo and xerogel carbons with pore size and pore-wall thickness that can be controlled by chemical synthesis conditions should be particularly promising electrode materials for EDLCs, which are generally based on activated carbons [3,18,19]. Functional groups are also important because they affect the electronic properties of the carbon itself and its surface polarizability and can attract–repel the ions with different effects on carbon wettability. Surface moieties may also be responsible for faradaic processes that are detrimental to the long cycle-life required by EDLCs.

We report the double-layer capacitive response of negatively charged electrodes based on activated carbons and aero/cryo/xerogel carbons in two ILs featuring the same anion and different cations of almost the same size, i.e. the 1-ethyl-3-methyl-imidazolium bis(trifluoromethanesulfonyl)imide (EMITFSI) and *N*-butyl-*N*-methylpyrrolidinium bis(trifluoromethanesulfonyl)imide ($PYR_{14}TFSI$) ILs (Scheme 1). The porosity, structure and surface chemistry of the carbons are compared to their capacitive response to highlight the role played by the chemistry and structure of the IL ions in the electric double-layer.

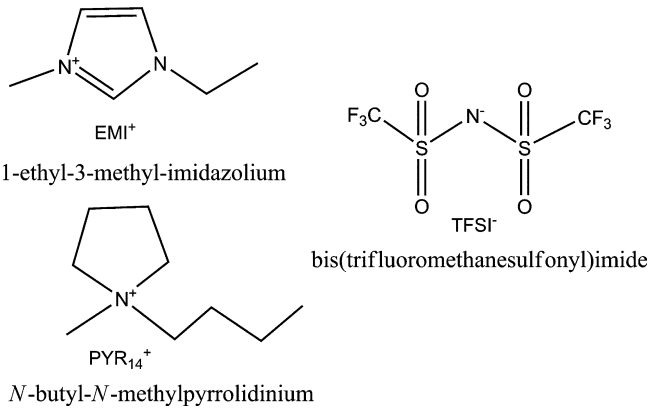

Scheme 1.

2. Experimental

The cryogel and xerogel carbons were prepared by polycondensation of resorcinol and formaldehyde with Na_2CO_3 as gelation catalyst in different molar ratios, followed by solvent exchange, freeze or RT drying, respectively, and pyrolysis at 1050 °C in Ar as in Ref. [20]. The aerogel carbon A1 was purchased from Marketech; the activated carbons were the pristine PICACTIF from Pica (AC) and the same carbon treated at 1050 °C in Ar for 2 h in order to remove surface moieties (ACT). FTIR spectra in reflectance mode (FTIR-ATR) were collected by a Perkin Elmer Spectrometer Spectrum ONE (FTIR-ATR) with 40 scans and 4 cm^{-1} resolution.

Nitrogen adsorption porosimetry measurements were carried out at 77 K with an ASAP 2020 system (Micromeritics); the carbon powders were dried for at least 2 h at 120 °C before testing. The N_2 adsorption isotherms were analyzed by the density functional theory (DFT) and the Barrett, Joyner and Halenda model (B.J.H., Harkins and Jura as thickness curve with Faas correction factor); the total pore volume (V_{tot}) was evaluated by the quantity of N_2 adsorbed at 77 K and $p/p^\circ = 0.995$. The DFT theory is the best for the analyses of the isotherms of micro-mesoporous carbons, and it is generally applied with the assumption of a slit-pore geometry [21]. However, this assumption may be not adequate for disordered carbons such as those we investigated, thus the mesoporous surface is here evaluated by the BJH model, which well fits data in the mesopore size range, assuming a cylinder pore geometry.

The carbon electrodes (0.64 cm^2 geometric area, 10–15 mg cm^{-2} carbon loading) were prepared by mixing 95% w/w carbon and 5% w/w polytetrafluoroethylene binder (Du-Pont) to yield a pasta which was then laminated on carbon coated aluminum grids (Lamart Corp.). The $PYR_{14}TFSI$ (ENEA-IDROCOMB) and EMITFSI (Solvent innovation) ILs were dried over night at 100 °C under dynamic vacuum (Büchi Glass Oven B-580) and displayed ca. 30 ppm of water checked by Karl Fisher titration (684 KF Coulometer Metrohm).

The voltammetric tests were carried out in dry box (MBraun Labmaster 130, H_2O and $O_2 < 1$ ppm) in T Swagelok-type cells using Ag quasi-reference electrode and double-layer carbon counter-electrodes with charge storage capability at least double that of the working electrodes; the cells were kept at the controlled temperature of 60 ± 2 °C by a Thermoblock (FALC). The electrochemical tests were performed with a Perkin–Elmer VMP multichannel potentiostat/galvanostat. The specific capacitance was evaluated by CV at 20 mV s^{-1} and in the electrode potential range −1.9/0.0 V vs. Ag.

Electronic resistivities of the carbon composite films were measured via four point technique by a Jandel multiheight probe.

X-ray diffraction measurements (XRD) were performed with a Philips X'Pert diffractometer, a Cu Kα($\lambda =$

1.5406 Å) radiation source and Ni filter by step-scanning mode (0.05° 2θ step; 5×10^{-2}° $2\theta\ s^{-1}$ scan rate). The size of the graphene crystals along the *c*-axis (L_c, normal to the graphene plane) and the *a*-axis (L_a, along the graphene plane) was evaluated from the half height width β of the reflexes (002) and (100) by the equation $L = k\lambda/\beta\cos\theta$, where $\lambda = 1.54$ nm and $k = 0.94$ for L_c and 1.84 for L_a [22].

The Raman spectra were recorded by a Raman Microscope RENISHAW Mod. INVIA, with Argon ion laser ($\lambda = 514$ nm, 5% of 300 mW full power, 4 scans, 10 s per scan, 2 cm^{-1} resolution, magnification 50×); the D1 and G band intensity ratios (I_{D1}/I_G) were averaged over the data obtained with different spectra collected on different parts of each sample.

3. Results and discussion

The investigated carbons, which were selected on the basis of their different nature and, mainly, different mesoporosity, were the C1 and C2 cryogel, the X1 xerogel, the A1 aerogel carbon and the activated carbon AC pristine and treated at 1050 °C in Ar for 2 h (ACT). This treatment removes surface moieties like oxygen and nitrogen functional groups, which often occur in activated carbons and repel hydrophobic ILs such as the EMITFSI and $PYR_{14}TFSI$, with a negative effect on the capacitive response of the carbon [23]. Indeed, Fig. 1 reports the FTIR-ATR spectra of the AC and ACT carbons and shows that the intensity of the bands of C═O at 1760 and 1570 cm^{-1}, and of CO_2 (chemiadsorbed on the surface) at 2340 cm^{-1} decrease after heat treatment [24].

Fig. 2a shows the N_2 adsorption–desorption isotherms of the aero/cryo/xerogel carbons and of the pristine and thermal-treated activated carbons. The isotherms are of type IV [21] and show that the heat treatment does not modify the porosity of the AC carbon, which exhibits a significantly higher micropore volume than C1, C2 and X1. Fig. 2b reports for the different carbons the trend of the differential specific pore volume (dV/dw) vs. pore width (w) calculated by the DFT theory, and shows that all the investigated carbons feature pores sufficiently wide to be filled

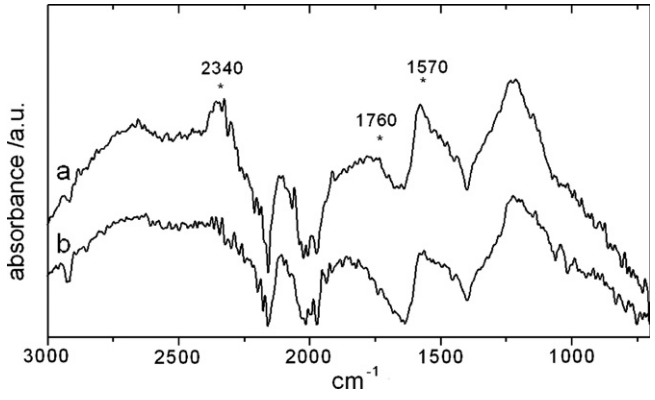

Fig. 1. FTIR-ATR spectra of (a) AC and (b) ACT carbons.

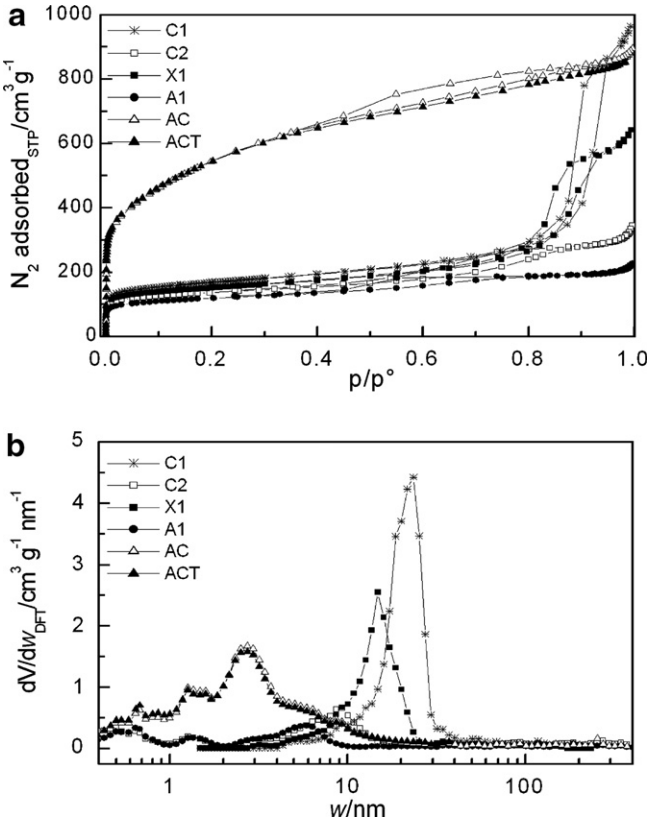

Fig. 2. (a) N_2 adsorption-desorption isotherms and (b) DFT specific differential pore volume vs. pore size of the C1, C2, X1, A1, AC, and ACT carbons.

with the IL ions. Indeed, pore-size distribution is centered at 2.7, 6, 9, 15 and 23 nm for the AC, A1, C2, X1 and C1 carbons, respectively; Table 1 shows the total pore volume (V_{tot}) and the mesoporous specific volume (V_{BJH}) and surface area (S_{BJH}) from the BJH model. The table also reports the double-layer capacitance responses of negatively polarized composite electrodes in the EMITFSI and $PYR_{14}TFSI$ ILs at 60 °C, as evaluated by the slope of the integral over time of the discharge voltammetric current vs. electrode potential plot. As an example, Fig. 3 reports the CVs of the C1 and ACT carbons (coulombic efficiency $\geqslant$99%) in terms of specific current and differential capacitance, the latter obtained by dividing the specific current by the scan rate.

The main result in Table 1 is that at 60 °C each carbon displays ca. double the specific capacitance in EMITFSI than in $PYR_{14}TFSI$. This can not be explained by a different accessible surface area of the carbons for the double-layer formation in the two ILs. Indeed, the maximum size of the EMI^+ and PYR_{14}^+ counterions involved in the double-layer is not very different: they are less than 1 nm wide [25,26] and all the examined carbons display pore-size distributions centered at values wider than 2 nm. The cause of the different capacitance in the two ILs is thus to be found in the different dielectric constant and thickness of the double-layer, which are related to the different properties

Table 1
Total pore volume (V_{tot}), BJH mesoporous specific volume (V_{BJH}) and surface area (S_{BJH}) of the carbon powders and specific capacitance of the carbon electrodes from CVs at 60 °C in EMITFSI and $PYR_{14}TFSI$

Carbons	V_{total} ($cm^3\ g^{-1}$)	V_{BJH} ($cm^3\ g^{-1}$)	S_{BJH} ($m^2\ g^{-1}$)	Specific capacitance ($F\ g^{-1}$)	
				EMITFSI	$PYR_{14}TFSI$
A1	0.36	0.19	170	52	23
C2	0.47	0.29	190	52	23
X1	0.99	0.78	255	56	33
C1	1.49	1.25	285	61	36
AC	1.38	0.66	845	85	50
ACT	1.34	0.63	810	107	87

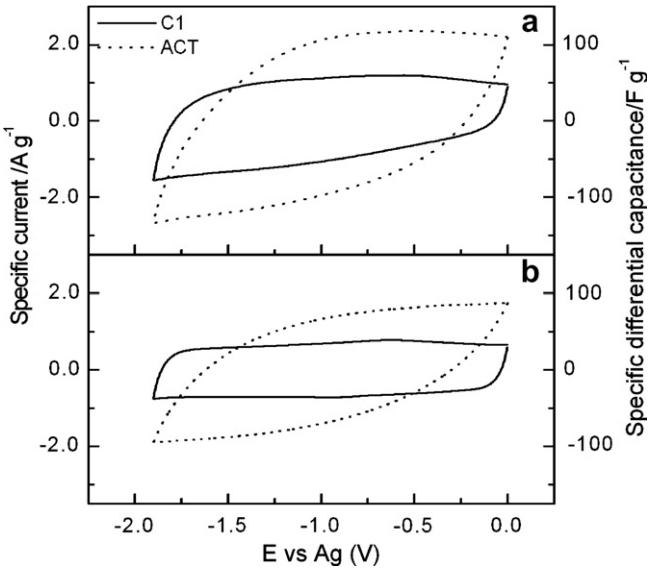

Fig. 3. Cyclic voltammetries of the C1 and ACT carbon electrodes at 20 mV s^{-1} and 60 °C in (a) EMITFSI and (b) $PYR_{14}TFSI$.

of EMITFSI and $PYR_{14}TFSI$ at the interface. Given that the ILs feature the same anion and different cations, the different capacitance responses are arguably related to the different polarizability and structure of the EMI^+ and PYR_{14}^+ counterions, thus suggesting that in the double-layer of negatively charged carbons the IL cations occupy the IHP.

While unambiguous values of dielectric constant at the interface of the two cations are not available [15,27–30], EMI^+ can be termed a *soft* cation with the positive electric charge delocalized in the imidazolium ring and a dipole moment presumably higher than that of the PYR_{14}^+, which features the electric charge in the sp^3 nitrogen atom and can thus be considered as a relatively *hard* cation. Consequently, the former should provide higher dielectric constant in the double-layer than the latter with a positive effect on the electrode capacitance. These considerations are well supported by the different bulk properties of EMITFSI and $PYR_{14}TFSI$ like viscosity, conductivity and normalized solvent polarity as well as by molecular dynamics studies [4,31]. Indeed, the viscosity and ionic resistivity at 25 °C of $PYR_{14}TFSI$, i.e. 85 mPa s and $5 \times 10^2\ \Omega$ cm [4], are higher than EMITFSI's, i.e. 34 mPa s and $1 \times 10^2\ \Omega$ cm [4], because of the higher cation–anion interactions in the former than in the latter, which in turn depend on the different polarizability of the cations and affect the different polarizability of the bulk IL.

In effect, the normalized solvent polarity E_T^N (defined on the basis of the 2,6-diphenyl-4-(2,4,6-triphenylpyridinium-1-yl)phenolate betaine solvatochromism in different solvents, with $E_T^N = 0$ for TMS and 1 for water) of $PYR_{14}TFSI$ (0.544) is lower than EMITFSI's (0.676) [32]. According to the E_T^N data, $PYR_{14}TFSI$ displays a lower affinity than EMITFSI towards the betaine dye, which is a large polarizable aromatic π electron system with a weak electron pair acceptor (the positively charged nitrogen atom) and a strong electron pair donor (the negatively charged oxygen ion) and, hence, well mimics the negatively charged carbon. This means that IL polarizability may also affect the double-layer thickness at the carbonaceous electrode.

The orientation of the IL cation under the applied electric field and its stereochemistry are also important for double-layer thickness. Conformational studies by spectroscopy proved that in imidazolium-based ILs the plane of the imidazolium ring is normal to the surface [33,34] and twists towards it when this latter becomes even more negatively polarized [12]. By contrast, it can be expected that the reorientation of the PYR_{14}^+ under the electric field is hindered both because of the strong interaction of the cation with the $TFSI^-$ anion and the steric hindrance of its alkyl groups [35]. Thus, the double-layer thickness l is wider in $PYR_{14}TFSI$ than in EMITFSI, and the electrode specific capacitance is lower in the former than in the latter.

The varying response of different carbons in the same IL is notable. Table 1 shows that when carbon materials of the same type are examined, such as the aero/cryo/xerogel carbons that are prepared by the same precursors with similar treatments (pyrolysis in inert atmosphere at high temperature) and that should exhibit the same surface chemistry, the specific capacitance increases with the carbon mesoporous specific surface. This trend is more marked for $PYR_{14}TFSI$. The highest specific capacitance for aero/cryo/xerogel carbons was displayed by C1, which featured 61 $F\ g^{-1}$ in EMITFSI and 36 $F\ g^{-1}$ in $PYR_{14}TFSI$. Significantly higher values were reached with the AC and ACT activated carbons, which respectively showed 85 and 107 Fg^{-1} in EMITFSI and 50 and 87 Fg^{-1} in

$PYR_{14}TFSI$, respectively. However, these values are not that high when compared to the mesoporous surface area of the AC and ACT activated carbons, which is three-fold higher than C1's. This shows that the nature and surface chemistry of the carbon plays a crucial role in its capacitive response, as also evinced by the fact that in both ILs the specific capacitance of the heat-treated ACT carbon is significantly higher than that of the pristine AC, which exhibits almost the same S_{BJH} as the former. This difference can be explained by the fact that the heat treatment partially removes hydrophilic moieties from the AC carbon, thus providing a better carbon permeation with the hydrophobic IL and, consequently, a higher accessible surface area for the double-layer charging process.

The removal of electron-withdrawing groups such as C=O also results in a higher delocalization of the electron in the carbon, with a positive effect both on specific capacitance and electronic resistance. Indeed, the composite electrode material based on ACT carbon displayed an electronic resistance of 5 Ω cm, which is lower than that of the AC carbon composite (8 Ω cm), and this is not related to a higher graphitization of the former, as demonstrated by the XRD and Raman spectroscopy investigations. The XRD spectra showed that all the investigated carbons (ACT, AC, C2, A1 and C1) are quite disordered and made by small graphene crystallites having a few (2–3) graphene layers with an interlayer distance (d_{002}) of 0.38 nm and 3.0–3.6 nm wide (L_a). These findings are in agreement with the results of the Raman spectroscopy, which indicated that the C1, C2, AC and ACT carbons feature almost the same microcrystalline structure. Indeed, the I_{D1}/I_G height ratio of the bands D1, attributed to graphene layer edges, and G, corresponding to the in-plane vibrational mode of surface graphene layers [36], is in the range 0.90–1.09. For the ACT carbon the I_{D1}/I_{G1} value is 1.09 and slightly higher than the AC's (of 0.97) and this is not due to different graphitization but, rather, can be ascribed to the increase of non-functionalized graphene edges occurring after the heat treatment. This treatment removes the surface moieties that are anchored on the AC graphite borders and promotes the in-plane electric contact among the carbon particles.

4. Conclusions

The main result of our study is that for the first time the importance of ion chemistry and structure for the capacitive response of carbonaceous electrodes in ILs is reported. Indeed, up to now only the carbon surface accessible by the electrolyte and the bulk properties of the IL, rather than the interface properties, have been considered in materials selection for high capacitance IL-based EDLCs. We demonstrate that the double-layer capacitance of negatively charged carbon electrodes is strongly determined by the cation polarizability, which affects the dielectric constant in the double-layer as well as double-layer thickness, which in turn also depends on the preferred orientation of the cation under the applied electric field. This suggests that the double-layer is constituted by a monolayer of cations up against the negatively charged carbon surface. Our data also demonstrate the importance of carbon porosity and surface chemistry in the double-layer capacitive response. Indeed, surface moieties affect the carbon's electrochemically accessible surface area and, more importantly, its electronic conductivity and polarizability. In fact, given the intimate contact of the carbon with the IL counterion, this latter property is particularly important for the capacitive response of the electrode in IL. Our study thus contributes to a better understanding of the properties of the electrified carbon-IL interface by providing insight not only into IL-based EDLCs but also into other IL-based electrochemical cells.

Acknowledgements

Dr. S. Passerini (ENEA-IDROCOMB, Casaccia, Italy) is acknowledged for providing the $PYR_{14}TFSI$ IL under the frame of the ILHYPOS UE Project (TST4-CT-2005-518307, Contract Number 518307).

References

[1] A.S. Aricò, P. Bruce, B. Scrosati, J.-M. Tarascon, W. Van Schalkwijk, Nature Mater. 4 (2005) 366.
[2] R. Kötz, M. Carlen, Electrochim. Acta 45 (2000) 2483.
[3] A.G. Pandolfo, A.F. Hollenkamp, J. Power Sources 157 (2006) 11.
[4] M. Galiński, A. Lewandowski, I. Stępniak, Electrochim. Acta 51 (2006) 5567.
[5] M. Ue, M. Takeda, A. Toriumi, A. Kominato, R. Hagiwara, Y. Ito, J. Electrochem. Soc. 150 (2003) A499.
[6] A. Lewandowski, M. Galinski, J. Phys. Chem. Solids 65 (2004) 281.
[7] C.O. Ania, J. Pernak, F. Stefaniak, E. Raymundo-Pinero, F. Beguin, Carbon 44 (2006) 3126.
[8] A. Balducci, U. Bardi, S. Caporali, M. Mastragostino, F. Soavi, Electrochem. Commun. 6 (2004) 566.
[9] A. Balducci, W.A. Henderson, M. Mastragostino, S. Passerini, P. Simon, F. Soavi, Electrochim. Acta 50 (2005) 2233.
[10] B.E. Conway, Electrochemical Supercapacitors, Kluwer Academic/Plenum, New York, 1999.
[11] C. Nanjundiah, S.F. McDevitt, V.R. Koch, J. Electrochem. Soc. 144 (1997) 3392.
[12] N. Nanbu, Y. Sasaki, F. Kitamura, Electrochem. Commun. 5 (2003) 383.
[13] O.J. Lanning, P.A. Madden, J. Phys. Chem. B 108 (2004) 11069.
[14] S. Riveira-Rubero, S. Baldelli, J. Phys. Chem. B 108 (2004) 15133.
[15] S. Baldelli, J. Phys. Chem. B 109 (2005) 13049.
[16] M. Hahn, M. Baertschi, O. Barbieri, J.C. Sauter, R. Kötz, R. Gallay, Electrochem. Solid-State Lett. 7 (2004) A33.
[17] O. Barbieri, M. Hahn, A. Herzog, R. Kötz, Carbon 43 (2005) 1303.
[18] S.A. Al-Muhtaseb, J. Ritter, Adv. Mater. 15 (2003) 101.
[19] E. Frackowiak, F. Beguin, Carbon 39 (2001) 937.
[20] C. Arbizzani, S. Beninati, M. Lazzari, F. Soavi, M. Mastragostino, J. Power Sources, in press.
[21] P.A. Webb, C. Orr, Analytical Methods in Fine Particle Technology, Micromeritics Instrument Corp., Norcross, 1997.
[22] B.E. Warren, Phys. Rev. 59 (1941) 693.
[23] H.P. Boehm, Carbon 32 (1994) 759.
[24] H. Günzler, H.U. Gremlich, IR Spectroscopy, Wiley-VCH, Weinheim, 2002.

[25] A.B. McEwen, H.L. Ngo, K. LeCompte, J.L. Goldman, J. Electrochem. Soc. 146 (1999) 1687.
[26] H. Shirota, A.M. Funston, J. Wishart, E.W. Castner Jr., J. Chem. Phys. 122 (2005) 184512.
[27] C. Wakai, A. Oleinikova, M. Ott, H. Weingärtner, J. Phys. Chem. B 109 (2005) 17028.
[28] F.V. Bright, G.A. Baker, J. Phys. Chem. B 110 (2006) 5822.
[29] C. Wakai, A. Oleinikova, M. Ott, H. Weingärtner, J. Phys. Chem. B 110 (2006) 5824.
[30] J. Wu, J.P. W. Stark, Meas. Sci. Technol. 17 (2006) 781.
[31] C. Schröder, T. Rudas, O. Steinhauser, J. Chem. Phys. 125 (2006) 244506.
[32] C. Reichardt, Green Chem. 7 (2005) 339.
[33] T.J. Gannon, G. Law, P.R. Watson, Langmuir 15 (1999) 8429.
[34] G. Law, P.R. Watson, A.J. Carmichael, K.R. Seddon, Phys. Chem. Chem. Phys. 3 (2001) 2879.
[35] T. Fujimori, K. Fuji, R. Kanzaki, K. Chiba, H. Yamamoto, Y. Umebayashi, S. Ishiguro, J. Mol. Liq. 131–132 (2007) 216.
[36] A. Sadezky, H. Muckenhuber, H. Grothe, R. Niessner, U. Pöschl, Carbon 43 (2005) 1731.

Available online at www.sciencedirect.com
ScienceDirect
Journal of Power Sources 178 (2008) 490–496
JOURNAL OF POWER SOURCES
www.elsevier.com/locate/jpowsour

High voltage, asymmetric EDLCs based on xerogel carbon and hydrophobic IL electrolytes

M. Lazzari, F. Soavi, M. Mastragostino *

University of Bologna, Department of Metal Science, Electrochemistry and Chemical Techniques, Via San Donato 15, 40127 Bologna, Italy

Received 23 October 2007; received in revised form 7 December 2007; accepted 8 December 2007
Available online 1 February 2008

Abstract

The preparation procedure, morphology and the surface chemistry of xerogel carbons, which exhibited up to 120 F g^{-1} in ionic liquid (IL) at 60 °C, are reported. Performance results of double-layer supercapacitors (EDLCs) featuring an asymmetric configuration with mesoporous xerogel carbon electrodes and hydrophobic ionic liquid electrolyte operating at 60 °C are also shown. The investigated ILs are 1-ethyl-3-methyl-imidazolium-bis(trifluoromethanesulfonyl)imide (EMITFSI) and *N*-butyl-*N*-methylpyrrolidinium-bis(trifluoromethanesulfonyl)imide (PYR_{14}TFSI). While the PYR_{14}TFSI features lower conductivity and determines slightly lower xerogel carbon capacitive response than EMITFSI, it enables a wider potential excursion for the negative electrode charging process. This is beneficial for high maximum cell voltages (V_{max}) and, thus, for both the specific energy and power of asymmetric EDLCs. The asymmetric configuration we developed, with higher carbon loading at the positive electrode than that at the negative, makes it possible to tune the potential excursion of each electrode so that the EDLCs with EMITFSI and PYR_{14}TFSI attain the safe V_{max} of 3.4 V and 3.7 V, respectively, and high specific energy of ca. 30 Wh kg^{-1} between V_{max} and $0.5V_{max}$ over several thousand cycles.

Keywords: Supercapacitor; Ionic liquid; Xerogel carbon; Asymmetric EDLC; Capacitance

1. Introduction

Much effort is being focused on the development, and operating temperature, of high specific energy, E_{max}, double-layer carbon supercapacitors (EDLCs). Indeed, one field of EDLC application is transportation requiring high-efficiency electrochemical energy storage/conversion systems, even above RT. Given that E_{max} depends on supercapacitor specific capacitance (C_{EDLC}) and maximum cell voltage (V_{max}) as in the following equation, when evaluated between V_{max} and $0.5V_{max}$:

$$E_{max} = \frac{3}{8} C_{EDLC} V_{max}^2, \quad (1)$$

the pursued strategies are basically devoted to the development of high specific double-layer capacitance carbons and of safe, non-aqueous electrolytes with a wide electrochemical stability window (ESW) and high ionic conductivity for high specific power [1–4].

Ionic liquids (ILs) of wide ESW and good conductivity above RT are under investigation for high-voltage supercapacitors operating at $T > RT$, where they work as "solvent-free" electrolytes. Note that the properties of these ILs like polarizability also directly affect the electrode/electrolyte interface and, thus, supercapacitor capacitance. For high specific capacitance in ILs the carbon electrodes should display a high surface area that is easily accessible to the IL ions involved in the double-layer formation. This can be achieved by optimization of carbon surface chemistry and morphology. Given that IL purity is of paramount importance for long supercapacitor cycle-life and a high level of purity is more readily attainable for hydrophobic ILs, hydrophilic moieties that may repel IL ions should be absent from the carbon surface. IL ions typically have a size in the order of 1 nm so that for fast double-layer charging processes the carbon surface should mainly be made up of large micropores and mesopores. Xerogel carbons that are characterized by hydrophobic surfaces and a mesopore surface area tunable by synthesis conditions thus look like good electrode materials for IL-based EDLCs. Their capacitance responses at 60 °C in such hydrophobic ILs as 1-ethyl-3-methyl-imidazolium-bis(trifluoromethanesulfonyl)imide (EMITFSI) and *N*-butyl-*N*-me-

* Corresponding author. Tel.: +39 051 2099798; fax: +39 051 2099365.
E-mail address: marina.mastragostino@unibo.it (M. Mastragostino).

0378-7753/$ – see front matter © 2007 Elsevier B.V. All rights reserved.
doi:10.1016/j.jpowsour.2007.12.029

thylpyrrolidinium-bis(trifluoromethanesulfonyl)imide (PYR_{14}TFSI) has been estimated at ca. 0.2 F m^{-2} of mesoporous surface area [5–10].

Since the mid-point of the ESW of the ILs is not usually found at the potentials of the discharged carbon electrodes, only by assembling asymmetric EDLC configurations featuring different loading of the same carbon at the two electrodes is it possible to charge each electrode up to the limit potential defined by IL stability and, hence, to reach maximum cell voltages significantly higher than those achievable with symmetric EDLC configurations [11].

We thus set out to develop xerogel carbons with a mesopore surface area higher than 500 m^2 g^{-1}, so as to provide at least 100 F g^{-1} at 60 °C in the hydrophobic ILs EMITFSI and PYR_{14}TFSI, and report the results. We also include the cycling performance of asymmetric EDLCs with a xerogel carbon with a mesopore area of 600 m^2 g^{-1} operating in EMITFSI and in PYR_{14}TFSI at 60 °C at high voltages over several thousands cycles. The viability of the asymmetric EDLC configuration was investigated with both ILs since the former is attractive for its higher ionic conductivity and the latter for its wider ESW.

2. Experimental

The xerogel carbons X1p, X2p and X3p were prepared by polycondensation of resorcinol and formaldehyde with Na_2CO_3 as gelation catalyst in different molar ratios, followed by solvent exchange, RT drying and pyrolysis at 850–1050 °C in Ar as in Ref. [10]; the pyrolysed carbons were then soft milled. The xerogel carbon powders were also treated in CO_2 (200 cm^3 min^{-1}) at 850–1050 °C over different time intervals (t_{CO_2}) and kept 1 h in Ar (200 cm^3 min^{-1}) at the same temperature in order to remove any surface moieties formed during activation; heating (10 °C min^{-1}) and cooling were carried out in Ar and the treated carbons are labelled X1a, X2a, X3a.

Nitrogen adsorption porosimetry measurements were carried out at 77 K with an ASAP 2020 system (Micromeritics); the carbon powders were dried for at least 2 h at 120 °C before testing. The N_2 adsorption isotherms were analyzed by density functional theory (DFT) and the specific surface area related to pores wider than 1.5 nm ($S_{>1.5nm}$) was evaluated from DFT mesoporous volume by assuming a cylindrical pore geometry. FTIR spectra in reflectance mode (FTIR-ATR) were collected by a PerkinElmer Spectrometer Spectrum ONE (FTIR-ATR) with 40 scans and 4 cm^{-1} resolution.

The carbon electrodes (ca. 0.6 cm^2 geometric area; 6–13 mg cm^{-2} carbon loading) were prepared by mixing 95% (w/w) carbon and 5% (w/w) polytetrafluoroethylene binder (DuPont) to yield a paste which was then laminated on carbon coated aluminum grids (Lamart Corp.).

The PYR_{14}TFSI (Solvent Innovation, 98%) and EMITFSI (Solvent Innovation, 99%) ILs were dried over night at 80 °C under dynamic vacuum (Büchi Glass Oven B-580) and displayed ca. 30 ppm of water as checked by Karl Fisher titration (684 KF Coulometer Metrohm).

We used Swagelok-type, "three electrodes" cells for single electrode and supercapacitor tests. A silver disk was used as quasi-reference electrode for the cyclic voltammetries and to check electrode potentials during supercapacitor galvanostatic cycling. The silver disk potential, measured in conventional cells prior to the electrochemical tests by adding the highly reversible redox couple ferrocene/ferrocinium (Fc/Fc^+) to the medium, was E_{Ag} (V) = (E_{Fc/Fc^+} + 0.200 ± 0.010); hereinafter the electrode potentials are given versus Fc/Fc^+ for comparison with literature. The cells were assembled in dry box (MBraun Labmaster 130, H_2O and O_2 <1 ppm) by facing two carbon composite electrodes and using a fiber glass separator (Durieux, 200 μm thick when pressed); for single-electrode studies, double-layer carbon counter-electrodes with charge storage capability significantly higher than that of the working electrodes were used so as not to limit the capacitive response of the working electrode. The cells were kept at a controlled temperature of 60 ± 2 °C using a Thermoblock (FALC). The electrochemical tests were performed with a PerkinElmer VMP multichannel potentiostat/galvanostat and a Solartron SI 1255 frequency-response analyzer coupled to a 273A PAR potentiostat/galvanostat. Impedance spectra were recorded with 5 mV ac perturbation in the frequency range of 50 kHz to 10 mHz.

3. Results and discussion

Table 1 summarizes the synthesis conditions and the porosity data of the xerogel carbons evaluated from the N_2 adsorption isotherms reported in Fig. 1. Fig. 2 shows the pore-size distri-

Table 1
Synthesis conditions in terms of resorcinol to gelation catalyst (*R/C*) and of water to resorcinol, formaldehyde and gelation catalyst (*D*) molar ratios, pH of the gelation bath and CO_2 activation time (t_{CO_2}); total pore volume (V_{tot}), percentage of pore volume ($V_{>1.5nm}$) and specific surface area ($S_{>1.5nm}$) related to pores wider than 1.5 nm, mean mesopore size (d_p) of the pristine (X1p, X2p, X3p) and CO_2/Ar treated (X1a, X2a, X3a) carbon powders from the DFT analysis of the corresponding N_2 adsorption isotherms at 77 K

Carbon	Synthesis conditions				Porosity			
	R/C	*D*	pH	t_{CO_2} (h)	V_{tot} (cm^3 g^{-1})	$V_{>1.5nm}$ (%)	$S_{>1.5nm}$ (m^2 g^{-1})	d_p (nm)
X1p	200	2.5	6.40	–	0.28	64	185	5
X2p	300	5.7	6.50	–	0.96	83	315	14
X3p	400	4	6.53	–	1.03	87	310	15
X1a	200	2.5	6.40	2.5	0.82	63	375	6
X2a	300	5.7	6.50	4.0	1.29	77	410	14
X3a	400	4	6.53	5.5	1.73	77	600	15

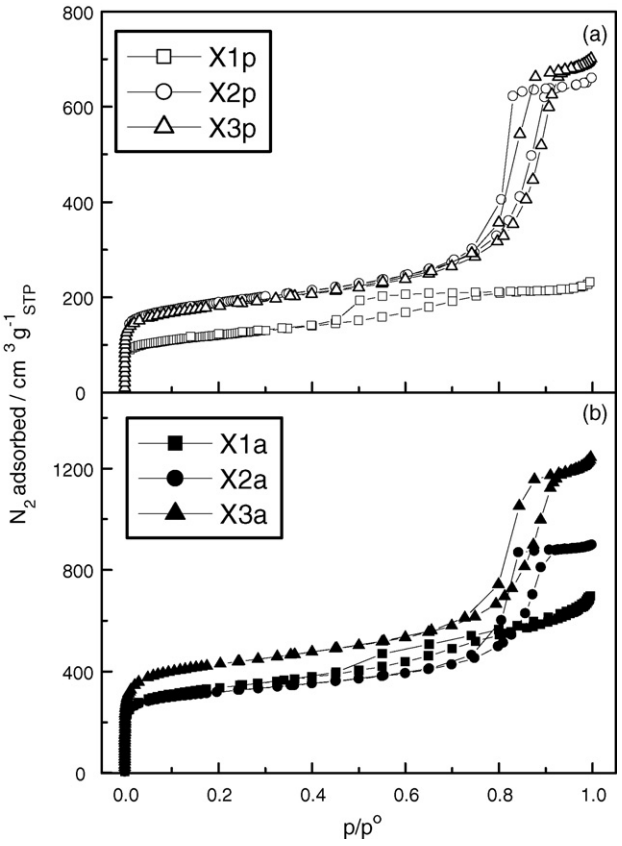

Fig. 1. N_2 adsorption/desorption isotherms at 77 K of (a) pristine and (b) treated xerogel carbons.

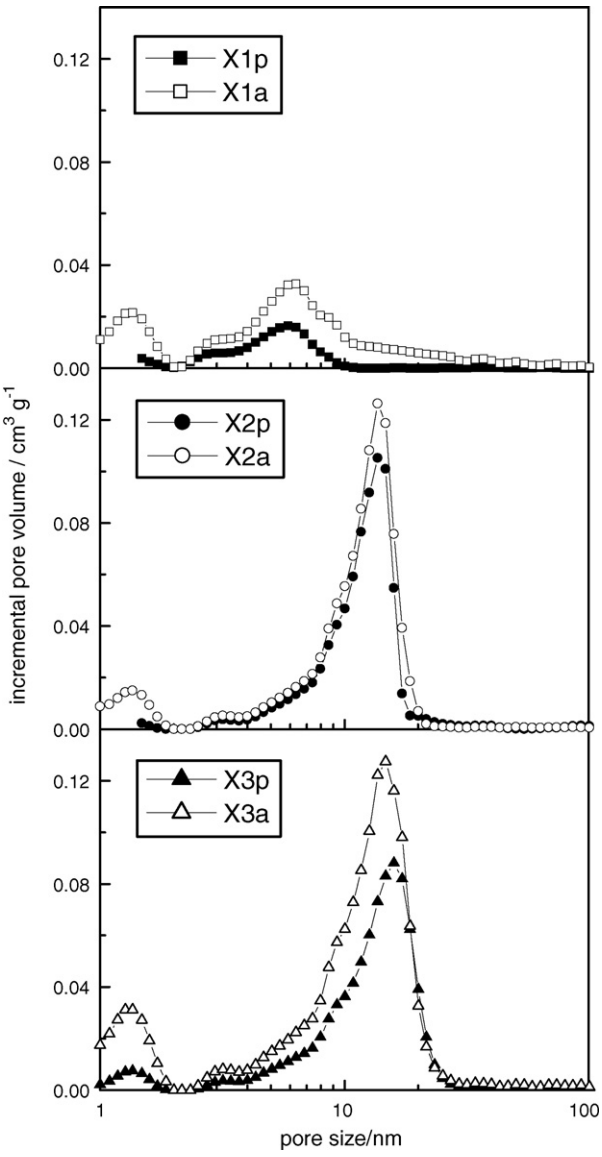

Fig. 2. DFT incremental pore volume vs. pore size of the pristine X1p, X2p and X3p and treated X1a, X2a and X3a xerogel carbons.

bution in incremental pore volume for the different carbons and shows that the pores in all the carbons are sufficiently wide to be filled with the ILs. Xerogel carbon X1p exhibits the lowest porosity, with 5 nm pores accounting for 64%. The data in Table 1 indicate that by increasing the *R*/*C* and *D* parameters from 200 to ≥300 and from 2.5 to ≥4, respectively, the total pore volume (V_{tot}) of the pristine carbon reaches 1 $cm^3\ g^{-1}$ while maintaining a high percentage of volume from pores >1.5 nm ($V_{>1.5nm}$). The increase of *R*/*C* and *D* also widens the pores to ca. 15 nm so that the gain in surface area is lower than expected. Indeed, the specific surface area related to pores wider than 1.5 nm ($S_{>1.5nm}$), i.e. to the mesopores and large micropores involved in the double-layer charging process, only doubles, roughly, with the X2p and X3p carbons. We thus treated the X1p, X2p and X3p xerogel carbons using a two-step procedure: CO_2 activation at 850–1050 °C for the increase of the surface area, followed by heat-treatment in Ar at the same temperature for the removal of any hydrophilic, oxygen-containing surface moieties formed along the previous activation step; the corresponding treated xerogel carbons are X1a, X2a and X3a. The data in Table 1 and Fig. 2 show that treatments significantly increased total pore volume (micropores included) of the carbons without modifying their mesopore size distribution, a fact that might be explained by the carbon pores' lengthening while retaining the same width. While an activation time of 2.5 h provided an $S_{>1.5nm}$ double that of X1p for carbon X1a, longer treatments of 4 and 5.5 h were necessary for X2a and X3a to yield $S_{>1.5nm}$ of 410 and 600 $m^2\ g^{-1}$, respectively. The FTIR-ATR spectrum of X3a in Fig. 3 indicates that the two-step activation procedure does not yield carboxyl-based acid surface moieties, which are the main cause of the hydrophilic behaviour of carbons and which should give strong absorption bands at ca. 1600 cm^{-1}; the weak and broad band in the region can rather be ascribed to aromatic C=C vibrations. Indeed, the main absorptions in the spectrum in Fig. 3, at 2160, 2030 and 1975 cm^{-1} and in the 900–1300 cm^{-1} region, are related to the C=O stretching in chetenes and cyclic anhydrides and to the C–O stretching in ethers, phenols and cyclic anhydrides, respectively, i.e. to basic or weak acidic moieties [12–14].

The surface features of the treated xerogel carbons enable a high IL uptake and, hence, high capacitive responses as shown by the data in Table 2, which reports the specific capacitances

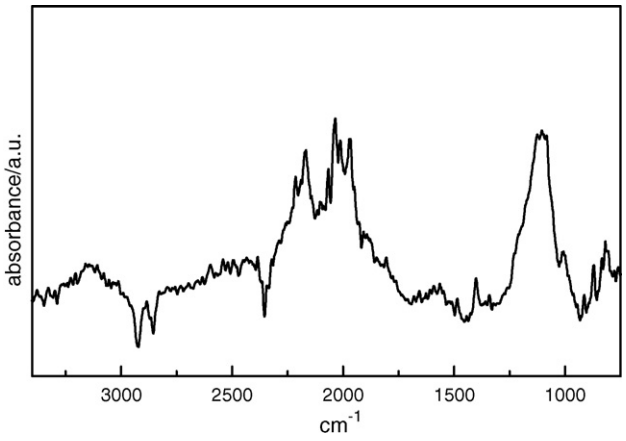

Fig. 3. FTIR-ATR spectrum of the X3a treated xerogel carbon.

Table 2
Specific capacitance (C) of the treated xerogel carbons in EMITFSI and $PYR_{14}TFSI$ at 60 °C in different potential ranges (ΔV, potentials given vs. Fc/Fc^+) as evaluated from the voltammetric discharges at 20 mV s^{-1} by the slope of the integral over time of the current vs. electrode potential

Carbon	EMITFSI		$PYR_{14}TFSI$	
	ΔV (V)	C (F g^{-1})	ΔV (V)	C (F g^{-1})
X1a	−2.1/−0.1	90 ± 6	−2.1/−0.1	75 ± 8
X2a	−2.1/−0.1	106 ± 6	−2.6/−0.1	87 ± 13
X3a	−2.1/−0.1	125 ± 6	−2.6/−0.1	108 ± 15
	−0.1/1.3	128 ± 12	−0.1/1.4	120 ± 20

(C) of the X1a, X2a and X3a carbons delivered in the two ILs at 60 °C in different electrode potential domains. When the same IL is considered, the specific capacitance increases in the order of X1a < X2a < X3a, i.e. with the carbon's $S_{>1.5nm}$. X3a, the carbon with the highest $S_{>1.5nm}$ of 600 m^2 g^{-1}, exceeds 100 F g^{-1} in both ILs, reaching 125 F g^{-1} in EMITFSI; notably these values were reached at high specific currents, higher than 2 mA mg^{-1}, as shown by the CVs reported in Fig. 4. For each negatively charged carbon, the specific capacitance is ca. 20% higher in EMITFSI than in $PYR_{14}TFSI$, as expected on the basis of the different nature of the ILs counterions involved in the double-layer, which also affect the potential limits for the charge/discharges at high coulombic efficiency [9]. While in EMITFSI the negative electrode cannot be polarized below −2.1 V versus Fc/Fc^+, mainly because of the presence of the labile acid proton of the imidazolium ring, in $PYR_{14}TFSI$ it is possible to reach −2.6 V versus Fc/Fc^+. Table 2 also reports the specific capacitance in the positive domain of the best-performing X3a carbon. In both the ILs the potential excursions of the positive electrodes are limited by the $TFSI^-$ anion stability and cannot exceed 1.6 V versus Fc/Fc^+ (higher than the value reported in Table 2). Given that the typical potential of the discharged electrodes is ca. −0.1 V versus Fc/Fc^+, the maximum potential excursion for the positive electrode can be 1.7 V, narrower than that achievable with the negative electrode, which is ca. 2.0 V in EMITFSI and 2.5 V in $PYR_{14}TFSI$. Thus, in a conventional symmetric configuration of EDLC, where the two electrodes have the same carbon loading and almost the same specific capacitance, i.e. the same charge storage capability, the maximum potential excursion for the negative electrode would be limited by that of the positive, as shown by the following equation:

$$\Delta V_- = \frac{C_+ w_+ \Delta V_+}{C_- w_-}, \quad (2)$$

where C_+, w_+, ΔV_+ and C_-, w_-, ΔV_- are the specific capacitance, carbon loading and maximum potential excursion of the positive and negative electrode, respectively. In other words, symmetric EDLCs can safely operate below 3.4 V with both the ILs and, particularly in the case of $PYR_{14}TFSI$, do not take full advantage of the electrolyte's wide ESW. Asymmetric configurations with positive-to-negative electrode mass loading ratios, $R_{+/-}$, higher than 1 would make it possible to widen the negative electrode potential excursions up to the values allowed by the ESW of the ILs while keeping the same ΔV_+, so that up to 4.2 V could be achieved with $PYR_{14}TFSI$-based EDLCs.

We then assembled asymmetric EDLCs with both ILs and the best performing X3a xerogel carbon using $R_{+/-} > 1$ as reported in Table 3, which also shows the total composite electrode mass loadings of the supercapacitors (w_{EDLC}, positive and negative electrodes together). The EMITFSI and $PYR_{14}TFSI$-based EDLCs were tested at 60 °C with $V_{max} \leq 3.4$ V and ≤3.7 V, respectively, in order to keep the cells sufficiently far from the envisioned potential limits in view of long-term cycling tests and with operating potentials still significantly higher than those feasible with commercial supercapacitors. Fig. 5 shows the galvanostatic profiles of the charge/discharge cycles at 10 mA cm^{-2} with $V_{max} = 3.3$ V and 3.7 V of the X3a/EMITFSI/X3a and X3a/$PYR_{14}TFSI$/X3a asymmetric EDLCs and of the corresponding electrodes collected after 5600 and 15,300 cycles, respectively, at 20 mA cm^{-2}; the dashed lines indicate the maximum electrode potential excursions permitted by the ILs. While in Fig. 5a the electrode potential profiles indicate that

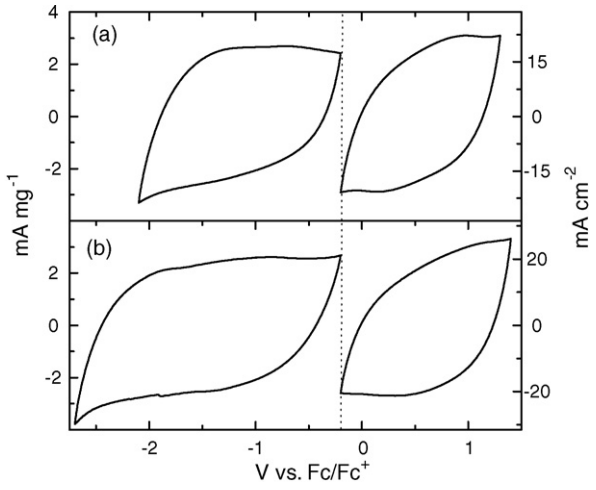

Fig. 4. CVs at 20 mV s^{-1} and 60 °C of X3a carbon electrodes in (a) EMITFSI and (b) $PYR_{14}TFSI$.

Table 3
Values of positive to negative mass loading ratio ($R_{+/-}$) and of total composite electrode mass loading (w_{EDLC}, positive and negative electrodes together) of the asymmetric EDLCs with EMITFSI and $PYR_{14}TFSI$ electrolytes, and maximum cell voltage V_{max}, supercapacitor specific capacitance (C_{EDLC}, on the basis of w_{EDLC}), maximum specific energy (E_{max}), equivalent series resistance (ESR, by the ohmic drop after 0.1 s from the beginning of discharge) and maximum specific power (P_{max}) at the 12,000th and 11,000th galvanostatic cycle, respectively, at 20 mA cm^{-2} and 60 °C

IL	$R_{+/-}$	w_{EDLC} (mg cm^{-2})	V_{max} (V)	C_{EDLC} (F g^{-1})	E_{max} (Wh kg^{-1})	ESR (Ω cm^2)	P_{max} (kW kg^{-1})
EMITFSI	1.4	20.4	3.4	26	31	15	9.5
$PYR_{14}TFSI$	1.6	15.0	3.7	21	30	20	11.4

in the X3a/EMITFSI/X3a EDLC electrode mass balance is almost optimized, the profiles in Fig. 5b indicate that in the X3a/$PYR_{14}TFSI$/X3a the $R_{+/-}$ parameter could be increased slightly in order to attain higher V_{max} by a wider sweep of the negative electrode potential ΔV_- while keeping the same ΔV_+.

Both supercapacitors were tested over several thousand cycles at 20 mA cm^{-2} and 60 °C; Table 3 reports the maximum cell voltage V_{max}, the specific capacitance (C_{EDLC}) and the maximum specific energy (E_{max}) of the supercapacitors after more than 10,000 galvanostatic cycles. At the 12,000th cycle, the X3a/EMITFSI/X3a EDLC delivers 26 F g^{-1} of total composite electrode materials and a maximum specific energy between 3.4 V and 1.7 V of 31 Wh kg^{-1}. At the 11,000th cycle, the supercapacitor with $PYR_{14}TFSI$ delivers a slightly lower capacitance of 21 F g^{-1} (as expected on the basis of single electrode tests) and the corresponding energy delivered between 3.7 V and 1.85 V is of 30 Wh kg^{-1}, a value which can be increased if a better electrode balancing that enables to reach at least 4.0 V is used. These results are very interesting not only because the E_{max} exceeds by 30% that delivered by symmetric EDLC with $PYR_{14}TFSI$ and commercial activated carbons [8], thus demonstrating the potency of the asymmetric configuration and of xerogel carbons, but mainly because they were quite stable over several thousand cycles as shown in Fig. 6. This figure reports the trend of C_{EDLC} over cycling at 60 °C and 20 mA cm^{-2} for the two EDLCs carried out with V_{max} up to 3.4 V in the case of X3a/EMITFSI/X3a and with V_{max} up to 3.7 V in the case of X3a/$PYR_{14}TFSI$/X3a (800 cycles were also performed with V_{max} = 3.9 V).

Table 3 also shows the maximum specific power P_{max} of the two EDLCs at 60 °C calculated by $P_{max} = V_{max}^2/(4ESR\, w_{EDLC})$, where ESR is the equivalent series resistance evaluated by the ohmic drop after 0.1 s from the beginning of the discharge at 20 mA cm^{-2}, roughly corresponding to the value attainable at 10 Hz by impedance spectroscopy.

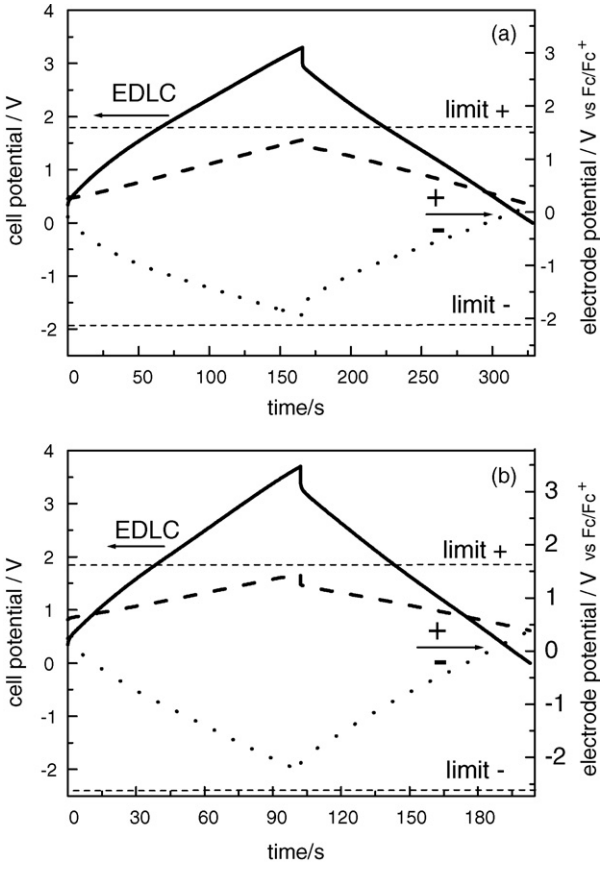

Fig. 5. Voltage profiles at 10 mA cm^{-2} and 60 °C of the (a) X3a/EMITFSI/X3a (5600th cycle, V_{max} = 3.3 V) and (b) X3a/$PYR_{14}TFSI$/X3a (15,300th cycle, V_{max} = 3.7 V) asymmetric EDLCs and of their positive and negative electrodes; dashed lines indicate maximum electrode potential excursions permitted by the two ILs.

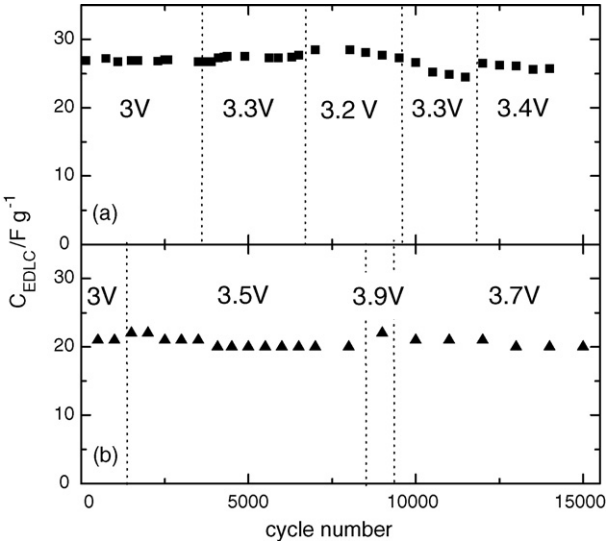

Fig. 6. Trend of supercapacitor specific capacitance (C_{EDLC}, in F per gram of total composite electrode materials) over cycling at 60 °C and 20 mA cm^{-2} of the (a) X3a/EMITFSI/X3a and (b) X3a/$PYR_{14}TFSI$/X3a asymmetric EDLCs with the indications of maximum cell voltages reached upon cycling.

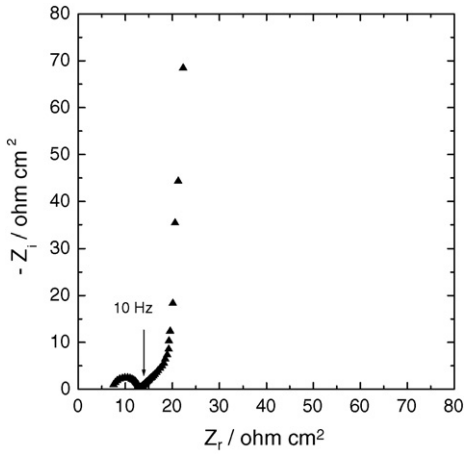

Fig. 7. Nyquist plot of the discharged X3a/PYR_{14}TFSI/X3a asymmetric EDLC at 60 °C (5×10^4 to 10^{-2} Hz frequency range).

The X3a/PYR_{14}TFSI/X3a EDLC displays a higher ESR than X3a/EMITFSI/X3a, mainly because of the ion conductivity of PYR_{14}TFSI, which is 6 mS cm^{-1} at 60 °C and lower than that of EMITFSI (25 mS cm^{-1} at the same temperature). However, the higher V_{max} of the former EDLC also ensures a higher P_{max} of 11.4 kW kg^{-1}. Note that the ESR in Table 3 is markedly affected by cell assembly. Indeed, the asymmetric EDLCs featured a very thick, 200 μm separator, which significantly contributes to ESR. This can be seen in the Nyquist plot of the X3a/PYR_{14}TFSI/X3a EDLC reported as an example in Fig. 7, where the impedance value at the highest frequency arising from electronic and ionic resistances is 7 Ω cm^2. A reduction of the ionic is feasible by using a 10-fold thinner separator, which does not limit the capacitance of the carbon electrodes because the high porosity of the X3a carbon provides an IL-reservoir for double-layer formation. On the other hand, we used home-made electrodes and it is well known that automatic lamination procedures help to decrease electrode contact resistances, which are mainly responsible for the resistive component of the high-frequency semicircle in the impedance spectrum in Fig. 7. Thus, the P_{max} values reported in Table 3 are to be taken as underestimated. The fast charge–discharge response of the X3a/PYR_{14}TFSI/X3a and X3a/EMITFSI/X3a EDLCs at 60° C is clearly evinced by the trends of their capacitance versus frequency reported in Fig. 8; in these plots the capacitance was calculated from the imaginary component of the impedance at each frequency and normalized for the different EDLCs to the corresponding limit capacitance at 10 mHz. Indeed, the double-layer charging process begins for both the EDLCs at 10 Hz and the capacitance reaches the limit value at ca. 10^{-1} Hz, which means that the maximum storage/delivery capability can be reached in ca. 10 s.

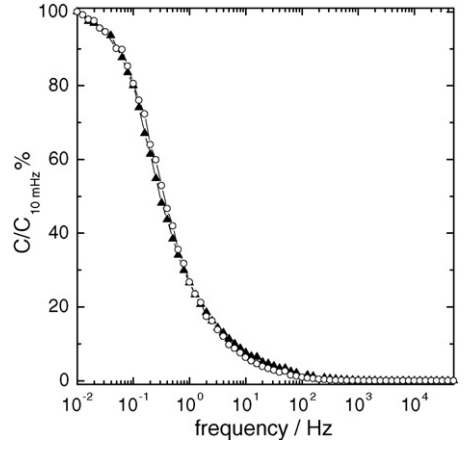

Fig. 8. Trends of the capacitance normalized to the limit value at 10 mHz (C/C_{10mHz}, %) vs. frequency of the (circle) X3a/EMITFSI/X3a and (triangle) X3a/PYR_{14}TFSI/X3a asymmetric EDLCs from impedance measurements at 60 °C.

4. Conclusions

CO_2 activation and heat treatment in Ar atmosphere of home-made xerogel carbons produced a mesoporous carbon featuring specific hydrophobic surface area $S_{>1.5nm}$ of 600 m^2 g^{-1} mainly from 15 nm pores and able to deliver more than 100 F g^{-1} in both EMITFSI and PYR_{14}TFSI ILs. We then developed asymmetric EDLCs with carbon loading at the positive electrode higher than that at the negative that makes it possible to charge each electrode up to the limit potentials defined by the ESW of each IL. Both EDLCs delivered over several thousands cycles at 60 °C a maximum specific energy of ca. 30 Wh kg^{-1} with V_{max} up to 3.4 V in the case of the X3a/EMITFSI/X3a and V_{max} of 3.7 V in the case of X3a/PYR_{14}TFSI/X3a, thereby outperforming commercial supercapacitors. Note that while 3.4 V is also attainable with a symmetric configuration, the V_{max} value of 3.7 V is achievable only by an asymmetric EDLC and, in the case of supercapacitors based on PYR_{14}TFSI, it represents a very safe value for long supercapacitor cycle life.

Acknowledgements

Work funded by the European Commission in the Sixth Framework Programme, Sub-programme Sustainable Surface Transport, under Contract No. TST4-CT-2005-518307 (Project ILHYPOS “Ionic Liquid-based Hybrid Supercapacitor”); all the partners in the Project are acknowledged.

References

[1] A. Burke, Electrochim. Acta 53 (2007) 1083–1091.
[2] A.G. Pandolfo, A.F. Hollenkamp, J. Power Sources 157 (2006) 11–27.
[3] J.R. Miller, Electrochim. Acta 52 (2006) 1703–1708.
[4] R. Kötz, M. Hahn, R. Gallay, J. Power Sources 154 (2006) 550–555.
[5] M. Galiński, A. Lewandowski, I. Stępniak, Electrochim. Acta 51 (2006) 5567–5580.
[6] A. Lewandowski, M. Galinski, J. Phys. Chem. Solids 65 (2004) 281–286.
[7] A. Balducci, W.A. Henderson, M. Mastragostino, S. Passerini, P. Simon, F. Soavi, Electrochim. Acta 50 (2005) 2233–2237.

[8] A. Balducci, R. Dugas, P.L. Taberna, P. Simon, D. Plée, M. Mastragostino, S. Passerini, J. Power Sources 165 (2007) 922–927.
[9] M. Lazzari, M. Mastragostino, F. Soavi, Electrochem. Commun. 9 (2007) 1567–1572.
[10] C. Arbizzani, S. Beninati, M. Lazzari, F. Soavi, M. Mastragostino, J. Power Sources 174 (2007) 648–652.
[11] M. Mastragostino, F. Soavi, J. Power Sources 174 (2007) 89–93.
[12] H.P. Bohem, Carbon 32 (1994) 759–769.
[13] A. Dandekar, R.T.K. Baker, M.A. Vannice, Carbon 36 (1998) 1821–1831.
[14] J.L. Figueiredo, M.F.R. Pereira, M.M.A. Freitas, J.J.M. Órfão, Carbon 37 (1999) 1379–1389.

Journal of Power Sources 185 (2008) 1575–1579

Contents lists available at ScienceDirect

Journal of Power Sources

journal homepage: www.elsevier.com/locate/jpowsour

Short communication

Safe, high-energy supercapacitors based on solvent-free ionic liquid electrolytes

Catia Arbizzani, Maurizio Biso[1], Dario Cericola[2], Mariachiara Lazzari, Francesca Soavi, Marina Mastragostino*

University of Bologna, Dipartimento di Scienza dei Metalli, Elettrochimica e Tecniche Chimiche, via S. Donato 15, 40127 Bologna, Italy

ARTICLE INFO

Article history:
Received 5 August 2008
Received in revised form 8 September 2008
Accepted 10 September 2008
Available online 19 September 2008

Keywords:
Ionic liquid
Double-layer supercapacitor
Hybrid supercapacitor
Activated carbon
Poly(3-methylthiophene)
Power-assisted HEV

ABSTRACT

Safety is the main concern for energy storage-system application in hybrid-electrical vehicles (HEVs) and ionic liquids (ILs) of low vapor pressure and high thermal stability represent a strategy to meet this key requisite. The use of solvent-free ILs in supercapacitors enables the high cell voltages required for increasing supercapacitor energy up to the values for power-assist application in HEVs. In order to exploit the wide electrochemical stability window of ILs, tailored electrode materials and cell configurations have to be used. The performance of asymmetric double-layer carbon supercapacitors (AEDLCs) and carbon/poly(3-methylthiophene) hybrid supercapacitors operating with different pyrrolidinium-based ILs are reported and compared. This study demonstrates that a design-optimized AEDLC operating with safe, solvent-free IL electrolyte meets cycling stability and the energy and power requisites for power-assisted HEVs at the investigated temperatures.

1. Introduction

The high specific power and very long cycle life make electrochemical double-layer carbon supercapacitors (EDLCs) key energy storage systems for sustainable transport based on hybrid electric vehicles (HEVs) [1–4]. Compared to batteries, supercapacitors feature significantly lower specific energy, i.e. 5 Wh kg^{-1} at maximum, so that even the best performing ones do not yet fulfill the specific energy requisites for power assist in strong-HEV. This application requires that a significant portion of the driveline power is electric and the targets of the electrochemical energy storage systems stated by the United States Advanced Battery Consortium (USABC) and the Department of Energy (DOE) are pulse power of 620 W kg^{-1} for 10 s over more than 3×10^5 shallow cycles and 7.5 Wh kg^{-1} total available energy. These requirements should be in the −30 °C/+60 °C duty temperature range, with safety being a primary target [3,4]. While recent advances in Li-ion batteries have raised their power performance up to target levels, serious concerns still remain about reliability and safety because of their low tolerance to such abusive conditions as overcharge and exposure to high temperatures. The EDLCs feature positive and negative electrodes identical in mass and composition and are charged/discharged by physical processes so that they are intrinsically safer than batteries. Furthermore, unlike batteries, the energy efficiency of EDLCs is higher than 90% so that the amount of released heat is small and can be easily dissipated [1,2]. Thus, supercapacitors of increased energy with respect to commercial ones could compete with Li-ion batteries in power-assisted HEVs, with the advantage of higher safety and reliability than the latter.

Given that the maximum energy (E_{max}) of the supercapacitor is directly related to its capacitance (C_{sc}) and to the square of the maximum operating voltage (V_{max}), as in Eq. (1)

$$E_{max} = \frac{3}{8} C_{sc} V_{max}^2, \quad (1)$$

when delivered between V_{max} and $1/2V_{max}$, the challenge in the supercapacitor field is to develop materials and configurations that make it possible to increase C_{sc} and V_{max}. The most powerful strategy for increasing supercapacitor energy is to raise the cell voltage above 2.5 V/2.7 V, the highest values for commercial systems based on organic electrolytes, without sacrificing cycle-life and safety. Much attention has thus been focused on ionic liquids (ILs) that feature high thermal and chemical stability, low vapor pressure, a wider electrochemical stability window (ESW) than conventional organic electrolytes' and are able to operate in high temperature

* Corresponding author. Tel.: +39 051 2099798; fax: +39 051 2099365.
E-mail address: marina.mastragostino@unibo.it (M. Mastragostino).
[1] Present address: Italian Institute of Technology, Via Morego 30, 16163 Genova, Italy.
[2] Present address: Paul Scherrer Institut, 5232 Villigen PSI, Switzerland.

0378-7753/$ – see front matter © 2008 Elsevier B.V. All rights reserved.
doi:10.1016/j.jpowsour.2008.09.016

regimes that are not feasible with commercial systems [5–11]. The challenge is to design solvent-free IL electrolytes that match these properties with conductivity at least as high as 10^{-3} S cm^{-1} to 10^{-1} S cm^{-1} in a wide-duty temperature range from ca. −30 °C to 60 °C. The high conductivity requisite is crucial for a low equivalent series resistance (ESR), which in turn affects supercapacitor power performance as per the maximum specific power P_{max} in Eq. (2)

$$P_{max} = \frac{V_{max}^2}{4\ ESR\ w_{sc}}, \quad (2)$$

where w_{sc} is the total composite electrode loading.

The most widely studied ILs for supercapacitor application are imidazolium and pyrrolidinium salts; while the former typically display the highest conductivities, the latter feature the widest ESWs, even exceeding 5 V. Table 1 reports conductivity, ESW, melting temperature, which is the limit for the use of ILs as solvent-free electrolytes, formula weight and density of N-butyl-N-methyl pyrrolidinium (PYR_{14}^+)- and N-methoxyethyl-N-methylpyrrolidinium ($PYR_{1(2O1)}^+$)-based ILs with bis(trifluoromethanesulfonyl)imide ($TFSI^-$) and trifluoromethanesulfonate (Tf^-) anions [5,11–16]. The PYR_{14}^+-based ILs freeze near 0 °C and the introduction of a methoxyethyl group on the nitrogen atom of the pyrrolidinium ring in $PYR_{1(2O1)}$TFSI lowers the freezing point to −95 °C and improve the conductivity properties, making this IL one of the most promising for the development of high voltage supercapacitors operating in a wide temperature range.

ILs require the use of specifically designed electrode materials, especially in regard to the electrode/IL interface properties and tailored supercapacitor configurations to take full advantage of their wide ESW. EDLCs with positive and negative carbon electrodes of equal mass, hereinafter termed symmetric EDLCs, do not feature the high V_{max} enabled by ILs because the potential of discharged carbon electrodes is generally far from the mid-point of the IL's ESW and upon charge the two electrodes experience the same potential excursion, so that V_{max} is constrained by the electrode that first hits the ESW limit. Indeed, despite the IL's wide ESW, symmetric EDLCs with PYR_{14}TFSI electrolyte cannot be cycled with coulombic efficiency >95%, which is a requisite for long cycle-life, when V_{max} is ≥3.5 V [9,11]. In IL-based EDLCs with different loadings of the same carbon at the positive and negative electrodes, here termed asymmetric EDLCs (AEDLCs), each electrode can experience different potential excursions and be charged up to the ESW limits of the electrolyte so that V_{max} values 1 V higher than those of commercial, symmetric EDLCs are feasible [10].

A further increase in specific energy with respect to IL-based AEDLCs might be achieved using pseudocapacitive electrode materials coupled to double-layer carbon electrodes in hybrid configurations (HYSC). Pseudocapacitive electrodes of specific capacitance significantly higher than carbons' and that can be charged/discharged several thousand times in aprotic IL by redox processes at potentials approaching the ESW limits should increase the capacitance performance of supercapacitors without sacrificing V_{max} and cycle-life. This is the case of poly(3-methylthiophene) (pMeT), which can be reversibly p-doped/undoped in pyrrolidinium-based ILs at suitably high electrode potentials with specific capacitance of 200–250 F g^{-1} when prepared in IL [18–20].

We report the results of a study designed to develop safe, high-energy AEDLCs and HYSCs based on PYR_{14}TFSI, PYR_{14}Tf and $PYR_{1(2O1)}$TFSI ILs for power-assisted HEV application. The performance at different temperatures of these IL-based AEDLCs and HYSCs with specifically designed carbon and pMeT electrodes is reported and discussed.

2. Experimental

The carbon used in AEDLC and HYSC supercapacitor was PICACTIF SUPERCAP BP10 (Pica) treated at 1050 °C in Ar for 2 h. This surface cleaning procedure was checked by thermogravimetric analysis (TGA) with a Mettler Toledo TGA/SDTA A851 System in the temperature range of 25–1050 °C under N_2 flow at a scanning rate of 20 °C min^{-1}.

Carbon porosity was evaluated by nitrogen adsorption porosimetry carried out at 77 K with an ASAP 2020 system (Micromeritics); the carbon powders were dried for at least 2 h at 120 °C before testing. The N_2 adsorption isotherms were analyzed by the Density Functional Theory (DFT) and the total pore volume (V_{tot}) was evaluated by the quantity of N_2 adsorbed at $p/p^\circ = 0.995$. The carbon electrodes (0.62 cm^2 geometric area) were prepared by mixing 95% (w/w) carbon and 5% (w/w) polytetrafluoroethylene binder (Du-Pont) to yield a paste that was then laminated on carbon-coated aluminum grids (Lamart Corp.).

The PYR_{14}Tf (99%, Solvionic), PYR_{14}TFSI (purum 98%, Solvent Innovation), $PYR_{1(2O1)}$TFSI (Evonik Industries) were dried over night at 80 °C under dynamic vacuum (Büchi Glass Oven B-580) before use; water content in IL was checked by Karl Fisher titration (684 KF Coulometer Metrohm).

The polymer electrodes for the HYSC supercapacitors were obtained by direct electropolymerization of pMeT in IL on a carbon paper aerogel current collector (Marketech). The polymerization bath was 1-ethyl-3-methyl-imidazolium bis(trifluoromethanesulfonyl)imide (EMITFSI, 99%, Solvent Innovation, dried before use)—1 M methylthiophene (Aldrich, distilled before use) with 0.1 M acid additive trifluoromethanesulfonimide (95%, Aldrich) which prevents consumption of the EMITFSI IL at the counter electrode. The polymer was grown by galvanostatic technique at RT and 5 mA cm^{-2} [ref. 18].

"Three-electrode" Swagelok cells were used for single-electrode and supercapacitor tests. For single-electrode studies, double-layer carbon counter-electrode with charge storage capability significantly higher than that of the working electrode was used so as not to limit the capacitive response of the latter. The reference electrode for cyclic voltammetries and for the evaluation of the electrode potentials during supercapacitor galvanostatic cycling was a silver disk; hereinafter the electrode potentials are given vs. the reversible redox couple ferrocene/ferrocinium (Fc/Fc^+, $E_{Fc/Fc^+} = E_{Ag} + 0.200 \pm 0.010$ V). The cells were assembled in dry box (MBraun Labmaster 130, H_2O and O_2 <1 ppm) using a fiberglass separator (Durieux, 200 μm thick when pressed). AEDLCs and HYSC supercapacitors featured w_{sc} of 15–20 mg cm^{-2} and 8 mg cm^{-2}, respectively. The electrochemical tests were performed with a PerkinElmer VMP multichannel potentiostat/galvanostat at temperatures controlled by a Thermoblock (FALC) or a cryostat (HAAKE K40).

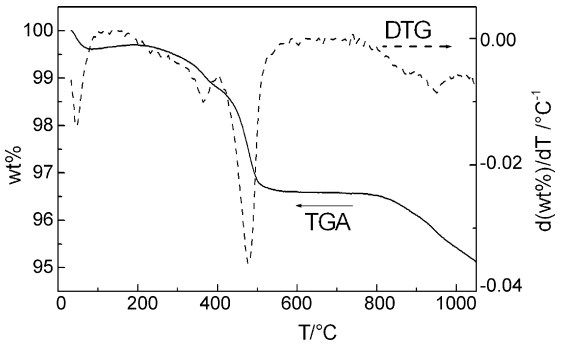

Fig. 1. TGA plot (solid line) and its differential (DTG, dashed line) of the pristine carbon.

Table 1
Conductivity (σ), ESW (evaluated with glassy carbon electrode), melting temperature (T_m), formula weight and density of ILs investigated for supercapacitor applications [5,11–16].

IL	σ (mS cm^{-1})		T_m (°C)	ESW at 60 °C (V)	Formula weight (g mol^{-1})	Density (g ml^{-1})
	RT	60 °C				
$PYR_{14}TFSI$	2.6	6.0	−3	5.5	422	1.41
$PYR_{14}Tf$	2.0	5.5	+3	6.0	291	1.28
$PYR_{1(201)}TFSI$	3.8	8.4	<−90	5.0	424	1.43

3. Results and discussion

To promote carbon wettability with the electrolyte, the surface of the carbon for our IL-based AEDLC and HYSC supercapacitors was cleaned by heat treatment at 1050 °C in Ar atmosphere before use. The TGA curve in Fig. 1 shows that this treatment was effective for the removal of surface acidic groups, which caused the main weight loss at 300–500 °C [21]. Such hydrophilic moieties can be deleterious not just for hydrophobic IL uptake but also for cycling stability because they are typically responsible for irreversible parasitic faradic processes [17,22].

The treated carbon (ACT) featured a total pore volume of 1.2 cm^3 g^{-1} and pore size distribution centered at 2.7 nm; 71% of pore volume was originated by pores wider than 1.5 nm, i.e. wider than IL ion size, and provided a surface area of 940 m^2 g^{-1} accessible to the electrolyte for the double-layer charging process. The ACT electrodes were tested in $PYR_{14}TFSI$, $PYR_{14}Tf$ and $PYR_{1(201)}TFSI$ ILs by cyclic voltammetry (CV) at 20 mV s^{-1} from the potential of the discharged electrode towards positive and negative potentials in order to evaluate capacitance response in the positive and negative domains and to identify the electrode potential ranges that ensure charge/discharge cycles of high coulombic efficiency. The high surface area of the ACT carbon amplifies the faradic contribution to the voltammetric currents related to IL oxidation and reduction when the potentials that mark the ESW limits are approached. Thus, the potential window within which it is possible to charge/discharge the high surface area carbon electrodes is narrower than the ESW reported in Table 1, which was determined with smooth, glassy carbon electrodes. At 60 °C the ACT carbon can be cycled at high efficiency (≥97%) in the range −2.6 V to +1.6 V vs. Fc/Fc$^+$ in the case of $PYR_{14}TFSI$ and $PYR_{14}Tf$ and −2.4 V to +1.6 V vs. Fc/Fc$^+$ in the case of $PYR_{1(201)}TFSI$. In these conditions the ACT carbon featured a specific capacitance of ca. 100 F g^{-1} in all the ILs, a value that decreased by ca. 20% when the temperature was lowered to RT. Given that the potential of the discharged carbon electrode is ca. −0.1 V vs. Fc/Fc$^+$, the negative electrode can sweep a 30% wider potential than the positive during the charge process, and, since the capacitance response is almost the same in the positive and negative domains, it has a higher charge storage capability than the positive. Thus, a proper electrode mass balancing requires 30% more carbon at the positive electrode so as to attain $V_{max} \geq 3.9$ V.

The AEDLC-A, AEDLC-B, and AEDLC-C supercapacitors were assembled with $PYR_{14}TFSI$, $PYR_{14}Tf$ and $PYR_{1(201)}TFSI$ solvent-free ILs, respectively, and ACT carbon electrodes with positive to negative electrode loading ratio (w_+/w_-) higher than 1 (Table 2). The AEDLCs were tested at 60 °C over several thousand galvanostatic charge/discharge cycles (>20,000 cycles) at 10–20 mA cm^{-2}, with $V_{max} > 3.5$ V and mainly ranging between 3.7 V and 4.0 V. The efficacy of the asymmetric configuration is demonstrated in Fig. 2, which shows the charge/discharge galvanostatic profiles of the AEDLC-C supercapacitor (left axis) with $PYR_{1(201)}TFSI$ electrolyte upon the 17,000th charge/discharge cycle at 10 mA cm^{-2} and 60 °C with $V_{max} = 3.8$ V and of its positive and negative electrodes (right axis) which reached the end-of-charge potentials of 1.6 V vs. Fc/Fc$^+$ and −2.2 V vs. Fc/Fc$^+$, respectively. The end-of-discharge potential of the two electrodes is higher than that at the first cycles (ca. −0.1 V vs. Fc/Fc$^+$) because of cell equilibration upon cycling. Table 2 reports the C_{sc}, ESR, E_{max} (from V_{max} to $1/2V_{max}$) and P_{max} values evaluated from discharge cycles carried out at 20 mA cm^{-2} and 60 °C with the reported V_{max} of the AEDLCs assembled with the different ILs. Given that it is feasible to assume that w_{sc} will be one-third of the supercapacitor module weight (w_{module}), the E_{max} values in Table 2 become 10–12 Wh kg^{-1}, i.e. double that of the EDLCs on the market at RT, whose cycling performance decreases as temperature increaes. This high-energy performance of IL-based AEDLCs was exhibited without sacrificing power and cyclability, the latter being tested by deep discharge cycles from V_{max} down to 0 V at 60 °C. The highest cycling stability was exhibited by the $PYR_{1(201)}TFSI$-based AEDLC-C, with a capacitance fade of 2% over 27,000 cycles performed with $V_{max} \leq 3.6$ V for the first 12,000 cycles and 3.7 V for the following 15,000 (3000 cycles were also carried out with $V_{max} = 3.8$ V), as

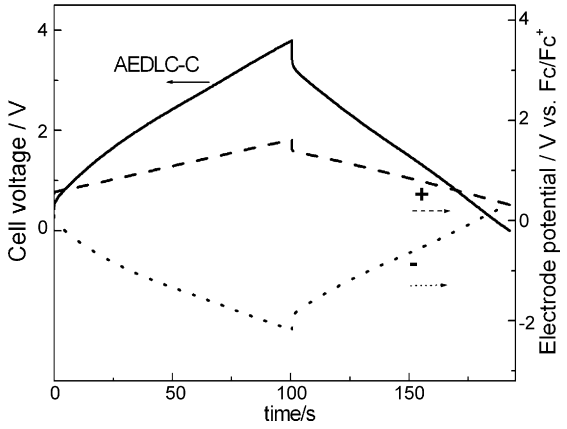

Fig. 2. Voltage profiles of the AEDLC-C supercapacitor with $PYR_{1(201)}TFSI$ electrolyte upon the 17,000th galvanostatic charge/discharge cycle at 10 mA cm^{-2} and 60 °C with $V_{max} = 3.8$ V and of its positive and negative ACT electrodes.

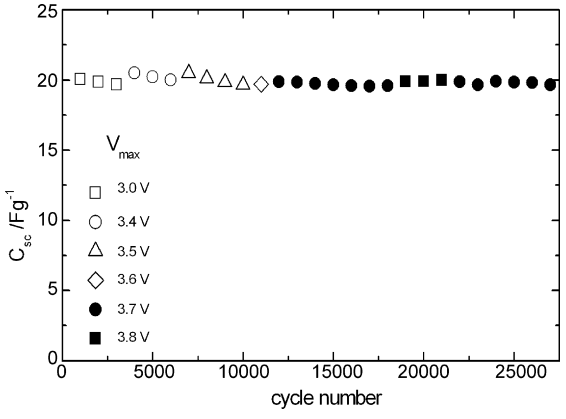

Fig. 3. Trend of specific capacitance (C_{sc}, in F g^{-1} of total composite electrode materials) over cycling at 60 °C and 20 mA cm^{-2} at different V_{max} of the AEDLC-C supercapacitor with $PYR_{1(201)}TFSI$ electrolyte.

Table 2
Positive to negative electrode loading ratio (w_+/w_-) of the AEDLC and HYSC supercapacitors with different ILs, and values of C_{sc}, ESR, E_{max} (delivered from V_{max} to $1/2V_{max}$) and P_{max} evaluated from galvanostatic cycles at ca. 1 A g^{-1} and 60 °C with the reported maximum cell voltage (V_{max}); specific values calculated considering only total composite electrode weight (w_{sc}).

Supercapacitor configuration	CODE	IL	w_+/w_-	V_{max} (V)	C_{sc} (F g^{-1})	ESR (Ω cm^2)	E_{max} (Wh kg^{-1})	P_{max} (kW kg^{-1})
Asymmetric EDLC	AEDLC-A	$PYR_{14}TFSI$	1.34	4.0	22	24	37	9.3
	AEDLC-B	$PYR_{14}Tf$	1.49	4.0	24	25	40	9.1
	AEDLC-C	$PYR_{1(2O1)}TFSI$	1.49	3.7	22	20	31	9.9
Hybrid supercapacitor	HYSC-A	$PYR_{14}TFSI$	0.74	3.9	32	35	51	13

shown by the C_{sc} trend vs. cycle number in Fig. 3. The AEDLC-A with $PYR_{14}TFSI$ featured 20% capacitance fade over 26,000 cycles with V_{max} between 3.6 V and 4.0 V, the last 20,000 being performed at the highest potential. The capacitance of the AEDLC-B supercapacitor with $PYR_{14}Tf$ decreased by 35% after 20,000 cycles, which were performed with V_{max} of 3.5 V/3.9 V over the first 8000 cycles and of 4.0 V in the following 12,000. The lower stability of the latter supercapacitor was mainly due to the fact that the hydrophilic character of $PYR_{14}Tf$ made it impossible to lower the water content in the electrolyte below 100 ppm with our drying procedure. On the other hand the dried, hydrophobic $PYR_{14}TFSI$ and $PYR_{1(2O1)}TFSI$ ILs featured ≤20 ppm of water. Thus, despite the higher formula weight of $PYR_{14}TFSI$ and $PYR_{1(2O1)}TFSI$ with respect to $PYR_{14}Tf$, which may eat into module gravimetric performance, we focused the following tests on the AEDLC-A and AEDLC-C systems. For a better comparison with practical performance of supercapacitors, average specific energy (E) and power (P) values were calculated from galvanostatic discharge curves at different current densities between V_{max}, and 1.35 V and at 60 °C and 20 °C using Eqs. (3) and (4):

$$E = i \int_{t_{V_{max}}}^{t_{1.35\,V}} \frac{V\,dt}{w_{module}} \quad (3)$$

$$P = \frac{E}{t_{1.35\,V} - t_{V_{max}}}, \quad (4)$$

respectively, where i is the current density, $t_{V_{max}}$ and $t_{1.35\,V}$ are the times at which the cells exhibit V_{max} and 1.35 V potentials and $w_{module} = 3w_{sc}$ is the expected weight of a complete supercapacitor module, including case. In Eqs. (3) and (4), 1.35 V was taken as end-discharge potential because it corresponds to that of the best performing EDLCs on the market, which operate between V_{max} and $1/2V_{max}$ with V_{max} = 2.7 V. The average E and P values of the AEDLC-A and AEDLC-C supercapacitors cycled with V_{max} of 3.9 V and 3.7 V, respectively, are shown in the Ragone plots in Fig. 4; the figure also highlights the requirement for power-assisted HEV application of electrochemical energy storage systems [3,4]. The 7.5 Wh kg^{-1} and 660 W kg^{-1} USABC target is met, and even exceeded, at 60 °C by both the AEDLCs and down to 20 °C only by the AEDLC-C with discharges at 10–20 mA cm^{-2} (0.5–1.0 A g^{-1}) from the fully charged state to 1.35 V, which corresponds to a D.O.D. of ca. 50%, as evaluated on the basis of practical charge values at the given rates. When the temperature is lowered from 60 °C to 20 °C, at i > 20 mA cm^{-2} the average specific energies of the AEDLCs decrease mainly because of the increase in the ohmic drop, that lowers the effective maximum cell voltage at which cell discharge begins. Because of the higher conductivity of $PYR_{1(2O1)}TFSI$ than $PYR_{14}TFSI$, the ohmic drop in the AEDLC-C is lower than in the AEDLC-A. Thus, despite the higher V_{max} of the latter, the former features higher practical energy and power values at both temperatures and has the extra advantage of being able to operate below RT because of the low freezing point of $PYR_{1(2O1)}TFSI$. These results were obtained with home-made cells; automated assembly and using a thinner separator than that featured by the AEDLCs would positively affect ohmic drop and E and P values.

To achieve higher specific energy than that of the IL-based AEDLCs, the $PYR_{14}TFSI$-based HYSC-A hybrid system was assembled with the same ACT carbon at the negative electrode and pMeT electropolymerized in IL as positive. We have already demonstrated that this electropolymerization enables pMeT electrodes to deliver specific capacitance of up to ca. 200 F g^{-1} in IL, i.e. double that of the double-layer carbons, in the potential range +0.3 V to +1.3 V vs. Fc/Fc$^+$ [18,19]. The HYSC-A cell was assembled with positive and

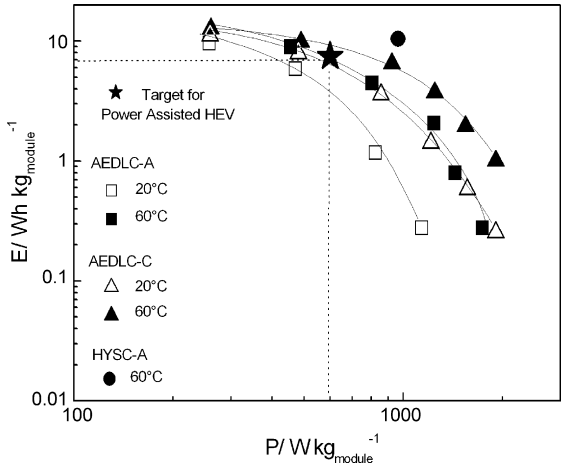

Fig. 4. Average specific energy (E) and power (P) values referred to expected module weight of IL-based AEDLC-A, AEDLC-C and HYSC-A supercapacitors from galvanostatic discharge curves at different currents and 20 °C and 60 °C between V_{max} and 1.35 V. For AEDLC-A, AEDLC-C and HYSC-A the V_{max} was 3.9 V, 3.7 V and 3.9 V, respectively; the currents were 5 mA cm^{-2}, 10 mA cm^{-2}, 20 mA cm^{-2}, 30 mA cm^{-2}, 40 mA cm^{-2}, 50 mA cm^{-2} for the AEDLCs (for AEDLC-A the data at 20 °C with i = 40 mA cm^{-2} and 50 mA cm^{-2} are not included) and 10 mA cm^{-2} for HYSC-A.

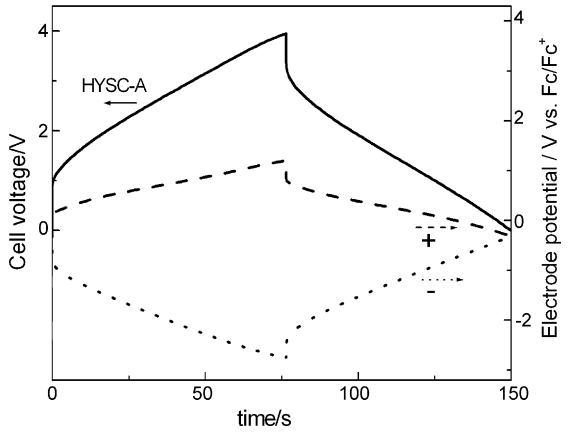

Fig. 5. Voltage profiles of the HYSC-A supercapacitor with $PYR_{14}TFSI$ electrolyte upon galvanostatic charge/discharge at 10 mA cm^{-2} and 60 °C with V_{max} = 3.9 V and of its pMeT positive and ACT negative electrodes.

negative electrodes with mass loading balanced on the basis of each charge storage capability, which in turn depends on specific capacitance and on the widest potential range for the electrode charge process. Table 2 shows the cycling performance at 60 °C of the HYSC-A, which was assembled with a w_+/w_- ratio <1 for a V_{max} of 3.9 V. The data were calculated from the galvanostatic profile at 10 mA cm^{-2} in Fig. 5, which also shows the potentials of the positive and negative electrodes of the HYSC-A system. The use of the pMeT electrode provides a 50% increase of C_{sc} and E_{max} with respect to those of the AEDLCs, i.e. 32 F g^{-1} and 51 Wh kg^{-1} are reached without sacrificing power; the expected E_{max} values of a complete module becomes at least 15 Wh kg^{-1}. The excellent performance of HYSC-A is highlighted in Fig. 4: the average values of E and P at 10 mA cm^{-2} and 60 °C for a hybrid supercapacitor module exceed the requirements for power-assisted HEVs. Note, however, that its cycling stability was not sufficiently long (data not reported). The HYSC-A's specific capacitance halved after 5000 cycles due to deterioration of the polymer electrode. Upon cycling, the positive electrode resistance markedly increased, presumably because pMeT swelling by IL worsened the electronic interchain conductivity in the polymer.

4. Conclusions

This is the first time that the performance at 60 °C and 20 °C of supercapacitors with different solvent-free ILs and featuring AEDLC and HYSC configurations are reported and compared for power-assisted HEV application. We demonstrate that pyrrolidinium-based AEDLCs meet, and even exceed at the highest temperature, the energy and power targets for this application, with cyclability over more than 20,000 cycles at 60 °C. Such asymmetric double-layer supercapacitors reach V_{max} of 4.0 V and E_{max} approaching 40 Wh kg^{-1} (only electrode materials included) so that they can compete with batteries and have the added advantage of inherently higher safety. While an IL-based hybrid supercapacitor with pMeT positive electrode electropolymerized in IL, negative carbon electrode and $PYR_{14}TFSI$ electrolyte delivers 30% higher energy than the AEDLCs, its cycling stability is not high enough to compete with the latter systems.

Acknowledgements

Work funded by the European Commission in the Sixth Framework Programme, Sub-programme Sustainable Surface Transport, under Contract No. TST4-CT-2005-518307 (Project ILHYPOS "Ionic Liquid-based Hybrid Supercapacitor"). All the partners in the Project are acknowledged. Evonik Industries provided $PYR_{1(2O1)}TFSI$.

References

[1] J.R. Miller, A.F. Burke, Interface 17 (2008) 53–57.
[2] A.F. Burke, Electrochim. Acta 53 (2007) 1083–1091.
[3] D. Howell, Energy Storage Research and Development, Vehicle Technology Program, 2007 Annual Progress Report, U.S. Department of Energy, Office of Vehicle Technologies Washington, DC, 2007, available at http://www1.eere.energy.gov/vehiclesandfuels/pdfs/program/2007_energy_storage.pdf.
[4] S.G. Stewart, V. Srinivasan, J. Newman, J. Electrochem. Soc. 155 (2008) A664–A671.
[5] M. Galiński, A. Lewandowski, I. Stępniak, Electrochim. Acta 51 (2006) 5567–5580.
[6] A. Lewandowski, M. Galinski, J. Power Sources 173 (2007) 822–828.
[7] M. Mastragostino, F. Soavi, J. Power Sources 174 (2007) 89–93.
[8] H. Liu, G. Zhu, J. Power Sources 171 (2007) 1054–1061.
[9] A. Balducci, R. Dugas, P.L. Taberna, P. Simon, D. Plée, M. Mastragostino, S. Passerini, J. Power Sources 165 (2007) 922–927.
[10] M. Lazzari, F. Soavi, M. Mastragostino, J. Power Sources 178 (2008) 490–496.
[11] M. Mastragostino, F. Soavi, in: J. Garche, C.K. Dyer, P. Moseley, Z. Ogumi, D. Rand, B. Scrosati (Eds.), Encyclopedia of Electrochemical Power Sources, Elsevier B.V., in press.
[12] S. Zhang, N. Sun, X. He, X. Lu, X. Zhang, J. Phys. Chem. Ref. Data 35 (2006) 1475–1517.
[13] Z.-B. Zhou, H. Matsumoto, K. Tatsumi, Chem. Eur. J. 12 (2006) 2196–2212.
[14] W.A. Henderson, S. Passerini, Chem. Mater. 16 (2004) 2881–2885.
[15] M. Conte, 23rd International Electric Vehicle Symposium (EVS23), Anaheim, CA, December 2–5, 2007.
[16] D. Cericola, Graduate Thesis, University of Bologna, Italy, October 2007.
[17] M. Lazzari, M. Mastragostino, F. Soavi, Electrochem. Commun. 9 (2007) 1567–1572.
[18] C. Arbizzani, S. Beninati, M. Lazzari, F. Soavi, M. Mastragostino, J. Power Sources 174 (2007) 648–652.
[19] M. Biso, M. Mastragostino, M. Montanino, S. Passerini, F. Soavi, Electrochim. Acta 53 (2008) 7967–7971.
[20] D.-W. Kim, S.R. Sivakkumar, D.R. MacFarlane, M. Forsyth, Y.-K. Sun, J. Power Sources 180 (2008) 591–596.
[21] J.L. Figueiredo, M.F.R. Pereira, M.M.A. Freitas, J.J.M. Órfão, Carbon 37 (1999) 1379–1389.
[22] A.G. Pandolfo, A.F. Hollenkamp, J. Power Sources 157 (2006) 11–27.

Journal of The Electrochemical Society, **156** (8) A661-A666 (2009)
0013-4651/2009/156(8)/A661/6/$25.00 © The Electrochemical Society

Dynamic Pulse Power and Energy of Ionic-Liquid-Based Supercapacitor for HEV Application

Mariachiara Lazzari,[z] Francesca Soavi,[z] and Marina Mastragostino[*,z]

Dipartimento di Scienza dei Metalli, Elettrochimica e Tecniche Chimiche, University of Bologna, 40127 Bologna, Italy

Asymmetric electrochemical double-layer carbon supercapacitors (AEDLCs) with *N*-methoxyethyl-*N*-methylpyrrolidinium bis(trifluoromethanesulfonyl)imide ($PYR_{1(2O1)}TFSI$) ionic-liquid electrolyte can safely cycle above room temperature with maximum cell voltage as high as 3.7 V over several thousand cycles and are thus promising candidates for hybrid electric vehicle (HEV) applications. Here, we report the energy and power performance of the $PYR_{1(2O1)}TFSI$-based AEDLCs in the −30 to 60°C temperature range evaluated by the conventional galvanostatic cycling and by the United States Advanced Battery Consortium and the U.S. Department of Energy (DOE) FreedomCAR benchmark protocols. The most outstanding finding is that the ionic-liquid-based supercapacitor meets the dynamic power and energy capability targets stated by DOE for power-assist HEVs.
 [DOI: 10.1149/1.3139046]

Manuscript submitted March 13, 2009; revised manuscript received April 27, 2009. Published May 28, 2009.

The market success of a clean transportation by hybrid electric vehicles (HEVs) needs high efficiency and safe and low cost electrochemical energy conversion systems. The performance requirements for these systems depend on the level of power-train hybridization, which increases from mild to full and plug-in HEVs, and on the kind of driving cycle. The targets set by the U.S. Advanced Battery Consortium (USABC) and the U.S. Department of Energy (DOE) for power-assist HEVs, i.e., the full HEVs with the highest level of hybridization, are pulse power of at least 625 W kg^{-1} for 10 s over more than 3×10^5 shallow cycles (25 Wh/cycle) and 7.5 Wh kg^{-1} total available energy, and for such application lithium-ion batteries are considered the best candidates.

Electrochemical double-layer capacitors (EDLCs), with positive and negative carbon electrodes charged/discharged by physical processes, satisfy the USABC power and cycle-life requirements for power-assist HEVs, but even the best performing on the market, which operate with organic electrolytes and maximum cell voltage (V_{max}) of 2.7 V, do not meet the specific energy target.[1-4] The EDLCs feature longer cycle life and higher specific power than batteries, are intrinsically more tolerant to such abusive conditions as overcharge and exposure to high temperatures, and, for the high energy efficiencies even >90%, can easily dissipate the amount of heat released upon the charge–discharge cycles. Thus, new-generation supercapacitors of increased energy may compete with lithium-ion batteries in power-assist HEVs, with the advantage of higher safety and reliability than the latter.

The cell voltage increase is the most powerful strategy to enhance supercapacitor energy and power, and it requires the use of electrolytes of wide electrochemical stability matched with high ionic conductivity, low vapor pressure, and high thermal stability window for safe operative regimes. This is the case of the *N*-methoxyethyl-*N*-methylpyrrolidinium bis(trifluoromethanesulfonyl)imide ($PYR_{1(2O1)}TFSI$) room-temperature molten salt, which remains liquid down to −95°C and is thus usable without solvents and which features a 5.0 V wide electrochemical stability window with conductivities of 1.10^{-4}–1.10^{-2} S cm^{-1} in the −30/ + 60°C temperature operation range of HEVs.[5-8]

Asymmetric electrochemical double-layer capacitors which feature positive and negative electrodes of different carbon loadings (AEDLCs), with $PYR_{1(2O1)}TFSI$ ionic liquid (IL) and specifically designed carbon electrodes, at 60°C can cycle with V_{max} up to 3.7 V over more than 20,000 deep cycles with a capacitance fade of 2% and outperform EDLCs on the market in terms of specific energy and power.[8]

Here, we present and discuss the results of a study carried out to test the power and energy performance of these $PYR_{1(2O1)}TFSI$-based AEDLCs in the −30 to 60°C temperature range for HEV application. Along with the traditional Ragone plots obtained by galvanostatic cycling at different current rates, the results of tests performed to evaluate the dynamic pulse power and energy features by the USABC and DOE FreedomCAR reference protocols are given. These benchmarks include the reference capacity test (RCT), which provides the available energy of the supercapacitor at various states of charge, and the hybrid pulse-power characterization (HPPC) that gives the dynamic power and energy capabilities at different states of charge and depths of discharge (DODs).[4,11,12] The results of the tests carried out to evaluate the feasibility of the use of IL-based AEDLCs for both 10 s pulse power assist and for 2 s pulse applications, such as 12 V start-stop (TSS), 42 V start-stop (FSS), and 42 V transient power assist (TPA), are given. The performance of the $PYR_{1(2O1)}TFSI$-based AEDLCs at 30°C is also compared to those estimated in Ref. 4 for commercial 2.7 V EDLCs.

Experimental

The $PYR_{1(2O1)}TFSI$-based AEDLC supercapacitors were assembled with electrodes (0.64 cm^2 geometric electrode area) based on the 95% w/w carbon–5% w/w poly(tetrafluoroethylene) binder (Du-Pont) composite material laminated on carbon-coated aluminum current collectors (Lamart Corp. grids of 3.7 mg cm^{-2} of geometric area) and cut from belts prepared by a preindustrial production line. The carbon was PICACTIF SUPERCAP BP10 (Pica), which was treated at 1050°C in Ar for 2 h before lamination to clean the carbon surface (demonstrated by thermogravimetric analysis and Fourier transform IR analyses) and to favor an uptake of the hydrophobic IL. The treated carbon (hereafter named ACT) maintained the same low level of graphitization of the pristine and displayed a total pore volume of 1.2 cm^3 g^{-1} with a pore size distribution centered at 2.7 nm. Seventy–one percent of the pore volume was originated by pores wider than 1.5 nm, i.e., wider than IL ion size, and provided a surface area of 940 m^2 g^{-1} accessible to the electrolyte for the double-layer charging process, as evaluated by the density functional theory analysis of its N_2 adsorption isotherm.[8,9] The positive and negative electrodes featured carbon-binder composite loadings of 10.5 and 6.3 mg cm^{-2}, respectively, so that the total loading for the two electrodes (w_{cm}) was 16.8 mg cm^{-2}. The cells (Swagelok type) were assembled in a dry box (MBraun Labmaster 130, H_2O and $O_2 < 1$ ppm) using a fiber glass filter as a separator (Durieux, 200 μm thick when pressed); the separator and electrodes were soaked under vacuum with the IL before the assembly. The

* Electrochemical Society Active Member.
[z] E-mail: mariachiara.lazzari@studio.unibo.it; francesca.soavi@unibo.it; marina.mastragostino@unibo.it

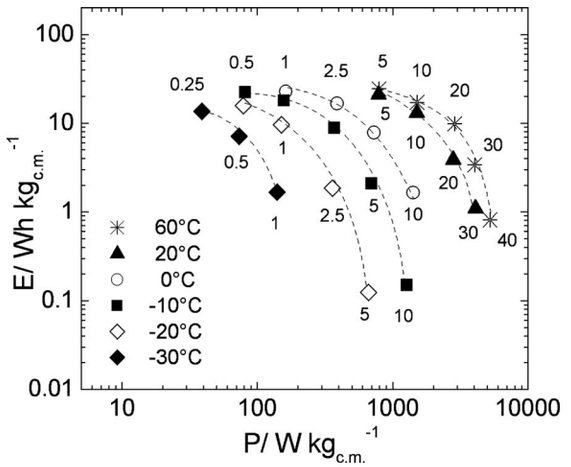

Figure 1. Traditional Ragone plot of the $PYR_{1(2O1)}TFSI$-based AEDLC supercapacitor at different temperatures. Specific energy (E) and power (P) values have been evaluated referring to the total carbon-binder composite loading as in Eq. 1 and 2, respectively, from galvanostatic discharges at different currents with V_{max} = 3.7 V and V_{min} = 2.035 V; the labels indicate the current densities in mA cm^{-2}.

$PYR_{1(2O1)}TFSI$ (Evonik Industries, 1.43 g mL^{-1} density) displayed $\leq$20 ppm of water checked by Karl Fisher titration (684 KF Coulometer Metrohm).

The electrochemical tests were performed with a Perkin-Elmer VMP multichannel potentiostat/galvanostat at temperatures controlled by a Thermoblock (FALC) or a cryostat (HAAKE K40), and the results were validated over more than 10 cells.

Results and Discussion

The $PYR_{1(2O1)}TFSI$-based AEDLC supercapacitors with ACT carbon electrodes were tested with V_{max} = 3.7 V and a minimum cell voltage (V_{min}) equal to 55% V_{max}, i.e., 2.035 V, in the temperature range of −30/ + 60°C at different currents by two different procedures. A traditional study was carried out by consecutive galvanostatic charge/discharge cycles, and then the supercapacitor was subjected to a test protocol tailored for HEV applications.

Figure 1 reports the traditional Ragone plots at different temperatures of the $PYR_{1(2O1)}TFSI$-based AEDLC with specific energy (E) and power (P) being evaluated from the galvanostatic discharges as in Eq. 1 and 2, respectively

$$E = \int_{t_{V_{max}}}^{t_{0.55\ V_{max}}} V\mathrm{d}t/w_{cm} \qquad [1]$$

$$P = E/(t_{0.55\ V_{max}} - t_{V_{max}}) \qquad [2]$$

where i is the current density, $t_{V_{max}}$ and $t_{0.55\ V_{max}}$ are the times at which the cells exhibit 3.7 and 2.035 V potentials, and w_{cm} is the total carbon-binder composite loading.

The data in Fig. 1 indicate that the $PYR_{1(2O1)}TFSI$-based AEDLCs can operate in a wide temperature range. The specific energy and power decrease with temperature because of the related decrease in the IL conductivity. Indeed, the latter impacts the Ohmic drop and thus the practical cell voltage at which the cell discharge begins; this is particularly evident at the highest currents. The equivalent series resistance (ESR) of the cell, evaluated from the Ohmic drop at the beginning of the discharge, increases from 15 ± 5 Ω cm^2 at 60°C to 410 ± 130 Ω cm^2 at −30°C (at each temperature, the dispersion in the ESR value is strictly related to the cell assembly, which was manually performed). At the lowest currents, when the temperature changes from 60 to −30°C, the cell specific capacitance referred only to the total composite loading varies from 26 to 16 F g^{-1} (corresponding to a single carbon electrode capacitance of ca. 100 and 60 F g^{-1}), and a fourfold increase in the current density at the two temperatures reduces the capacitance values by 25 and 75%, respectively. At 30°C, the $PYR_{1(2O1)}TFSI$-based AEDLCs capacitance compares well with that of commercial EDLCs operating with conventional organic electrolytes. The capacitance decrease of the IL-based supercapacitor with temperature decrease is related to the nature of the carbon/solvent-free IL interface. Indeed, in the solvent-free IL, the double layer is constituted by a monolayer of ions up against the charged carbon surface; therefore the capacitance is strictly related to IL polarizability, which affects the dielectric constant in the double layer as the conductivity of the bulk electrolyte.[9,10]

The characterization of the $PYR_{1(2O1)}TFSI$-based AEDLCs for HEV applications was performed following the standards stated by DOE in the "FreedomCAR Battery Test Manual for Power-Assist Hybrid Electric Vehicles"[11] and in the "FreedomCAR Ultracapacitor Test Manual."[12] To evaluate if supercapacitors may replace batteries in power-assist HEVs, which need modules with a specific available energy of at least 7.5 Wh/kg for 10 s 625 W/kg pulses at 30°C, we followed the standard tests reported in the former manual, slightly modified following the indications reported in the latter one, which takes into account the different natures of the charge/discharge processes in supercapacitors with respect to batteries. The FreedomCAR Ultracapacitor Test Manual was properly developed to evaluate the supercapacitor performance for quite conventional applications, such as 12 V TSS, 42 V FSS, and 42 V TPA, which require 800, 600, and 650 W/kg pulse powers (referred to the total module weight), respectively, with an available energy of 3 Wh/kg over 2 s pulses.

The protocol that we adopted includes the RCT and the HPPC in the −30/ + 60°C temperature range, including 30°C, which is the reference temperature of DOE targets. According to Ref. 4, the specific parameters evaluated by such tests and reported in the following refer to a total module mass (w_{module}), which is twice the total composite electrode mass, i.e., $w_{module} = 2w_{cm}$, so as to include the other components' weights.

The RCT test is carried out to evaluate the total available energy of the supercapacitor at various states of charge and for different DODs. It was performed by a 5C galvanostatic charge up to V_{max} = 3.7 V, a potentiostatic charge at this potential for ca. 10 min, and a galvanostatic discharge at 5C down to V_{min} = 2.035 V. The 5C current rate, i.e., that for the supercapacitor full discharge in 1/5 h (12 min), may be evaluated referring to the theoretical charge Q_t, which is given by Eq. 3

$$Q_t = C(V_{max} - V_{min}) \qquad [3]$$

where C is the supercapacitor capacitance. However, as reported above, the $PYR_{1(2O1)}TFSI$-based AEDLC capacitance and practical cell voltage excursion upon the discharge, which is always narrower than $V_{max} - V_{min}$, vary with temperature. Thus, we experimentally determined the current densities for 5C discharge rates at −30, −20, 0, 30, and 60°C, and the values are reported in Table I. The table also shows the experimental specific capacity ($Q_{100\%\ DOD}$) and the specific energy ($E_{100\%\ DOD}$) delivered upon the 5C discharges with 100% DOD. Figure 2 shows the plots of the cell potential and of the specific cumulative energy removed during the discharge (E_{DOD}) vs DOD from the RCT test at 5C and 30°C. E_{DOD} is evaluated from the discharge profile between V_{max} = 3.7 V and the potential, which marks the DOD (V_{DOD}, with 2.035 V < V_{DOD} < 3.7 V), by using Eq. 4

$$E_{DOD} = i\int_{t_{V_{max}}}^{t_{V_{DOD}}} V\mathrm{d}t/w_{module} \qquad [4]$$

where $t_{V_{DOD}}$ is the time at which the cells exhibit the V_{DOD} voltage.

Table I. Values at different temperatures of current density, specific capacity ($Q_{100\%\ DOD}$), and specific available energy ($E_{100\%\ DOD}$) delivered upon the RCT discharge between V_{max} = 3.7 V and V_{min} = 2.035 V (DOD = 100%) at the 5C rate of the $PYR_{1(2O1)}$TFSI-based AEDLC. Specific values are referred to the module weight ($w_{module} = 2w_{cm}$).

T (°C)	5C rate (mA cm^{-2})	$Q_{100\%\ DOD}$ (mAh g^{-1}_{module})	$E_{available,100\%\ DOD}$ (Wh kg^{-1}_{module})
60	0.92	5.0	15
30	0.92	5.0	15
0	0.66	4.7	13
−20	0.55	3.5	9
−30	0.37	2.2	6

The HPPC characterization, which provides the dynamic power and energy capabilities over the V_{max}/V_{min} voltage range by a test profile that incorporates both discharge and regenerative pulses, was performed as follows. The test begins with a 5C galvanostatic/potentiostatic charge at a given cell potential, followed by a rest period. Then, a sequence that consists of a 10 s discharge pulse at the I_{dis} current, a 5 s open-circuit voltage (OCV) step, a 10 s regenerative pulse at the $I_{reg} = 75\%I_{dis}$ current, and a 5C galvanostatic discharge with 10% DOD is repeated until the V_{min} cutoff potential is reached.[11,12] This sequence represents an accelerated test because the suggested OCV period should be in the range 30–60 min. The pulse currents are set in relation to the supercapacitor maximum current (I_{max}), which is a characteristic feature of the electrochemical device and which corresponds to the current required to cause an immediate (i.e., <0.1 s) 20% voltage drop in a fully charged device.[12] The I_{max} of the $PYR_{1(2O1)}$TFSI-based AEDLC reported in Table II significantly decreases moving from 60 to −30°C because the voltage drop is proportional to ESR, and the latter increases when temperature decreases. The pulse sequence can be performed at two different I_{dis} currents: for the "low-HPPC" test, the I_{dis} is 25% I_{max}; for the "high HPPC," the I_{dis} is 75% I_{max}. Table II reports the I_{dis} current densities that we adopted in the HPPC tests at different temperatures. For the reference operative condition of 30°C, the order of magnitude of I_{max} is 20 mA cm^{-2}; thus the low and high HPPC I_{dis} current densities are of ca. 5 and 15 mA cm^{-2}, respectively. The low HPPC sequences at −20 and −30°C were not performed because the corresponding I_{dis} could not be considered "pulse" current being lower than the 5C rates at the same temperatures (see Table I).

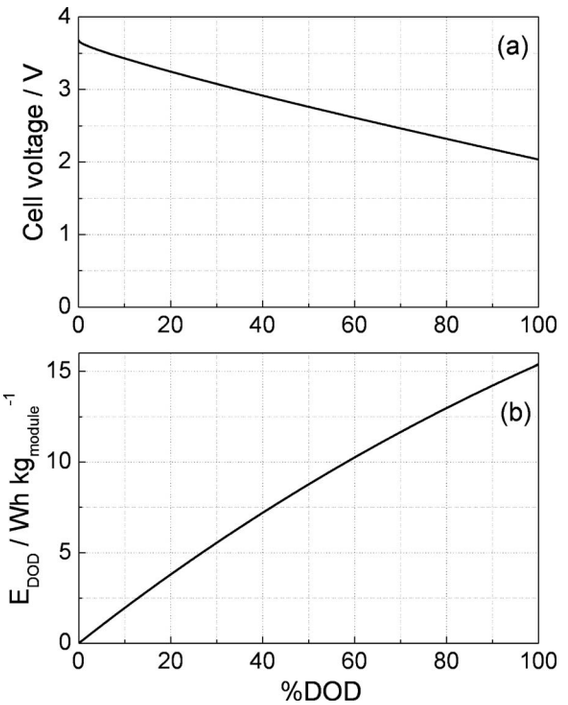

Figure 2. (a) Cell voltage vs DOD and (b) specific cumulative energy (E_{DOD}, referred to module weight) vs DOD from the RCT discharge at 5C and 30°C with V_{max} = 3.7 V and V_{min} = 2.035 V of the $PYR_{1(2O1)}$TFSI-based AEDLC supercapacitor.

Figure 3 reports the voltage profile of the $PYR_{1(2O1)}$TFSI-based AEDLC upon the low HPPC test at 30°C. The specific discharge (P_{dis}) and regenerative (P_{reg}) pulse-power capabilities are calculated from the HPPC sequence as in Eq. 5 and 6

$$P_{dis} = 2.035(V_0 - 2.035)/(R_{dis}w_{module}) \quad [5]$$

Table II. Maximum (I_{max}) and discharge pulse (I_{dis}) currents and DOD limits (DOD_{min},DOD_{max}) for low and high HPPC tests at different temperatures with pulse times (Δt_{pulse}) of 10 and 2 s of the $PYR_{1(2O1)}$TFSI-based AEDLC. For each temperature, the C-rate is calculated referring to the corresponding experimental capacity $Q_{100\%\ DOD}$ reported in Table I.

T (°C)	I_{max} (mA cm^{-2})	HPPC	I_{dis}		Δt_{pulse} (s)	DOD_{min}–DOD_{max} (%)
			mA cm^{-2}	C-rate		
60	20	Low	5	34C	10	7–84
					2	2–92
		High	15	102C	10	24–55
					2	10–78
30	15	Low	4	22C	10	5–85
					2	2–92
		High	10	61C	10	18–63
					2	7–80
0	6	Low	1.5	9.5C	10	1–85
					2	0–91
		High	5	29C	10	23–56
					2	10–73
−20	2	High	1.4	12C	10	10–65
					2	3–75
−30	0.5	High	0.4	5.6C	10	1–76
					2	0–80

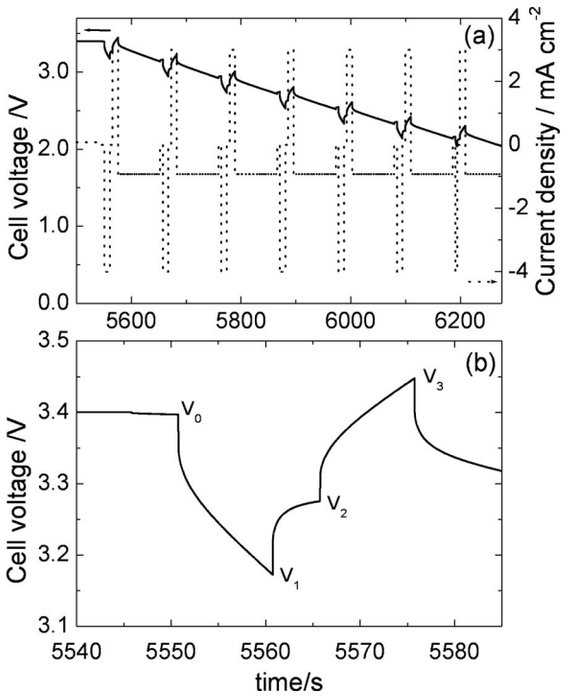

Figure 3. (a) Cell voltage (solid line) and current density (dotted line) vs time upon the low HPPC test at 30°C of the $PYR_{1(2O1)}TFSI$-based AEDLC and (b) magnification of the cell voltage profile during the first discharge/regenerative pulse.

$$P_{reg} = 3.7(3.7 - V_2)/(R_{reg} w_{module}) \quad [6]$$

where R_{dis} and R_{reg} are the discharge (R_{dis}) and regenerative (R_{reg}) pulse resistances, which are given by

$$R_{dis} = (V_1 - V_0)/I_{dis} \quad [7]$$

$$R_{reg} = (V_3 - V_2)/I_{reg} \quad [8]$$

As marked in Fig. 3b, V_0 and V_2 are the cell potentials at the beginning of the discharge and regenerative pulses, respectively, and V_1 and V_3 are the potentials at the end of these pulses. The 10 s pulse sequence can be used even to calculate the P_{dis}, P_{reg}, R_{dis}, and R_{reg} values for a pulse time (Δt_{pulse}) of 2 s. This can be done by using in Eq. 7 and 8 the V_1 and V_3 values evaluated after 2 s from the beginning of the pulses.

R_{dis} and R_{reg} depend on the $(V_1 - V_0)$ and $(V_3 - V_2)$ values, which in turn include the Ohmic drop/rise and the linear variation in the cell voltage over time, which is an intrinsic characteristic of the capacitive charge/discharge process of the supercapacitor (see Fig. 3b). Hence, unlike batteries, supercapacitors feature R_{dis} and R_{reg}, which increase with Δt_{pulse}, as shown by the pulse resistance values calculated from 10 and 2 s low HPPC tests at 30°C and at different DODs of the $PYR_{1(2O1)}TFSI$-based AEDLC reported in Fig. 4. Consequently, the P_{dis} and P_{reg} evaluated from the 10 s sequence are systematically lower than those from the 2 s pulses, as evidenced by the pulse-power capability vs DOD plots reported in Fig. 5, which were obtained from the low and high HPPC tests at 30°C of the AEDLC. In Fig. 5 the P_{reg} axis has been properly scaled, as suggested in Ref. 11 and 12 to match P_{dis} with the target value of $P_{reg} = 80\%$ of P_{dis}.

Given that at DOD = 100% and 0% P_{dis} and P_{reg} are zero (see Eq. 5 and 6), the interpolation of the pulse-power data in Fig. 5a and b should cross the y-axis origins. However, the HPPC sequence is cut when $V_1 \leq 2.035$ V or $V_3 \geq 3.7$ V; hence the lowest and highest values of V_0 and, consequently, the maximum (DOD_{max}) and minimum (DOD_{min}) DOD, at which complete discharge and regenerative pulses take place, depend on I_{dis}, I_{reg}, R_{dis}, R_{reg}, and Δt_{pulse}. For the $PYR_{1(2O1)}TFSI$-based AEDLC, full duration pulses are feasible only within the DOD limits reported in Table II, which thus cut the P_{dis} and P_{reg} vs DOD plots. At 30°C, 10 s pulses can be performed in the DOD ranges of 5–85% by low HPPC and of 18–63% by high HPPC, as marked in Fig. 5. Within such DOD limits, the P_{dis} and P_{reg} values evaluated by the two tests at low and high currents are very similar. In both cases the discharge and regenerative curves cross at $P_{dis} = 1250$ and 2400 W kg^{-1} for 10 and 2 s pulses, respectively, and at DOD of 24%. The power at this cross point, which represents the maximum value simultaneously satisfied

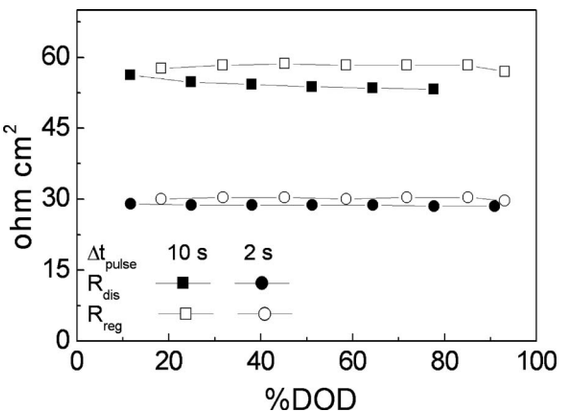

Figure 4. R_{dis} and R_{reg} values at different DODs of the $PYR_{1(2O1)}TFSI$-based AEDLC evaluated from low HPPC test at 30°C with $\Delta t_{pulse} = 10$ and 2 s.

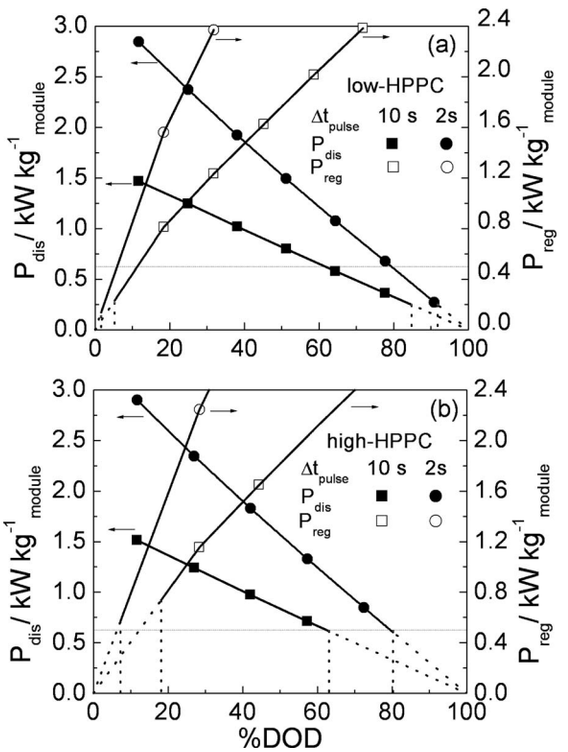

Figure 5. Discharge (P_{dis}) and regenerative (P_{reg}) pulse-power capability referred to module weight vs DOD of the $PYR_{1(2O1)}TFSI$-based AEDLC at 30°C from (a) low HPPC and (b) high HPPC tests with $\Delta t_{pulse} = 10$ and 2 s. The horizontal dashed line indicates the DOE 10 s P_{dis} goal.

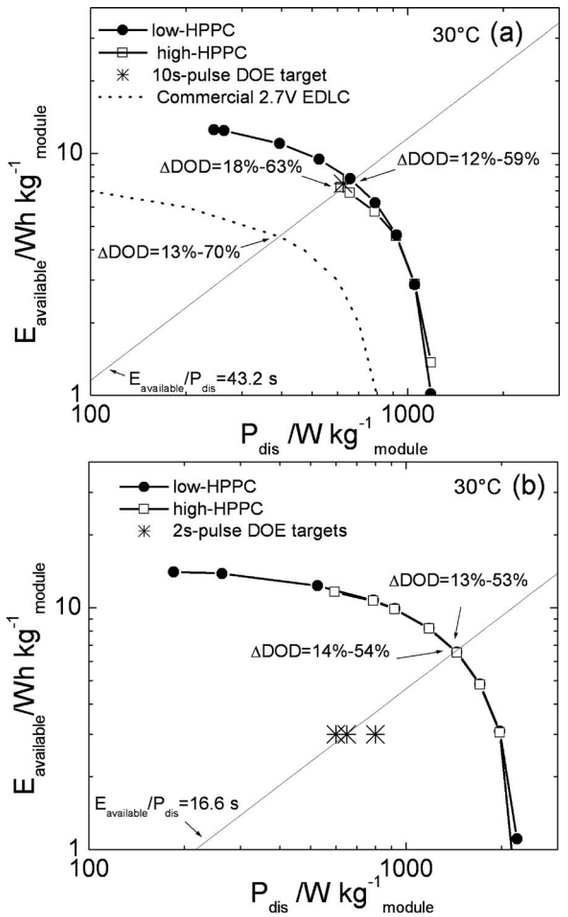

Figure 6. Available energy ($E_{available}$) vs discharge pulse-power capability (P_{dis}) at 30°C of the $PYR_{1(2O1)}$TFSI-based AEDLC referred to module weight from low and high HPPC tests with (a) Δt_{pulse} = 10 s and (b) 2 s. (∗ = DOE targets; dotted line: commercial EDLCs operating with V_{max} = 2.7 from Ref. 4).

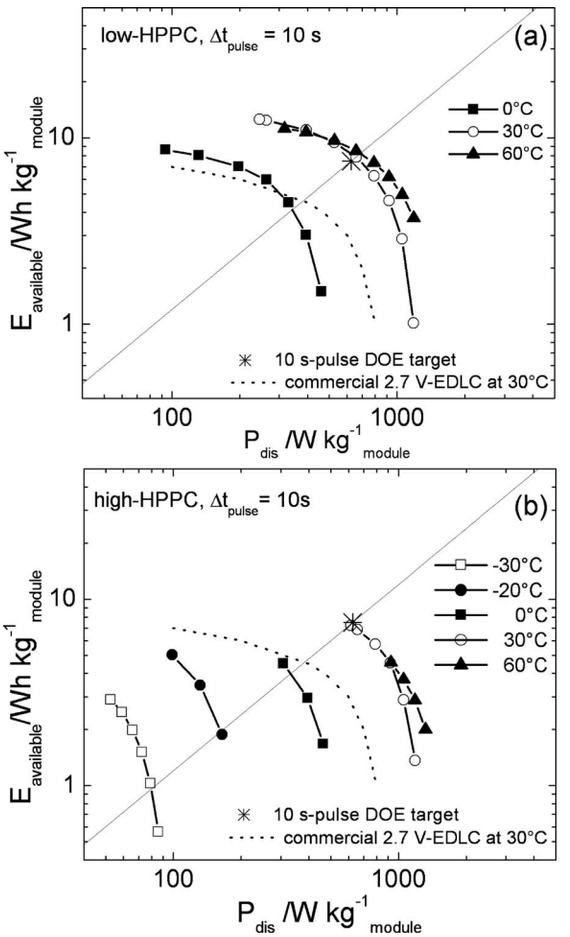

Figure 7. Available energy ($E_{available}$) vs discharge pulse-power capability (P_{dis}) with Δt_{pulse} = 10 s of the $PYR_{1(2O1)}$TFSI-based AEDLC referred to module weight from (a) low HPPC and (b) high HPPC tests at different temperatures (∗ = 10 s pulse DOE target; dotted line: commercial EDLCs operating at 30°C with V_{max} = 2.7 from Ref. 4).

in the discharge and the generative pulses, is significantly higher than the DOE target, which is evidenced by a horizontal line in the two figures.

Starting from the cross point of the discharge and regenerative pulse-power curves, as the demand for power lowers, the usable DOD range (ΔDOD), within which the condition P_{reg} = 80% P_{dis} is satisfied, widens. Consequently, the specific available energy ($E_{available}$), which is the energy that can be removed during a 5C discharge over the ΔDOD range and that corresponds to the difference between the E_{DOD} values at the two ΔDOD limits, increases. As an example, for a 10 s low HPPC at 30°C, P_{dis} = 625 W kg^{-1} and P_{reg} = 500 W kg^{-1} at DOD = 61% and 11% (Fig. 5a), where the E_{DOD} are 10.40 and 2.14 Wh kg^{-1} (Fig. 2b), respectively. Hence, the energy available in ΔDOD = 11–61% is 8.26 Wh kg^{-1}. For the 10 s high HPPC test, a P_{dis} of 625 W kg^{-1} is feasible within a ΔDOD, which is limited by the 18% DOD_{min} value for the regenerative pulse and 62% for the discharge pulse.

The trend of the energy available in a ΔDOD range where given discharge and regenerative pulse powers are met vs P_{dis} is described by "HPPC–Ragone plots" such as those shown in Fig. 6-8. Figure 6a reports the HPPC–Ragone plots at 30°C of the $PYR_{1(2O1)}$TFSI-based AEDLC from the 10 s low and high HPPC tests of the IL-based supercapacitor and the DOE goal for 10 s pulse applications in power-assist HEVs; the figure also reports the expected performance of a commercial EDLC operating with V_{max} = 2.7.[4] Figure 6b shows the HPPC–Ragone plots at 30°C obtained from 2 s low and high HPPC tests with the indication of the DOE goal for 2 s pulse applications in HEV.

The most striking result is that, as evidenced in Fig. 6a, the $PYR_{1(2O1)}$TFSI-based AEDLC meets the requirement for power-assist HEV application, and because of the high V_{max} of 3.7 V it can deliver an $E_{available}$ energy sufficiently high to compete with batteries for 10 s, 625 W/kg pulses. Figure 6b shows that the HPPC–Ragone plots shift to higher P_{dis} values when pulses are shortened to 2 s, so that at 30°C the IL-based supercapacitor significantly overcomes the performance required for the 12 V TSS and 42 V FSS and TPA applications in HEVs, which represent a quite "conventional" use of supercapacitors in transportation.

The HPPC tests of the $PYR_{1(2O1)}$TFSI-based AEDLC were also run in the temperature range of −30/+60°C, and Fig. 7 and 8 report the corresponding HPPC–Ragone plots. At −30 and −20°C, only the high HPPC tests were performed because the I_{dis} current for the low HPPC characterization is lower than that corresponding to a 5C rate (at the same temperature). Figures 7 and 8 demonstrate that the $PYR_{1(2O1)}$TFSI-based AEDLC can cycle between −30 and +60°C, which is the envisioned temperature range for HEVs. At $T \geq 30°$ the IL-based supercapacitor meets the power-assist HEV targets, and

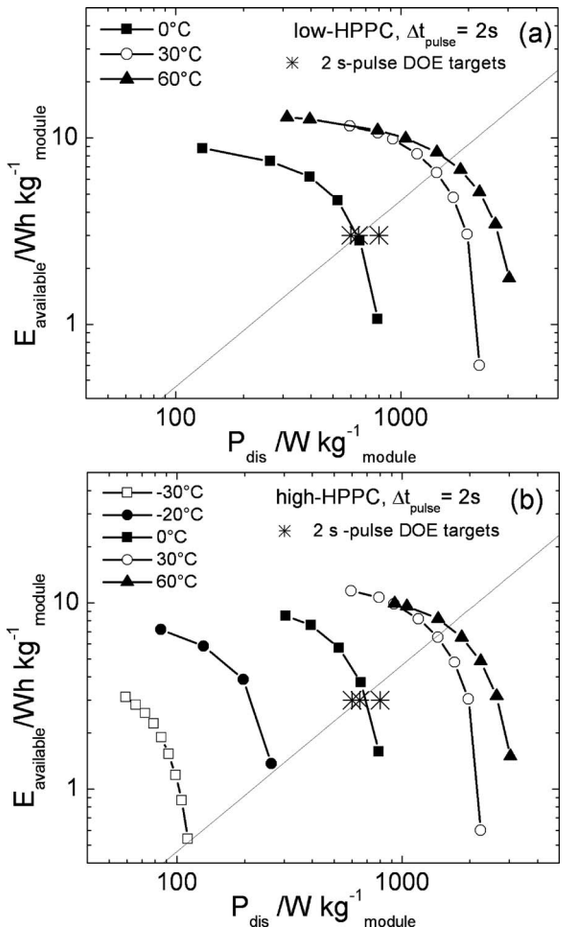

Figure 8. Available energy ($E_{available}$) vs discharge pulse-power capability (P_{dis}) with $\Delta t_{pulse} = 2$ s of the $PYR_{1(2O1)}TFSI$-based AEDLC referred to module weight from (a) low-HPPC and (b) high-HPPC tests at different temperatures (* = 2 s pulse DOE targets).

at 0°C it features a performance similar to that exhibited at 30°C by the commercial EDLC. At 0°C the $PYR_{1(2O1)}TFSI$-based AEDLC also satisfies the 2 s pulse DOE requirements.

Conclusions

This paper reports on the results of an experimental study carried out to evaluate the dynamic pulse power and energy features of IL-based supercapacitors by the USABC and DOE FreedomCAR reference protocols for HEV. The $PYR_{1(2O1)}TFSI$-based AEDLC can operate between −30 and +60°C with a high V_{max} of 3.7 that makes it possible to meet at $T \geq 30$°C the challenging energy and power targets stated by DOE for power-assist HEVs and at $T \geq 0$°C the standards for the 12 V TSS and 42 V FSS and TPA 2 s pulse applications if the ratio $w_{module}/w_{cm} = 2$ is accomplished. This is a very demanding condition because the w_{module} is affected by the electrolyte mass, which fills the carbon pores and separator and in turn depends on the carbon pore volume and the electrolyte density. In the supercapacitors based on solvent-free IL, the carbon electrode pores are filled with the electrolyte at the maximum ion concentration, and the IL amount in the pores could be in excess with respect to that required for the double-layer charge/discharge. Hence, reduction in carbon pore volume to < 1 cm^3 g^{-1} without sacrificing specific capacitance would be beneficial to the component weight distribution in the module.

This work demonstrates that the use of $PYR_{1(2O1)}TFSI$ IL in AEDLC is a powerful strategy to develop high voltage supercapacitors that might compete with lithium-ion batteries in power-assist HEVs with the added advantage of inherently higher safety.

Acknowledgments

Work funded by the European Commission in the Sixth Framework Programme, Sub-programme Sustainable Surface Transport, under contract no. TST4-CT-2005-518307 (Project ILHYPOS "Ionic Liquid-Based Hybrid Supercapacitor"). Evonik Industries and Leclanché Lithium GmbH are acknowledged for the useful collaboration in the project.

Dipartimento di Scienza dei Metalli, Elettrochimica e Tecniche Chimiche, University of Bologna assisted in meeting the publication costs of this article.

References

1. J. R. Miller and A. F. Burke, *Electrochem. Soc. Interface*, **17**(1), 53 (2008).
2. A. F. Burke, *Electrochim. Acta*, **53**, 1083 (2007).
3. D. Howell, Energy Storage Research and Development, Vehicle Technology Program, 2007 Annual Progress Report. U.S. DOE, Office of Vehicle Technologies Washington, D.C. (2007), available at http://www1.eere.energy.gov/vehiclesandfuels/pdfs/program/2007_energy_storage.pdf.
4. S. G. Stewart, V. Srinivasan, and J. Newman, *J. Electrochem. Soc.*, **155**, A664 (2008).
5. Z.-B. Zhou, H. Matsumoto, and K. Tatsumi, *Chem.-Eur. J.*, **12**, 2196 (2006).
6. S. Ferrari, E. Quartarone, P. Mustarelli, A. Magistris, S. Protti, S. Lazzaroni, M. Fagnoni, and A. Albini, *J. Power Sources*, In press
7. M. Mastragostino and F. Soavi, in *Encyclopedia of Electrochemical Power Sources*, J. Garche, C. K. Dyer, P. Moseley, Z. Ogumi, D. Rand, and B. Scrosati, Editors, Elsevier, New York (In press).
8. C. Arbizzani, M. Biso, D. Cericola, M. Lazzari, F. Soavi, and M. Mastragostino, *J. Power Sources*, **185**, 1575 (2008).
9. M. Lazzari, M. Mastragostino, and F. Soavi, *Electrochem. Commun.*, **9**, 1567 (2007).
10. S. Baldelli, *J. Phys. Chem. B*, **109**, 13049 (2005).
11. INEEL, "FreedomCAR Battery Test Manual for Power-Assist Hybrid Electric Vehicles," Prepared for the U.S. Department of Energy (2003).
12. INEEL, "FreedomCAR Ultracapacitor Test Manual," Prepared for the U.S. Department of Energy (2004).